OPTICAL SPECTROSCOPY OF Ti^{3+} and Cr^{3+} IONS IN SOME CRYSTALLINE AND GLASSY MATERIALS

FAREED F RASHEED

Department of Physics and Applied Physics

University of Strathclyde

Thesis submitted for the degree of Doctor of Philosophy in Physics

December 1988

CHAPTER 5 (Contd) Page

Abstract

This thesis reports optical absorption and luminescence studies of Ti^{3+} doped glasses and ionic crystals and of Cr^{3+}-doped glasses. The ion-lattice coupling of Ti^{3+} in $A\ell_2O_3$, $YA\ell O_3$ and YAG was studied via the temperature dependence of the optical spectra, the different coupling strengths being reflected in the optical properties of these systems. A comparison of the relative quantum efficiencies in these crystals showed that the excited state decay of Ti^{3+} in $YA\ell O_3$ is purely radiative up to T = 300K, in contrast to the behaviour in $A\ell_2O_3$ and YAG. Absorption and time resolved luminescence measurements were also carried out for Ti^{3+} doped phosphate glass of different Ti^{3+} concentrations, which showed the importance of inhomogeneous broadening in such materials.

An important component of this study was concerned with Cr^{3+} doped glasses, where in addition to the general absorption and luminescence, the site selection spectroscopy and time resolved techniques were carried out. The $^2E \rightarrow {}^4A_2$ transition was investigated using the fluorescence line narrowing (FLN) to understand the structural and dynamic properties of the homogeneously broadened transitions, which are normally obscured in glasses by the inhomogeneous broadening, the origin of which lie in the disorder nature of the glassy materials. The distorted symmetry of the high field sites was investigated using Zeeman spectroscopy coupled to the fluorescence line narrowing, where the

Zeeman splittings of the $^2E \rightarrow {}^4A_2$ transitions were measured to reveal weak trigonal distortion of the predominantly octahedral symmetry in these glasses.

Acknowledgments

I would like to express my gratitude and thanks to Professor B Henderson for his guidance, continuous encouragment and kindness during the course of this study. Many thanks are due to Dr K P O'Donnell for his help with the experimental work and discussions during most of the period of this work and also to Dr Carol Trager, who helped me complete an important part of this work with her computing experience. I still remember with thanks Dr P N Gibson for his experimental help in the early stages of this study. I greatly appreciated the helpfulness of the academic, technical and clerical staff in the Department of Physics and Applied Physics and particularly Mr D Clark for his help in constructing and developing some of the experimental apparatus. Also a special mention for the friendship, helpfulness and good spirit of my colleagues in the Solid State Spectroscopy group, especially Messrs A Marshall, M Gilmartin and B Williamson. Many thanks are due to my wife for her patience and encouragement throughout this work and also for her help with the drawing of many figures. Finally, I wish to thank Mrs Jean Lindores for her extra effort and patience to get this work typed in a short period.

CHAPTER ONE

1. TRANSITION METAL IONS DOPED LASER MATERIALS

1.1 Introduction

The properties of optically active centres in solids have been the subject of study for several reasons. Firstly, such centres have electronic states separated by energies of the order of few electron volts, and the absorption and emission of electromagnetic radiation involve photons of visible or near visible light. Secondly, the optical spectroscopy can be regarded as a probe of the environment at the dopant ion site, giving information about the structure and properties of the electronic states and their interaction with the ions of the host lattice in which they have been incorporated. Thirdly, they are of technological importance in the new and fast growing fields of solid state lasers and opto-electronics.

No perfect solid is known in nature. All solids contain growth imperfections, impurities, vacancies, or dislocations. Such defects in solids change their optical properties, by creating energy levels in the band gap between which optical transitions take place as a consequence interaction with an electromagnetic radiation. The colours of different solids are due to their absorption of certain wavelengths when exposed to white light; a process of subtractive colouration.

A host material containing transition metal ions is usually absorbed weakly in the visible, making possible transmission of the luminescence from the ion. As a general rule host crystals readily accept substitutional impurities into the crystal structure. In particular, compounds like oxides, fluorides and other inorganic insulators are suitable hosts for transition metal ions; since the energy gap between the valence and the conduction bands is large, such crystals are transparent in the visible region of the electromagnetic spectrum. The transition metal ions (T.M.I.) which substitute in many inorganic materials have an incomplete outer shell, readily substitute in many such ionic crystals having energy levels separated by less than the gap energy photons, so resulting in an absorption and emission in the visible region. The rest of this chapter is devoted to reviewing the developments of tunable solid state laser materials, in particular, the spectroscopy of (T.M.I.) doped in crystals and glasses. The characteristic energy levels of those materials have been considered using static crystal field theory to calculate the splitting of energy levels in crystal fields of different strength and symmetries.

In chapter 2 we consider the effects of dynamic lattice and showed how the electron-phonon interaction modulates electric transitions yielding vibronic transitions (broad bands) as well as pure electronic transitions (sharp lines). The origins of such transitions is discussed. A description of the experimental techniques used in this study is given in chapter 3. The optical properties of Ti^{3+}-doped crystals and glasses is given in chapter 4. Particular attention is given to the polarized emission and absorption characteristics of Ti^{3+}, doped sapphire ($A\ell_2O_3$) Ti^{3+}:YAG ($Y_3A\ell_5O_{12}$), and Ti^{3+}:YAP ($YA\ell O_3$) crystals. We also measured the effect of temperature on the bandwidth of the broadband emission of the Ti^{3+}:doped crystals. Phosphate glass doped with Ti^{3+} ions of different concentrations have been studied using time resolved spectroscopy and decay rate measurements. In chapter 5 we discuss the behaviour of Cr^{3+} ions dopants in several glass hosts studied using standard absorption and emission spectroscopy to understand the effects of the glass host compositions and the temperature on the shape of the optical spectra, type of luminescence and the efficiency of the emission. Time resolved spectroscopy has been used to differentiate between different sites occupied by Cr^{3+} in those systems. Chapter 6 is devoted to the application of Fluorescence Line Narrowing (FLN) to the energy level structure of Cr^{3+}:glass systems, which cannot be recognized by conventional optical techniques due to the gross inhomogeneous broadening of the $^2E \rightarrow {}^4A_2$ transitions in glassy material. An overall conclusion of the results yielded is presented at the end of this study.

1.2 Tunable Solid State Laser Materials

Although the essential idea of stimulated emission was introduced by Einstein a long time ago,[1] the research into lasers didn't materialise until Schawlaw and Townes[2] considered the necessary conditions for population inversion in the three and four-level systems. These workers also considered the precise mechanism by which inversion could lead to amplification of the stimulated emission in the microwave, infrared and optical regions. The acronym LASER means light amplification by the stimulated emission of radiation. In the first laser, discovered by Maiman[3] in (1960), the gain medium was a solid ionic crystal (Ruby). The host crystal ($A\ell_2O_3$) was activated by the transition metal ion (Cr^{3+}) which gives rise to a sharp (R-line) red emission at (694.3 nm). Some three years after the discovery of the Ruby laser, the first tunable solid state laser action was achieved at Bell Laboratories by Johnson et al.[4] who used Ni^{2+}:MgF_2. This was followed by developments of the theory of laser action ending on a higher vibrational level of the ground state,[5] as well as the employment of many other Ni^{2+} and Co^{2+} doped crystals.[6,7] After the discovery of Nd:YAG and dye lasers, the work on tunable transition metal ion laser crystals slowed down, till the late 1970s, when J.C. Walling et al.[8] developed the Alexandrite laser. This laser system is broadly tunable in the wavelength range 710-820nm and operates at room temperature. There has since been a resurgence of the interest in solid state laser materials, mostly on the trivalent ions Cr^{3+} and Ti^{3+}, and on divalent ions like Ni^{2+}, Co^{2+} and V^{2+}.

Rare earth ions with their 4f electronic shell shielded by the higher 5S and 5d shells, have a weak interaction with the host lattice, so the emission from these ions is mostly as zero phonon sharp lines. The one exception appears to be the 4f ion Ce^{3+} which interacts more strongly with the host lattice. At present $Ce:LaF_3$ operates on the shortest laser emission wavelength, λ=285.5nm.[9] Other rare earth ions such as Ho^{2+} and Sm^{2+} also based on sharp lines just as in $Sm^{2+}:CaF_2$;[10] where vibronic lasing action is achieved[11] at low temperature. In 1974 Johnson et al.[12] obtained room temperature tunable laser action from the $Ho^{3+}:BaY_2F_8$. These last two examples involve sensitization of the laser action by Er and Tm which act to enhance the absorption of light. Other laser systems includes colour centres and semiconductor lasers.[13] Transition metal ions differ from the rare earth's, because of the strong interaction between electrons in the outer shell (3d) of the ion and the host lattice vibrations (discussed in detail in chapter 2). Many important parameters such as laser wavelength, gain cross section, and the nature of laser operation (3 or 4-level) change with different hosts.[14]

Transition metal ion (T.M.I) doped solids have the potential as lasers tunable in the red-infrared spectral range. The ($3d^3$) ion Cr^{3+} has been doped into such hosts as garnets (e.g. GSGG, YGG, GSAG... etc.), Chrysoberyl ($BeA\ell_2O_4$) and the weak crystal field material ($ZnWO_4$). Unlike Cr^{3+}:YAG and ruby these materials could be tunable utilizing the broad $^4T_2 \rightarrow {}^4A_2$ transition.

The other interesting transition metal ion is Ti^{3+}, which has only one electron in the outermost shell ($3d^1$). When doped into sapphire ($A\ell_2O_3$), Ti^{3+} emits into a very broad band giving a wide laser tuning range between (660 to 1060 nm) at room temperature.[15]

Two other crystals and one glass host for Ti^{3+}, YAG, YAP and phosphate glass have been studied by the author. Laser action in some ion-doped glasses was reported early in the 1960s using Nd,[16] Yb and Gd[13] for which the line emission was broader than its counterpart in the crystals. Transition metal ion doped in glasses may be of importance in the developments of new solid state lasers (see chapter 5). However, the drawbacks with glassy laser materials are the low thermal conductivity, small quantum efficiency and efficient non-radiative decay from the excited state. More comprehensive studies of glass structural properties might lead to improvements in the growth and formulation of optical glasses, which in turn could reduce the advantages that crystal lasers have over glasses, especially in terms of cheap, large samples of laser material. On the other hand a growth of crystallites in glass matrices (ceramics) also promise improvement of the quantum yield for laser action. Transition metal ion doped materials offer the potential for high energy storage and high pulse and output power.

This potential derives from the low oscillator strength of their laser emission bands, and consequently the slow rate of spontaneous emission. It also derives from the fact that the host materials are often hard, durable, stable, and longlived with high thermal conductivity (with the exception of glasses). On the other hand the low oscillator strength has a disadvantage which is the low gain, and the need for highly efficient cavities. Activities in crystal growth and some theoretical methods for new laser material selection[16] are proceeding with more intensive spectroscopic and structural studies to find new candidates for laser action and to optimize the optical properties for the current laser materials. Tunable transition metal ion lasers are now covering the range from 660nm to 2280nm (see figure (1.1)).[17]

Tunable lasers based on solid state materials become important in a number of applications, including spectroscopy, remote sensing and LIDAR. Several of the new solid state lasers offer broader tunability and higher output powers than the more common tunable dye lasers. Some devices operate in wavelength regions not accessible by dyes. The study of tunable solid state lasers has helped to stimulate basic research in transition metal ions and colour centre physics, as well as challenging the technology of crystal growth.

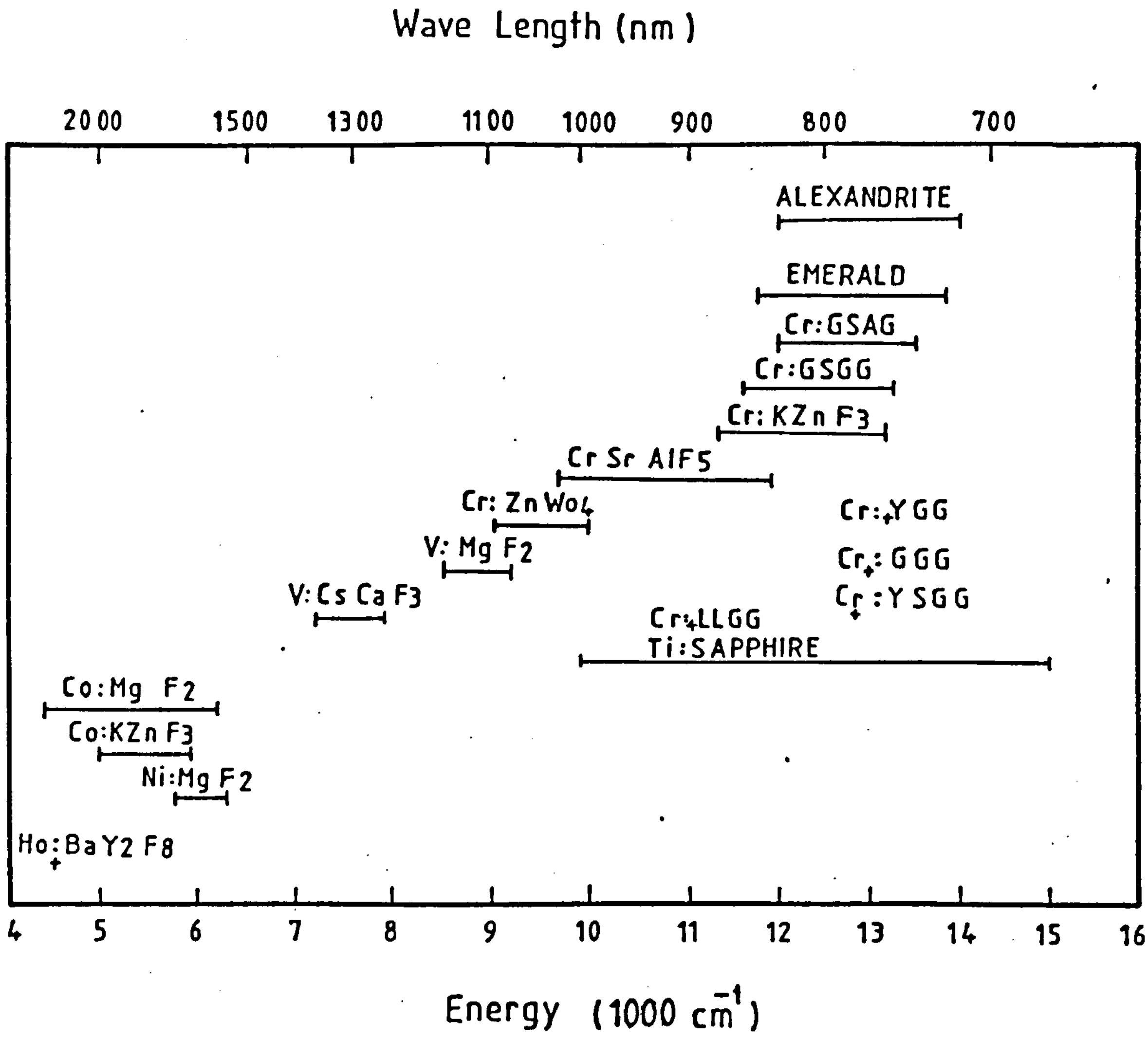

Fig 1.1 Wavelength coverage of tunable T.M.I. lasers (after J C Walling[17]).

1.3 Transition Metal Ions as Active Centres

Transition metal ions are characterized by an incomplete outer 3d shell and in consequence a number of low lying energy levels between which optical transitions can take place. These ions when added in a low concentration to an insulating material make them optically active. because the (3d) electrons are not well screened from the electrostatic fields of the ions in the crystal, their spectroscopic properties are strongly influenced by their environment, especially by the vibrations of the ligand ions. These vibrations lead to broadening of the optical transition and the optical spectra of (T.M.I.) are characterized by both broad and sharp transitions. Lattice vibrations may also lead to non-radiative relaxation processes from the excited state which could reduce the efficiency of luminescence. Transitions within $(3d^n)$ configuration are parity forbidden, because they belong to the same electronic configuration. In the case of the R-line emission of the $(3d^3)$ configuration, i.e. the $^2E \rightarrow {}^4A_2$ transition, they are both spin and parity forbidden, and the radiative lifetime is typically of the order of milliseconds. If the transition is between two states of the same spin multiplicity then the singly (parity only) forbidden transitions are one or two orders of magnitude stronger (see section (2.5)).

The dominance of one process or another is illustrated by the simplified energy level diagram of ($3d^3$) (T.M.I.) in octahedral crystal field [18] (figure 1.2) where only two excited states are shown. This diagram is drawn for normalized energy of the low lying states, and the normalized energy of the state E/B is plotted against the normalized strength of the electrostatic crystal field, Dq, the constant of normalization being (B), the Racah parameter.

It can be seen that the $^4T_2 \rightarrow {}^4A_2$ transition will dominate in materials where (Dq/B) is below the crossover point (shown with the dashed line), i.e. below 2.2, this case described as the low field case. Materials with (Dq/B) values > 2.2 are referred to as high field systems. Intermediate cases have values near Dq/B ≅ 2.2. Cr^{3+} in $BeAl_2O_4$, the garnets and different glasses are examples of this situation, typically both transitions being seen at room temperature.

1.4 Classification of Materials

The case of the ($3d^3$) ions (Cr^{3+}) will be used to demonstrate the classification of materials according to the crystal field strength. Table 1.1 shows the three types of crystal fields where (Δ) is the energy difference between ($^4T_2$) and (^2E) levels. The value of (Δ) can vary by some (± 2500 cm^{-1}).[19] For ruby Δ ~ 2300 cm^{-1}, while for Alexandrite ($Cr^{3+}:BeAl_2O_4$) it is ~ 800 cm^{-1}, and vibronic emission is predominant in the case of Cr^{3+} doped elpasolite

($Cr^{3+}:K_2N_aS_cF_6$) in which $\Delta = -1000$ cm^{-1}.[20] In Cr^{3+}:glasses the Dq/B value covers a wide range of values corresponding to an intermediate to low crystal field which categorizes them as candidates for broad vibronic transitions. The effects of crystal fields on the splitting of the free ion energy levels and the nature of the transitions between these levels will be explained in detail later. However, it is noted by Jorgensen[21] that, when the ligand ion is fixed and the transition metal ions varied, the energy difference between the (t_{2g}) and the (e_g) orbitals of a single electron in cubic crystal field, i.e. 10 Dq increases in the following order:

$Mn^{2+} < Ni^{2+} < Co^{2+} < Fe^{2+} < V^{2+} < Fe^{3+} < Cr^{3+} < V^{3+} < Co^{3+} < Mn^{4+}$.

In octahedral coordinates, where six negatively charged ligand ions are equidistant from the central T.M.I., then the sign of the crystal field potential is the same as that calculated for a case of negative point charges (see Fig 1.3). The potential at a point (x,y,z) at a distance $r \ll R$ from the centre is[22]:

$$V(x,y,z) = \frac{6e}{R} + \frac{35er^4}{4R^5}\left(x^4 + y^4 + z^4 - \frac{3}{5}\right) + \text{higher terms} \qquad (1.1)$$

where R is the interatomic distance. In equation (1.1) the first term of the equation has no angular variation; it changes the energy of all d-electrons on the central ion by the same amount. While the second term gives rise to a spin operator term. Most importantly it may be shown that (Dq) varies with the interatomic

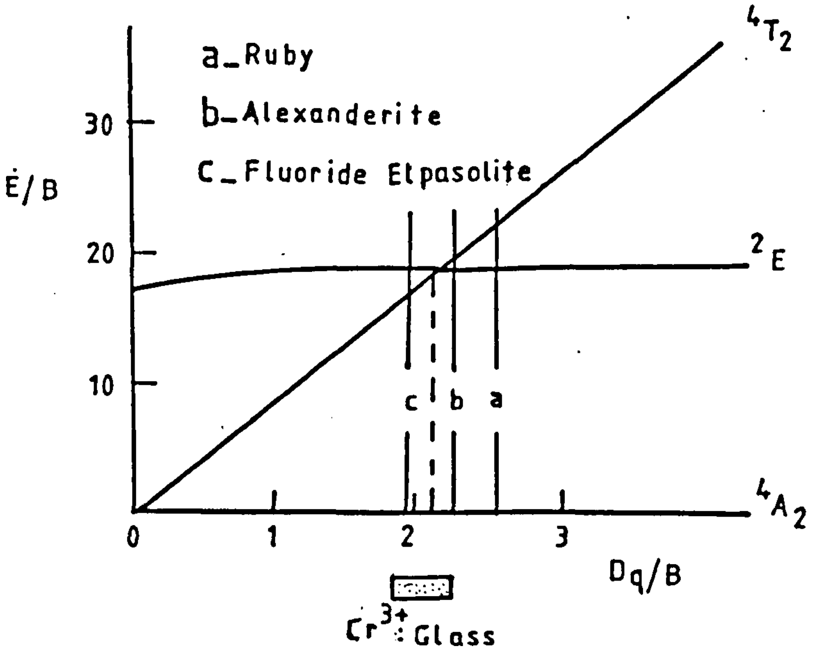

Fig 1.2 Energy level diagram for $3d^3$ ions in octahedral crystal field with different Dq values.

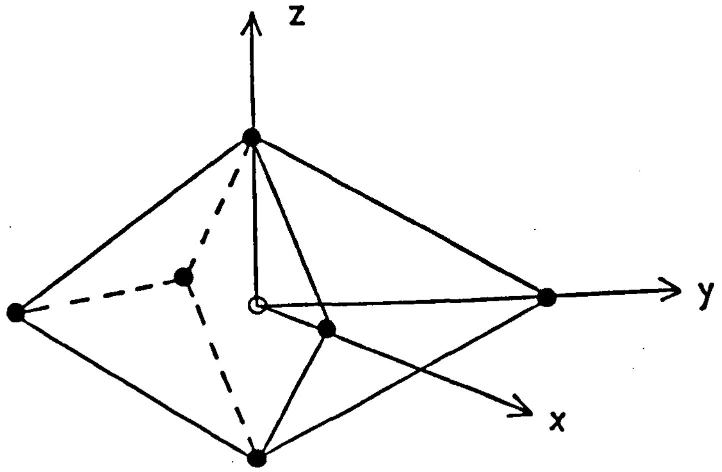

Fig 1.3 An ion in a cubic crystal field.

distance (R) as (R^{-5}) implying that compounds with larger interatomic spacings are in general characterized by lower fields.

1.5 Concentration Quenching

When (T.M.I.) are doped into a host material in low concentrations, they may be considered as isolated optical centres, each one acting independently of all others. It is well known that luminescence efficiency decreases if the activator concentration is increased above a certain value, the so-called critical concentration (X_C). This phenomenon is called the concentration quenching: as the concentration of the ions increases, individual ions begin to interact electrostatically. As a result the energy of one ion may be transferred to a neighbouring ion. All explanations of the concentration quenching involve in one way or another the phenomenon of energy transfer. Consider two luminescent centres (A) and (B): if we excite into the centre (A), this excitation may be transferred to ion (B). Disregarding the obvious case of energy transfer by radiative processes we consider a transfer to occur non-radiatively. A condition for transfer to occur between (A) and (B), One of the energy levels of B must be degenerate with the excited level of (A), as illustrated in (fig 1.4).

The interaction between the two centres may proceed via two essentially different mechanisms, (i) by Coulomb interaction between the particles of (A) and (B), the only possible interaction if the two centres are so far apart that their charge clouds do not overlap, and (ii) when the charge clouds do overlap, transfer may also occur by exchange interaction between the electrons of (A) and (B).

A general theory of the concentration quenching was proposed by Dexter and Schulmann[23]. Their model assumes that when the dopant concentration increases above the critical concentration, the distance between the dopant ions becomes so small that the energy transfer between these ions occurs enabling the excitation to migrate through the crystal until it reaches sites at which de-excitation may occur non-radiatively. These sites (Killer sites) may be other impurities, defects, surface sites, etc..., all of which may be present in a real crystal. An example is (Cr^{3+}:Al_2O_3), where it was found[24] that the excitation migrates from one isolated (Cr^{3+}) to another isolated (Cr^{3+}), until in the vicinity of (Cr-Cr) pair to which it transfers its energy non-radiatively. It was found[25,26] that for crystals with (Cr^{3+}) concentrations of (0.3-0.4) atm % transfer between isolated ions vanishes. Finally, for many transition metal ion-doped solids it was known that a decrease in the decay time as well as a reduction in the quantum efficiency, as the concentration of the dopant ion increases, obviously such factors may limit possible laser operation.

1.6 Energy Levels of Transition Metal Ions in Solids

1.6.1 The free ion

The transition metals (iron group) are the elements after Ca(40) in the periodic table when the (3d) shell is being filled. In ionic solids such elements use the outer (4S) electrons and some (3d) electrons in forming ionic bands, so the resulting electronic configuration is:

$$1S^2 2S^2 2p^6 3S^2 3p^6 3d^n \quad \text{where} \quad (n < 10)$$

In table (1.2) we can see some of the (T.M.I.) with their electronic configuration. The partly empty (3d) shell of these ions has a number of energy levels between which optical transitions take place.

Table 1.1 Classification of materials according to the crystal field

Transition	Type of Field	Dq/B	$\Delta(^4T_2-^2E)$	Type of emission
$^2E \rightarrow {}^4A_2$	High	>2.2	>0	sharp line
$^4T_2, ^2E \rightarrow {}^4A_2$	Intermediate	~2.2	~0	mixture of sharp lines and broad band
$^4T_2 \rightarrow {}^4A_2$	low	<2.2	<0	broad band

Table 1.2 Electronic Configuration of some Transition Metal Ions

T.M.I.	Electronic Configuration
Ti^{3+}	$1S^2\ 2S^2\ 2p^6\ 3S^2\ 3p^6\ 3d^1$
V^{3+}	$3d^2$
V^{2+}, Cr^{3+}	$3d^3$
Mn^{3+}	$3d^4$
Mn^{2+}, Fe^{3+}	$3d^5$
Fe^{2+}, Co^{3+}	$3d^6$
Co^{2+}	$3d^7$
Ni^{2+}	$3d^8$
Cu^{2+}	$3d^9$

As mentioned above the interaction between these (3d) electrons (which are outside the ion core) and the electric fields of the neighbouring ions (the crystal field) are very strong.

Because the crystal lattice on which the ions reside is not static, each optical centre takes part in the vibrational motion of the host. In consequence, the electronic levels are modulated by lattice vibrations. It is convenient to consider theoretically the states of the free ion, then to take the interaction with the static neighbouring ions into account and then consider the effects due to vibrational motion of the ion in the crystal. The energy level (E) and the eigenfunction (ψ) of the ions are found in the Schrödinger equation:

$$H\psi = E\psi$$

The free ion Hamiltonian (H_{FI}) can be written as:

$$H_{FI} = H_o + H_{e-e} + H_{s-o} \qquad (1.2)$$

where H_o is the summation of the kinetic energy of electrons, and the potential energy of the electrons in the nucleus field, i.e.

$$H_o = \sum_i \left[\frac{p_i^2}{2m} + V_{(R_i)}\right] \qquad (1.3)$$

$$H_{e-e} \equiv \frac{1}{4\pi\epsilon_o} \sum_{i>j} \frac{e^2}{r_{ij}}$$

is the electrostatic Coulomb interaction energy between the outer electrons

$$H_{s-o} = \sum_i \xi\,(r_i)\,\ell_i . s_i$$

is the spin-orbit interaction energy.

For atoms of low atomic number (Z) the effect of the Coulomb interaction H_{e-e} between the outer electrons is bigger than that of the spin-orbit coupling.

To solve the wave equation for the free ion Hamiltonian (Eqn. (1.2)) it is treated as the unperturbed Hamiltonian since (as could be seen in (Eqn. (1.3)) (H_o) is the sum of a single electron terms, the eigenfunctions of (H_o) are products of single electron eigenfunctions characterized by the quantum numbers n, ℓ, m_ℓ, m_s. When Coulomb and the spin-orbit interactions are included in the Hamiltonian, the eigenfunctions are described by quantum numbers of the total orbital angular momentum $\bar{L} = \sum_i \bar{\ell}_i$, total spin angular momentum $\bar{S} = \sum_i \bar{S}_i$, and the total angular momentum $\bar{J} = \bar{L} + \bar{S}$. For transition metal ions, the interaction among the (3d) electrons results in the formation of electronic states which can be represented by ($^{2S+1}L_J$) and the representations are labelled (S,p,D,F,....) according to L = 0,1,2,3,...

1.6.2 Static crystal field

When an ion is introduced into a crystal, the observed spectra may include both sharp lines and broad bands, whereas for free ions sharp lines only are expected. This suggests that the electrostatic field acting on the ion in the crystal is important. This electrostatic crystal field reflects the symmetry of the crystalline environment of the ion, and this symmetry leads to a classification of each crystal field. Three common crystal arrangements are shown in figure (1.5). In octahedral symmetry (lablled O_h) a central cation is situated at the centre of the six equally spaced, negative point charges (-Ze) each a distance of (a) from the origin along the orthogonal axes $\pm x$, $\pm y$, $\pm z$. When four negative ions are placed at the vertices of a regular tetrahedron at the centre of which is the cation (figure 1.5(ii)). The crystal field is said to have tetrahedral symmetry (labelled T_d). In figure (1.5 (iii)) the crystal field due to eight ions with equal charge (-Ze) at the eight vertices of a regular cube is said to have cubic symmetry. The commonest arrangements found is of a six neighbouring anions, slightly distorted from perfect octahedral symmetry. Elongations or compressions along <111> direction of the cube lead to trigonal symmetry and tetragonal distortions occur along a <100> direction. More complex distortions lead to even lower symmetry. However octahedral crystal field component is the strongest and the weak component is the one of lower symmetry.

Wavefunctions and energy levels in octahedral fields are usually calculated first and then the weak lower symmetry crystal field introduced using a perturbation theory. Hence an ion in a solid which is subjected to an electrostatic field originating from the surrounding ligands could be described by the Hamiltonian:

$$H = H_{FI} + H_C \qquad (1.4)$$

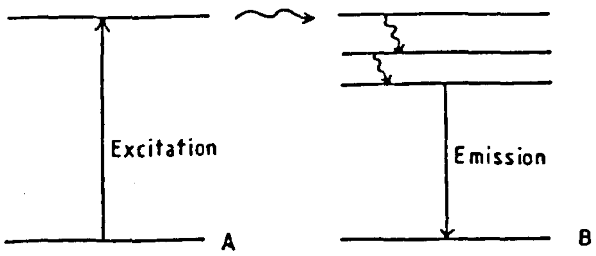

Fig 1.4 Energy transfer process between two centres.

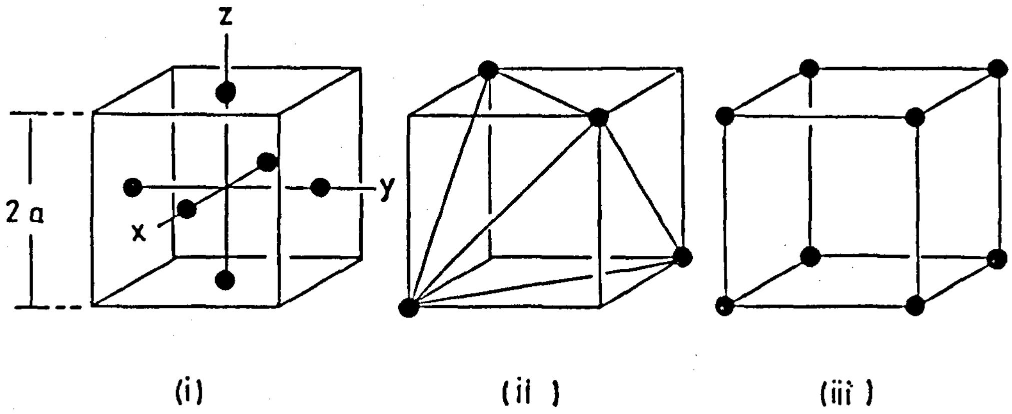

Fig 1.5 Some types of crystal symmetry
(i) octahedral (ii) tetrahedral (iii) cubic

where H_c is the crystal field Hamiltonian term which represent the interaction energy of the outer electrons of the dopant ion with the electrostatic crystal field.

The determination of the eigenstates and the eigenvalues of the Hamiltonian in Eqn (1.4) depends on the relation between the sizes of the different components of that Hamiltonian.

1.6.3 The classification of crystal field

We mentioned above for free ions that the possible electronic states can be represented by ($^{2S+1}L_J$) and these states are in the form of (S,P,D,...). In a static crystal field the energy levels of the ion are split by the crystal field. The way that these energy levels split as the symmetry of the Hamiltonian is reduced can be found from the character tables of the various symmetry groups. For example, the effect of cubic crystal field in splitting the free ion energy levels into a number of sublevels can be seen in table (1.3). It is convenient to classify the strength of the crystal field (H_c) in terms of its magnitude relative to other terms of the Hamiltonian, Eqn (1.4), three different situations arise:

Table 1.3 The splitting of Russel-Saunders states by cubic electrostatic crystal field

L	Free ion spectroscopic notation	Splitting
0	S	A_1
1	P	T_1
2	D	$E + T_2$
3	F	$A_2+T_1+T_2$
4	G	$A_1+E+T_1+T_2$
5	H	$E+2T_1+T_2$
6	I	$A_1+A_2+E+T_1+2T_2$

(a) Weak crystal field

$$H_C \ll H_{e-e} \ll H_{s-o}$$

When H_C is disregarded initially, and the free ion Hamiltonian must be solved, H_C is then considered as a perturbation on the free ion energy levels. The $^{2S+1}L_J$ eigenfunctions of the free ion are adopted as basis functions for the perturbation H_C. This weak field approach is suitable for trivalent rare earth ions, where the screening of the active 4f electrons from the lattice ions leads to the weak crystal field.

(b) Intermediate crystal field

$$H_{s-o} < H_c < H_{e-e}$$

H_{s-o} is ignored and the effect of H_c on individual (3d) states is calculated first. Since H_c is an orbital operator, the free ion L functions are used as basis functions to calculate the matrix elements of H_c from which new crystal field orbital states are formed. Spin-orbit coupling is taken then as a perturbation on the new states.

(c) Strong crystal field

$$H_c > H_{e-e} > H_{s-o}$$

In this case the crystal field term, H_c is added to Eqn (1.3), i.e.

$$H_o' = H_o + H_c \tag{1.5}$$

is first solved, the eigenstates of H_o' being labelled according to the irreducible representation of the symmetry group of H_o'. When H_{e-e} is taken as a first perturbation, the eigenstates are labelled as $^4A_1$, $^4A_2$, ^2E, $^4T_1$, $^4T_2$ for the case of cubic symmetry (further details could be found in ref [38] and [36]. Later the H_{s-o} could be considered as a perturbation on the new states.

Since for T.M.I., the effect of crystal field has a strong influence on the ion doped in a solid, where the value of H_c is about the same order of H_{e-e}. So, either the strong or the intermediate crystal field approach can be adopted[36] in calculating the wave function and energy levels.

1.7 Static Field Effects on Energy Levels

Since the major component in a crystal field is still the octahedral part, we will start to interpret the gross features of the spectrum on the basis of this symmetry, while the additional fine structure may be caused by the (trigonal, tetragonal, orthorhombic, etc.) symmetries.

1.7.1 Single d-electron in crystal field

We consider first the $(3d^1)$ configuration which has a single electron in the outer d-shell. In the free ions, the $(3d^1)$ state has five degenerate d-orbitals which have charge density patterns shown in figure (1.6).

The geometrical properties of these charge density patterns may be written as

Fig 1.6 Octahedral crystal field orbitals formed from $3d^1$ electron wavefunctions.

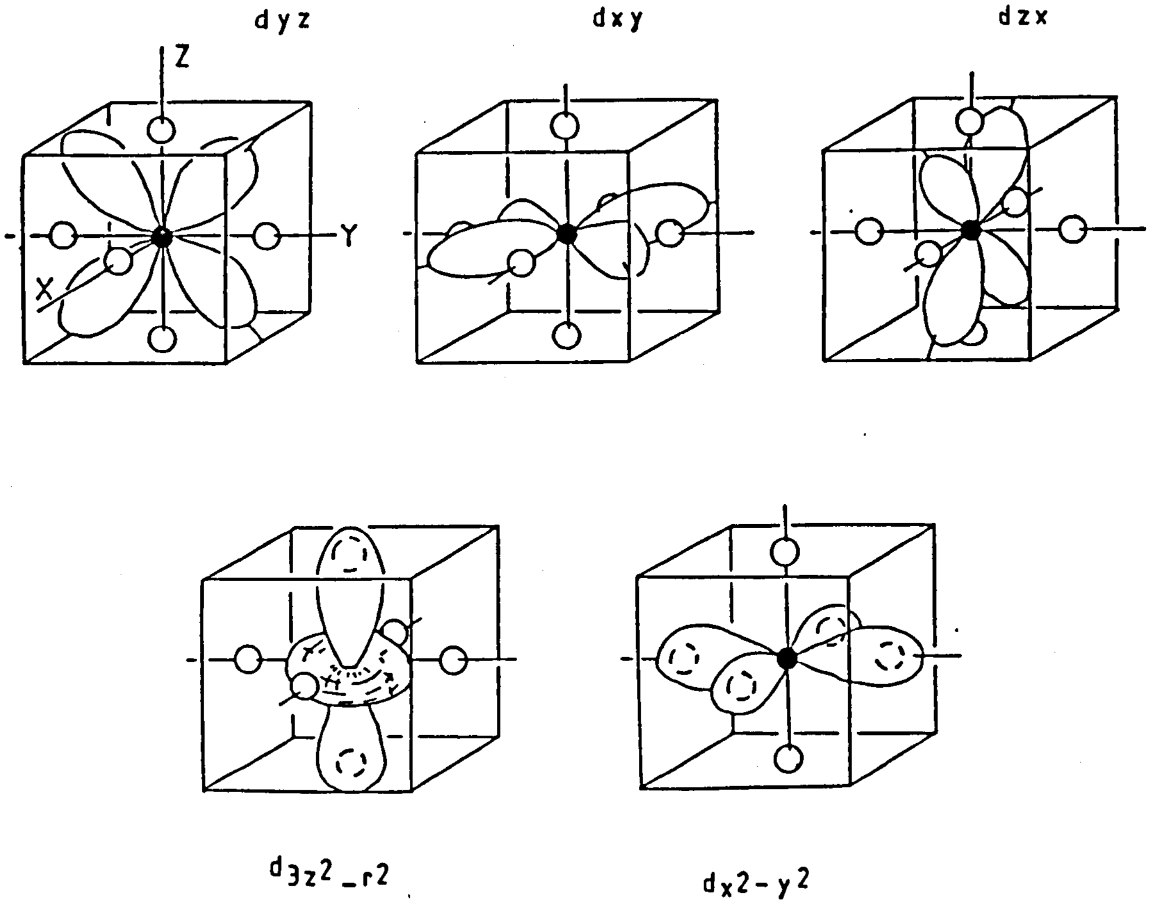

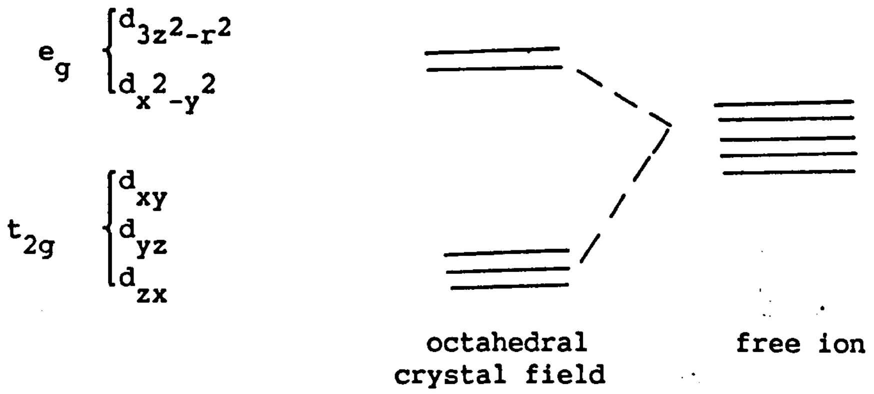

In octahedral symmetry it is evident that the lobes of the orbitals t_{2g} ~ d_{xy}, d_{yz}, d_{zx} point between the negatively charged ligand ions. These three orbitals are equally affected by the crystal field and are degenerate. The other two orbitals e_g ~ $(d_{3z^2}-r^2)$ and $(d_{x^2}-y^2)$ also have exactly the same energy in octahedral symmetry and both point towards the ligands which tend to destabilize these two orbitals with respect to the three (t_{2g}) orbitals. In other words the e_g orbitals are higher in energy than the t_{2g} orbitals. The energy difference between (e_g) and (t_{2g}) is equal to (10 Dq), where (Dq) is a parameter which characterizes the strength of the octahedral field. This energy separation then provides a mechanism by which an incident photon can be absorbed promoting an electron from a lower level to an upper one. From the fact that the spectral lines associated with such transitions fall in the visible region of the spectrum, it is evident that the energy separation produced by the field is very considerable. A typical value is (20,000)cm^{-1}[27], equivalent to (2.5 e.v.).

1.7.2 Multielectron case

The calculation of eigenfunctions and eigenvalues for multi-electron ions with $(3d)^n$ configuration in an octahedral crystal field is more complicated because of the Coulomb interaction between the (3d) electrons. The Coulomb interaction is characterized by Racah parameters (A), (B) and (C) which shift and split the energy levels by amounts which must be added to the single electron splitting of (10 Dq). The free ion levels of the $(3d)^3$ ion are the $({}^{2s+1}L_J)$ states which are ^4F, ^4P, ^2P, ^2D, ^2F, ^2G, ^2H of which ^4F is lowest in energy. In spectroscopy, where we measure differences in energy, a common term, 3A, may be ignored. Thus the energy levels are quoted in terms of (Dq) only. The values of B and C vary from one ion to another, and for the same ion, from one host to another. Tanabe and Sugano[28] formulated a diagramatic approach in which the reduced energies E/B are plotted as a function of (Dq/B) for constant values of $\gamma = C/B$. In general $\gamma \sim (4.0\text{-}5.0)$ through the transition metal series. The energies E/B are calculated from the matrix elements of the Coulomb and crystal field energies.[28] The plot of (E/B) against (Dq/B) shown in figure (1.7) is for a $(3d^3)$ ion which is shown for typical values of (B) and (C). E is the energy of the level and all energies were plotted relative to the lowest level, as can be seen in figure (1.7), the free ion levels are split into new crystal field levels classified[29] by irreducible representations of the octahedral (O_h) group (A_1, A_2, E, T_1, T_2).

These are a group theoretical notations related to the symmetry of the orbital wave function in an octahedral crystal field. The ground state of the free ion (^4F) is split into ($^4A_2$), ($^4T_2$) and ($^4T_1$) levels, whereas the (4_p) state does not split by the octahedral field. (4_p) states transform as the ($^4T_1$) state representation of the (O_h) group. In consequence there are two ($^4T_1$) states derived from two different free ion levels. The ^2G term splits into $^2A_1$, ^2E, $^2T_1$ and $^2T_2$ terms as shown in figure (1.7).

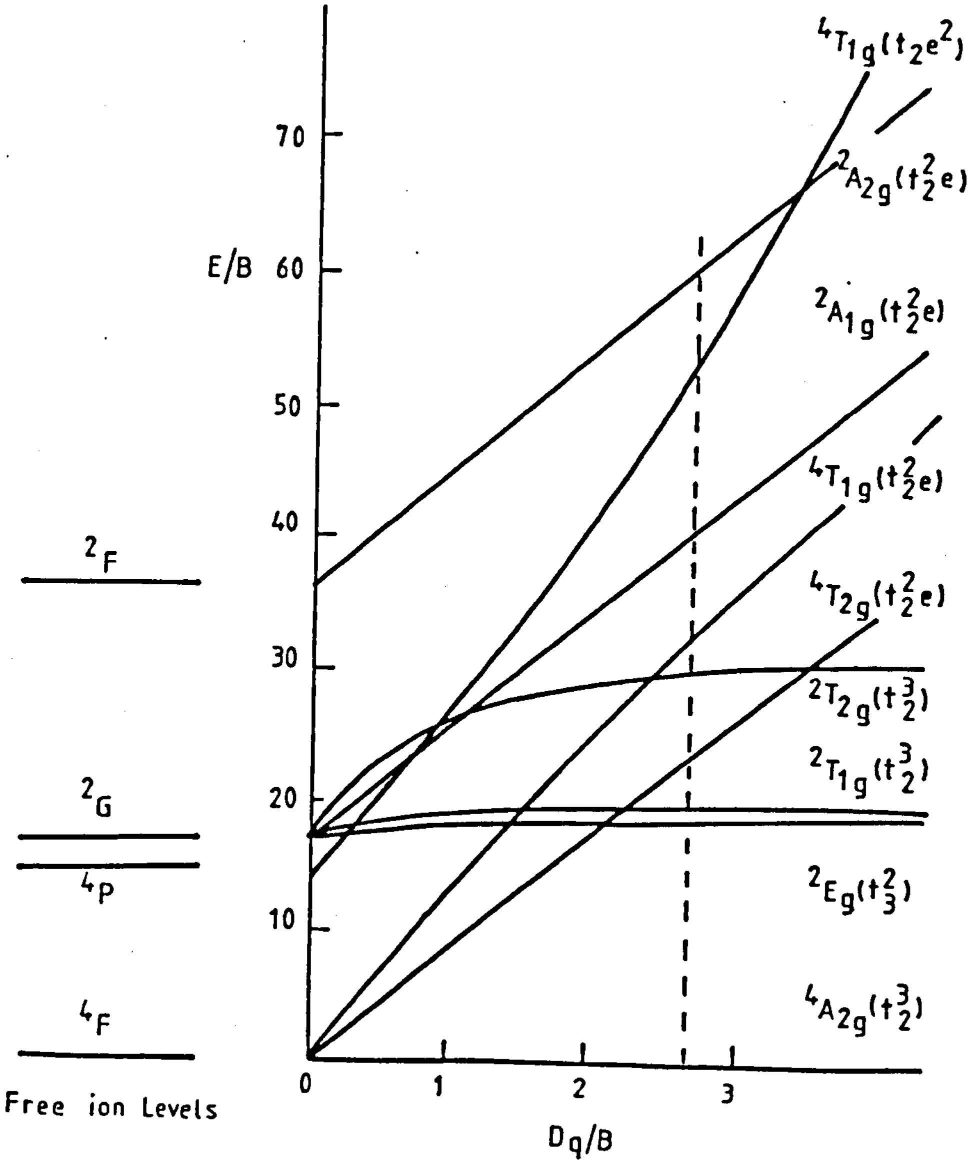

Fig 1.7 Energy levels of 3d^3 configuration showing the effect of octahedral crystal field, the free ion levels are shown on the left hand side of the diagram.

CHAPTER TWO

EFFECTS OF LATTICE VIBRATIONS (DYNAMIC CRYSTAL FIELD)

2.1 Introduction

Some of the transitions between energy levels on 3d ions give rise to broad bands in the absorption or the emission and others give rise to narrow lines. This is due to the interaction of the (3d) electrons of the transition metal ions with the lattice vibrations. The vibrational states of the lattice are described in terms of phonons, the quantized units of vibrational energy.[30] The characteristic properties of phonons in crystalline lattices are explained in several texts.[30,31] So far we have considered only the static effects of the crystal field. Lattice vibrations cause dynamical strains which modulate the frequency of the optical transitions, leading to frequency modulated sidebands.

2.2 The Electron-phonon Interaction

The crystal potential in the presence of strains associated with lattice vibrations can be written as:[32]

$$V_c^v = V_1\varepsilon + V_2\varepsilon^2 + \ldots \qquad (2.1)$$

where V_c^v describes the interaction energy of the ion with the time varying crystal field, and V_1, V_2,... are the coupling parameters which are functions of the electronic coordinates of the dopant ion.

The strain ϵ may be expressed in terms of phonon creation and annihilation operators as:[32]

$$\epsilon = \sum_{\omega} \left[\frac{\hbar\omega}{2MV_{\omega}^{2}}\right]^{1/2} (a_{\omega} + a_{\omega}^{*}) \qquad (2.2)$$

where ω is the frequency of the particular vibration, M is the mass of the crystal and V_{ω} is the velocity of sound of frequency ω. The dynamical Hamiltonian for the ion-lattice system may be written as:

$$H = H_{FI} + H_{C}' + H_{L} \qquad (2.3)$$

where H_L is the lattice Hamiltonian given by

$$H_{L} = \frac{1}{2} \sum_{q} \hbar\, \nu_{q} (a_{q}^{*} a_{q} + a_{q} a_{q}^{*})$$

a_q^*, a_q are the creation and annihilation operators respectively for phonons in q-space.[30] H_C' is the summation of two components V_C^o and V_C^v, in which the first term is the crystal field potential when the ions are in their average positions and V_C^v is given in Eqn (2.1). A Hamiltonian of the form (Eqn (2.3)) but including only the H_{FI} and the V_C^o terms has eigenstates which we denote by $|i\rangle$; the eigenstate of the lattice Hamiltonian, H_L are denoted by $|n\rangle$. The eigenstates of the ion lattice system are simply the product $|i,n\rangle$. The probability of an electronic dipole transition from an initial state $|i,n\rangle$ to a final state $|f,m\rangle$ then depends on the square of the matrix element:

$$\langle f,m|D|i,n\rangle = \langle f|D|i\rangle\langle m|n\rangle$$

in which from the orthogonality properties of the harmonic oscillator function $\langle m|n\rangle = 0$, unless $m = 0$. Hence the only allowed transitions are those where the lattice state remains unchanged, i.e. only sharp purely electronic transitions are allowed. The case of present interest is when V_C^v is small but $\neq 0$, and may be taken into account by perturbation theory. In order to do this we must reconsider Eqn (2.1), considering only the first term in the expansion, i.e.

$V_C^v = V_1\epsilon$ is the perturbation added to the unperturbed Hamiltonian:

$$H = H_{FI} + V_C^o + H_L \tag{2.4}$$

It may then be shown that the eigenstates $|i,n\rangle$ of the unperturbed Hamiltonian are replaced by new eigenstates ($\psi_{i,n}$) where:

$$\psi_{(i,n)} = |i,n\rangle + \sum_{j,\omega} \alpha_{j,\omega}|j,(n+1)_\omega\rangle + \sum_{j,\omega} \beta_{j,\omega}|j,(n-1)_\omega\rangle \tag{2.5}$$

where the 2nd and the 3rd terms of the right hand side are the states of one phonon more and one phonon less mixed into the original state. Other mixing of states by the terms of order ϵ^2 are ignored as they are very small. In octahedral symmetry the $^4A_{2g} \rightarrow {}^2E_g$ transition in matrix form is:

$$\langle \psi(^4A_2,m)|D|\psi(^2E,n)\rangle$$

where $\psi(^4A_2,m)$ and $\psi(^2E,n)$ are the eigenstates for the ground and excited levels, respectively.

When m=n, we have the matrix element of the zero-phonon transition. This transition is forbidden by both parity and spin. However spin-orbit coupling mixing between spin quartet and spin doublet relaxes the spin selection rule enabling a weak transition to take place. This transition is said to be a magnetic dipole transition.

In the zero-phonon case, the electron-phonon interaction is not involved. when this interaction is included, there is a mixing between states of (n+1) and (n-1) vibrational states with $|^2E,n\rangle$ and with $|^4A_2,n\rangle$. The transition

$$\langle \psi(^4A_2,n+1)|D|\psi(^2E,n)\rangle$$

is an example for this transition. The non-zero components of this matrix element are transitions involving a phonon as well as a photon. Transitions of more than one phonon could also occur, but these are very weak for a small electron phonon interaction. Because of the relaxation of the parity selection rule caused by odd parity lattice vibrations, the intensity of the sideband process relative to the purely electronic no-phonon transition is higher. An example of this case is the V^{2+} ion in MgO, where the zero-phonon transition is a magnetic dipole in nature,[33] whereas the sideband is electric dipole.[34] In contrast, in ruby the $^2E \rightarrow {}^4A_2$ zero-phonon line and its one-phonon sideband are both induced by electric dipole processes.[35]

2.3 The Configurational Coordinate Model

Both electronic (sharp lines) and vibronic (broad bands) transitions which may coexist in certain systems can be explained using the configurational coordinate model. The separation of the electronic and the ionic variables of the Hamiltonian for transition metal ions in a solid was done using the Born-Oppenheimer approximations (the adiabatic approximation).[36] The total energy E is:

$$E = E_o^{(a)} + \sum_k \hbar\, \omega_k^{(a)} (n_k + \frac{1}{2}) \qquad (2.6)$$

where $E_0^{(a)}$ is the electronic energy for a particular electronic state (a) at the average position of the vibration, $\omega_k^{(a)}$ is the angular velocity of mode (k) and n_k gives the number of quanta of vibrational energy (number of phonons) in mode (k) above the zero point energy of the harmonic oscillator. The ion-lattice system can be described by crude "Born-Oppenheimer states"

$$\psi_a(r_i, R_\ell(o))\ \chi_a(R_\ell)$$

where $\psi_a(r_i, R_\ell(o))$ is the eigenstate of an ion in the static lattice, and $\chi_a(R_\ell)$ is the vibrational lattice state. There are many normal modes of vibration (k), which should be taken into account. In order to simplify the analysis of transitions between various ion-plus-lattice states, only the breathing mode radial in-phase pulsations of the ions about the transition metal ion are taken into account. The distance from the transition metal ion to the first shell of the surrounding ions is labelled by Q, the configurational coordinate, a variable of the lattice state. This Q-value oscillates about its equilibrium value $Q_o(a)$. The crude Born-Oppenheimer wave functions are written as:

$$\psi(n, Q_o(a))\chi_a(Q)$$

and the state energies are written as:

$$\left.\begin{aligned} E^{a}_{(Q)} &= E^{(a)}_{o} + V^{(a)}_{(Q)} \\ E^{b}_{(Q)} &= E^{(b)}_{o} + V^{(b)}_{(Q)} \end{aligned}\right\} \qquad (2.7)$$

where the system is in the electronic states (a) and (b), respectively, $V^{(a)}{}_{(Q)}$ and $V^{(b)}{}_{(Q)}$ take the form of Morse potential functions[36] which may be approximated as harmonic potentials, figure (2.1). The lattice states $\chi_a(n)$ and $\chi_b(m)$ can be represented by $|n\rangle$ and $|m\rangle$, where (n) and (m) are the numbers of phonons above the zero points energy in the two harmonic oscillators, (figure (2.1)). For the sake of simplicity, it is usually assumed that the vibrational frequencies in states (a) and (b) are the same, but the average value of the configurational coordinate Q is different due to the difference in the electron lattice coupling. The energy E_{dis} in figure (2.1) is a measure of the difference in coupling between the two states; it can be parameterized using a dimensionless constant, the Huang-Rhys parameter (S) [68]

$$E_{dis} = S\hbar\omega \qquad (2.8)$$

Emission and absorption transitions in figure (2.1) are represented by vertical arrows. This is the Frank-Condon approximation which states that optical transitions take place so fast that the nuclear coordinates do not change during the transition. For broad bands

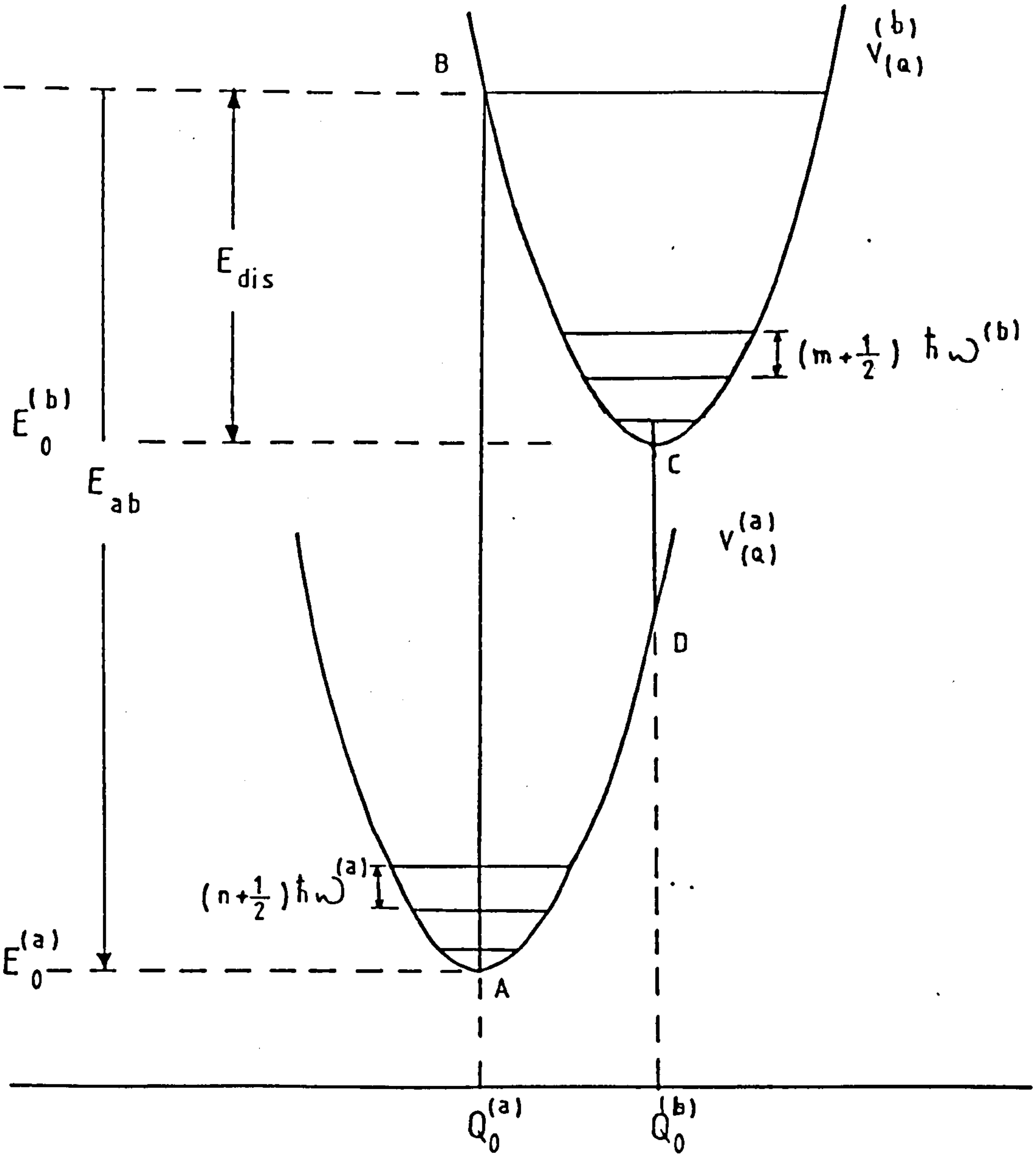

Fig 2.1 The configurational coordinate diagram in the harmonic approximation for the electronic states a and b. The vibrational frequencies in the two electronic states are assumed to be the same.

the absorption and emission arrows have different lengths, indicating that band peaks occur at different photon energies. The horizontal lines inside the two parabolae represent the quantized vibrational energies of a harmonic oscillator. To show how the zero-phonon energies for the ground and excited states are different, we assume a model of a simple hydrogenic-ion in a lattice. This has a total energy

$$E_n = \frac{\alpha}{n^2 a_o} + \frac{1}{2} kx^2 \qquad (2.9)$$

The first term on the right hand side represents the electronic energy, while the second term is the vibrational energy. In this equation, x is the vibrational displacement, a_o is the mean lattice spacing and $x << a_o$. In consequence, the energy of the ground state is,

$$E_a = \frac{A}{a_o} + \frac{1}{2} kx^2$$

and that of the excited state is,

$$E_n = \frac{A}{n^2(a_o+x)} + \frac{1}{2} kx^2 \qquad (2.10)$$

The expansion in the excited state occurs because of the different charge distribution relative to the ground state. Using the binomial expansion in equation (2.10) gives:

$$E_n = E_{on} + Bx + \frac{1}{2} kx^2 \qquad (2.11)$$

where $E_{on} = \frac{A}{n^2} a_o$, and $B = \frac{E_{on}}{a_o}$.

Rearranging equation (2.11), we obtain:

$$E_b = E_{ob} + \frac{1}{2} k(x - \frac{B}{k})^2 - \frac{B^2}{2k} \qquad (2.12)$$

for the energy of the excited state (b). We see in equation (2.12) that this energy is still parabolic in x, although the vibration is about a new position x = B/K, rather than x = 0. Also the coupling between the electron and the lattice has reduced the excited state energy by the value $(B^2/2k)$. It is more usual to represent the distance from the central ion to the neighbouring ion by the (Q) values, as we have done in figure (2.1). Although the arrows AB and CD represent the most probable transitions, it is still possible that transitions originating at Q-values other than $(Q_o^{(a)})$ and $(Q_o^{(b)})$ can occur. Large displacements between the ground and excited states parabolae give rise to broad band absorption and emission spectra as illustrated in figure (2.2). Once the ion is in an upper vibrational level of the excited state (due to absorption) it decays non-radiatively to the zero vibrational level (B→C) (fig.2.1) and luminescence transitions at low temperatures originate predominantly at the value of $Q_o^{(b)}$, i.e.

from the centre of the zero vibrational level of the excited state. The peak of the emission band is shifted to lower energies than the absorption band peak, this separation is referred to as the Stokes' shift $(2S\hbar\omega)$. The only overlap between the two bands is at the zero-phonon line (see figure (2.2)). When the temperature is raised, the higher vibrational levels of the excited state become occupied and part of the transition known as anti-Stoke shift component occurs on the other side of the zero-phonon line.

2.4 Radiative Transition Probabilities and Selection Rules

When an active ion is exposed to electromagnetic radiation with a proper resonant frequency radiative transitions could occur. The interaction energy of the ion with the radiation field can be written as:

$$H = \sum_i [e\bar{r}_i . \bar{E} + \mu(\bar{\ell}_i + 2\bar{S}_i).\bar{B}] \tag{2.13}$$

where the first term represents the electric dipole radiative process, and the second is the magnetic dipole process, $\bar{D}_e = \sum_i e\bar{r}_i$ and $\bar{D}_m = \mu(\bar{\ell}_i + 2\bar{S}_i)$ are the electronic and magnetic moments of the electron respectively. $\bar{E}$ and $\bar{B}$ are the electric field intensity and the magnetic flux density respectively. The relative strengths of these two transitions are approximately:

$$(ea_0E)^2/(\mu_B B)^2 = 1/\hbar^2(2ma_0c)^2 \approx \frac{1}{10^{-5}}$$

For an electric dipole process, the matrix element for absorption transition between two states (a) and (b) is $\langle b|D_e|a)$, while the matrix element for the magnetic dipole process is given by $\langle b|D_m|a\rangle$. In order to determine whether or not an optical transition will take place between the two states, we need to evaluate these two matrix elements, since they have the value of zero between states of different spin (s), the selection rule may be stated as

$$\Delta s = 0$$

This selection rule may be relaxed when spin-orbit coupling is taken into account, e.g. as in the $^2E \rightarrow {}^4A_2$ transition mentioned in section (2.2). A weakly allowed transition then occurs.

Since the ($3d^n$) wavefunctions have even parity, whereas (D_e) is an odd parity operator. So the matrix element of (D_e) is zero when states (a) and (b) have the same parity, that electric dipole transitions are forbidden between such states is the Laporte selection rule. However since (D_m) is an even parity operator and matrix elements of (D_m) will have non-zero values between states formed from the same ($3d^n$) configuration. Magnetic dipole transitions can be orders of magnitude weaker than the allowed electric dipole transitions. The selection rule may be relaxed by the admixture of higher lying odd parity states such as from the

$(3d^{n-1})4p$ configuration. However for ions in octahedral symmetry sites there are no odd parity crystal field terms so no electronic states may be admixed and the magnetic dipole process is the only radiative transition to exist. In this situation odd parity phonons may relax the selection rule. Alternatively static distortions from the octahedral symmetry may occur which may add small odd parity distortions, so enabling the electric dipole transition to be the dominant radiative transition. We now examine the transition probability in the presence of the vibrational interaction. We write the total wavefunction $\Psi(r_i,Q)$ as the Born-Oppenheimer product

$$\Psi(r_i,Q) = \psi_i(r_i,Q)\,\chi_i(n) \tag{2.14}$$

where r_i is the electronic coordinate and Q is the nuclear coordinate. The first term of the right hand side of equation (2.14) represents the electronic wavefunctions while the last term is the vibrational wavefunction for the system in the electronic state (i) and the oscillator state (n) and (m) of states (a) and (b) respectively.

The probability for absorption transitions between states (a) and (b) to take place is proportional to the square of the matrix element,

$$\langle\psi_b(r_i,Q)\chi_b(m)|D|\psi_a(r_i,Q)\chi_a(n)\rangle$$

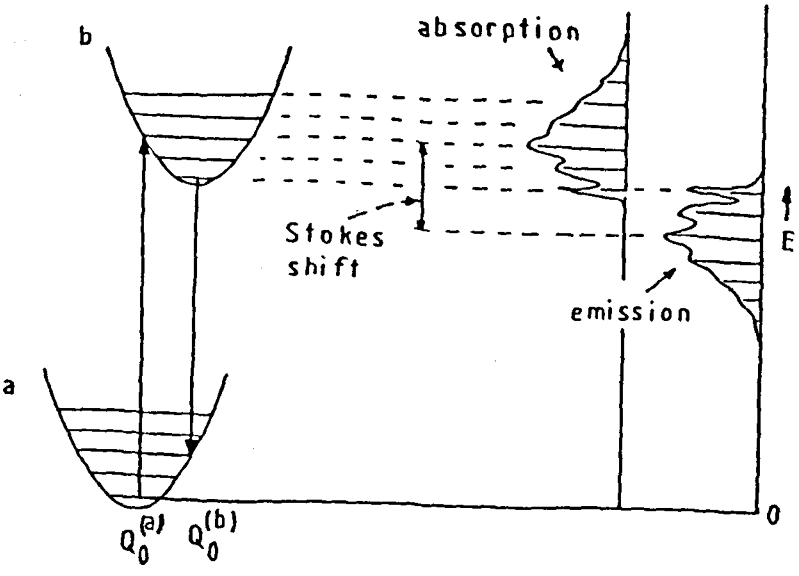

Fig 2.2 Absorption and emission transitions between states a and b. The zero-phonon line occurs at the same frequency in absorption and emission.

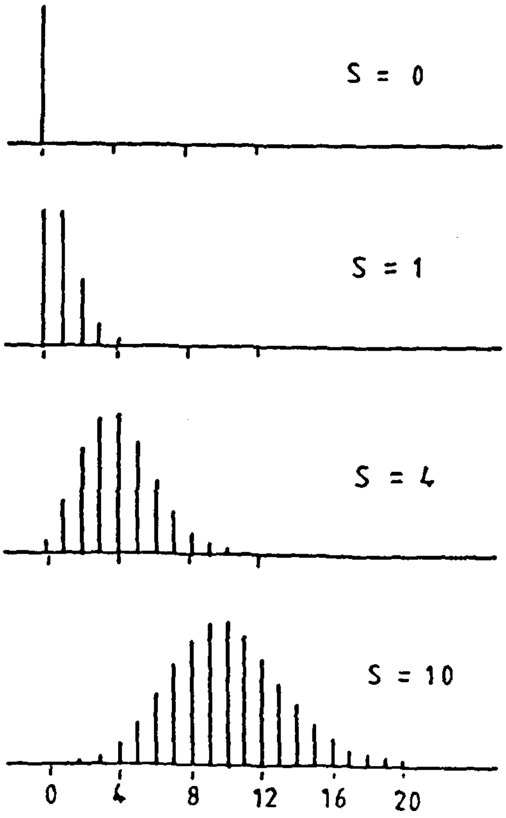

Fig 2.3 The relative intensities of the different 0 → m transitions change with the strength of the coupling factor (S). The envelope of the individual intensities gives the predicted band shape.

so the transition probability for absorption transition between the electronic-vibrational state (a,n) to the electronic-vibrational state (b,m) is:

$$W_{a,n-b,m} = P_{ab}|\langle\chi_b(m)|\chi_a(n)\rangle|^2$$

where $$P_{ab} = |\langle\psi_b(r_i,Q)|D|\psi_a(r_i,Q)\rangle|^2$$

represents the purely electronic transition probability. When only the n=0 vibrational state is occupied, e.g. at T = 0K, the probability of a transition to the mth vibrational level in the excited electronic state varies as:[37]

$$|\chi_b(m)|\chi_a(n)\rangle|^2 = \frac{\exp(-s)s^m}{m!} \qquad (2.15)$$

where (s) is the Huang-Rhys factor seen in equation (2.8). The relative values of equation (2.15) of the overlap integrals for transitions characterized by different values of (s) are plotted in figure (2.3). The lowest energy line 0→0 is the zero-phonon transition, and since it is between pure electronic states, it is a sharp transition. While the other 0→m transitions occur at higher energies involving the creation of (m) phonons in the excited state and appear as side bands accompanying the zero-phonon lines. Since there is a wide spectrum of lattice vibrational frequencies rather than the single breathing mode, the side bands depicted in figure (2.3) should appear as continuous bands rather than a series of sharp lines. The band shape becomes more symmetrical as the (s) value goes to higher numbers. Now once the system is raised to state (b), it quickly thermalized and at low temperatures only $\chi_o(0)$ level is occupied, so radiative downward transitions are possible and by using the same argument as in the case of the absorption transition the emission transition from state (b,0) to state (a,n) depends on the square of the matrix element:

$$\langle \psi_a(r_i,Q) | \bar{D} | \psi_b(r_i,Q) \rangle \langle \chi_a(n) | \chi_b(0) \rangle$$

We can see in figure (2.2) that the zero phonon line for both emission and absorption occur at the same frequency and the shapes of the absorption and emission bands are mirror images of each other in the configurational coordinate model.

2.5 Intensity of Transitions

The strengths of optical transitions are usually expressed in terms of the oscillator stength (f), a quantity proportional to the transition probability. For spin and parity allowed transitions, the oscillator strength is approximately unity. For transition between states of the same spin multiplicity, since all terms are of even parity, the electronic dipole transition is forbidden. The parity selection rule may be released by either odd-parity state distortion or by odd-parity lattice vibrations. Denoting the matrix element of the static or instantaneous odd-parity field between even and odd-parity states by $\langle V_{odd} \rangle$, then the degree of admixture of odd and even-parity states is given by ~ $\langle V_{odd} \rangle / \Delta E_{eo}$, where ΔE_{eo} is the energy separation between the even and the odd-parity states. Hence the oscillator strength of the parity forbidden transition is given by:[38]

$$f_e^{\,(forb)} \sim f_e^{\,(allow)} \times \left[\frac{\langle V_{odd} \rangle}{\Delta E_{eo}} \right]^2$$

where $f_e^{\,(allow)}$ is the oscillator strength for the parity allowed transition. Assuming crude values of $V_{odd} \sim 10^3$ cm^{-1} and $\Delta E_{eo} \sim 10^5$ cm^{-1}, we find $f_e^{\,(forb)} \sim 10^{-4}$ while for magnetic dipole transitions fm ~ 10^{-6}. For the case of transitions between terms of different spin multiplicities, oscillator strengths are even smaller, and for the electric dipole and magnetic dipole transitions they are 10^{-7} and 10^{-9} respectively.

2.6 Linewidth and Bandshape

Optical spectra of T.M.I. doped solids may consist of sharp zero-phonon lines and broad vibronic transitions. Ti^{3+} usually emits into a broad band (Ti:$A\ell_2O_3$, Ti:YAP, Ti:YAG and Ti:glass) associated with the transition $^2E \rightarrow {}^2T_2$. However it is possible to detect the zero-phonon lines at low temperatures. For Cr^{3+} doped solids (crystals and glasses) the spectra are characterized by two types of transitions related to different sites. From figure (1.7) the separation of energy levels of the same configuration, e.g. as for the transition:

$$(t_{2g}^{3})^{4}A_{2g} \rightarrow (t_{2g}^{3})^{2}E_{g}$$

is almost unchanged at large values of (Dq/B). However, those levels belonging to different electron configurations are proportional to (10 Dq), as in the case of the spin allowed transition

$$t_{2g}^{3}\ {}^{4}A_{2g} \rightarrow (t_{2g}^{2}e_{g})^{4}T_{2g}, (t_{2g}^{2}e_{g})^{4}T_{1g}$$

since the form of (t_2) and (e) orbitals are different, the electron lattice coupling of the ion in the $^4A_2$ and ^2E states should be similar but different from that in the $^4T_1$ and $^4T_2$ states.

In figure (2.4) we note a large lateral displacement between the $^4T_2$ and $^4A_2$ parabolae and a small displacement for ^2E state. For Cr^{3+} ions in strong crystal field sites, the ^2E level is lower than the $^4T_2$ and $^4T_1$ and the transitions between the ^2E level and the ground state $^4A_2$ is characterized by a small value of (s) and a strong zero-phonon line, with a sideband at low temperatures. If the temperature is raised so that the $^4T_2$ level is populated there is emission from the $^4T_2 \rightarrow {}^4A_2$ transitions which is characterized by broad band (high value of s).

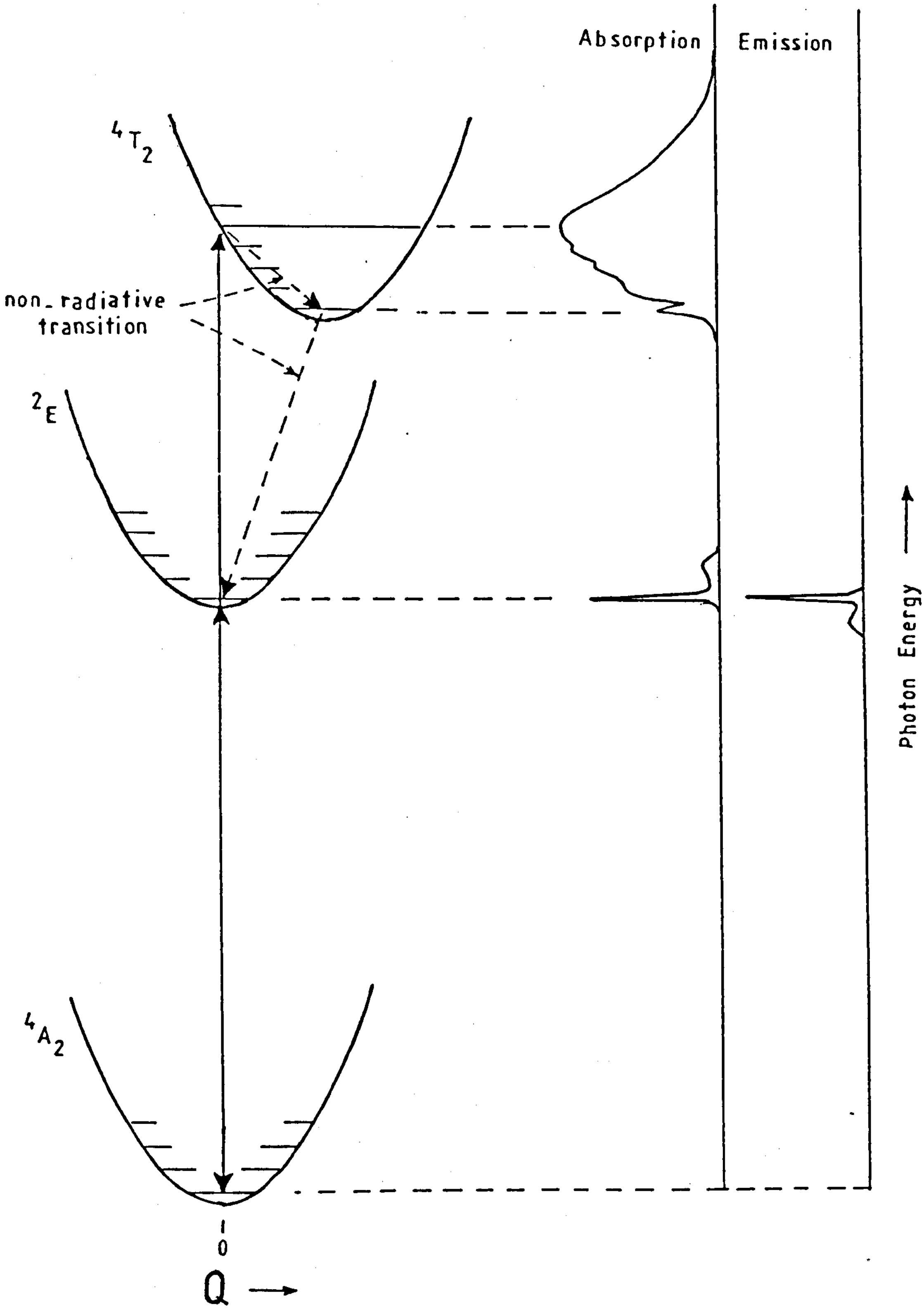

Fig 2.4 Configurational coordinate diagram for a high field site of Cr^{3+} doped crystal. Relative absorption and emission of the $^4T_2$ and ^2E levels are shown at the right hand side (after Henderson and Imbusch[36]).

It should be mentioned that although the lineshape changes, the total absorption intensity is independent of temperature.[36] The intensity of the zero-phonon line is given by:

$$I_o \exp\left(-s \coth \frac{\hbar\omega}{2kT}\right)$$

which decreases with increasing temperatures. For $s \ll 1$, the zero-phonon line intensity becomes

$$I_o \left(1-s \coth \left(\frac{\hbar\omega}{2kT}\right)\right)$$

while the sideband intensity increases with temperature as

$$I_o \, s \coth \left(\frac{\hbar\omega}{2kT}\right).$$

The transition bandwidth varies with temperature as:[39]

$$\Delta\nu_{(T)} = \Delta\nu_{(o)} \left(\coth \frac{\hbar\omega}{2kT}\right)^{1/2} \tag{2.16}$$

where $\Delta\nu_{(T)}$ is the width of the broad band at temperature (T), $\Delta\nu_{(o)}$ is the low temperature bandwidth while $\hbar\omega$ is the energy of the single mode assumed to be interacting with the electron.

Equation (2.16) shows that the bandwidth increases with increasing temperature.

2.7 Non-radiative Processes

The decay of an excited ion to a lower energy state may occur either radiatively or non-radiatively. Vibrational energy may accompany both emission or absorption of radiation. However in some cases the quantum efficiency of the emission is reduced from unity and the excited-to-ground state transition occurs by a non-radiative process in which only vibrational energy of the lattice is released. There are various different vibrational relaxation processes. The direct process involves the relaxation between two electronic states of an ion with energy separation within the range of phonon energies in the host lattice. The transition probability for a one-phonon direct process relaxation between the excited $|b,n_k\rangle$ and ground states $|a, n_k+1\rangle$ at temperature T in which one phonon is created may be written as:

$$\omega_{ba}^{(dir)} = \omega_{ba}^{(dir)}(0)\ (n_k + 1) \qquad (2.17)$$

where (n_k) is the phonon occupancy in mode (k), and $\omega_{ba}^{(dir)}(o)$ is the transition probability for a direct process (b) to (a) at T = 0. $\omega_{ba}^{(dir)}$ varies as the cube of the energy gap between levels (a) and (b),[36] where the gap energy $\Delta\epsilon = \hbar\omega_k$. The Raman and Orbach relaxation processes are examples of two-phonon relaxations. In the Raman process where a high energy phonon k_1 is annihilated and a higher energy phonon k_2 created the energy difference is obtained from the electronic system during the transition from (b) to (a). Figure (2.5) identifies an intermediate electronic state (t) through which Raman process takes place at an energy higher than the phonon energies. If the energy differences E_t-E_a and E_t-E_b within the range of the phonon energies, relaxation takes place via the Orbach process.

Relaxation out of a particular level leads to homogeneous or lifetime broadening. Coupling of the transition metal ion to the vibrating lattice yields a temperature broadening through a Raman scattering of thermal phonons. In consequence, the zero-phonon lines of the T.M.I. in solids may be significantly broadened at high temperatures.

Non-radiative transitions may also occur between levels which have much larger energy gaps than the most energetic lattice phonons (so-called multiphonon emission). However, since the probability of radiative decay increases as the cube of the energy gap between two adjacent levels, then as the energy gap increases, the non-radiative process should involve a larger number of phonons and then transition probability becomes smaller. In consequence, transitions between levels with large separation in energy will be predominantly radiative while those between levels separated by a small energy gap will be mainly non-radiative. A quantum

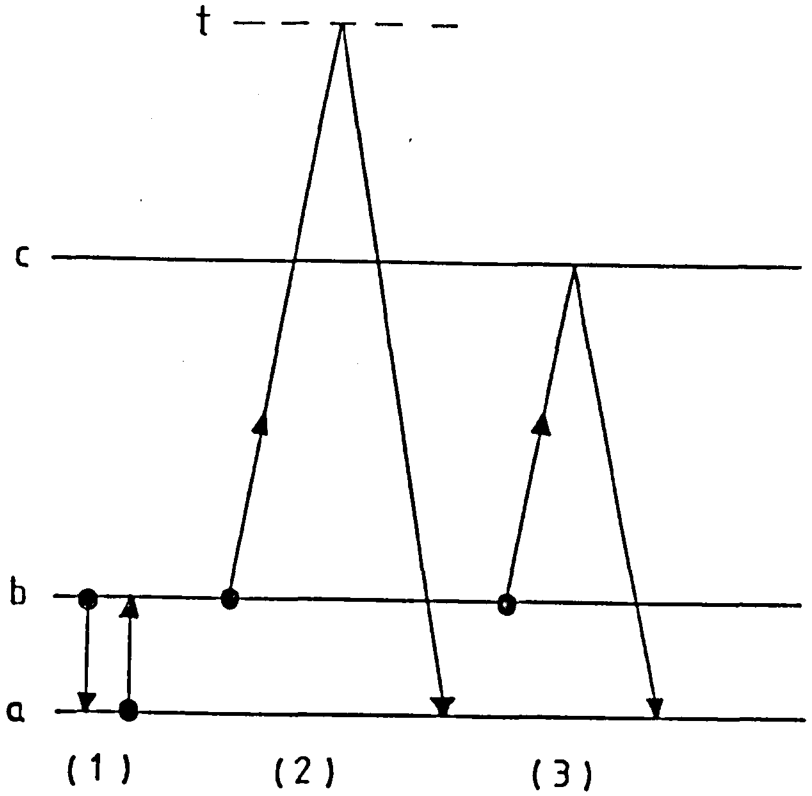

Fig 2.5 Phonon-induced relaxation processes between states (a) and (b). (1) is the one-phonon direct process relaxation, (2) is a two-phonon Raman relaxation process from (b) to (a) proceeding through a virtual intermediate state (t) and (3) is a two-phonon Orbach process from (b) to (a) proceeding through a real electronic state (c).

efficiency of less than unity reflect the competition that occurs between radiative and non-radiative processes.

Measurements of the excited state lifetimes may be used to demonstrate that as the energy gap to the lower level decreases there is a decrease in the lifetime.[40] Measurements of the excited state lifetime and quantum efficiency make it possible to calculate[41] the multi-phonon transition rate, as can be seen in figure (2.6) where both radiative and non-radiative processes are evident. The total decay rate becomes:

$$\frac{1}{\tau} = \Sigma \frac{1}{\tau_i}$$

summed over all processes radiative and non-radiative (of which there are several processes)[36] and,

$$\frac{1}{\tau} = \frac{1}{\tau_r} + \frac{1}{\tau_{nr}} = \omega_r + \omega_{nr} \qquad (2.18)$$

where ω_r is the radiative decay rate, ω_{nr} is the non-radiative decay rate. The quantum efficiency, η, is then given by:

$$\eta = \frac{\omega_r}{\omega_r + \omega_{nr}} \qquad (2.19)$$

hence, ω_{nr} can be calculated from equations (2.18) and (2.19)

Measurements of this type have been reviewed at length by Henderson and Imbusch.[36] From these measurements it was noticed that the non-radiative decay rate decreases exponentially with the increase in energy gap between two levels.

For T.M.I. doped in solids, the interaction between the ion and the surrounding environment is not weak and analysis of non-radiative processes is complicated. In this case account must be taken of non-adiabatic terms in the Born-Oppenheimer approximation which enables the mixing of other electronic states into (ψ_a) state leading to this state changing to one of lower energy with the excess energy being released as vibrational energy. The probability of the non-radiative process then depends on the difference in coupling strength between the ion and the lattice in the two states (i.e. the s-value) and the energy gap between the states (the number of phonons involved in transition p). To calculate the value of the non-radiative transition probability, two approximations are used: first, that the system is harmonic, and secondly, that the electron phonon coupling is linear. The transition probability is given as:[42,43]

$$\omega_{ba}^{nr} = \frac{2\pi}{\hbar} |M|^2 \exp[-s(1+2n_\omega)](1+n_\omega^{-1})^{p/2} \; I_p[2s(n_\omega(n_\omega+1))^{1/2}] \qquad (2.23)$$

where $M = \langle a|H|b\rangle$, is the electronic matrix element

I_p is the modified Bessel function of order p

n_ω is the phonon occupancy.

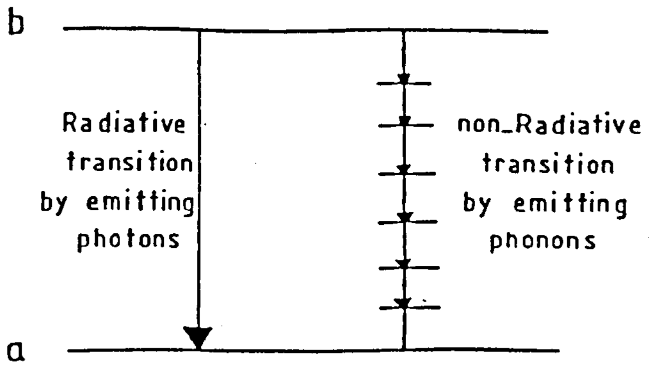

Fig 2.6 Radiative and non-radiative transitions between two levels a and b.

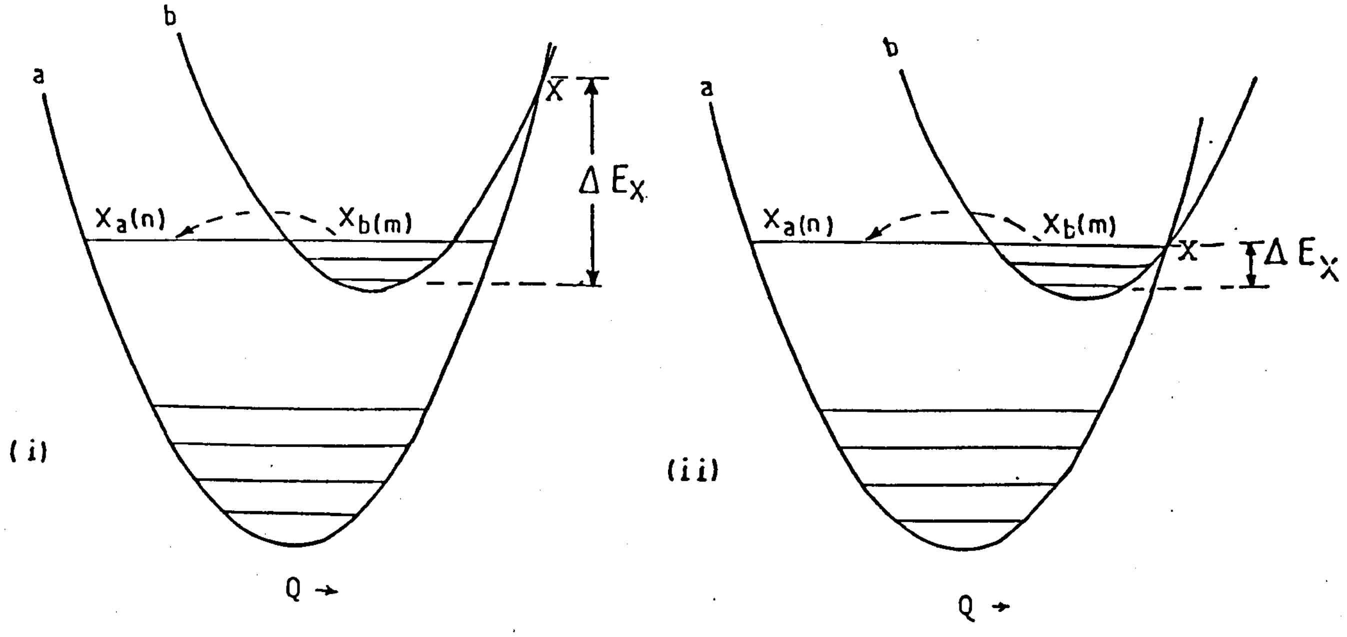

Fig 2.7 Schematic diagram of non-radiative transition between states a and b with two different crossover energies, where the non-radiative energy is maximum when the crossover point is level with the two vibrational potential curves.

For very small values of s (s << 1), the relation in equation (2.23) turns out to be:

$$\omega_{ba}^{nr} = (1+n_{\omega})^{p}$$

which is identical to the result for rare earth ions,[44] where (p) is the only important parameter. For T.M.I. the Huang-Rhys factor may be large and the temperature dependence of the non-radiative decay is a function of both (s) and (p) (Eqn (2.23)). A further complication is the variation of the energy gap with temperatures which also affect the non-radiative decay rate through the value of (p).

In T.M.I. doped solids, non-radiative decay competes with the radiative process even across large energy gaps, so that large values of (p) are involved, a distinction from the behaviour of rare earth ions. Obviously the larger the value of (p) the weaker the value of non-radiative process relative to radiative process.

Because in the transition from state (b) to state (a) $\psi_b\chi_b(m) \rightarrow \psi_a\chi_a(n)$ may yield many phonons due to the difference in electronic energy between states (b) and (a), the overlap integral, $\langle\chi_a(n)|\chi_b(m)\rangle$, plays a major role in determining the non-radiative transition process.. If the two wave functions $\chi_a(n)$ and $\chi_b(m)$

have maxima at the same Q-values, the overlap integral will be maximised. The two different cases are shown in figure (2.7). Consider that (i) the two wavefunctions have different values of maximum vibrational energy at different Q-values and (ii) the two wavefunctions have the same Q-value at the crossover point (x). When the overlap integral is a maximum value at the x-point, the non-radiative transition is maximum. Struck and Fonger[45,46] developed a general theory based on the configurational coordinate model in the harmonic approximation. They used this model to interpret experimental measurements of the non-radiative decay rate. The effect of other modes of the vibrational spectrum and the effect of the temperature on the energy gap was taken into account by Sturge[42] in his work on Co^{2+} in $kMgF_3$. He attributed the discrepancy between the theoretical and the experimental values of the non-radiative decay rate to the unharmonicity effect.

CHAPTER THREE

EXPERIMENTAL DETAILS

3.1 Introduction

The high sensitivity of transition metal ions to variations in their environment makes them particularly useful as high resolution spectroscopic probes. Spectroscopic investigations have been carried out on several different samples including Ti^{3+} doped crystals, glass and Cr^{3+} ion dopants in a variety of inorganic glasses. The availability of tunable dye lasers makes it possible to use techniques such as site selective spectroscopy to investigate the mechanism of line broadening in transition metal doped glasses. For Ti^{3+} doped crystals the anisotropic luminescence behaviour from sites of different symmetry has also been studied. Distributions of different sites for transition metal ions have been studied by time resolved spectroscopy using either phase sensitive detection or by using a delay between the excitation light and the emitted signal. We have also applied Zeeman spectroscopy in conjunction with fluorescence line narrowing to study the spectrum of two level vibrational modes coupled to the 3d-electron in vitreous matrices.

3.2 Cryogenic Techniques

For work at low temperatures, two types of cryostats were used. Firstly, a superconducting magnet contained in a liquid He cryostat equipped with optical access was used for Zeeman splitting measurements of the emission spectra, (figure (3.1)). The superconducting magnet was capable of magnetic fields up to 5.7 tesla at temperatures in the range 1.6-4.2K. The cryostat used to perform some FLN experiments at 4.2K as well as some temperature dependence measurements was an Oxford Instruments variable temperature cryostat (Model MD-04) shown in figure (3.2) used with the Oxford Instrument (Model 3120) temperature controller. In this cryostat the helium space is connected to the exchange space by a needle valve. The exchange space is in contact with a copper rod onto which samples were fixed. Temperature control was affected by means of a Rhfe thermometer and a heater mounted on the exchange block.

In order to avoid sample heating by the laser beam, as low a laser light intensity was used as was possible. A closed cycle refrigerator system was also available for some measurements, with a considerable advantage in the ease of operation, giving excellent optical access and a wide operational temperature range (8-300K). The system is shown in figure (3.3). There are three major components, (i) an (CTI-cryogenics) air-cooled compressor (model Sc), (ii) a vertical mounting cold head (CTI model 22SC) and (iii) the vacuum shroud which is designed to allow optical access through 50mm diameter windows in three orthogonal directions. The vacuum shroud is sealed by a double O-ring piston seal. Provision is made for electrical leads into the vacuum space for temperature measurement and control using a temperature sensor attached to the

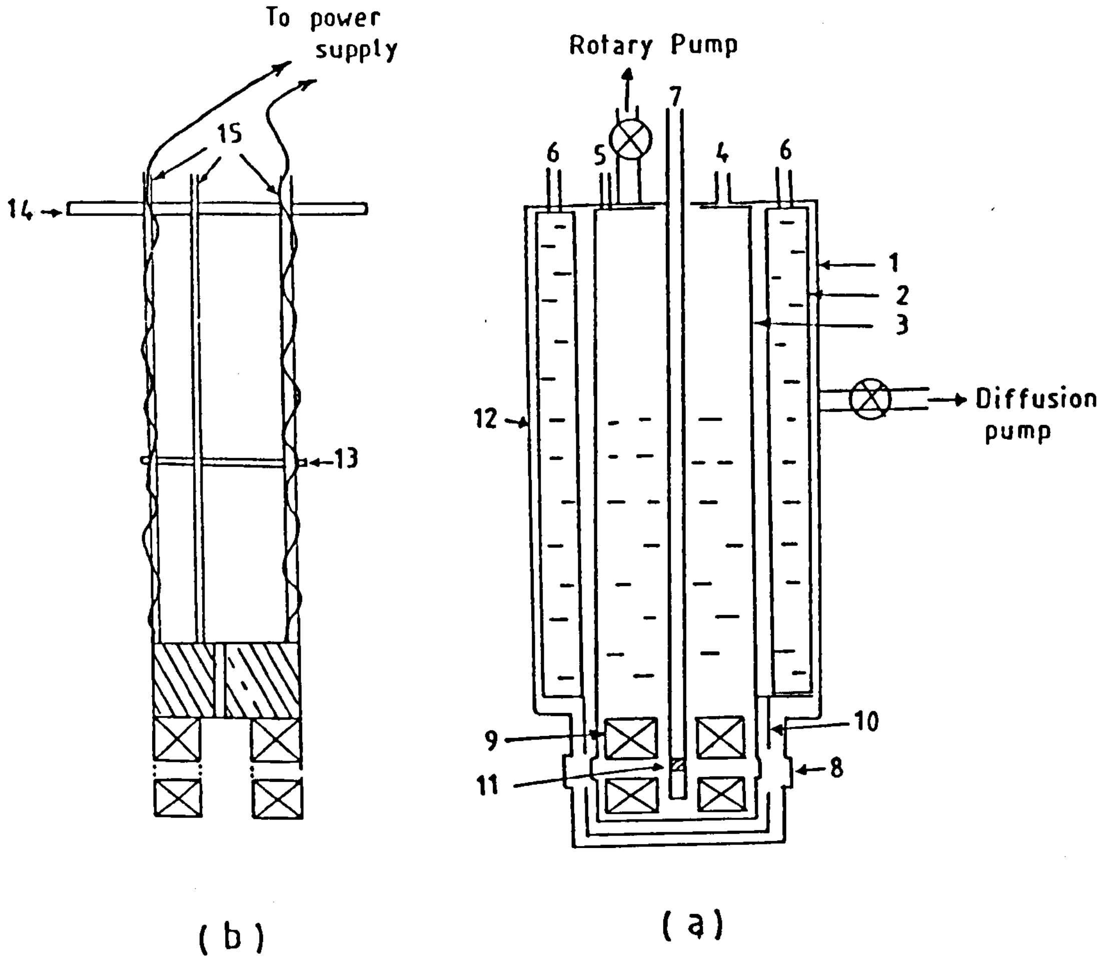

Fig 3.1 Liquid He cryostat with the superconducting magnet
(a) Cryostat with S.C.M. (magnet holder is not drawn)
(b) Magnet holder.
1. outer liner, 2. Liq. N_2 dewar, 2. liq. He reservoir,
4. liq. He inlet, 5. He-gas release, 6. liq. N_2 inlet,
7. sample rod, 8. optical windows, 9. S.C.M.,
10. radiation shield, 11. sample, 12. vacuum space,
13. spacer, 14. top plate, 15. triangular rods structure.

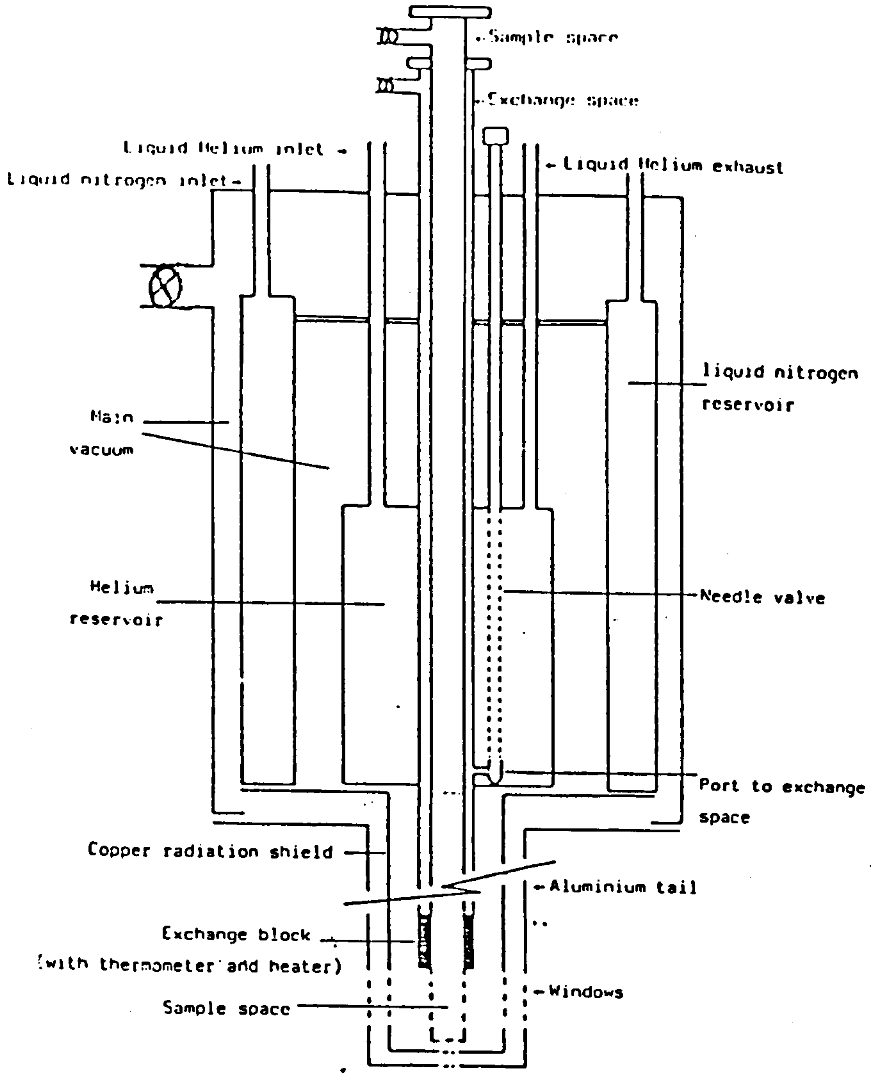

Fig 3.2 Variable temperature liquid He cryostat.

Figure (3.3) Closed Cycle Refrigeration System.

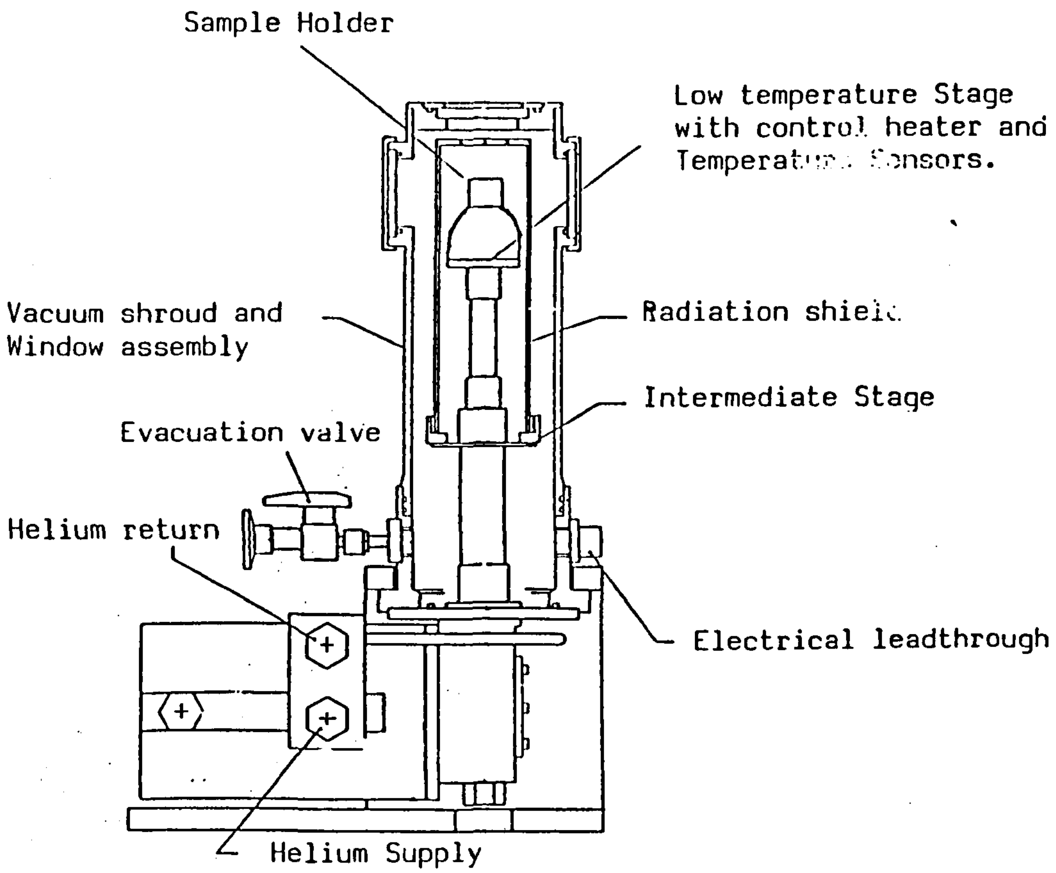

The Cold Head

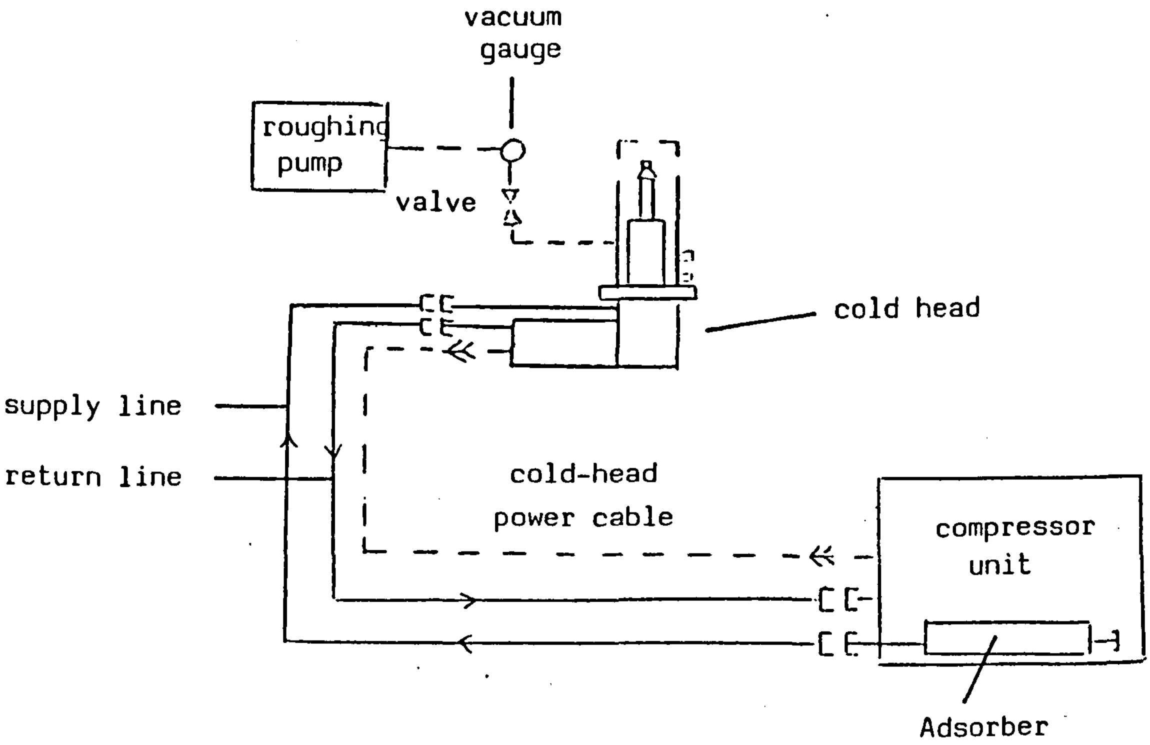

cold finger and a heater surrounding the cold finger. A DC-80 CTI cryogenic temperature controller was used to control the sample temperature variations.

3.3 Optical Absorption Measurements

Optical absorption measurements provide a straightforward way of finding the energy of allowed transitions from the ground state of an ion to its excited states. If a light beam passes through a medium (see figure (3.4)), the loss of intensity due to absorption by the medium (neglecting scattering light) will be equal to:

$$\Delta I(\nu) = I_o(\nu) - I(\nu) = N(\nu)h\nu V \qquad (3.1)$$

where $I_o(\nu)$ is the incident light intensity and $I(\nu)$ is the transmitted intensity, $N(\nu)$ is the number of photons of mode (ν) per unit volume in the beam and V is the velocity of the beam.

The fraction $\frac{dI(\nu)}{I(\nu)}$ of the intensity lost in traversing an

infinitesimal thickness $d\ell$ is proportional to $d\ell$, so that

$$\frac{dI(\nu)}{I(\nu)} = -\alpha_{(\nu)}d\ell$$

hence

$$I(\nu) = I_o(\nu)\exp(-\alpha_{(\nu)}\ell) \qquad (3.2)$$

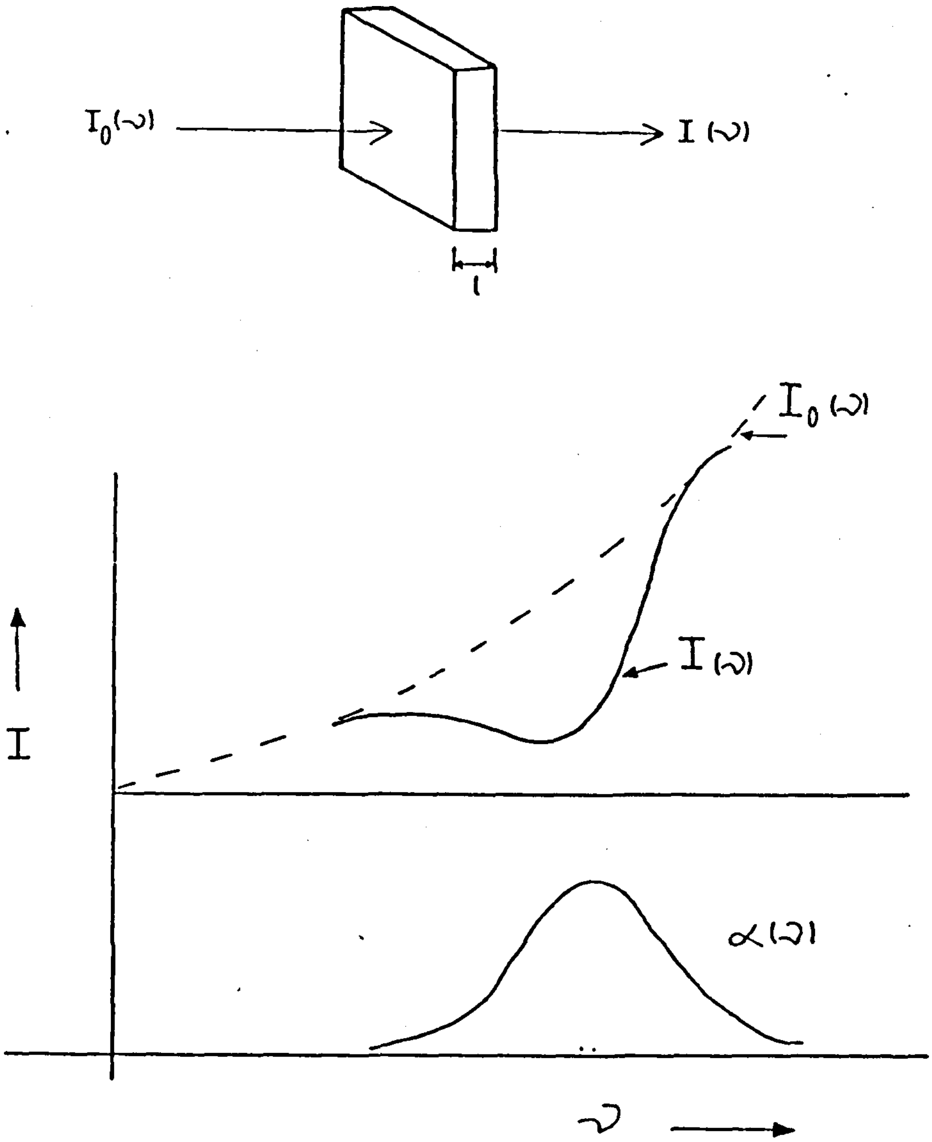

Fig 3.4 Intensity reduction of the light beam on passing through a medium.

where the absorption coefficient, $\alpha(\nu)$ is a frequency and polarization dependent. Equation (3.2) may be written as:

$$\alpha(\nu) = \frac{1}{\ell} \ell n \frac{I_o(\nu)}{I(\nu)} \tag{3.3}$$

Experimentally $I_o(\nu)$ and $I(\nu)$ are measured and $\ell n \frac{I_o(\nu)}{I(\nu)}$ plotted as a function of wavelength.

The experimental arrangement for absorption measurements is shown in figure (3.5). Light from a tungsten lamp is focused onto the entrance slit of a 1/4m monochromator. The exciting wavelength is scanned between 400-1000nm using the monochromator. Monomchromator radiation is then focused onto the sample held at room temperature or near 77K in a liquid N_2 cryostat in which the sample is again attached to a copper cold finger. The radiation passing the sample is collected by a lens and focused onto a silicon photodiode detector. The signal is processed via an electronic interface by a BBC 32K minicomputer which also controlled the wavelength drive of the monochromator and corrected the signal for the spectral dependence of the detection system. For rather small samples (e.g. $5\text{x}1\text{x}1\text{mm}^3$ $Ti^{3+}A\ell_2O_3$, YAP, YAG) the optical absorption was measured using a commercial spectrophotometer (Beckmann) operating between 275-900nm in which the light is split into two beams (sample and

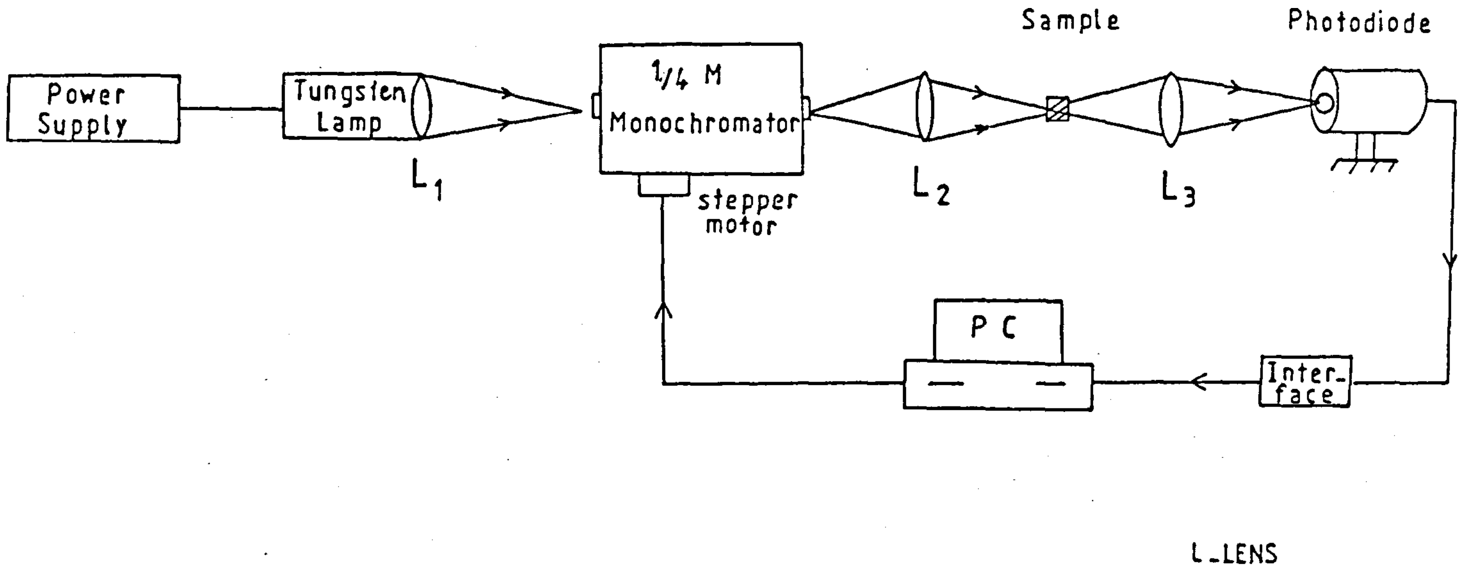

Fig 3.5 Absorption measurements arrangements.

probe beams). The absorption strength is given by the difference between the intensity of these two beams.

3.4 Photoluminescence

3.4.1 General luminescence measurements

A general experimental arrangement for measuring luminescence spectra is shown in figure (3.6). The system was used for detecting both unpolarized and polarized luminescence. The emission from the sample is collected at a right angle to the excitation direction, in order to reduce the scattered laser light and then dispersed through a Monospek 1000, 1 metre monochromater, operated with a grating of 1200 lines/mm blazed at 500 nm. The signal emerging from the output slit of the monochromator is detected by a Hamamatsu (R666) GaAs photomultiplier tube in the spectral range up to 920nm, or a liquid N_2 cooled North Coast Scientific (Eo-817L) Ge-detector for the broad emission bands from Cr^{3+} doped glasses which extend beyond 1.3μm. The signal from the P.M.T. detector is amplified with a Keithley 427 current amplifier and either recorded on a chart recorder or spectrally processed via a computer interface with a personal computer (P.C.). A range of filters were used in front of the input slit of the monochromator, to cut down any unwanted stray light. The excitation source was a 2020-03 Spectra Physics Ar^+ laser which could be used as a single or multi-line source or a 380D Spectra Physics ring dye laser using

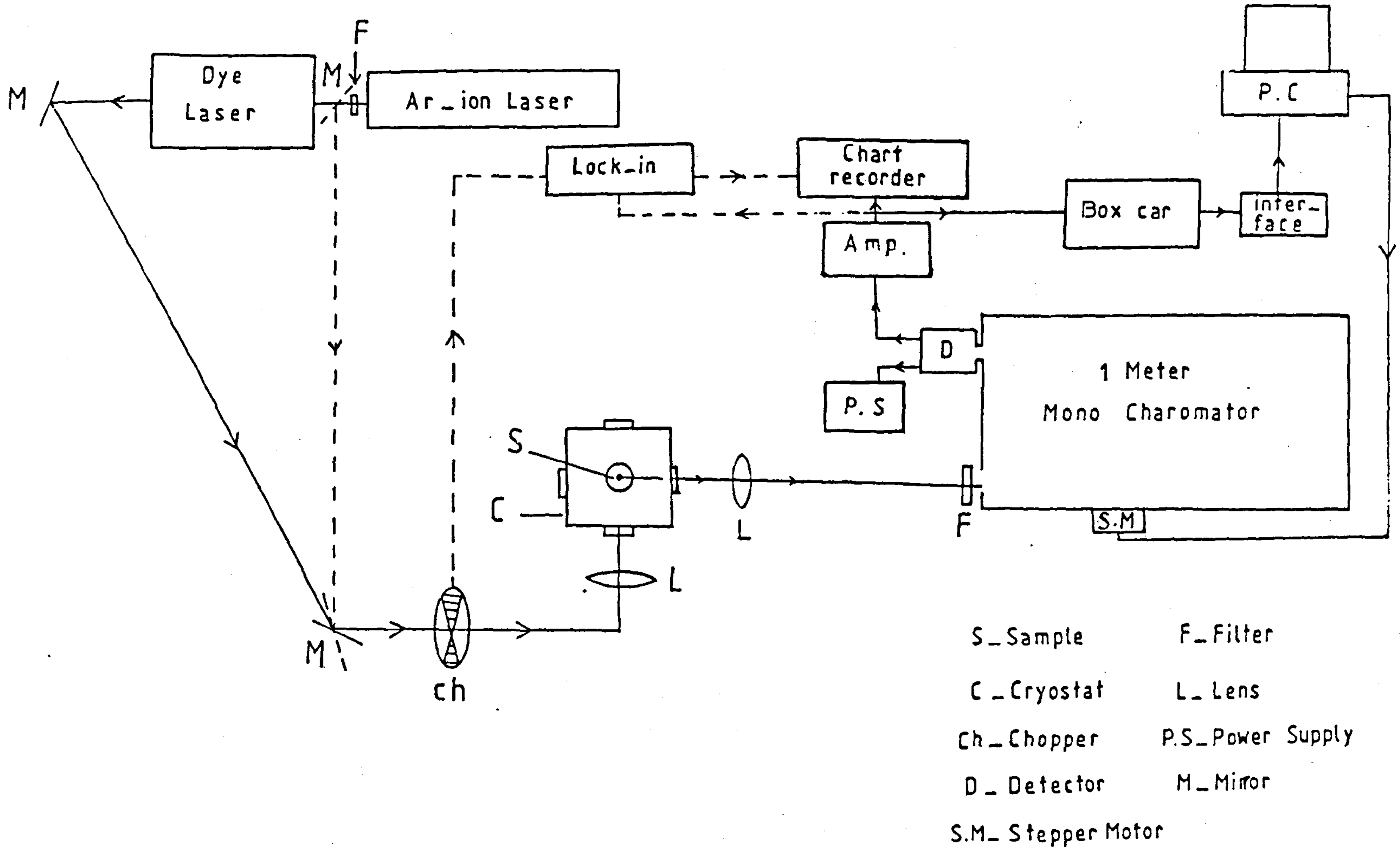

Fig 3.6 General arrangement for the photoluminescence.

DCM or Rhodamine-6G dyes pumped by a 2020-05 Ar^+ laser. A diolite diode laser was used as a near infra-red source in the range around 780-787nm for excitation of the Cr^{3+} doped fluoro-zirconate glass.

3.4.2 Polarized excitation/luminescence spectroscopy

The emission from optical centres in sites with octahedral symmetry is unpolarized. However, ions in sites with symmetry lower than octahedral exhibit anisotropy. Ruby is an example of an anisotropic emitter in which the axes of all the Cr^{3+} ions in a crystal point in the same direction. However in the case of Cr^{3+} ions occupying orthorhombic symmetry sites in MgO, the six equivalent distortion axes are equally populated. In consequence the total absorption is isotropic, so that when excited with unpolarized light, the number of ions in the distinct but equivalent sites are equally excited and the overall emission is isotropic even though the individual centres absorb and emit anisotropically. However, excitation using light along a particular crystal direction results in different absorption by the different centres and the overall emission is anisotropic. By studying the anisotropy of the luminescence relative to the polarization of the excitation light the orbital degeneracies of the states involved in the transition and axes of symmetry of the luminescence centres in the crystal may be identified.

For these experiments the same steady state emission arrangement shown in figure (3.6) was used. However a half waveplate ($\lambda/2$) is insereted in front of the sample, in order to rotate the polarization axis of the pumping light. In addition, a linear polarizer is placed before the input slit of the monochromator.

3.5 Time Resolved Spectroscopy

In time resolved luminescence measurements the output from the current amplifier was fed to the input connector on either a lock-in detector or a boxcar integrator. We discuss the different techniques separately.

3.5.1 Phase sensitive detection

Phase sensitive detection may be used to recover weak signals. By modulating the required signal at a particular frequency and detecting using an amplifier set to this frequency only, it is possible to get rid of frequency component (e.g. noise) other than the signal which should be at the modulation/detection frequency.

An essential characteristic which may be used in the phase-selection technique is that unwanted signals may be "nulled out" and so it will not be detected, while only a signal with a certain phase will be recorded. This may be explained by reference to figure (3.7).

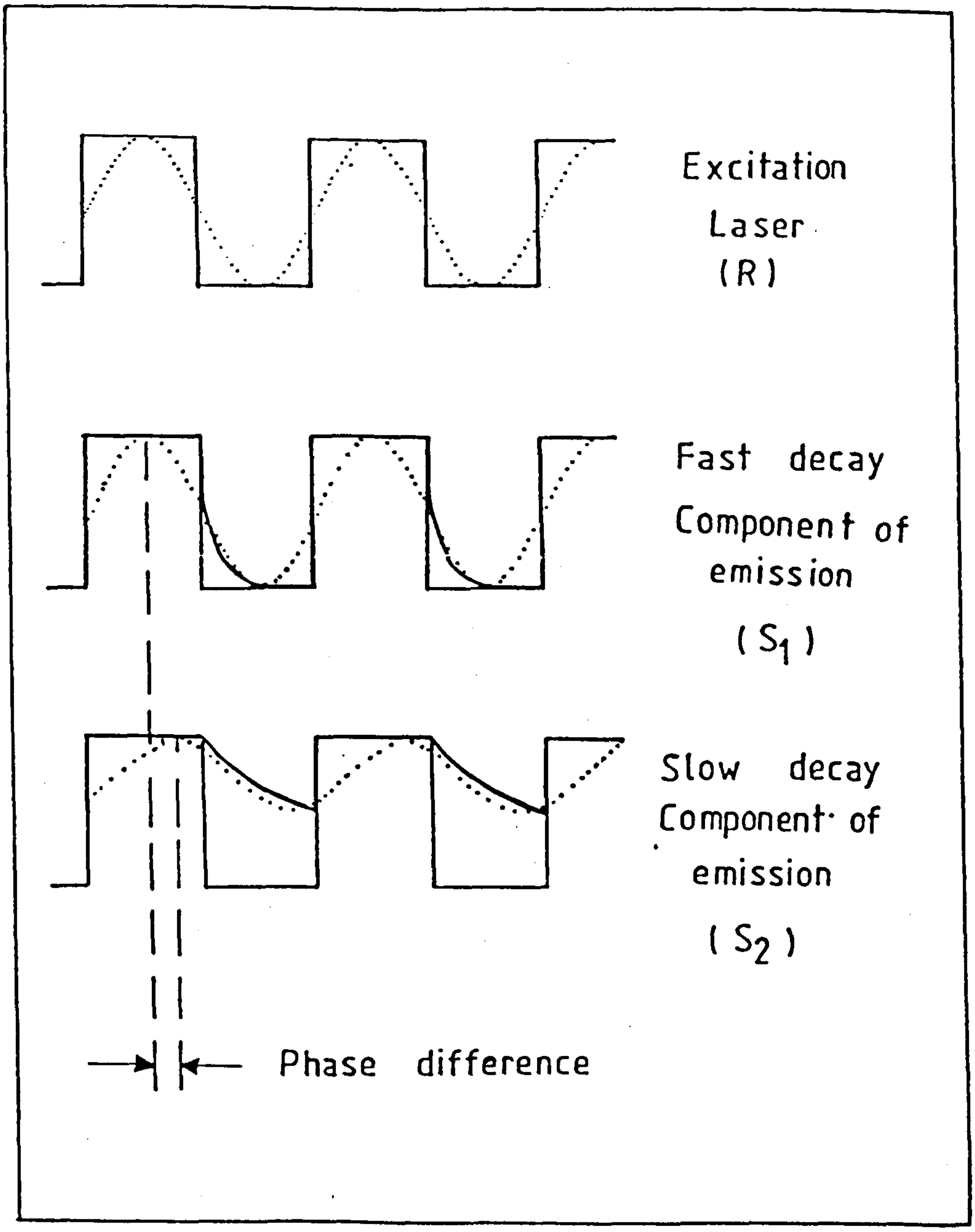

Fig 3.7 Luminescence components with different lifetimes have different phase relationships with the reference signal (R).

The pumping light is chopped with a mechanical chopper with a variable frequency control unit. The modulated signal from the current amplifier is detected with a lock-in amplifier. Two signals S_1, S_2 with different lifetimes will increase and decrease under chopped excitation at different rates as shown: the lock-in detector will see two overlapping signals but with different phases relative to the reference signal, R. If the reference signal R is adjusted to be in phase with one of the two signals that signal will have a maximum value, while the other signal will be lower than its maximum value. If the phase of R can be adjusted, then the signals S_1 and S_2 can be reduced to zero (nulled) or adjusted to a maximum value. In this way it is possible to separate out different emission components, provided that they have different phases. This technique was used by Engstrom and Mollenauer[47] in studies of ruby.

In order to measure the radiative lifetimes, τ_R, the difference in phase setting of the lock-in amplifier between the nulled and peak settings, i.e. Q, is related to the angular chopping frequency, ω, through

$$\tan Q = \omega \tau_R$$

or

$$\tau_R = \frac{\tan Q}{2\pi f} \qquad (3.4)$$

3.5.2 Box car detection

In this technique the amplified output from the photomultiplier is connected to the input of a boxcar integrator in place of the lock-in detector. This signal is connected to an (SR245) computer interface module, controlled by an opus PCII using a software package for recording and analysing various types of spectra. The boxcar is triggered on the reference signal from a mechanical chopper. The spectral dependence of the emission was obtained by driving the monochromator grating with a stepper motor. The emission spectra are scanned for zero time delay and after a finite delay when only signals remaining after the delay are detected.

The boxcar was used in one of two different ways, using wavelength scanning, or, time scanning. In wavelength scanning the computer interface was triggered using a signal generator, to send signals from the boxcar output to the (PC) at a rate matching the monochromator stepping rate. The (PC) software is set up so that each data point corresponds to a different wavelength and the time delay set to the appropriate time range. Two different triggers were used: because the boxcar samples have to have the same relationship to the exciting level (i.e. at a fixed delay after the pulse falling edge) thus were triggered from the chopper reference signal. The rate at which samples were recorded depended upon being matched to the stepping rate of the monochromator meter, so that the wavelength of the monochromator was the same as that calculated by the boxcar software. This rate, which is independent of the chopping frequency, was controlled by an external (TTL) pulse from a signal generator. Figure (3.8) shows the connections to the boxcar and the interface module.

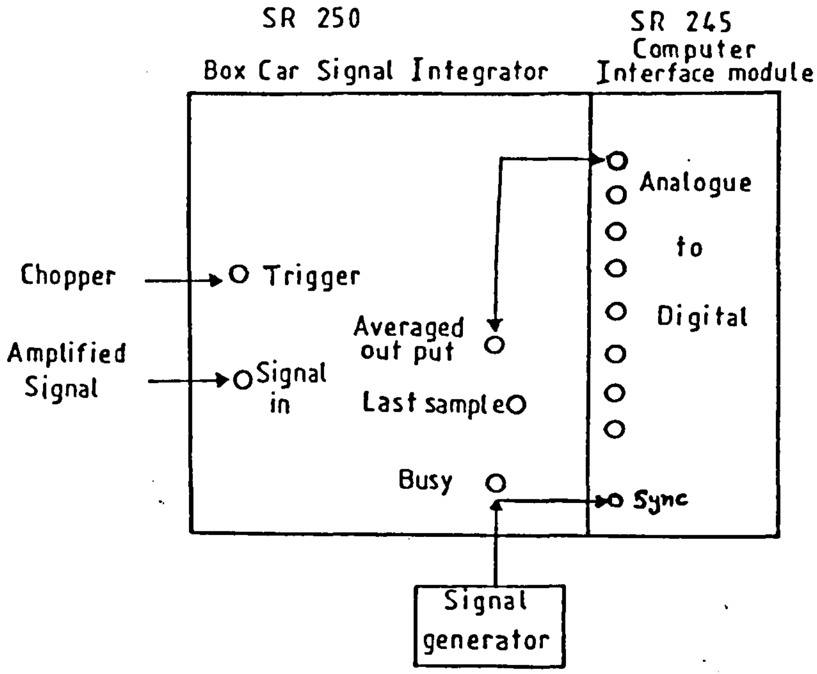

Fig 3.8 Schematic diagram of the boxcar integrator and the computer interface.

The decay rates of different emission signals were measured using time scanning. The computer interface was triggered from the "busy output" of the boxcar (shown in figure (3.8)). The time range scans were controlled by the PC software by controlling the boxcar externally via the computer interface. This facilitates control of the initial and final delay by applying an increasing analogue voltage to the "external delay multiplier" on the boxcar. The samples were taken from the "last sample" output on the boxcar integrator.

For all time resolved spectra (time scans and the spectral dependence measurements) only the photomultiplier tube detector was used. The response of the Ge-detector is not fast enough to follow these pulses.

3.6 High Resolution Spectroscopy

3.6.1 Fluorescence line narrowing

Optical zero-phonon lines in solids are "inhomogeneously broadened" by random disorder associated with the existence of a large number of different crystal field sites. The inhomogeneous broadening in glass samples may extend to many hundreds of wavenumbers, obscuring information about the homogeneously broadened sharp lines at individual sites. Broad band pumping excites all ions and results in broad band emission. In order to probe this inhomogeneous broadening, a narrow band laser may be used to excite a small subset of ions with the result that an appreciable narrowing of the broadband emission may occur. This is the basis of the fluorescence line narrowing (FLN) technique. FLN has been widely studied in rare earths[48,49] and to a lesser extent in T.M.I. doped glasses.[50]

In Cr^{3+} doped glasses the range of crystal field sites is such that emission occurs from both ^2E and $^4T_2$ states. Pumping into the broad $^4A_2 \rightarrow {}^4T_2$, $^4T_1$ absorption bands does not result in a significant narrowing of the luminescence. To affect fluorescence line narrowing in this case, the excitation should be targeted at the ^2E level which will emit resonantly between two purely electronic levels. This resonance fluorescence line narrowing (RFLN) is illustrated in figure (3.9).

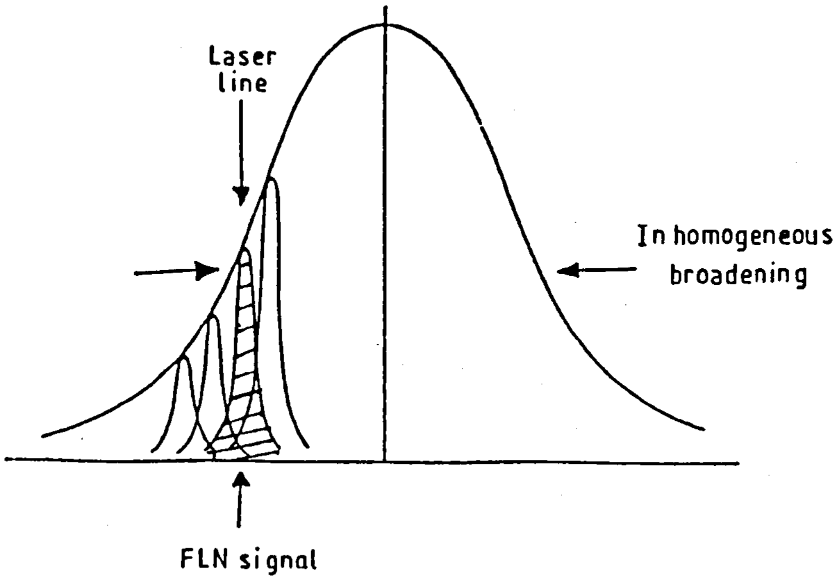

Fig 3.9 Inhomogeneous broadened line whose shape is an envelope of a large number of homogeneous broadened lines showing a spread in their centre frequencies.

Exploitation of FLN requires a high resolution laser, such as a single-mode ring dye laser. The Spectra Physics 380D is such a laser which is capable of linewidths down to ~ 150 Khz. More specifically we have used linewidths of ca 200 MHz. The sample is cooled in a variable temperature cryostat to obtain larger $^2E \rightarrow {}^4A_2$ signals and also to measure the temperature dependence of the broadening of the FLN line. The FLN line was measured using a high resolution monochromator. Since in RFLN the emission occurs at the same wavelength as excitation, it may be difficult to extract the signal from the intense scattered exciting radiation. To overcome this we use a time delay after the laser pulse using a Delta-Development signal integrator. This avoids exposure of the P.M.T. to a strong laser light which may saturate the detection system. Because it is difficult to avoid some excitation reaching the detector we also used a double mechanical chopper in which the slots in the two chopper wheels were 180° out of-phase. The two wheels are synchronously driven using a single connecting shaft, one is positioned in the excitation beam just before the sample and the second between the sample and the detection system. To ensure that the second wheel blocks out all of the scattered light and yet maximizes the emission signal from the sample, the blades in the first wheel have a larger area than those in the second wheel (see figure (3.10)). Displacement between the two chopper wheels was large enough to accommodate the tail of the MD-04 liquid helium dewar and the cold finger liquid nitrogen cryostat (see section 3.2). However a single chopper only was used with the closed cycle

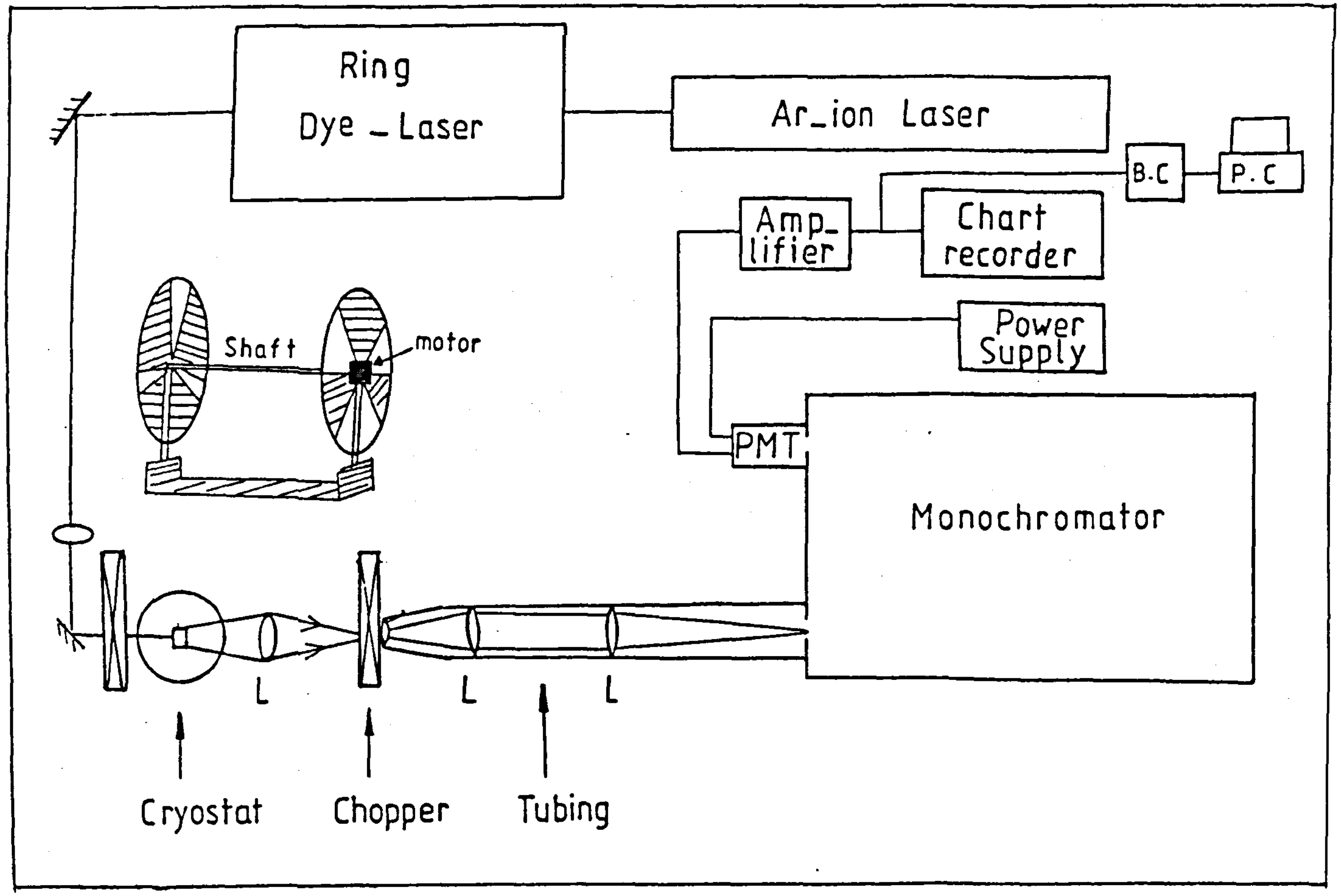

Fig 3.10 FLN experimental arrangement.

refrigerator because the optical access head was too large to insert between the two blades of the double chopper system. The single chopper blade had two sets of slots, each of odd numbers, one set of slots being used for excitation and the other to pass the emitted radiation.

The basic idea of both chopper systems is to apply an on-off gate, alternately shielding the P.M.T. from the laser radiation which excites the sample and then blocking the laser beam while the fluorescence is measured. This arrangement had the additional advantage that it eliminates the fast $^4T_2$ emission which overlaps the tail of the ^2E emission. By detecting the ^2E emission after a certain delay, the faster $^4T_2$ emission will have decayed to a very small value, as indicated in figure (3.11).

The chopper system was designed to have a laser pulse width of ~ 0.8ms, a detection gate of 8.2ms width and a time delay of 1.4 ms between the excitation and the detection of the signal. These values could be varied by changing the speed of the chopper system. However, the choice of optimum values should take into account, that to achieve a maximum signal, the excitation time should be of the same order as the lifetime of the ^2E emission. Consequently, an excitation aperture in the chopper wheel which results in a pulse width of the order of ms will maximize the signal. Preliminary measurements showed that the radiative decay time of the ^2E emission is of the order of ~ 1ms for the silicate glasses. The delay time

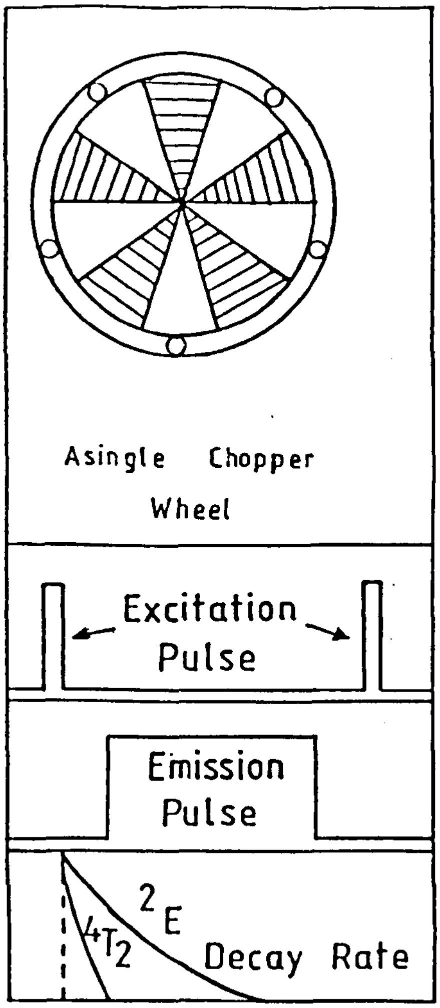

Fig 3.11 FLN detection principles utilizing the difference in the decay rates.

is chosen so that most of the $^4T_2$ emission has decayed when the chopper slot is opened to enable the detection of the ^2E emission alone. Of course, the detection gate must be open long enough to allow the detection of the ^2E emission. FLN experiments are not possible using slow mechanical chopper rates if the decay times are fast. It is possible in the $^2E \rightarrow {}^4A_2$ transition of Cr^{3+} doped glasses at low temperature because the radiation decay times are comparatively long. After passing the chopper, the signal is collimated, and focused using lenses onto the input slit of the monochromator. To avoid scattered laser light and reflections from lenses, sample, mirrors, etc., an enclosed tube covers the path between the chopper and the monochromator slit as illustrated in figure (3.10) was used. The detection system is then much the same as that used in the DC luminescence measurements. The signal is recorded either on a chart recorder or stored as a data file in the PC for detailed processing and analysis utilizing the SR265 package facilities. This is especially important in measurements of the temperature dependent broadening of the FLN lines where many runs were required to offset the progressive weakening and increasing noise of the signal with increasing temperature.

3.6.2 Zeeman spectroscopy

Although the orbital degeneracy of the energy levels of $3d^3$ ions in solids is lifted in lower symmetry sites, there remains some spin degeneracy which may be raised by an applied magnetic field, leading to spectra splittings that may be measured in high resolution spectroscopy. The energy of an ion with spin S (neglecting any zero field splitting) in a magnetic field B is given by:

$$E = \underline{\mu}.B$$

$$= m_S g_L \mu_B B$$

where g_L is the Lande g-factor or the spectroscopic splitting factor, μ_B is Bohr magneton, and the quantization of m_S is along the magnetic field. For Cr^{3+} ion S is either 1/2 or 3/2. The R-line transitions, in which we are particularly interested, involves the ^2E (S = 1/2) and $^4A_2$(S = 3/2) levels. The energy splitting in an octahedral field is shown in figure (3.12): the resulting spectral components are circularly ($\sigma\pm$) and linearly polarized.[36] The splittings are determined by the difference in g-values of the participating states.

Electron paramagnetic resonances (EPR) measurements were carried out using a Q-band cavity to find the ground state g-value for two Cr^{3+} doped glass samples.

For the $^2E \rightarrow {}^4A_2$ transition in glasses the gross inhomogeneous broadening due to the multi-site occupancy by Cr^{3+} ions is greatly in excess of the Zeeman splitting. In order to resolve the different Zeeman components it it necessary to combine the FLN and Zeeman effects in a single experiment. It may then also be possible to measure the circular polarization of these transitions

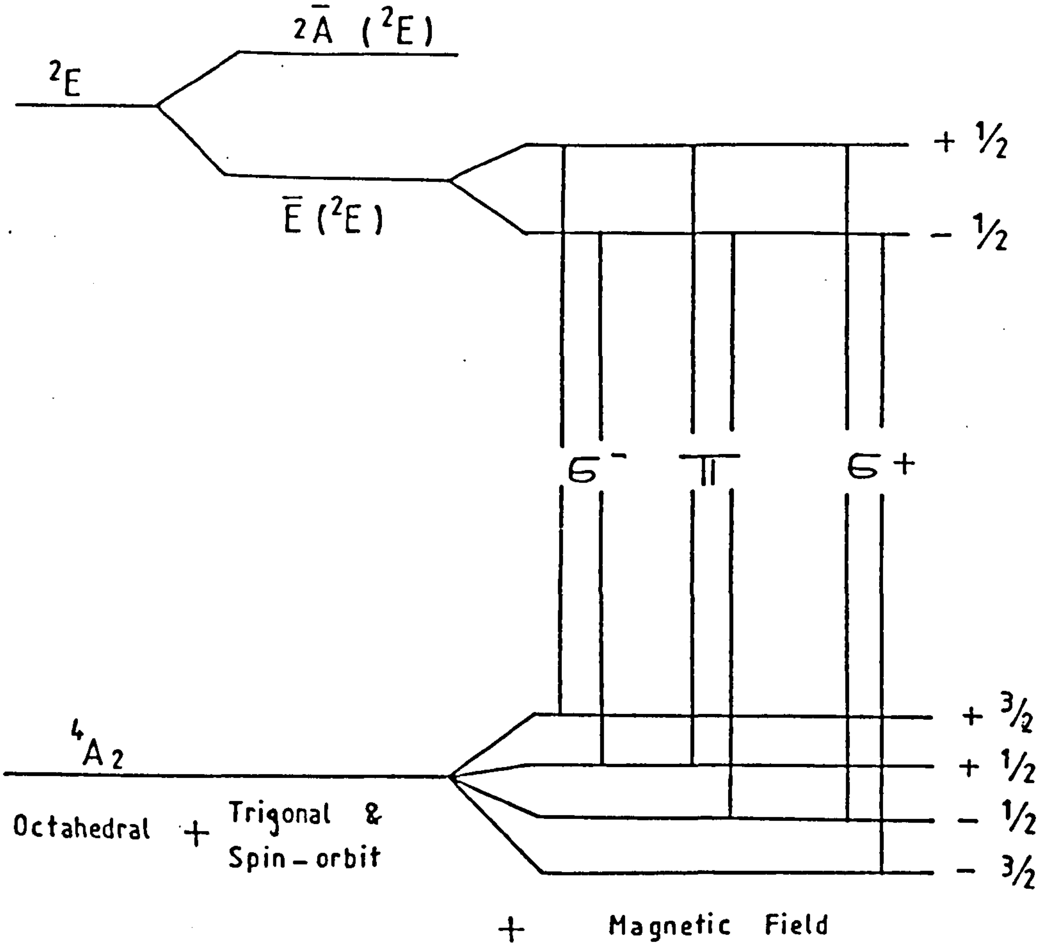

Fig 3.12 Zeeman splitting prediction of ^2E and $^4A_2$ states of Cr^{3+} ion under a trigonally distorted octahedral crystal field and a magnetic field, where transitions are only expected from the lower $\bar{E}(^2E)$ state at low temperature (selection rules will be discussed later in chapter 6).

in the magnetic field. The experimental arrangement is shown in figure (3.13).

The excitation source is the ring dye laser operating with DCM dye in order to perform RFLN in a magnetic field. The field in the range 0-5.7 tesla was derived from the superconductivity solenoid. However, because of the large diameter of the cryostat neither the single chopper nor the double chopper assembly could be used. Instead, two electronically synchronized choppers were fixed at 90^0 to chop the exciting and emitted radiation, so as to achieve a synchronous on-off gating as discussed above for FLN studies. To monitor the synchronization, the reference output of each chopper was connected to an oscilloscope channel. Luminescence parallel to the magnetic field was focused on the second chopper and then onto the monochromator input slit. A photoelastic modulator (P.E.M.) followed by Glan-Taylor prism was located in the emission path for magnetic circular polarization detection. The P.E.M. consists of a vibrating quartz bar which modulates the birefringence of the quartz at 50 kHz. When the amplitude of vibration is set to $\lambda/4$ then the emission through the prism oriented at 45^0 to the vibrational axis is a measure of the intensity difference of the right and left circularly polarized emission $I_{(\sigma+)} - I_{(\sigma-)}$. The modulator driver provides a 50 kHz reference signal fed into the lock-in amplifier to produce a D.C. output for $I_{(\sigma+)} - I_{(\sigma-)}$. Further details are given in chapter 6.

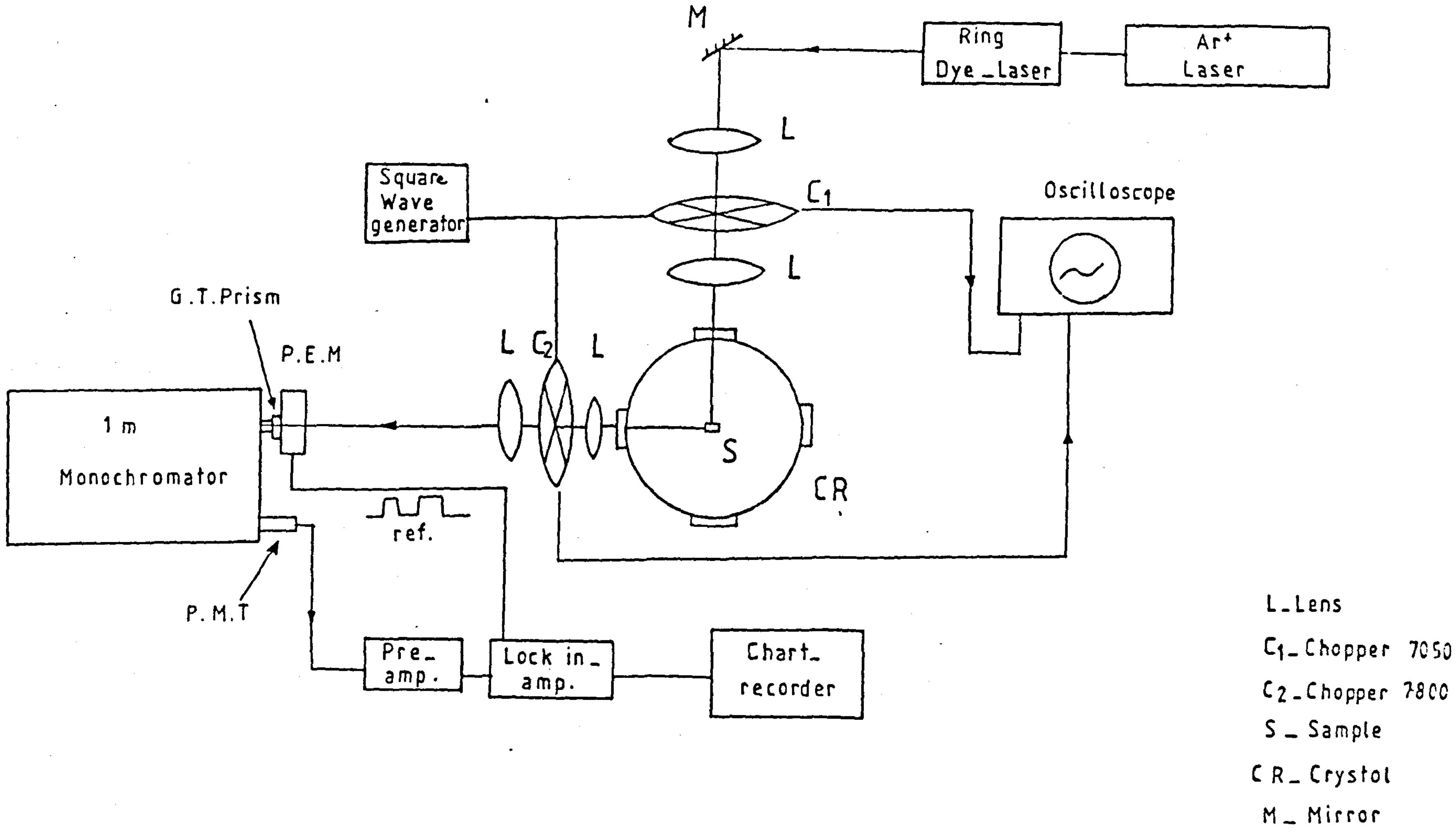

Fig 3.13 Experimental arrangement for the magneto-optical effects.

3.7 Calibrating the Spectral Response of the Detection System

In order to get true values for the spectral dependence measurements, the spectral response of the grating monochromator and detectors, as well as the spectrum of a reference radiation source (tungsten lamp) are required.

We let $M(\lambda)$ be the spectral output of the tungsten lamp at wavelength, λ, and $R(\lambda)$ be the real spectral output intensity at wavelength λ calculated using the blackbody radiation equation:

$$E = \frac{2hc^2}{\lambda^2} \cdot \frac{1}{e^{hc/kT}-1} \qquad (3.5)$$

The temperature, T, of the tungsten filament may be measured using a pyroelectric detector. Values of E may then be calculated for different values of (λ) at particular temperatures. And the spectral correction function $S(\lambda)$ defined as

$$S(\lambda) = \frac{R(\lambda)}{M(\lambda)} \qquad (3.6)$$

may be used at different wavelengths to obtain the corrected spectral output $C(\lambda)$ of any spectrum. If $I(\lambda)$ is the intensity at wavelength λ measured using a certain detector then the corrected signal is given by

$$C(\lambda) = I(\lambda) \cdot S(\lambda) \qquad (3.7)$$

This correction of the spectral response has been carried out for photoluminescence systems having in common the Monospek 1000 monochromator but with different photodetectors, i.e. the GaAs photomultiplier and the Ge-detector (see section 3.3.1) in the ranges 400 nm - 900 nm and 650 nm - 1400 nm respectively. Using the P.M.T. does not affect the spectral values very much, since its response function is almost constant with wavelengths for most of the spectral ranges used in our experiments. However the correction is still needed for the monochromator grating response.

for the germanium detector the correction was very important since its intensity varies considerably with the wavelength as shown in figure (3.14). In figure (3.15) the spectrum of the Li-borate glass (G8382) emission shows the effects of the detection system response on the real spectrum. A computer programme was written, utilizing the above information to facilitate the corrections of individual spectra which had been stored as data files. The output could be formatted as $I(\lambda)$ versus λ, $I(\bar{\lambda})$ versus $\bar{\lambda}$ or $I(E)$ versus E.

3.8 Measurements of the Spectral Moments

Because of the characteristic optical bandshapes of solids, sharp features are not always easily identified, e.g. in cases such as the

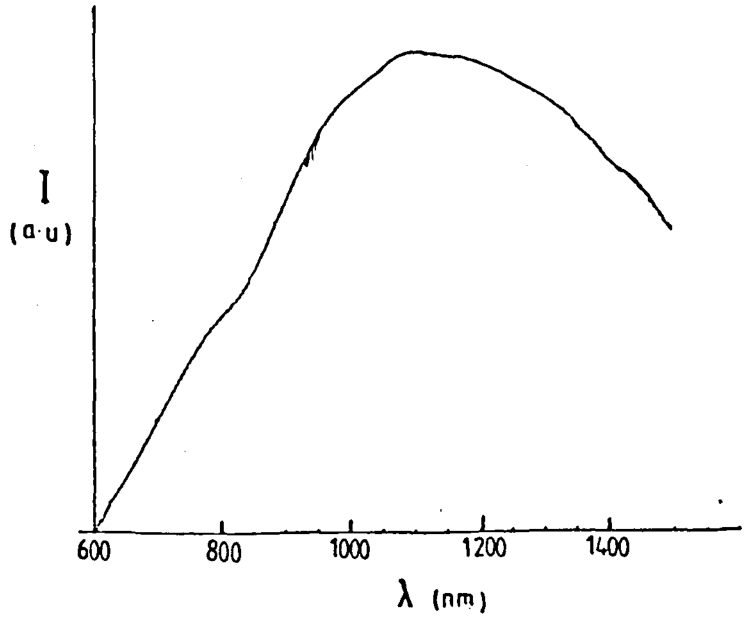

Fig 3.14 The spectral intensity for the tungsten lamp measured by the Ge-detector.

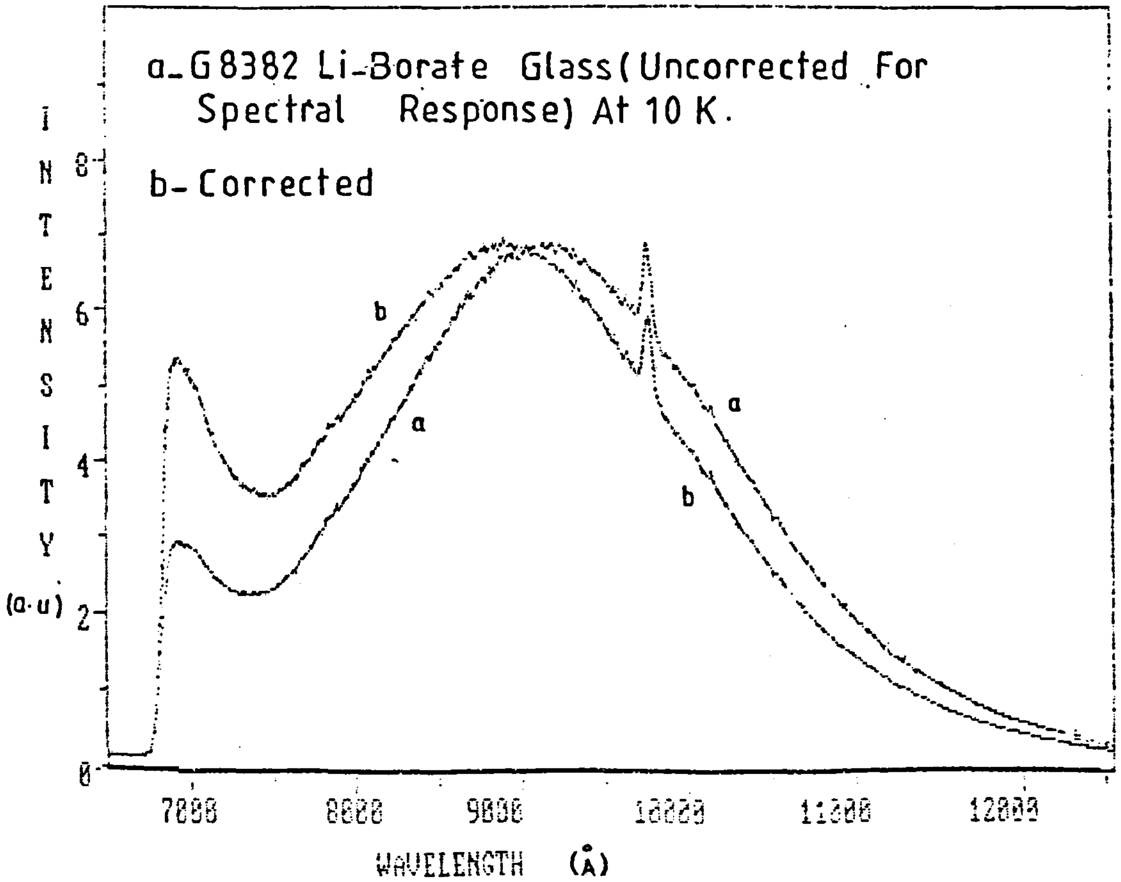

Fig 3.15 The effect of spectral response of the experimental detection system.

$^4T_2 \rightarrow {}^4A_2$ transition of Cr^{3+} doped glasses and the broad emission band of Ti^{3+} doped samples, it is often useful to calculate the moments of the bandshape.

This is illustrated in figure (3.16) which shows a broadband spectrum from which the following moments can be calculated:[36]

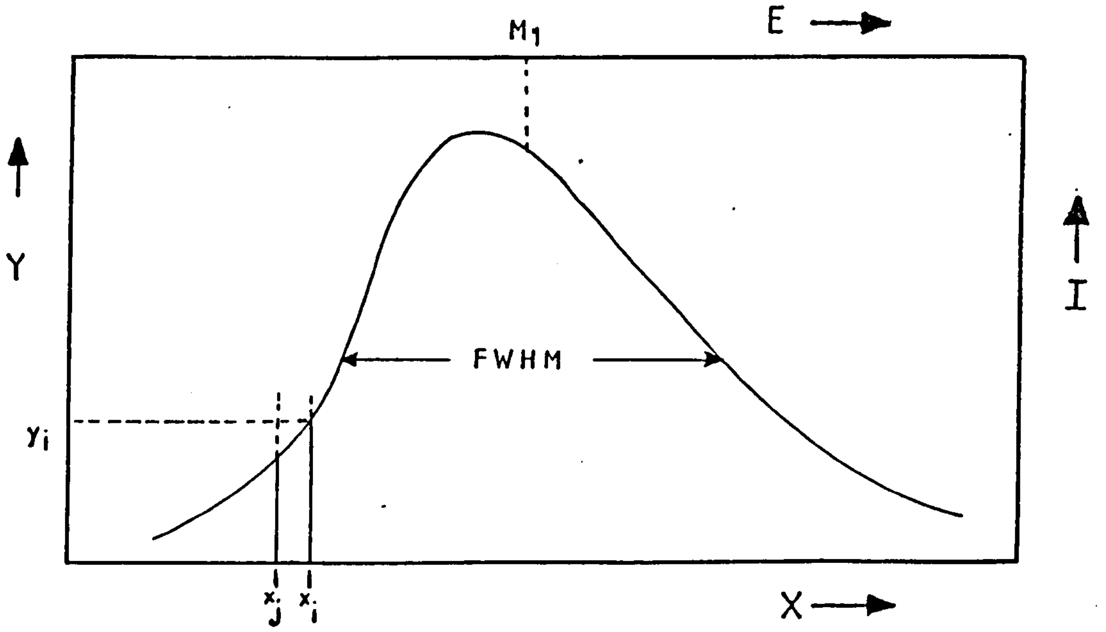

Fig 3.16 Band shape characterization of a broad band where the centroid (M_1) and the (FWHM) (which is related to (M_0)) are both shown.

(a) the area under the curve in figure (3.16) M_0 which is a measure of the integrated intensity of the spectrum can be found as:

$$M_0 = \int_{X_{i-1}}^{X_i} y dx = \sum_i y_i (X_i - X_{i-1})$$

(b) The first moment, defined as:

$$M_1 = \bar{X} = \frac{\int xydx}{\int ydx} = \frac{\sum\limits_i x_i y_i (x_i - x_{i-1})}{\sum\limits_i y_i (x_i - x_{i-1})} = \frac{1}{M_0} \sum_i x_i y_i (x_i - x_{i-1})$$

measures the position of the centroid of the spectrum.

(c) The second moment is related to the bandwidth (FWHM) of the spectrum, as can be seen in the relation

$$H^2 = 8\ell n2\ M_2$$

where H is the (FWHM).

3.9 Experimental Samples

The optical techniques discussed above were used to study a variety of problems in Ti^{3+} or Cr^{3+} doped crystals and glasses. The experimental samples consisted of three Ti^{3+} doped crystals and one glass and Cr^{3+} doped into different glasses. Full details are given in the appropriate chapters of the experimental results.

CHAPTER FOUR

4. SPECTROSCOPY OF Ti^{3+}:DOPED CRYSTALS AND GLASSES

4.1 Introduction

Interest in the spectroscopic properties of Ti^{3+} in crystals and glasses was renewed following the first demonstration of a Ti^{3+} ion doped solid state laser ($Ti^{3+}:Al_2O_3$).[51,15] This laser has proved to be broadly tunable in the visible and the near infra-red region and to operate at room temperature. Other desirable features are the durability of the host, the size and optical quality of the crystal to produce energies and beam qualities needed for many applications. Information gained from work on Cr^{3+} doped hosts led to detailed understanding of vibronic transitions in such solid state lasers. However Ti^{3+} doped sapphire shows a large Stokes' shift and broader tuning range than Cr^{3+} lasers. Moreover the excited state absorption which is an impediment factor for the operation of the Alexandrite laser at high temperatures is absent from $Ti^{3+}:Al_2O_3$. Because of these advantages and the rapidly improving growth techniques for production of good quality Ti^{3+} doped crystals,[52] it seems probable that there will be a variety of materials as candidates for laser operation. Ti^{3+} ions differ in their optical properties in different host materials because of the sensitivity of the d-orbitals to the surrounding, since the upper laser energy levels of Ti^{3+} depend linearly on the ligand field. Hence using different hosts may change the laser tuning range of the Ti^{3+} laser. In an early study, McClure[53] studied the crystal

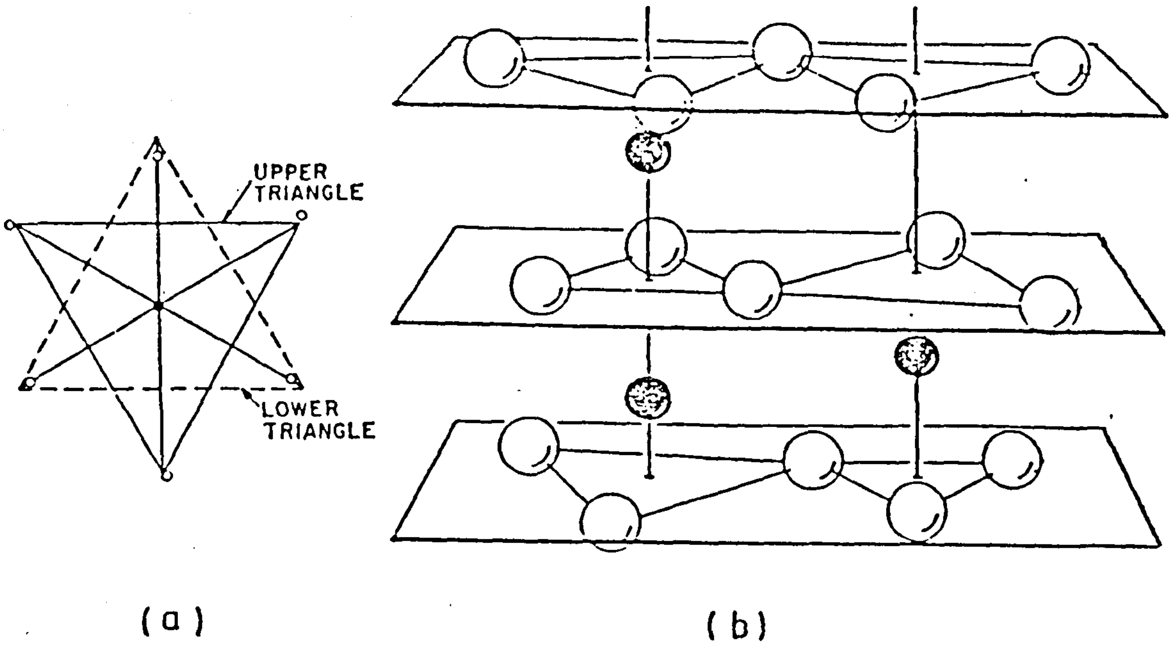

Fig 4.1 Crystal structure of sapphire, a - top view for only two planes of atoms, b - sideview where the open circles forming triangles of O^{-2} ions, while the dark circles are the $A\ell^{3+}$ ions at the trigonal axis.

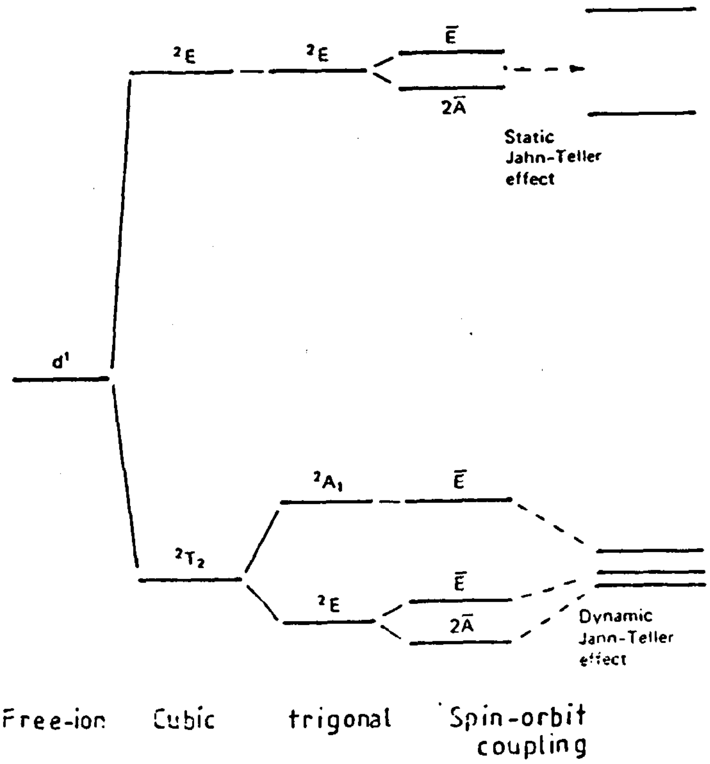

Fig 4.2 Energy level splitting of the Ti:$A\ell_2O_3$ due to the combined effects of trigonal crystal field, spin orbit coupling and the Jahn-Teller effect.

structure and the optical absorption spectrum of $Ti^{3+}:Al_2O_3$, his interpretation for the spectra based on the point charge model. The ^2D free ion state splits mainly by the octahedral component of the crystal field in the sapphire host into two levels separated by ~ 19000 cm^{-1}. The excited ^2E state does not split in a trigonal field, rather is the orbital degeneracy removed by the Jahn-Teller effect. Subsequent measurements of the far infra-red transmission of $Ti^{3+}:Al_2O_3$ by Nelson et al.[54] attributed the observed zero-phonon lines observed in absorption to the electronic levels of Ti^{3+} in sapphire lattice. This assignment was later supported by theoretical calculations (Mcfarlane et al.)[55] of the energy levels of a single d-electron in the corrundum crystalline field subjected to Jahn-Teller distortion. This theoretical study showed that static crystal field theory alone cannot account for the experimental observations of the magnetic field dependence of the far infra-red spectra of the crystal. Joyce et al.[56] reported anisotropic g-values of the ground state ($g_{\parallel} = 1.11$ and $g_{\perp} < 0.1$); from Zeeman splitting, same values measured using the EPR technique.[57]

4.2 Crystal Structure of Ti^{3+} Doped Crystals

Suitable host materials for Ti^{3+} ion lasers require a strong electrostatic crystal field to produce a large splitting of the five-fold degenerate ^2D-state of the free Ti^{3+} ion, and a strong electron-phonon coupling to make broadband tuning possible. The host crystal must have a larger band gap than the Ti^{3+} ion splitting to avoid absorption transition to the degenerate levels in the conduction band. The sapphire ($A\ell_2O_3$) crystal structure is the same structure as Ti_2O_3 and so is ideal for Ti^{3+} substitution at the $A\ell^{3+}$ sites. In addition it has good heat conductivity and high stability. Other potential hosts for Ti^{3+} are the garnets, in which laser action on the Cr^{3+} ion is already realized.[58] It is anticipated that the spectroscopic properties of Ti^{3+} in garnets (e.g. YAG) will differ from those in sapphire, because the crystal field is weaker and because the Ti^{3+} occupies a site with inversion symmetry. In consequence, it is to be expected that the Ti^{3+}:YAG fluorescence is red shifted, and will be longer lived, compared with the $Ti^{3+}:A\ell_2O_3$.

4.2.1 $Ti^{3+}:A\ell_2O_3$

The crystal structure of sapphire is shown in figure (4.1); pairs of $A\ell$ atoms are arranged along the c-axis and surrounded by trigonally distorted oxygen octahedra which leaves the point group symmetry at the $A\ell$ site as C_{3v}. When Ti^{3+} ion substitutes in $A\ell_2O_3$ crystal, it directly replaces the $A\ell^{3+}$ ion on these trigonally symmetric sites. This substitution differs from the substitution of Cr^{3+} in $A\ell_2O_3$ (ruby) because the replacement of $A\ell^{3+}$ by Ti^{3+} involves an increase in the ionic radius of ~ 33% ;(the ionic radii are 0.51 Å and 0.76 for $A\ell^{3+}$ and Ti^{3+} respectively) compared with an expansion of only 20% for Cr^{3+}.

The free ion configuration of Ti^{3+} consists of a single 3d electron outside a closed Argon Shell. The ion level ^2D is split into an upper doubly degenerate ^2E state and a lower triply degenerate $^2T_2$ state, due to a cubic crystal field. The ground state $^2T_2$ is shown to be further split by the trigonal field into $^2A_1$ and ^2E in figure (4.2). Spin-orbit interaction will cause further splitting of the lower ^2E state into $\bar{E}$ and $2\bar{A}$ states (using the C_{3v} double group symmetry labels; the upper $^2A_1$ is now labelled as $\bar{E}$, although it is not affected by the spin-orbit coupling). This energy level scheme which takes into consideration only the effect of the static crystal field, cannot explain the experimental splittings measured for the lowest energy levels.[54,56] However, Mcfarlane[55] obtained good agreement with the experimental results by including the effect of dynamic Jahn-Teller effect[81] in the $^2T_2$ state, which led to reduced splittings by virtue of quenching the trigonal field and the spin orbit coupling.[59] See section (4.3). The large splitting of the excited ^2E state is due to a strong Jahn-Teller effect.[53]

4.2.2 Ti^{3+}:YAG

Garnets have a body centred cubic lattice with space group I_a3d. The structure is built up from oxygen polyhedra surrounding the trivalent cation; dedecahedra with eight-fold oxygen coordinates, six-fold octahedra and four-fold tetrahedra. The general formula is $A_3B_5O_{12}$, with each unit cell having eight such formula units. The shape of these sites is seen in figure (4.3). The Yttrium

Aluminium oxide Garnet (YAG) has the chemical compositions $Y_3Al_5O_{12}$, containing 160 ions per unit cell (96 oxygen, 24 yttrium and 40 Aluminium ions). The occupation of the different sites depends on the size of ions involved, with the large yttrium ion, Y^{3+}, occupying the dodecahedral site, with the Aluminium ions occupying both octahedral and tetrahedral sites. The environment of the trigonally distorted octahedral site occupied by Al^{3+} ion is shown in figure (4.4) where the inversion symmetry may be recognized by the parallel triangles of Aluminium, yttrium and oxygen ions, with a slight rotation about the normal axis of the triangles with respect to each other. Ti^{3+} ion substituted for the Al^{3+} ion occupies these trigonally distorted octahedral sites.[60,61]

4.2.3 Ti^{3+}:YAP

The host crystal yttrium ortholuminate ($YAlO_3$) has a perovskite crystal structure, hence the acronym YAP (Yttrium Aluminium Perovskite) analogous to YAG. The general formula of the perovskites is ABO_3; the basic structure is shown in figure (4.5). The overall symmetry for the perovskite is orthorhombic.[62] The unit cell of $YAlO_3$ consists of four distorted perovskite units, which results in a monoclinic perovskite-like pseudocell[63] shown inside the orthorhombic unit cell, figure (4.6).

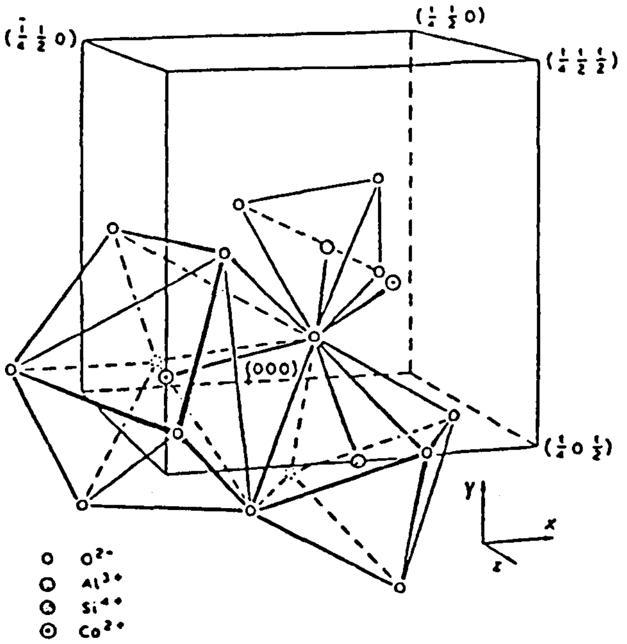

Fig 4.3 Grossularite structure showing 3 types of symmetry; octahedral, tetrahedral and dodecahedral (after Abrahams and Geller[61]).

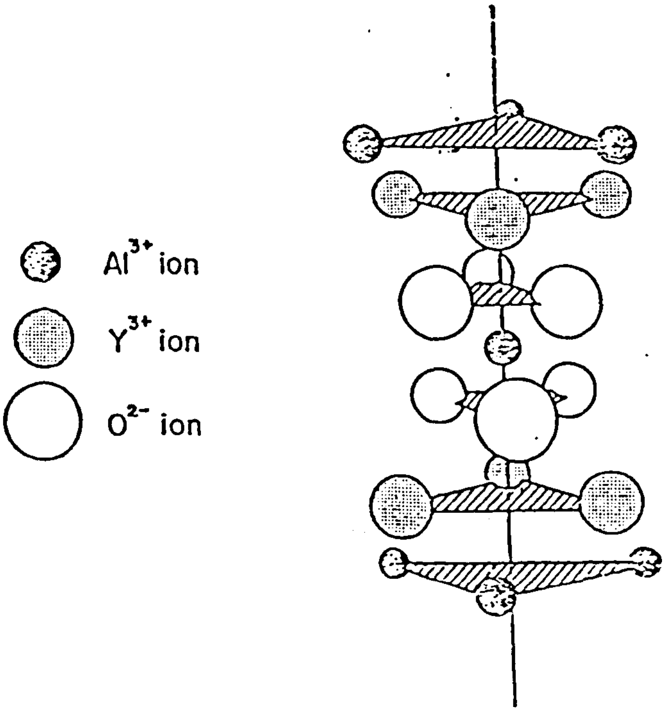

Fig 4.4 Symmetry structure of Al^{3+} in trigonally distorted cubic field in the YAG crystal.

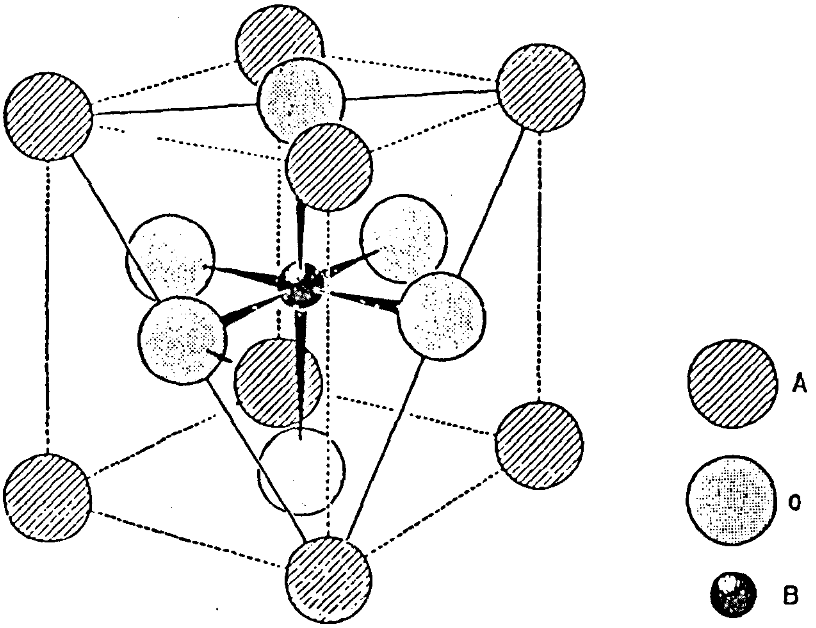

Fig 4.5 The general perovskite structure.

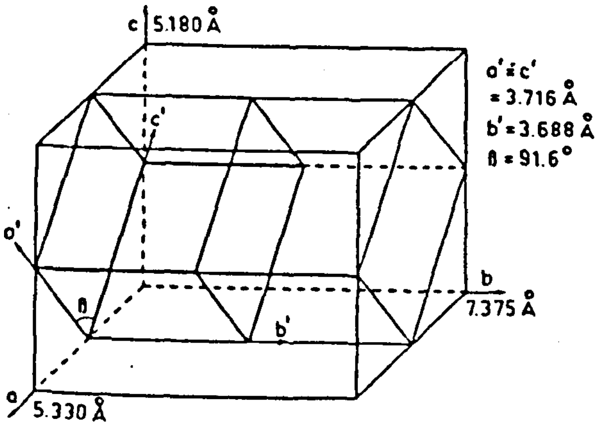

Fig 4.6 The relationship between the orthorhombic unit cell and the monoclinic pseudo cell in $YA\ell O_3$ (after Diehland Brandt[63]).

4.2.4 Ti^{3+}:doped glass

The interest in Ti^{3+}:doped solids is not restricted to crystalline materials, since there are many potential applications for Ti^{3+} doped glasses[64] in addition to their potential for tunable lasers. It is thought that in glasses the Ti^{3+} ion occupies slightly distorted octohedral symmetry sites. These symmetry characteristics were determined by ESR and optical absorption spectroscopies.[64,65] Measurements of the g-values can be used to obtain the ground state energy level separation and identify the type of distortion involved. The observed anisotropy[66,65] of the Ti^{3+} g-value in glasses demonstrates that the optical centre does not occupy perfect octahedral crystal fields. Trigonal or tetragonal field components cause the g-value of Ti^{3+} ion to differ markedly from the free electron value (2.0023) and to be axially symmetric with principal g-values, $g_{\parallel}$ and $g_{\perp}$. In trigonal fields, the Ti^{3+} ion is characterized by $g_{\parallel} > g_{\perp}$, as in the case of Ti^{3+}:Al_2O_3.[57] For the broad assymetric ESR spectra of Ti^{3+} in glasses, the opposite situation obtains and the g-values for different Ti^{3+} doped glasses have $g_{\parallel} < g_{\perp}$.[57,66,67] Calculations of the g-value for Ti^{3+} in phosphate and borate glasses assume that the cubic term in the crystal field expansion is dominant and tetragonal terms are treated as a perturbation. Since coupling between the ^2E and $^2T_2$ states is very weak and the spin-orbit interaction is ignored the effective g-value is determined to be ~1.92 - 1.94.[65] In contrast for Ti^{3+} ions in trigonal symmetry with the cubic terms >> trigonal term similar results are determined. However when the trigonal field is not much weaker than the cubic symmetry there is an appreciable mixing of the excited ^2E state into $^2T_2$ when the observed g-values are $g_{\parallel} = 1.07$ and $g_{\perp} < 0.1$ in, for example, $Ti^{3+}:Al_2O_3$. Hence the tetragonal symmetry is assumed for the site distortion of the octahedral crystal field for Ti^{3+} doped glasses. In tetragonal symmetry site the positioning of six octahedral ions is distorted along one of the axes (i.e. only two ligands will be affected). The reduction in symmetry from octahedral (O_h) to tetragonal (D_{4h}) leads to five levels.[38] The excited ^2E state is split by the tetragonal symmetry into B_{1g} and A_{1g} levels and the ground $^2T_2$ state results into B_{2g} and E_g. This is illustrated in figure (4.7).

4.3 Vibronic Transitions of Ti^{3+} ions in crystals

The d-d transition probability of Ti^{3+} ion is described by the matrix $\langle\psi_f|H|\psi_i\rangle$, where both states can be written as Born-Oppenheimer products

$$\psi(r,Q) = \phi(r,Q)\ \chi(Q) \qquad (4.1)$$

composed of a purely electronic wavefunction (which depends parametrically on both electronic and vibrational coordinates) and the vibrational wave function (which depends only on the vibrational coordinate). Hence equation (4.1) may be written as:

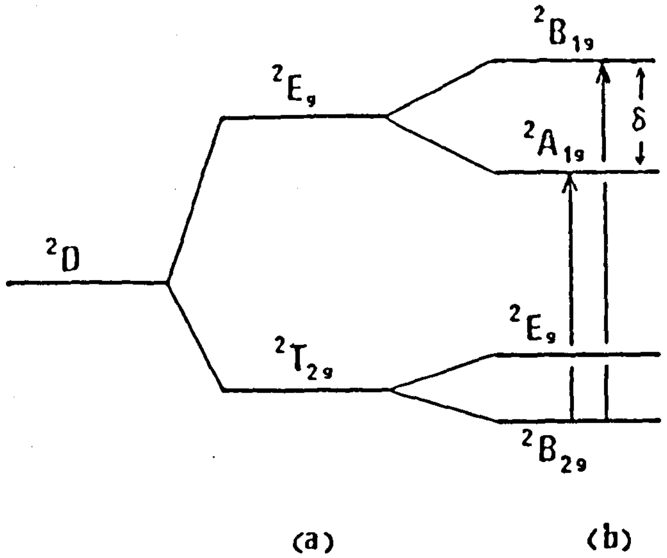

Fig 4.7 Energy level splitting of Ti^{3+}:glass with (a) octahedral field and (b) tetragonal field.

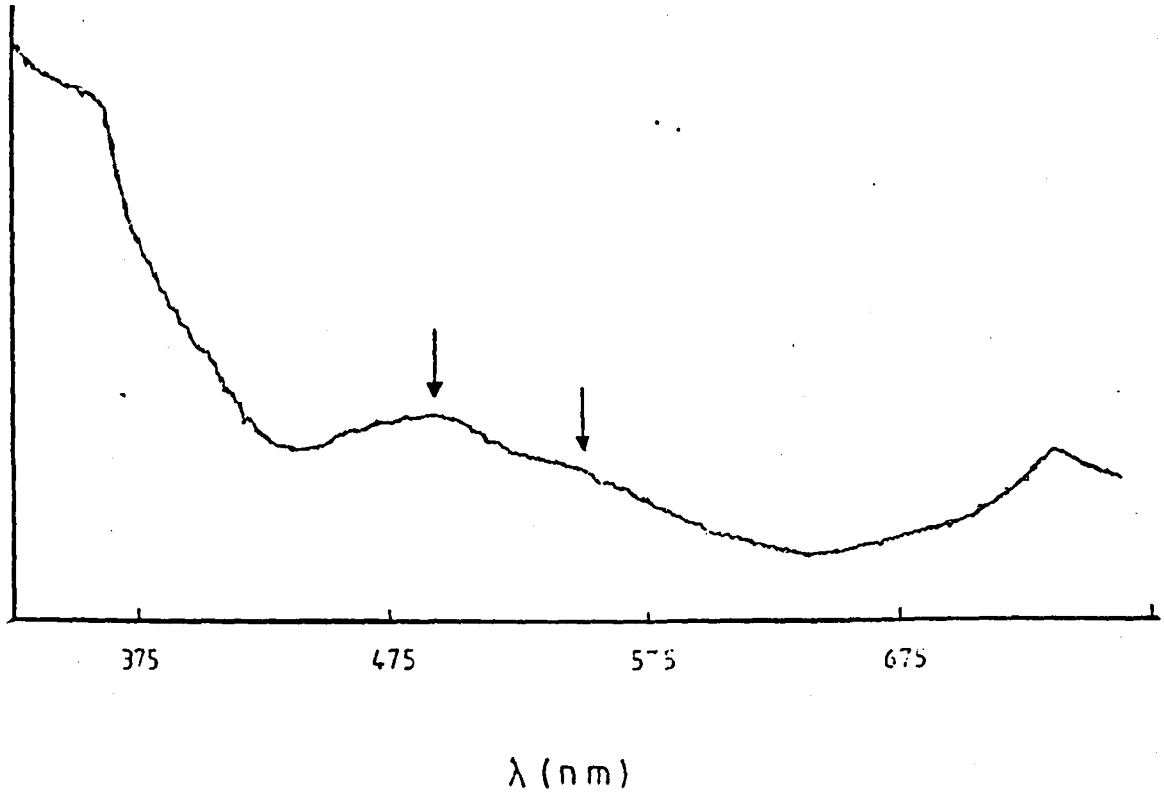

Fig 4.9 The absorption spectrum for $Ti^{3+}:Al_2O_3$.

$$\langle \psi_i(r,Q)|H|\psi_f(r,Q)\rangle = \langle \Phi_i(r,Q)|H_e|Q_f(r,Q)\rangle . \langle \chi_i(Q)|\chi_f(Q)\rangle \qquad (4.2)$$

where the first part of the R.H.S. of equation (4.2) represents the radiative transition probability. For the calculation of the vibronic matrix element, the Frank-Condon approximations (harmonic approximations) are assumed, and the overlap integral of the thermalized vibrational states was calculated by Huang and Rhys[68] as shown in section (2.4).

The splitting of the ^2E state (measured optically in the absorption spectra as will be seen later) is too strong (2342 cm^{-1}) to be due to L-S coupling (only 150cm^{-1}),[55] and which is further quenched due to the Ham effect.[59] Hence the ^2E state splitting is described only by the Jahn-Teller effect. Confirmation that the ^2E splitting is due to the Jahn-Teller effect, is the observation of only one zero phonon line in the absorption spectrum at 4K.[69] Since the Jahn-Teller effect will remove only the electronic degeneracy leaving the vibronic degeneracy unaffected. There is only one (n=0) vibronic level on which originates the only zero-phonon line. Any other source of splitting could cause more than one zero-phonon line.

Both the ground and the excited state splittings can be explained by the interaction of these two levels with the E_g-phonon mode. This coupling is explained in detail in ref.[55,70] The phonon coupling with the two levels is shown in figure (4.8). For the ground state

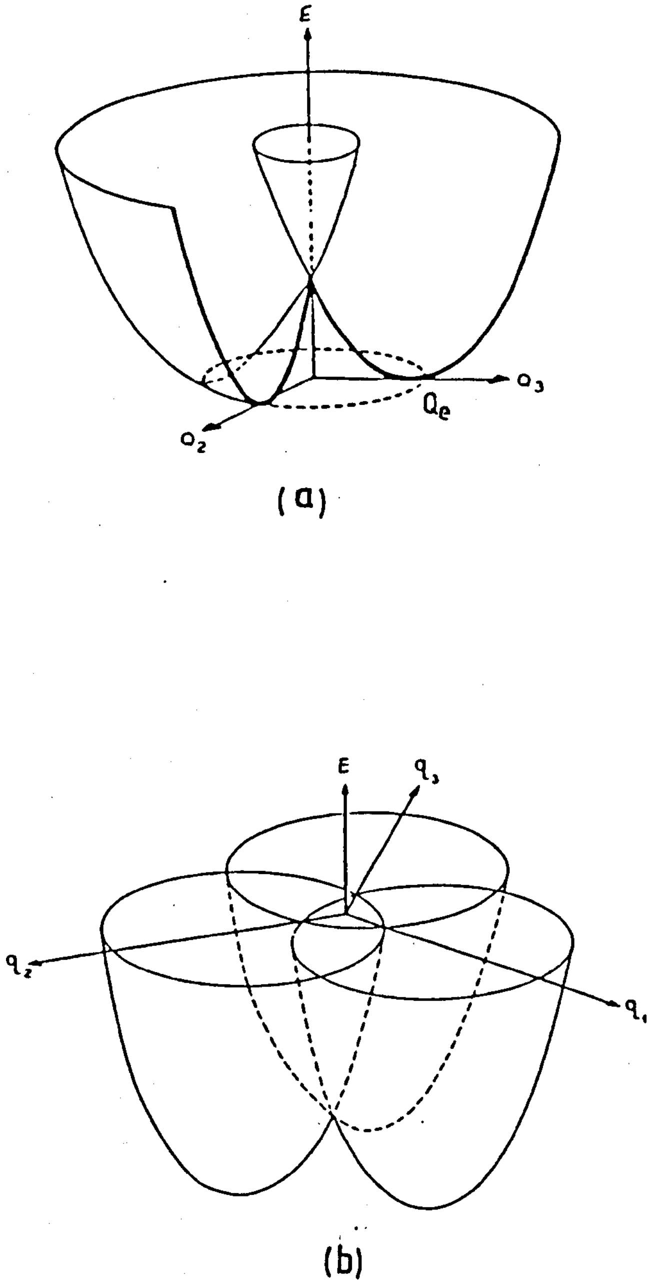

Fig 4.8 The potential curves of the Jahn-Teller split Ti^{3+} levels in $A\ell_2O_3$ showing the phonon coupling with a - the doubly degenerated ^2E state, b - the triply degenerated $^2T_2$ ground state (after Sturge[70]).

$^2T_2$ the minima of the three paraboloids are vibronically degenerate in (Q,E) space, where the coupling between the three electronic potentials due to the trigonal field and the spin-orbit coupling led to the splitting of the energy levels of the paraboloids in each case into three levels. It can be seen from figure (4.8) that the minimum of the E_g state forms a circle with the radius Q_e in the (Q_2,Q_3) plane, the projection of this circle onto the $^2T_2$ level paraboloids gives the vibronic levels into which the fluorescence transition occurs, resulting in the broadband fluorescence. Calculations[69] of the Jahn-Teller effect in $Ti^{3+}:Al_2O_3$ and Ti^{3+}:YAG showed that the Jahn-Teller constant is larger in the former and this is associated with the stronger crystal field in this crystal.

It must be considered for the transition probability that all transitions are basically equally forbidden d-d transitions in terms of the electric dipole transition, since the matrix element $\langle\psi_i|e.\bar{r}|\psi_f\rangle$ equals zero for $\psi_{i,f(\mathrm{even})}$ and $e.\bar{r}_{(\mathrm{odd})}$. In this case only the admixture of wave functions of odd parity like the p wave function can relax the parity forbiddenness. Two static wave functions of different parity can be linked by non-centrosymmetric crystal field. The strength of the coupling is determined by the matrix element $\langle d_{\mathrm{even}}|V_{\mathrm{odd}}|P_{\mathrm{odd}}\rangle$, i.e. by the odd parity fraction of the crystal field. This is correct for $Ti^{3+}:Al_2O_3$, but not for the case of Ti^{3+}:YAG where the Ti^{3+} ion site has inversion symmetry. However the centrosymmetric P_{odd} cannot be dynamically mixed with d-wave function at centrosymmetric sites although can be linked by odd-parity phonons. The strength of the coupling is then determined by the matrix element $\langle d_{even}|Phonon_{odd}|d_{odd}\rangle$. Here we conclude that the lifetime of Ti^{3+}:YAG is longer than that of Ti^{3+}:sapphire in which a static radiative decay rate is involved. The dynamically induced radiative rates of Ti^{3+}:YAG depends on temperature to a greater extent than that of sapphire.[71]

4.4 Optical Absorption Measurements

Ti^{3+} samples used are a 0.1 wt % $Ti^{3+}:A\ell_2O_3$ purchased from (union carbide) USA. Three Ti^{3+} doped in $A\ell_2O_3$, YAG and $YA\ell O_3$ crystals each with 0.1 wt % of Ti^{3+} supplied by Dr B Cockayne of the RSRE (Malvern, UK). A number of Ti^{3+} doped phosphate glasses with different concentrations of Ti^{3+} ions (0.1, 0.5, 0.6, 1, 2, wt %) were obtained from Dr F Cusso (Madrid, Spain) the composition of the glass are (62 P_2O_5, 24 Na_2O, 14 $A\ell_2O_3$ wt %). Another two samples (0.003 wt % Cr^{3+}:YAG and 0.1 wt % Cr^{3+}:YAP) were used for comparison with the time resolved spectra, both samples supplied by the RSRE. The absorption spectra of Ti^{3+} doped crystals and glasses at room temperature were measured using the Beckmann spectrophotometer. The absorption spectrum of $Ti^{3+}:A\ell_2O_3$ in figure (4.9) shows the blue-green absorption band expected from a $^2T_{2g} \rightarrow {}^2E_g$ transition of the d^1 ion in an octahedral crystal field. The shoulder on the long wavelength side of the spectrum is due to a splitting of the ^2E_g excited state by the static Jahn-Teller effect.[53] The main peak is located at ~ 488 nm, while the shoulder is at 551 nm. These values agree with values resulted from an approximation analysis of this transition into two Gaussian curves.[72] The strong absorption at the high energy side is attributed to the Ti^{4+} charge transfer band.[73,74] Another absorption at the low energy side can be seen, which could be apart Of the N.I.R. band of low intensity centred at ~ 800 nm[69,74] and assigned to a Ti^{3+} ion in low symmetry sites (caused by adjacent point defects, or interstitial sites). The intensity of this IR band increases with increased Ti^{3+} concentration. Polarized absorption showed that the π-polarized absorption is stronger in intensity than the σ-polarized one (contrary to the main Ti^{3+} absorption band). A post growth annealing of samples caused a drastic reduction in this band.[73] The high loss in the lasing band of $TiA\ell_2O_3$ which results in high lasing threshold and low efficiency is assigned to the IR absorption.[73] For Ti^{3+} doped YAG the absorption spectrum is shown in figure (4.10). Weak absorption peaks are evident at ~ 504 and 586nm, associated with Ti^{3+} ion transition between the $^2T_{2g}$ and the ^2E_g states. Another band on the high energy side of the spectrum has not been identified, although it may have the same origin as that reported at 390nm in ref.[71]. At even higher energy a strong absorption band is also observed, which is the YAG analogue of the charge transfer band observed in Ti^{3+}:sapphire. Even though strong Cr^{3+} R-line emission overlapping the Ti^{3+} ion emission was observed especially at room temperature, no absorption was identified with the Cr^{3+} ion. The splitting of the excited state level is directly measured from the difference in photon energy of the two absorption peaks. The splitting of 2770 cm^{-1} is somewhat larger than the splitting of 2340 cm^{-1} observed in $Ti^{3+}:Al_2O_3$, although the crystal field is stronger in Al_2O_3 than YAG. This result was somewhat controversial, the splitting of the ^2E_g excited state being due to crystal field effects alone or due to the strong Jahn-Teller effect.

The absorption spectrum of Ti^{3+}:YAP crystal shows blue-shifted components compared to Al_2O_3 and YAG. From this observation it was concluded that the orthorhombic site in YAP led to a larger energy splitting of ^2E and $^2T_2$ states than in Al_2O_3 and YAG. Figure (4.11) shows the two distinctive broad bands to be peaked at ~ 440nm and 520nm, giving an excited state splitting of ~ 2800 cm^{-1}, indicating that the Jahn-Teller effect also is important in the excited state of the ^2E state of Ti^{3+} in YAP. Strong absorption at the high energy side of the spectrum is assumed to be due to a charge transfer band. A weak absorption band peaked at ~ 620nm appears to have the same origin as the IR band in $Ti^{3+}Al_2O_3$. A comparison between the absorption spectra of Ti^{3+}:doped phosphate glass samples of two different concentrations is shown in figure (4.12). The well distinctive broad bands in the lower curve are due to the stronger absorption of the higher concentration (0.6 % wt T_iO_2) sample. The main peak of the spectrum is centred at ~ 566 nm with a weaker intensity shoulder at ~ 691 nm. This absorption is responsible for the purple colour of both samples. Comparing this result with the absorption spectra of the three crystals

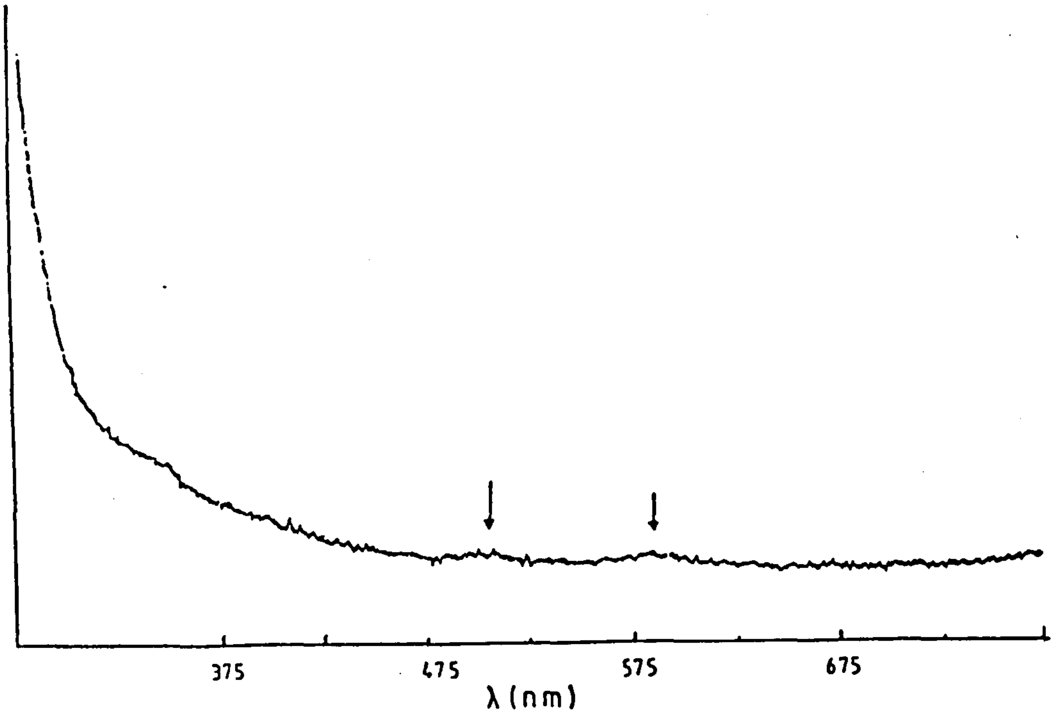

Fig 4.10 Ti^{3+}:YAG absorption spectrum.

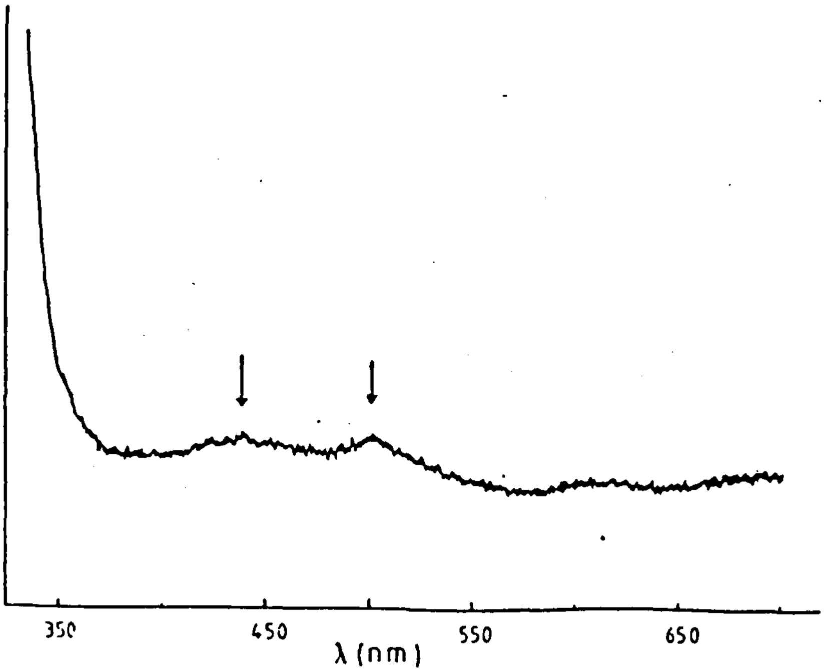

Fig 4.11 Absorption spectrum of Ti^{3+}:YAP.

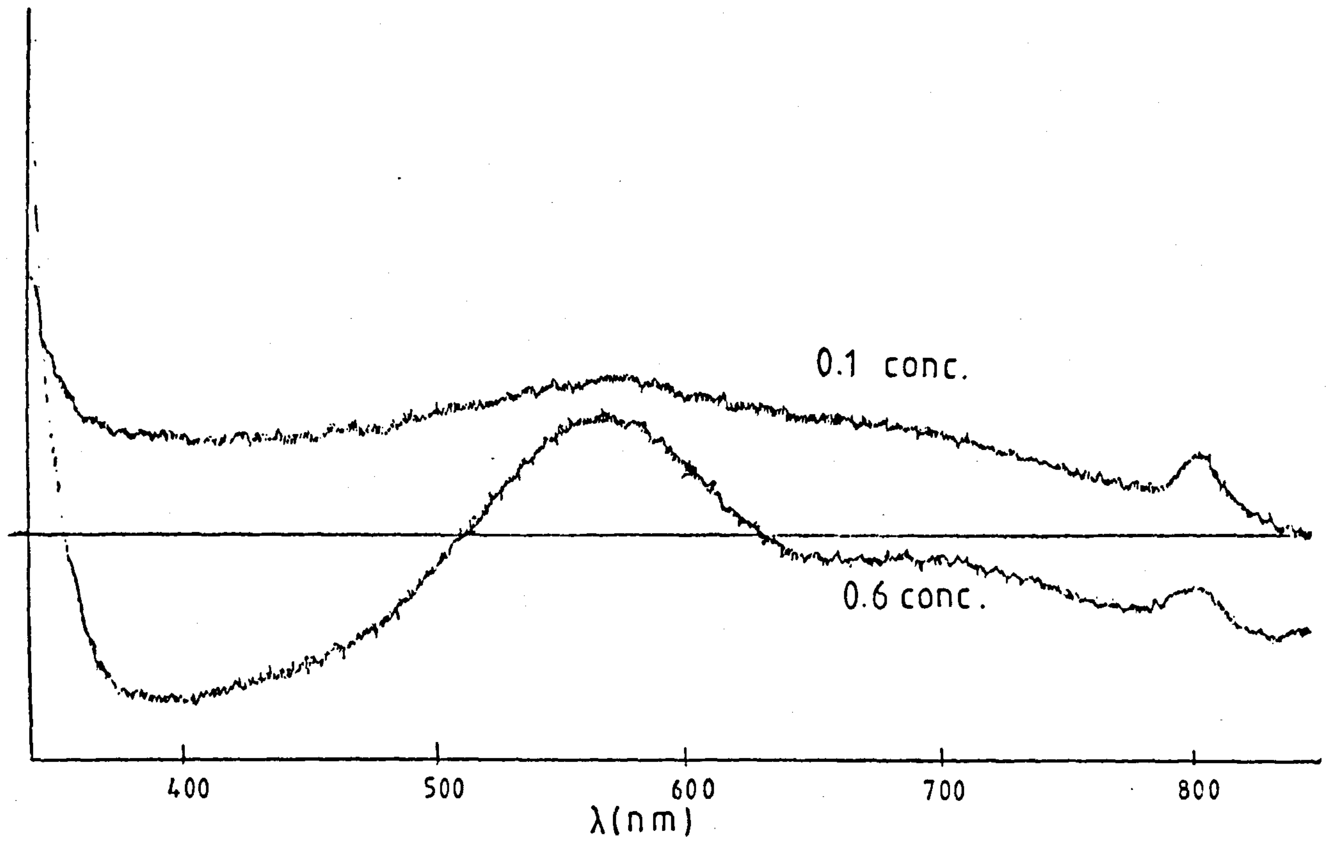

Fig 4.12 Absorption spectrum of Ti^{3+}:phosphate glass for two different Ti^{3+} ion concentrations.

indicates a strong red shift of the Ti^{3+} absorption in the glass. Absorption measurements of $Na_2O-P_2O_5$ glasses doped with Ti^{3+} revealed even larger splittings between the two substates of the excited ^2E_g state in borate glasses due to the larger spread of crystal field sites occupied by Ti^{3+} ions in these glasses.[65] For the same reason the absorption intensity of phosphate glasses is higher, the existence of two different absorption peaks is analogous to the previous crystal cases. The strong charge transfer band is similar to that resolved in a Ti^{3+} doped barium borosilicate glass.[64] A comparison between different hosts of Ti^{3+} ion is given in table (4.1).

4.5 Luminescence Measurements

4.5.1 Ti^{3+} doped crystals

The emission spectrum from $Ti^{3+}:Al_2O_3$ excited using all lines from an Ar^+ laser is shown in figure (4.13) as a broad band emission starting from 600nm and extends to ~ 1150 nm, with the peak at ~ 767nm at room temperature. This $^2E_g \rightarrow {}^2T_{2g}$ vibronic band is compared with the 10K spectrum in figure (4.13). The only sharp features at room temperature are ca 692-694nm, these features being due to unintentional but ubiquitous Cr^{3+} impurity in the $Ti^{3+}:Al_2O_3$ host crystal.[75] The concentration of Cr^{3+} impurity is much larger in the Malvern sample than in the Union carbide crystal, so much so that the strong R_1-R_2 doublet and phonon side band can be clearly

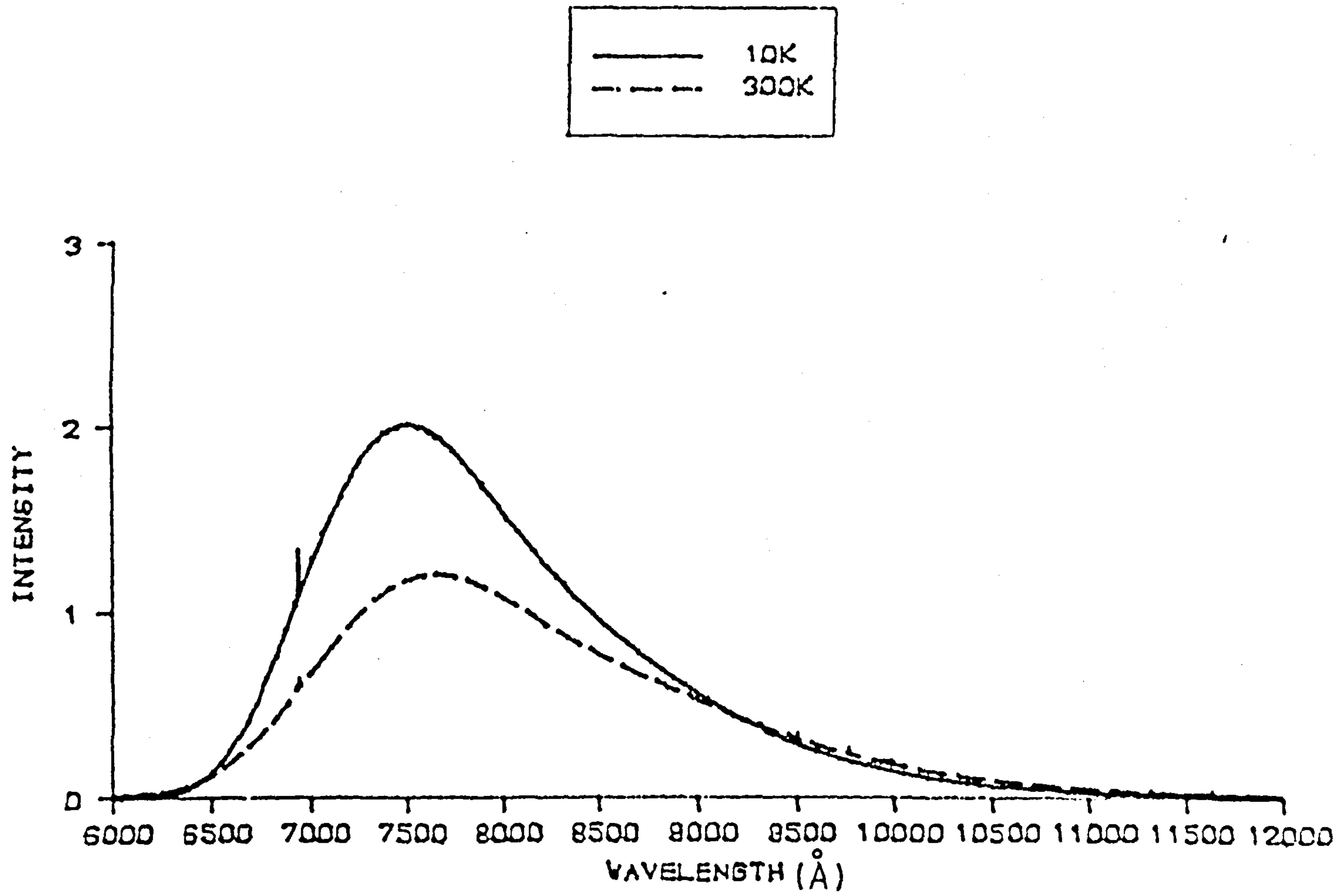

Fig (4.13) TIAL203 EMISSION AT 10K AND 300K
(Union Carbide Sample)

identified in figure (4.14). Under conditions of high spectrometer sensitivity at T = 10K, fine structure is observed on the high energy edge of the emission band; as figure (4.15) shows there are three zero-phonon lines due to transitions from the lower ^2E_g level of the excited state to the three sublevels of $^2T_{2g}$ ground state. Replicas of phonon sideband are also observed at lower energies. At 77K spectrum also shows an anti Stokes' shifted side band at the high energy side of the Z.P.L., which is due to transition from the first phonon level of the excited state to the zero-phonon level of the ground state (see figure (4.16)).

In table (4.2) the spectral values measured from luminescence spectra at 10K and 300K are given in detail. The red shifted peak at room temperature is due to the lowering of the crystal field at higher temperature which leads to a smaller splitting. Values of the splitting δ_1 and δ_2 between $^2T_2$ sublevels identified in figure (4.2) are 38 and 108 cm^{-1} respectively, in good agreement with those measured in infra-red measurements.[54] Inhomogeneity by lattice strains in the host crystal may cause different Z.P.L. linewidths compared with those measured in ref.[75,76].

In preliminary luminescence measurements at low and high temperatures, figure (4.17) shows strong Cr^{3+} impurity emission overlapping the broad Ti^{3+} band in Ti^{3+}:YAG; this was determined using lifetime measurements and by comparison of the Cr^{3+}:YAG and Ti^{3+}:YAG spectra, figure (4.18). It is evident that the Ti^{3+} ion

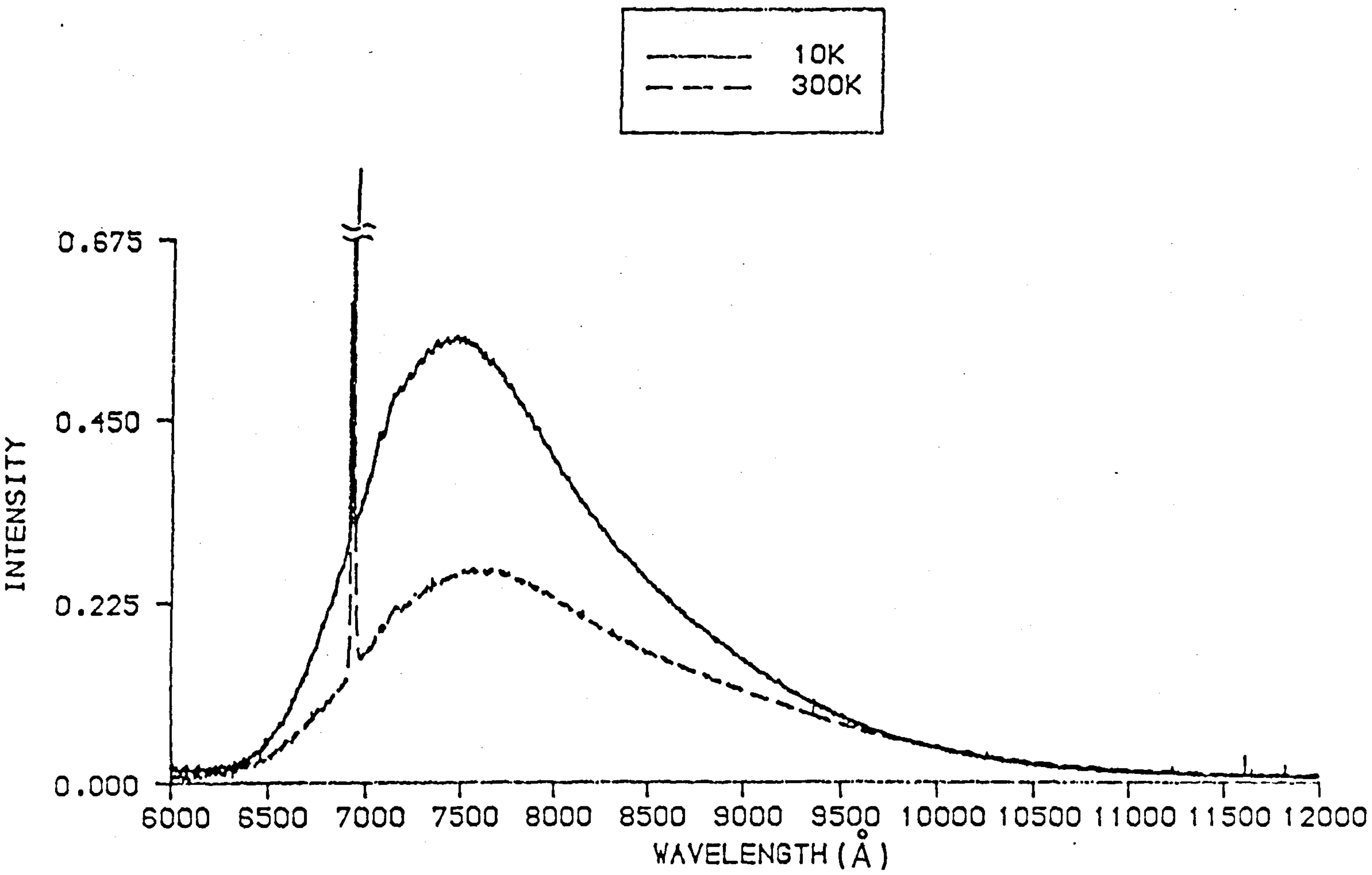

Fig(4.14) EMISSION OF TIAL.203 AT 10K AND 300K
(Malvern Sample)

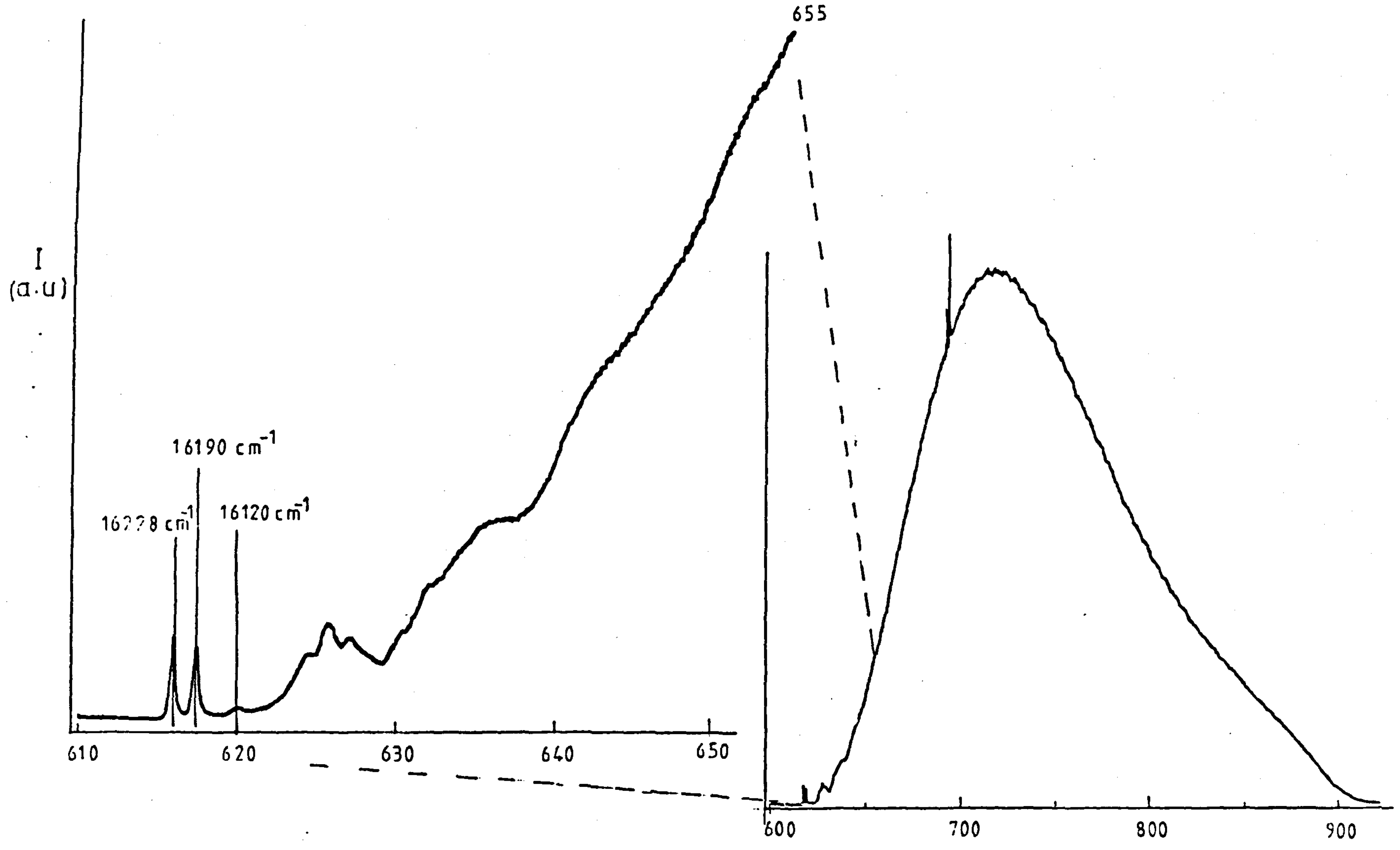

Fig 4.15 Luminescence of Ti^{3+}:Al_2O_3 at 10K.

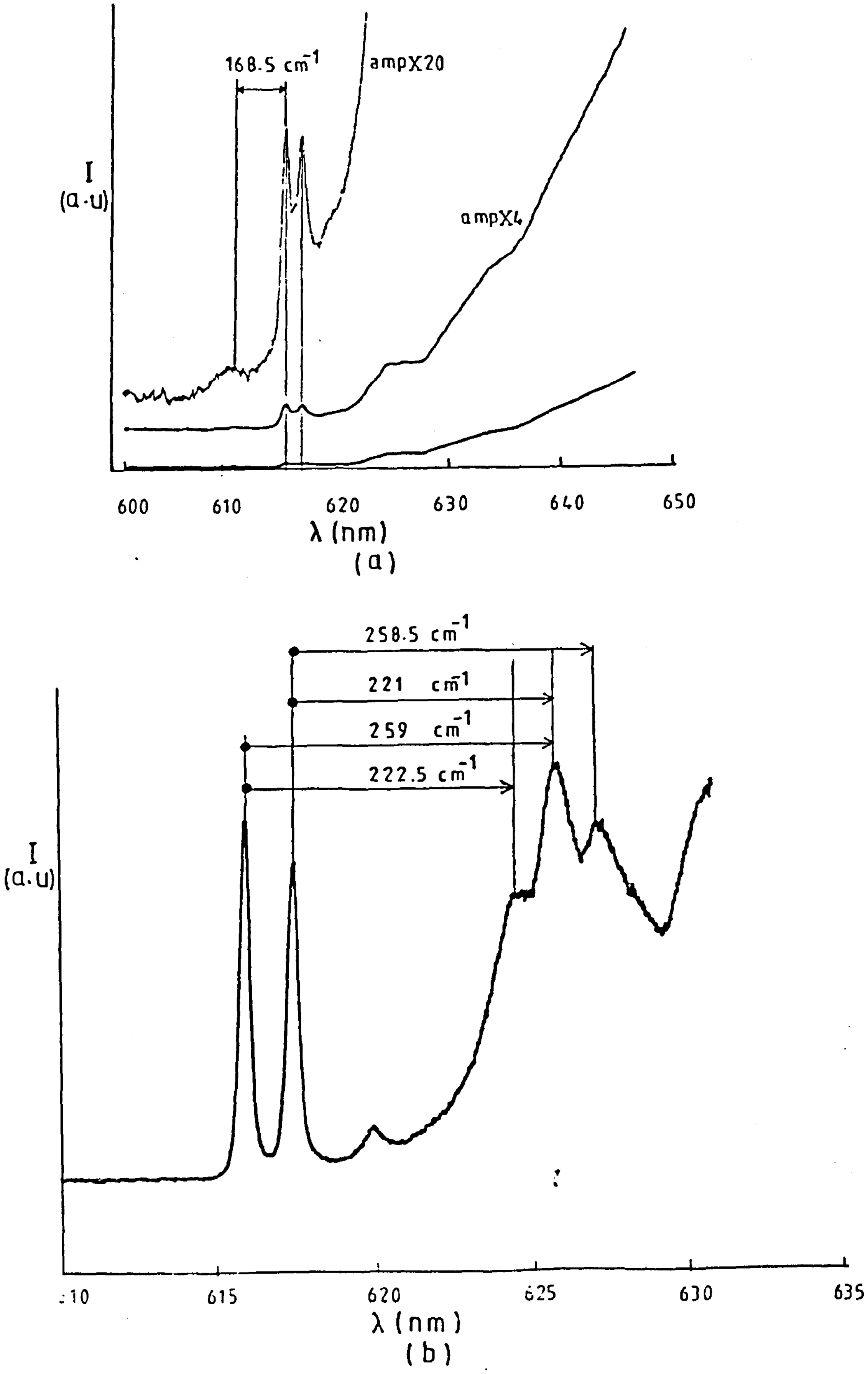

Fig 4.16 The high energy side of the $TiA\ell_2O_3$ emission spectrum showing the zero-phonon lines and phonon side bands at (a) 77K (b) 10K.

Table 4.1 Comparison between absorption spectra of Ti^{3+} in different hosts.

Sample	Main peak cm^{-1}	Secondary peak cm^{-1}	Splitting in ^2E_g cm^{-1}	Dq	Shift in main peak relative to the glass
$Ti^{3+}:Al_2O_3$	20492	18149	2343	2049	13.8%
Ti^{3+}:YAG	19840	17065	2775	1984	10.9%
Ti^{3+}:YAP	22730	19920	2810	2273	22.3%
Ti^{3+}:glass	17668	14472	3196	1767	

Table 4.2 Experimental spectral values of emission for Ti^{3+}:sapphire (all values measured in cm^{-1})

Zero-phonon lines	16228,	16190,	16120
Z.P.L. linewidth	8.9,	10.5,	19.2
Ground state energy splitting	38,	70	
1st phonon sideband	16005.5,	15969,	15931.5
Ground state phonon energy:			
1st mode	222.5,	221	
2nd mode	259,	258.5	
Excited state phonon energy	168.5		
Emission band peak at 300K	13035		
" " " " 10K	13282		

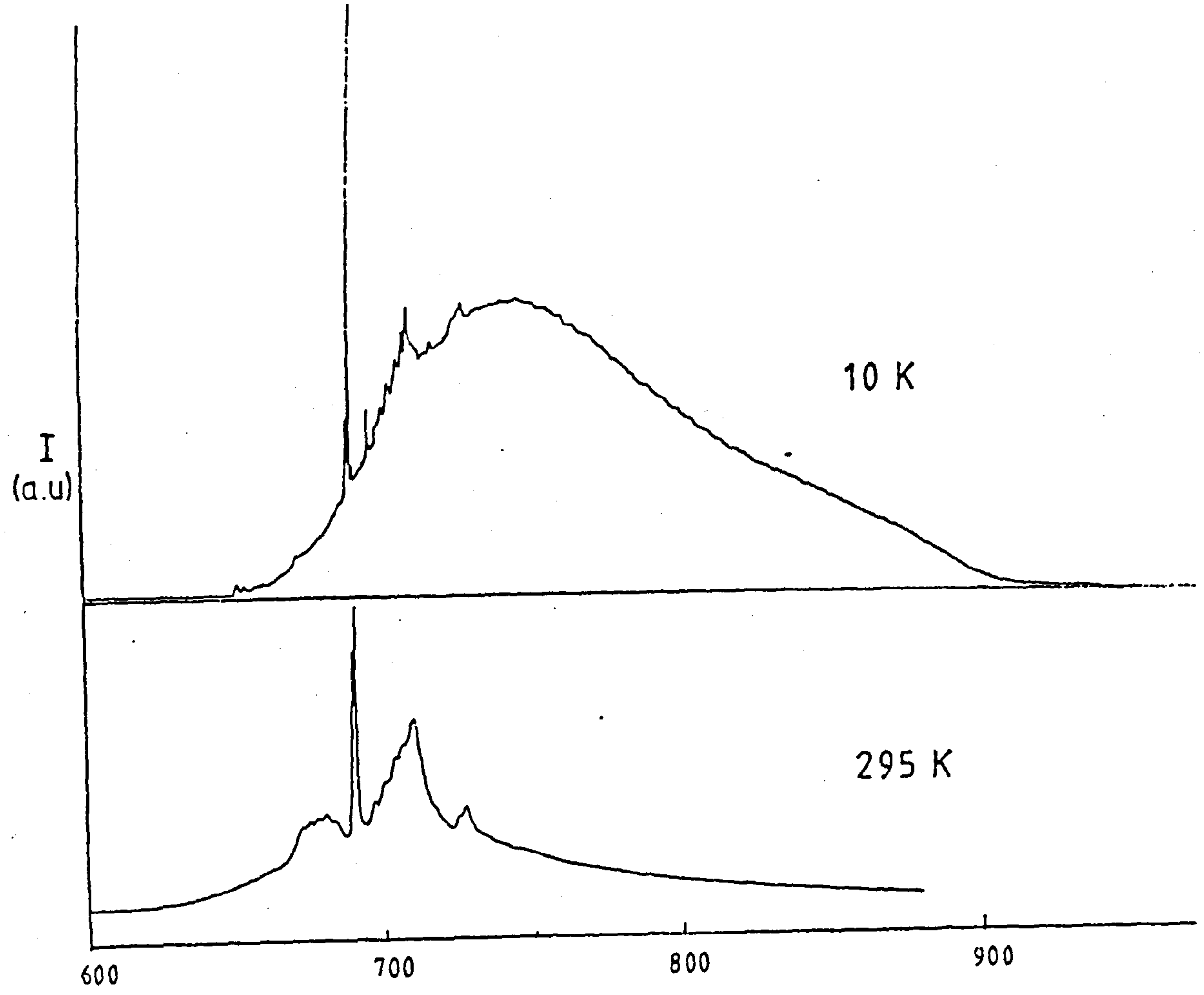

Fig 4.17 Ti^{3+}:YAG luminescence at 10K and 295K with 150mW Ar (all-lines) excitation.

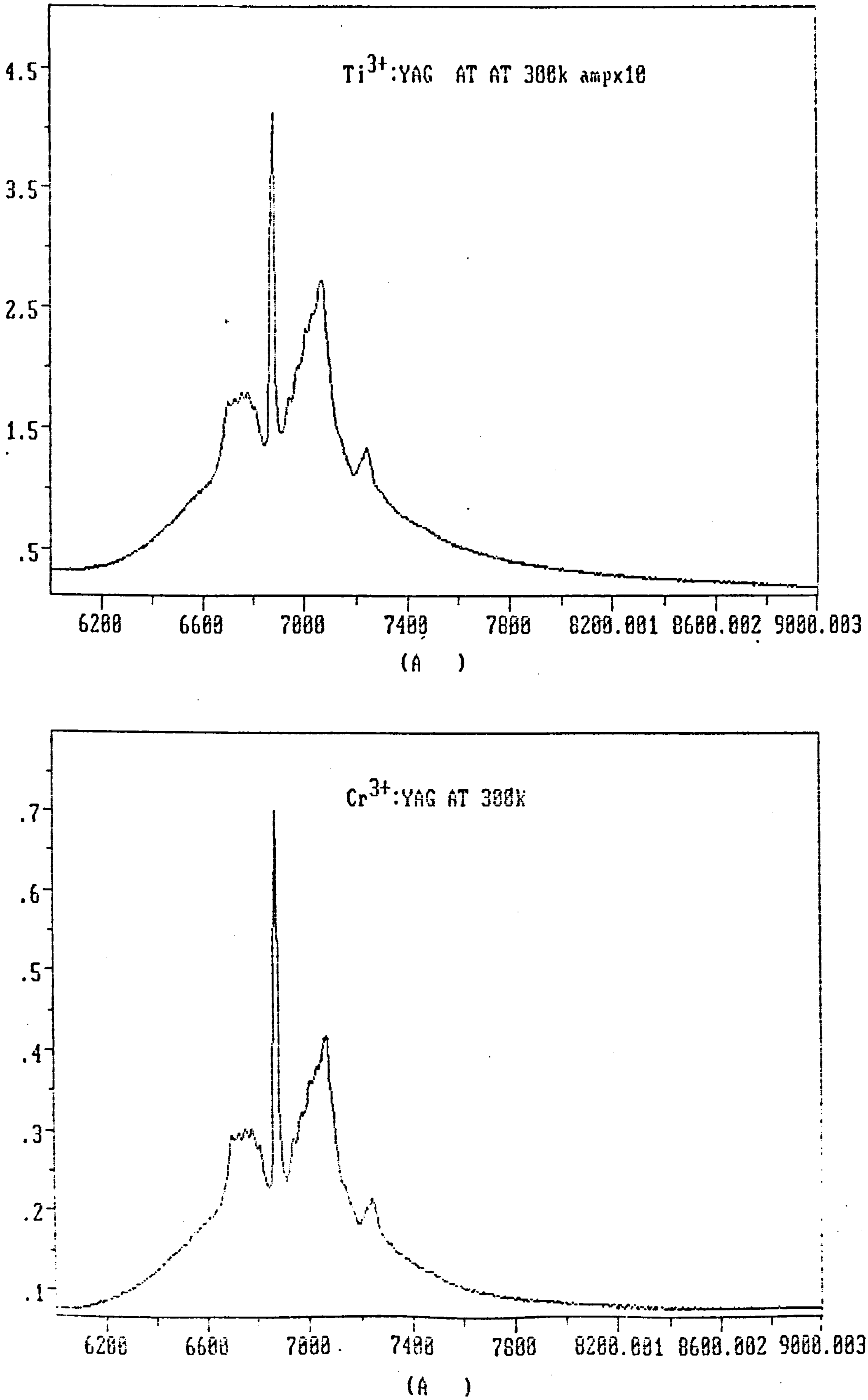

Fig 4.18 Comparison between Ti^{3+}:YAG and Cr^{3+}:YAG crystals showing the dominant Cr^{3+} impurity emission in the (Malvern) sample.

concentration in the YAG crystal is weak compared with that of the Cr^{3+} ion at least in high temperature measurements. Indeed the broad Ti^{3+} band shows itself mainly at lower temperatures as can be seen in figure (4.17), where the 488nm Ar^+ line was used for the excitation in both cases. However the Cr^{3+} ion emission is still strongly existed. Fortunately, the Cr^{3+} spectra may be eliminated by utilizing the large difference in decay rates between the two ions, an ideal situation for the phase sensitive detection (P.S.D.) (see chapter 3). The Cr^{3+} and Ti^{3+} emission may be separately nulled out and the individual luminescence spectra recorded at temperatures in the range 10-300K. The luminescence spectrum of this crystal at 30K figure (4.19) shows a broad band started from 650nm and extended to ~ 1170nm, peaked at ~ 770nm and with a width (F.W.H.M.) of 2750 cm^{-1}. At high temperature 250K the luminescence intensity is reduced to about one fifth of its value at 30K and the bandwidth increased to 3470 cm^{-1}. At high resolution it is possible to identify sharp structures at the high energy side at low temperature spectrum due to the $^2E_g \rightarrow {}^2T_{2g}$ zero-phonon lines and their attendant phonon side bands as can be seen in figure (4.20). The one phonon sideband is due to interaction with a single phonon mode of energy ~ 140cm^{-1}. These spectral characteristics are summarised in Table (4.3). The fluorescence spectrum between 520nm and 820nm for Ti^{3+}:YAP at 10K with the 488nm line of 100mw as a source of excitation is shown in figure (4.21). The overall broad band is blue shifted relative to Al_2O_3 and YAG. The inset to figure (4.21) reveals a single zero-phonon line at 5396 Å of 29cm^{-1}

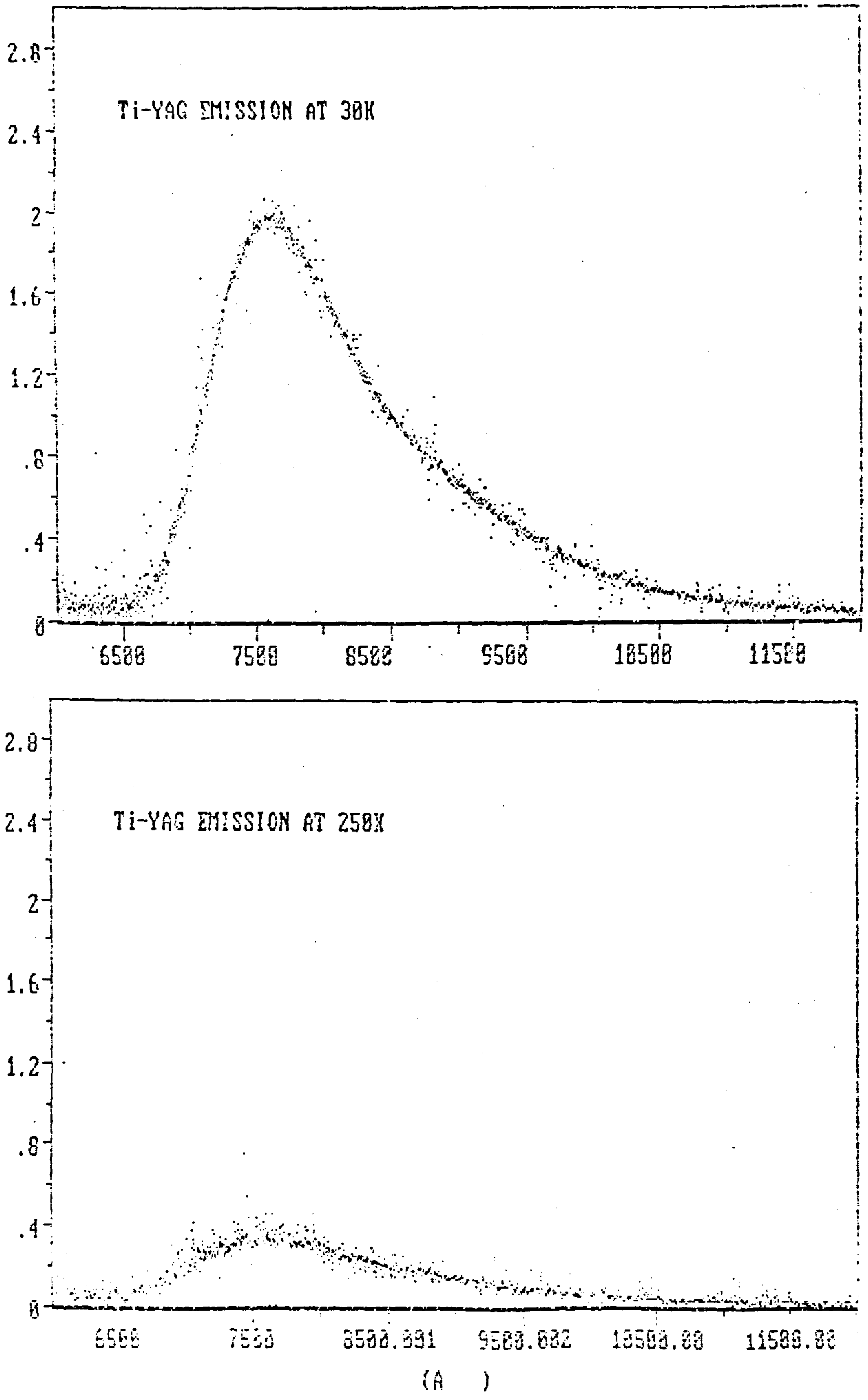

Fig 4.19 Ti YAG luminescence using Ge-detector and phase sensitive detection technique to null the Cr^{3+} emission from the spectra.

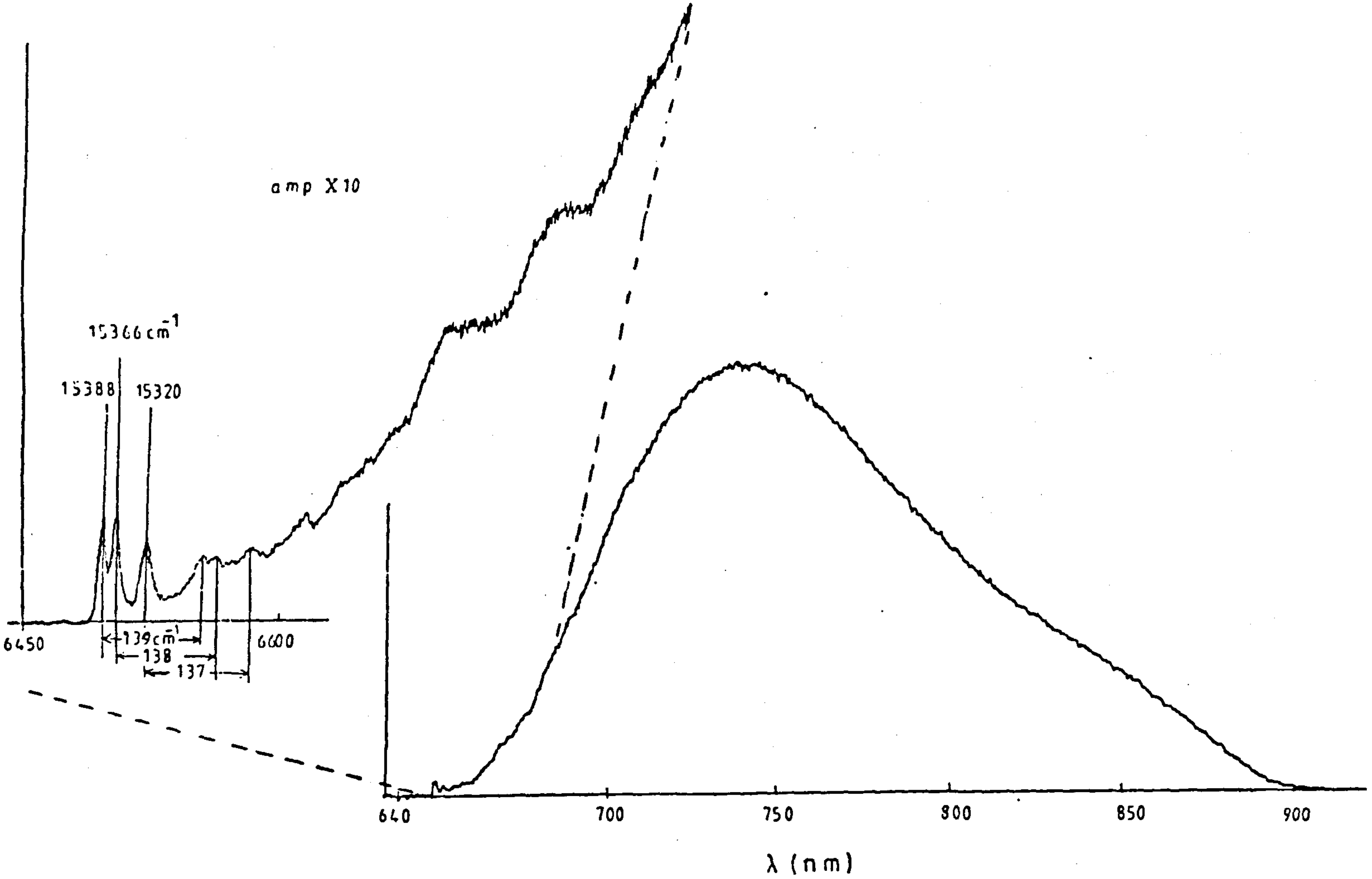

Fig 4.20 Ti YAG luminescence showing fine structures at the high energy side of the spectrum, the zero phonon lines and the phonon-side band features also shown in the inset.

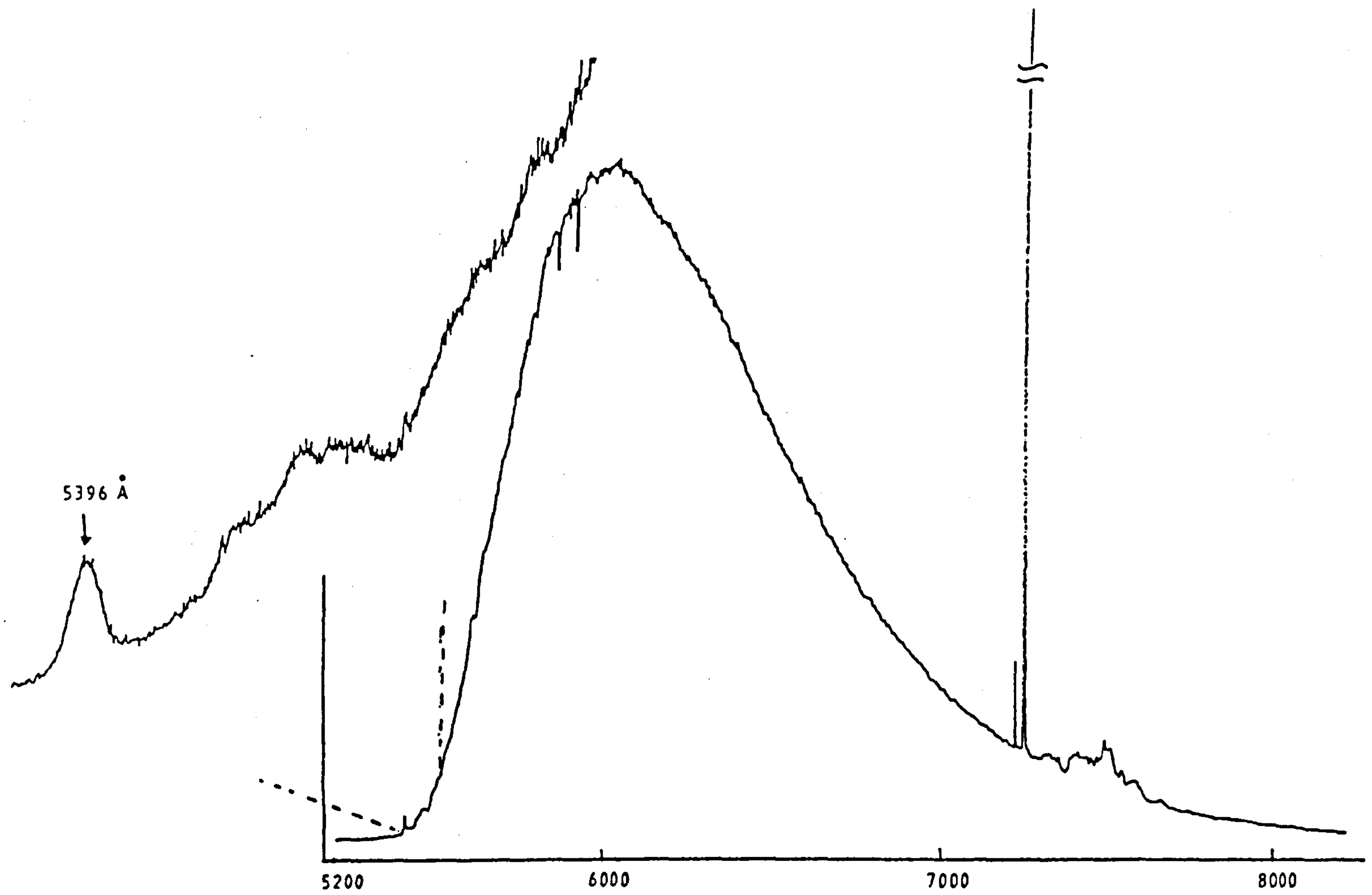

Fig 4.21 Luminescence spectrum of Ti YAP crystal at 10K irradiated with the 488nm line of the Ar^+ laser.

width and an accompanying phonon side band. Also apparent are two absorption lines at λ = 585 and 589nm which appear only at low temperatures. The R-line emission at 7213 Å and 7239 Å (at 10K) and their vibronic sideband are also observed on the long wavelength edge of the broad band. Note that to record the correct band shape proper account must be taken of the spectrometer/grating polarization anomaly. The broad band which peaked at 603nm at 10K shifted to 606nm at room temperature. The line width of the zero-phonon line is due to inhomogeneous broadening by strain associated with the presence of lattice defects.

Table 4.3 Spectroscopic values from Ti^{3+}:YAG luminescence (all values are in cm^{-1})

Z.P.L.		15388,	15366,	15320
Ground state energy level splittings		22,	68	
1st Phonon side bands		15249,	15229,	15185
Ground state phonon energy:	1st mode	139,	160	
	2nd mode	138,	181	
Emission band peak (250K)		12987		
" " " (30K)		13072		

4.5.2 Ti^{3+} ions in glasses

The random distribution of atoms in a glass matrix leads to a different interplay between homogeneous and inhomogeneous broadening of the absorption and emission transitions of T.M.I. doped glasses compared with that in crystals. The major difference between optical centres in crystals and glasses is that in the later cases there exist a multiplicity of sites at each of which the centre emits or absorbs at a slightly different frequency from the others. A detailed description of the glass structure and its effects on spectroscopy is discussed in the next chapter for Cr^{3+}-doped glasses. However we have compared the luminescence of Ti^{3+} doped in crystals and glass. Figure (4.22) shows the luminescence of a Ti^{3+}:phosphate glass at two different temperatures. The shape of the spectrum is a featureless broad band. A search for the zero-phonon and phonon-assisted structure of this broad band spectrum was unsuccessful, apparently due to the massive inhomogeneous broadening in glasses. This is clearly illustrated in figure (4.23). There are two aspects of figure (4.22) worthy of note compared with those of crystals. The first is the shift of the band peak towards longer wavelengths as the temperature decreases. As we discuss subsequently, this phenomenon also occurs in Cr^{3+}:glasses. At high temperatures, the lower energy $^2T_2$ level is more vibronically populated and therefore for the same value of excitation wavelength, the gap between the two states becomes wider, hence the emission peak moves towards lower wavelength value. The

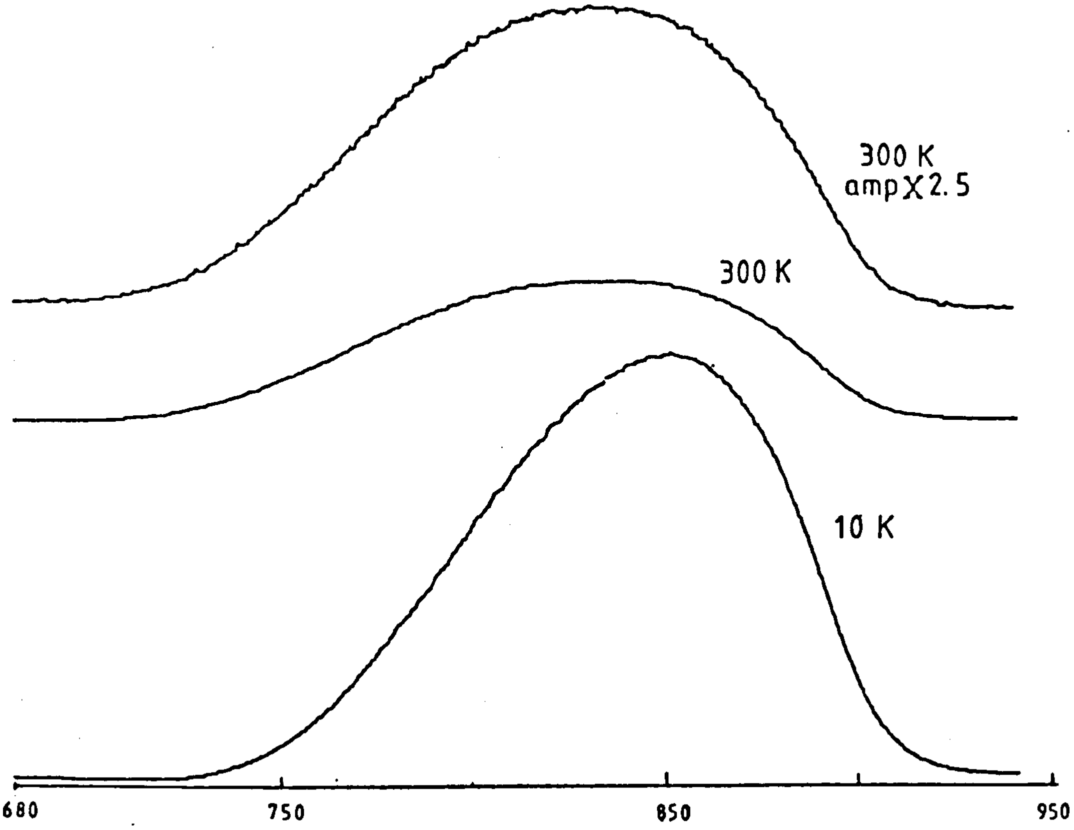

Fig 4.23 Ti:phosphate glass (0.1% conc.) emission at 10K and 300K (using a photomultiplier tube).

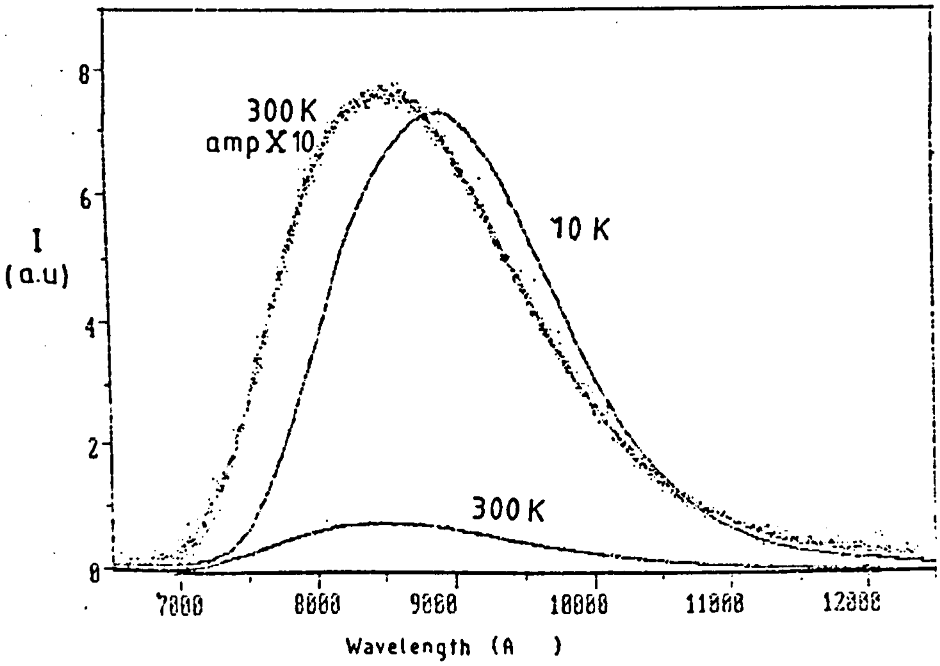

Fig 4.22 Luminescence of Ti:phosphate glass at 10K and 300K (using a Ge-detector).

second aspect of note is the fact that non-radiative transition probability increases with temperature which may lead to a change in the spectral shape and to the sharp reduction of the emission intensity which we discuss later.

Selective excitation spectroscopy may be used to understand the mechanism of inhomogeneous broadening associated with ions in different sites. This can be seen by comparing spectra excited at the same excitation intensity (100 mw) but at different excitation wavelengths; viz. λ = 633nm, λ = 670nm lines from the Ar^+ ion pumped ring dye laser and all-lines output from the Ar^+ ion laser. The sample temperature of 10K was used for spectra shown in figure (4.24). It can be seen from these spectra that the excitation at a longer wavelength led to spectra with a peak position at a longer wavelength. Apparently sites excited at shorter wavelengths have larger Dq values relative to sites excited with longer wavelength lines, and hence emit at shorter wavelengths. The band width of the emission excited with the Ar^+ (All-line) output is larger due to the excitation of a much larger number of sites with the different (and broader) lines of the Ar^+ ion laser. The intensity differences of the different excitation emission curves is caused by different amounts of absorption of light from different wavelengths. This can be related to the absorption spectrum.

Luminescence spectra for the same glass, but with different Ti^{3+} ion concentration were examined at the same conditions (488nm excitation

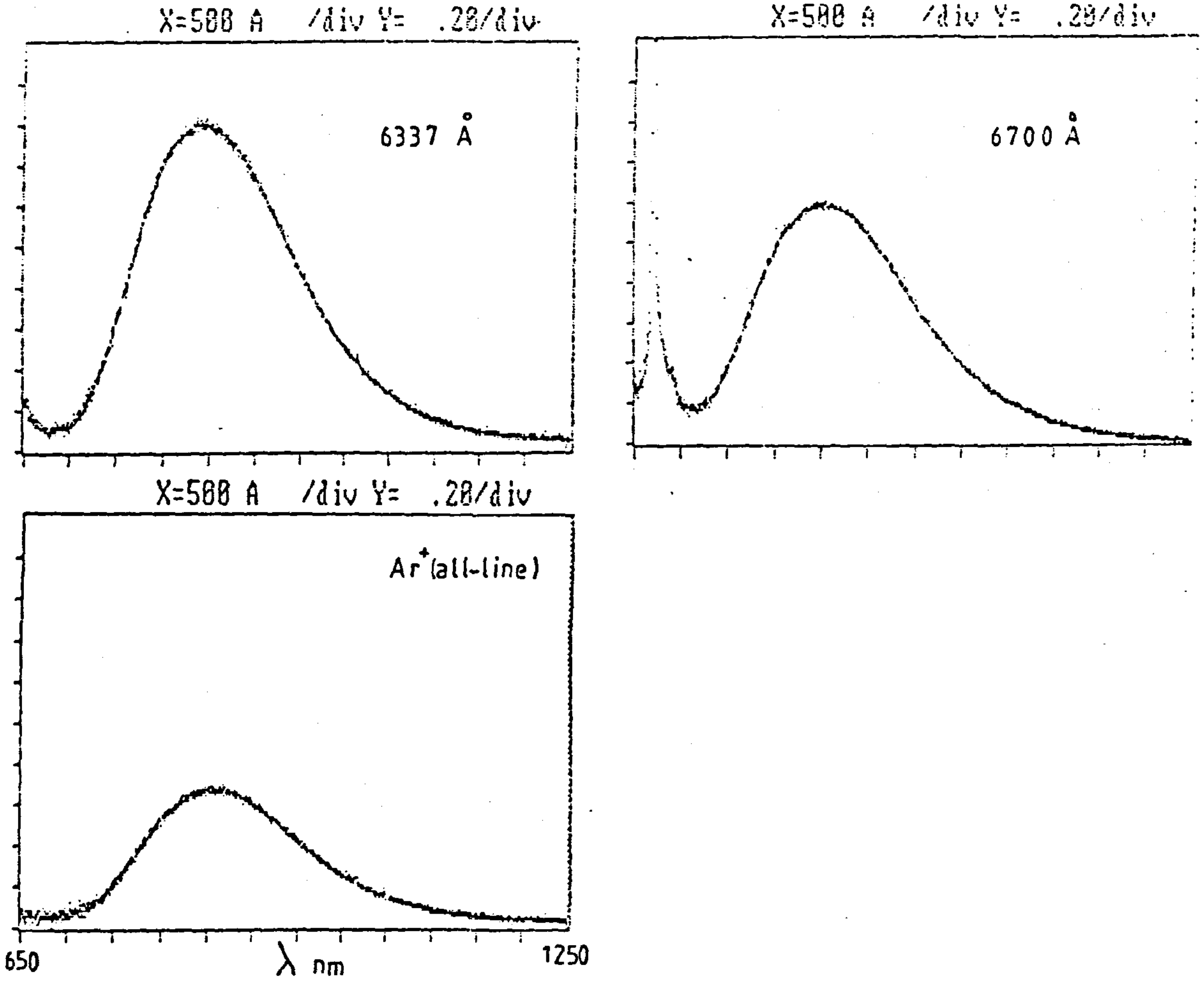

Fig 4.24 Ti:glass (0.1 conc.) emission excited with different wavelengths.

and 10K temperature). Three luminescence spectra are shown in figure (4.25), where the sample luminescence intensity looks as inversely proportional to the concentration value of the Ti^{3+} ion. This relation could be due to the concentration quenching (see section 1.5), values for integrated intensity of the emission and peak positions against the concentration of Ti^{3+} ion for the above mentioned spectra are plotted in figure (4.26).

4.6 Temperature dependence and decay rate measurements

Referring to figure (4.13), it can be seen that the width of the broad $^2E_g \rightarrow {}^2T_{2g}$ transition of $Ti^{3+}:Al_2O_3$ increases with the increase of temperature. The peak of the transition is red shifted as the sample's temperature increases. The band centroid, M_1, plotted against temperature in the range (10-300)K in figure (4.27), increases linearly with increasing temperature. The transition energy between the ^2E and $^2T_2$ levels is given by $\Delta E = 10Dq$, where $Dq \propto 1/a^5$, and (a) is the lattice parameter which varies with the temperature as

$$a = a_o + \Delta a(T) \qquad (4.3)$$

where a_o is the lattice parameter at low temperatures. Since

$$\frac{1}{a^5} = \frac{1}{a_o^5}\left[1 + \frac{\Delta a(T)}{a_o}\right]^{-5} \approx \frac{1}{a_o^5}\left[1 - 5\,\frac{\Delta a(T)}{a_o}\right]$$

Hence $\Delta E = \Delta E_o - 5\left[\frac{\Delta a(T)}{a_o}\right]\Delta E_o$, so the peak energy at high temperature

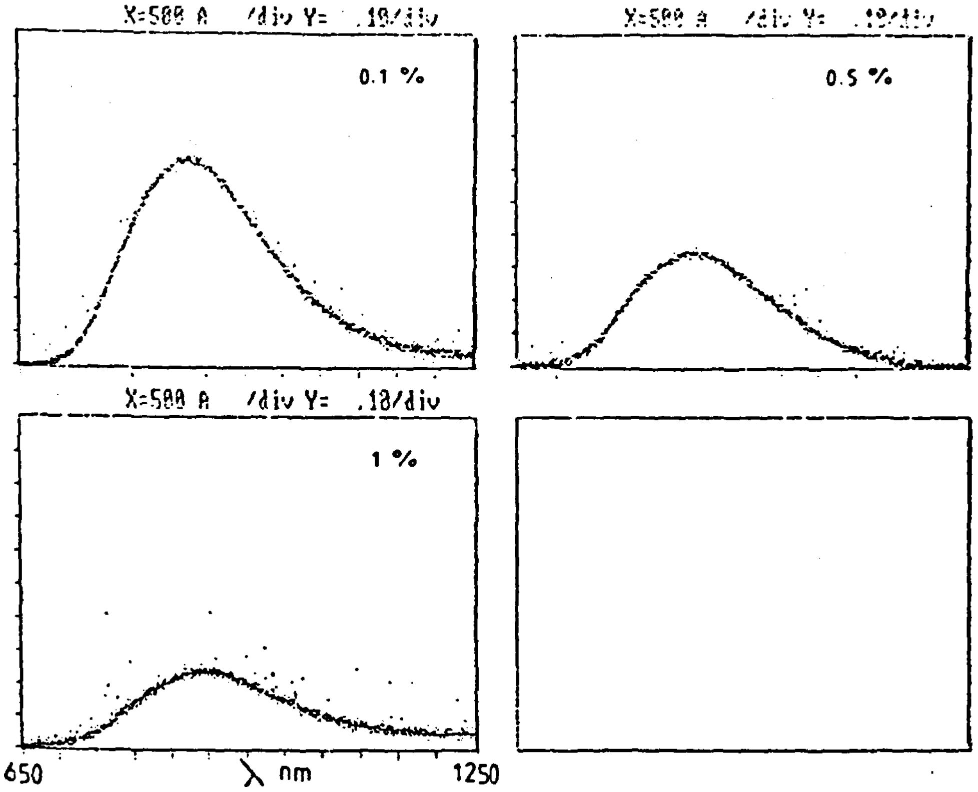

Fig 4.25 Emission spectra of Ti:phosphate glass with different Ti^{3+} ion concentration.

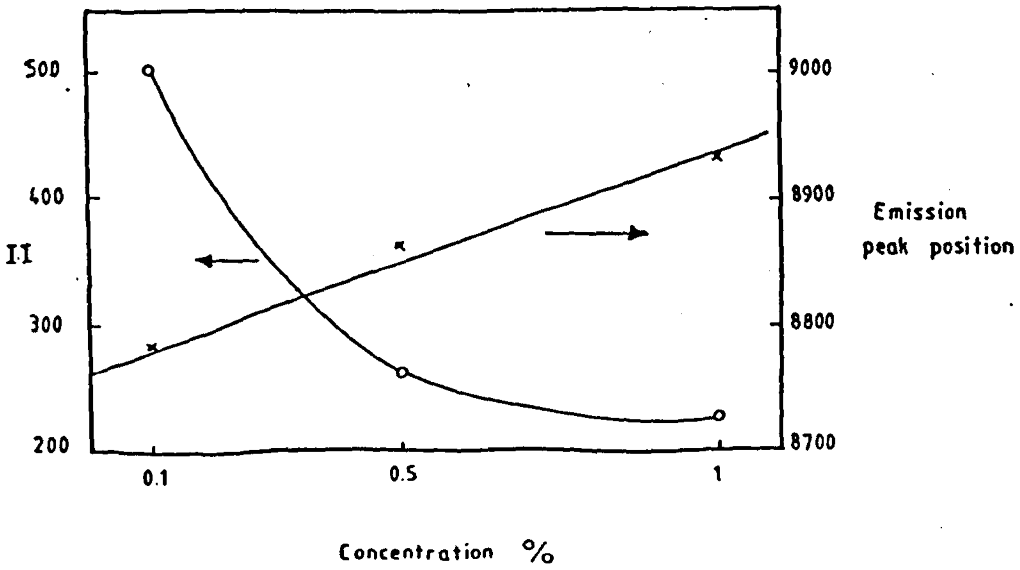

Fig 4.26 Effect of Ti^{3+} ion concentration on the emission characteristics of the Ti^{3+}:phosphate glass.

is reduced relative to the low temperature peak energy. In other words the band peak shifts to lower energies as the temperature of the sample increases.

The broadening of the transition is due to the coupling of the electron to lattice vibrations (as shown in chapter 2). The luminescence bandwidth Γ_T has been measured in the temperature range (10-300)K and plotted against temperature T in figure (4.28). The bandwidth is almost constant in the temperature range 10-100K, and then increases. The theoretical bandwidth temperature relationship is given by

$$\Gamma_o^2 = \Gamma_T^2 \tanh\left[\frac{\hbar\omega}{2kT}\right] \tag{4.4}$$

in which Γ_o and Γ_T are the bandwidths at zero and high temperature, respectively. The above relation is least squares fitted to the temperature dependence data in figure (4.28). Γ_o is found to be 2490 cm^{-1}, and the calculated value for the phonon energy is 385 cm^{-1}. Similar temperature depencdence bandwidth measurements for Ti^{3+}:YAG was carried out and the values are shown in figure (4.29), from which Γ_o and $\hbar\omega$ found to be 2760 cm^{-1} and 295 cm^{-1} respectively.

The luminescence intensity, M_o, for $Ti^{3+}:Al_2O_3$ is also plotted against temperature in figure (4.30). It can be seen that the

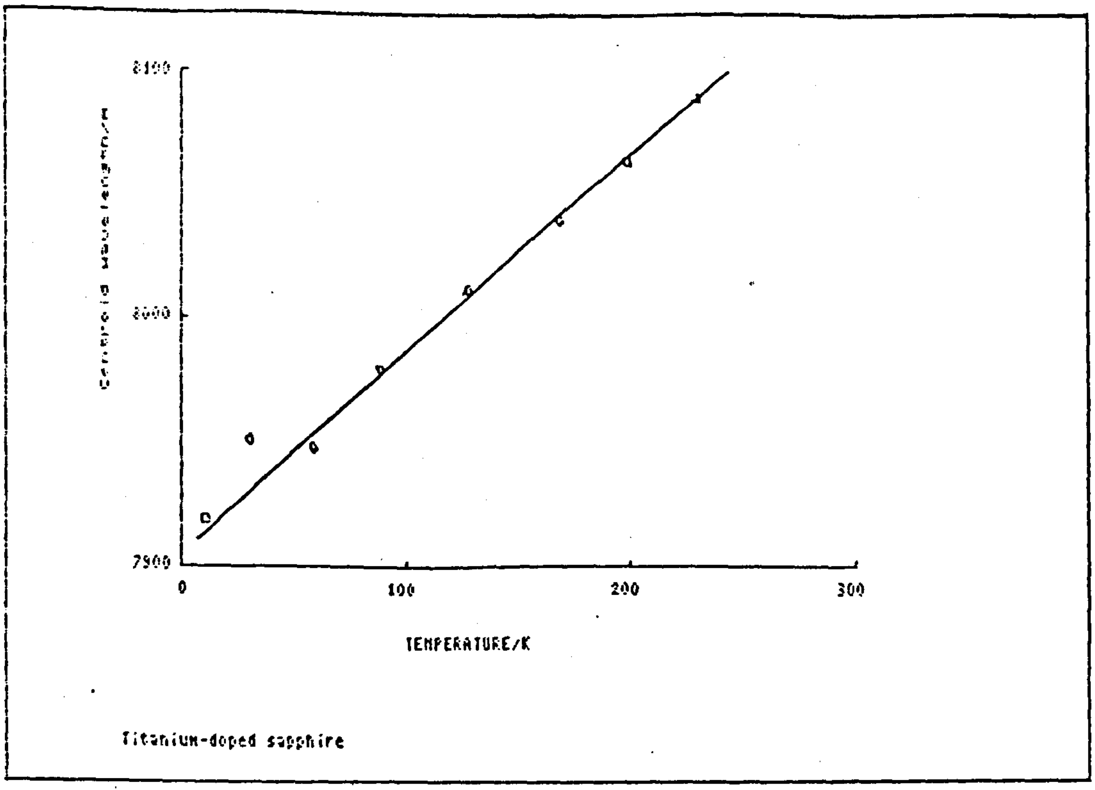

Fig 4.27 Temperature effect on the centroid position of $TiAl_2O_3$.

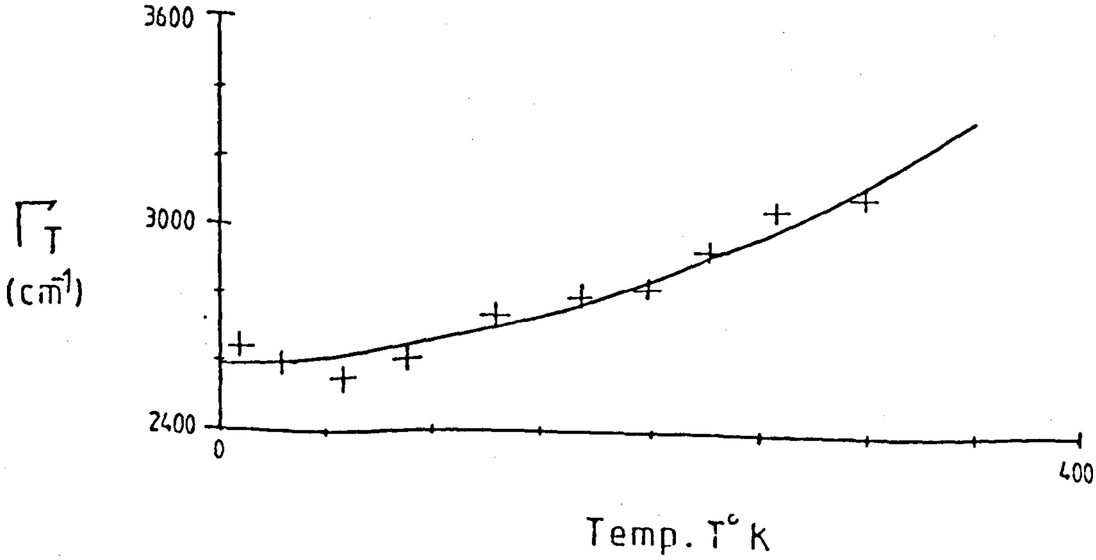

Fig 4.28 Temperature dependence bandwidth for $TiAl_2O_3$.

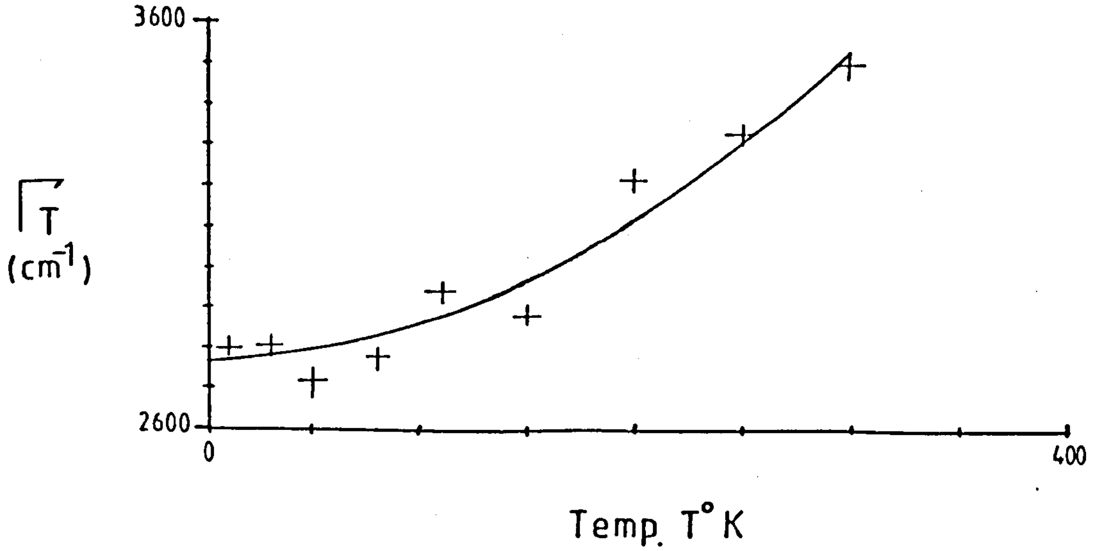

Fig 4.29 Temperature dependence bandwidth for Ti:YAG.

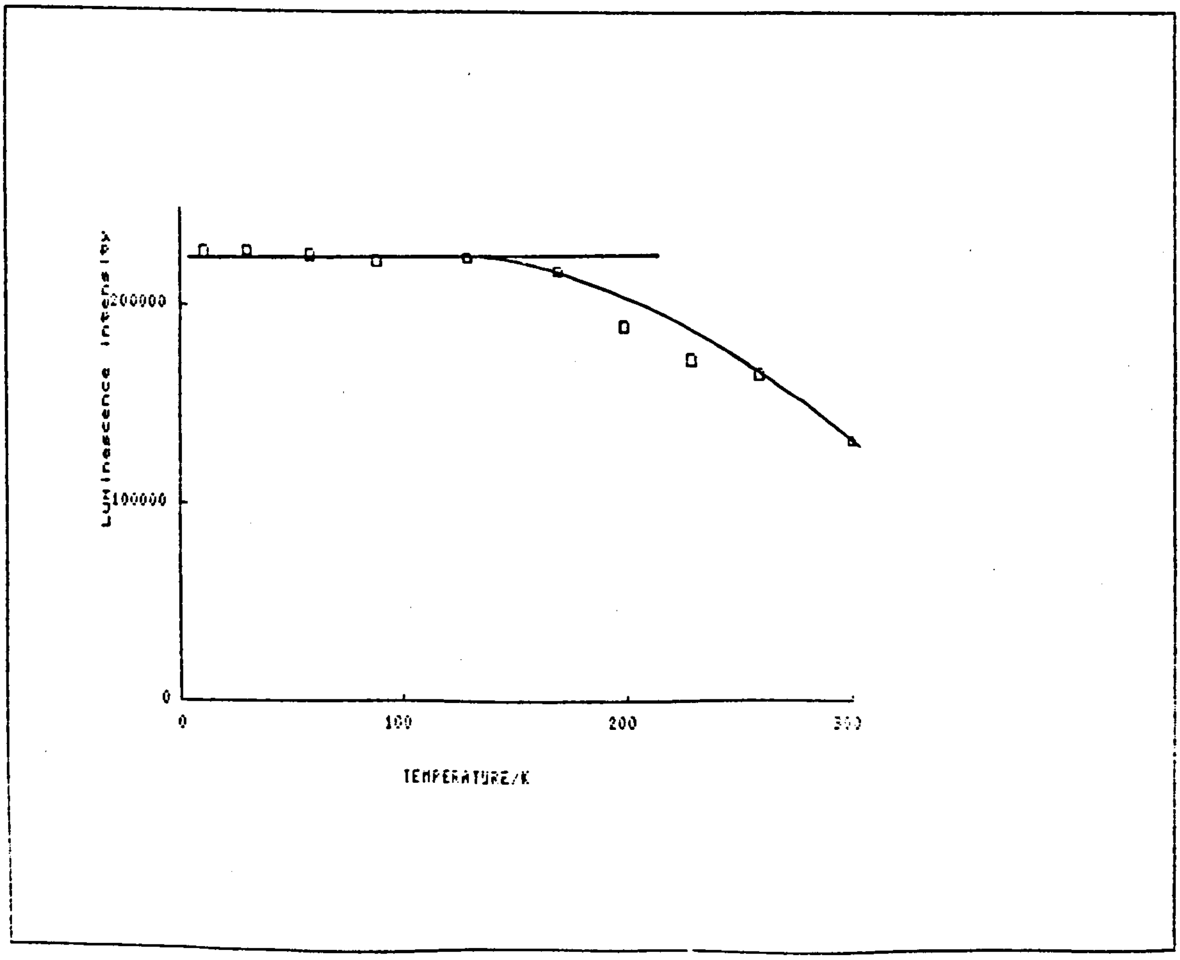

Fig 4.30 Effect of temperature on the luminescence intensity of $TiAl_2O_3$.

intensity stays almost constant at low temperatures up to ~ 160K, after which it drops sharply. The explanation for this intensity reduction at high temperatures could be attributed to the competing non-radiative processes.

Understanding the different decay elements out of the excited states is crucial for predicting the laser characteristics of a material. Non-radiative transitions of the Ti^{3+} ion occur by tunnelling out of the excited state into the ground state. The effects of the non-radiative processes may be assessed from measurements of the temperature dependence of the luminescence lifetime. The fast decay rate of $Ti^{3+}:Al_2O_3$ (ca 3.8 μ_s at 4K) makes reliable measurements of the lifetime by lock-in techniques or using the boxcar integrator almost impossible. However a crude measurement made at 10K using a chopper wheel with 100 slots gave a value of 4.2 μ_s, which is in reasonable agreement with other measurements (ca 3.8 μ_s).[69,75] In these early measurements, the lifetime was observed to be constant below T = 150, above which temperature it decreases to 3.2 μ_s at room temperature and to 0.3 μ_s at 500K. This thermally induced reduction is due to thermal quenching caused by strong electron-phonon coupling, and the Jahn-Teller effect, which activates non-radiative transitions at high temperatures.

The quantum efficiency, η, of an optical emission process is defined as the ratio of the probability of the radiative transition (τ_R^{-1}) to the total transition probability (τ_t^{-1}), i.e.

$$\eta = \frac{\tau_R^{-1}}{\tau_t^{-1}} \tag{4.5}$$

where τ_R and τ_t are the radiative and total lifetimes, respectively. Hence using equation (4.5) we can see that the quantum efficiency at 300K is still ~ 84% of its low temperature value, assuming the total decay at low temperature to be purely radiative. This high efficiency is due to the small Frank-Condon overlap between the vibrational sidebands of the ground state and the thermalized vibrational states of the excited ^2E level. Measurements of the luminescence decay rate of the transition $^2E \rightarrow {}^2T_2$ in Ti^{3+}:YAG showed that the decay curves were exponential. The radiative lifetime of 51 μs at 10K is more than an order of magnitude larger than that of Ti^{3+} in sapphire. The lifetime at room temperature is very much faster, being measured as $\tau_t = 4.4\ \mu s$. In earlier work Bantien et al.[71] obtained a value of $2\mu s$. This strong reduction in the luminescence lifetime at 300K relative to the low temperature value is consistent with a quantum efficiency of around 9%.

The total decay rate τ_t^{-1} may be written as the sum of radiative and non-radiative processes,

i.e.
$$\tau_t^{-1} = \tau_R^{-1} + \tau_{NR}^{-1} \tag{4.6}$$

The radiative rate dependence on temperature is described in the form:[77]

$$\tau_R^{-1} = \tau_{stat}^{-1} + \tau_{vib}^{-1} \coth(\hbar\omega/2kT) \qquad (4.7)$$

where τ_{stat}^{-1} is pure radiative decay rate, while τ_{vib}^{-1} is the phonon assisted decay rate. In addition to this vibrational increase in the radiative rate, there is also an increase in the non-radiative rate with increasing temperature.

$$\tau_{NR}^{-1}(T) = \tau_{NR}^{-1} \cdot \exp(-\Delta E/kT) \qquad (4.8)$$

where ΔE is the activation energy, and the total decay rate is

$$\tau_t^{-1} = \tau_{stat}^{-1} + \tau_{vib}^{-1} \coth\left(\frac{\hbar\omega}{2kT}\right) + \tau_{NR}^{-1} \exp(-\Delta E/kT) \qquad (4.9)$$

In consequence the sharp decrease in the lifetime and the low quantum efficiency of the Ti^{3+}:YAG is probably due to the high radiative transition rate at high temperature compared with $Ti^{3+}:Al_2O_3$.

For Ti^{3+}:YAP there is also an increase in the integrated intensity as the temperature increases, as shown in figure (4.31) and figure (4.32). The intensity remains essentially constant in the range

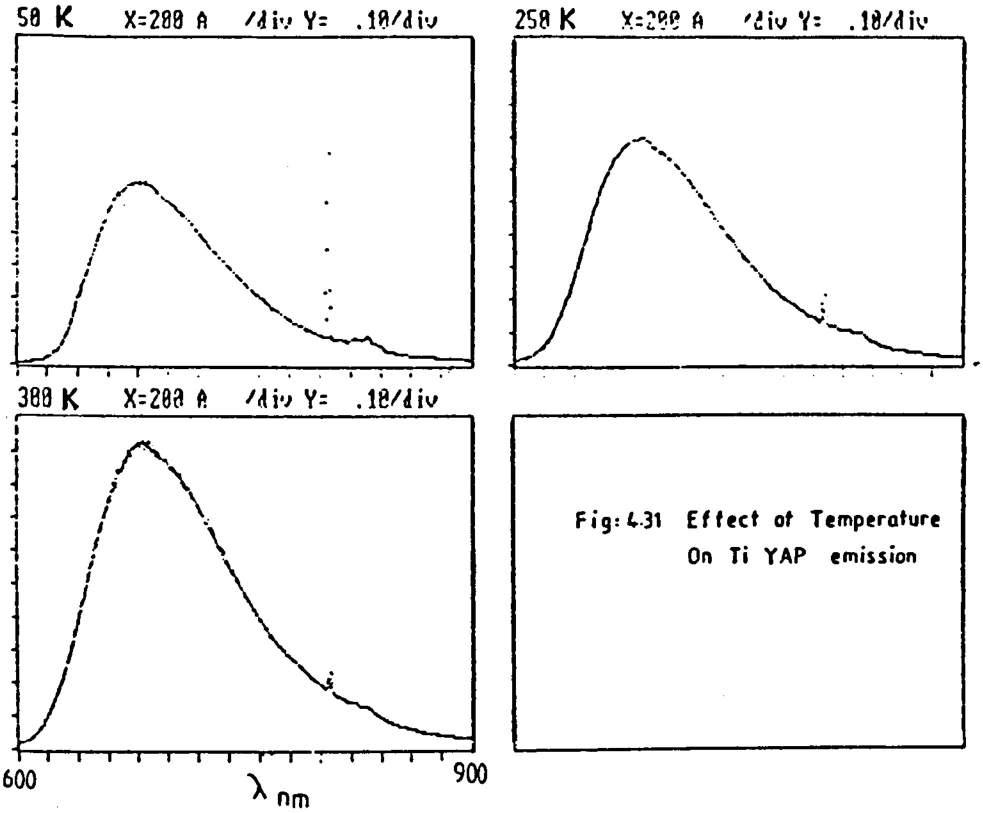

Fig: 4.31 Effect of Temperature On Ti YAP emission

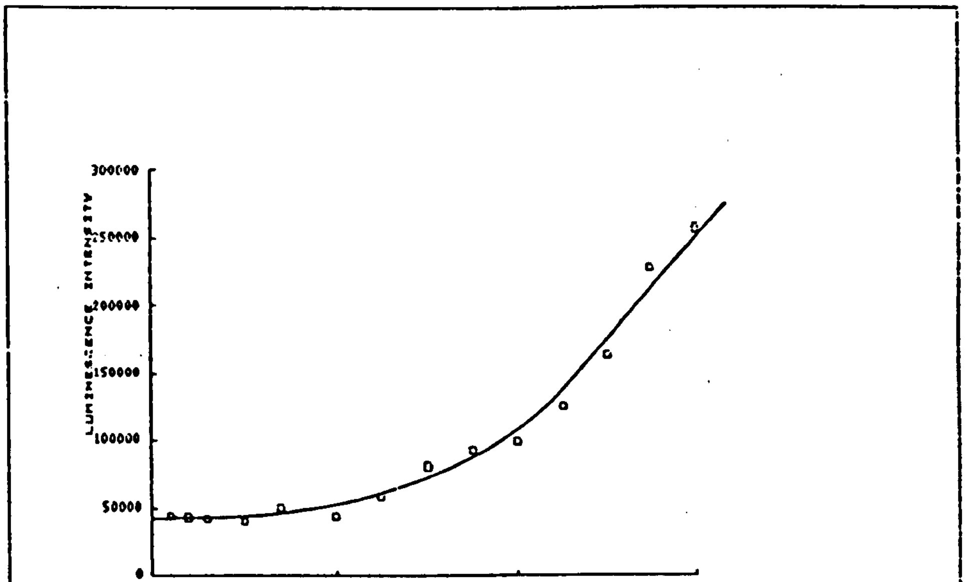

Fig 4.32 Temperature dependence integrated intensity of Ti:YAP.

(0-120)K. However at higher temperatures, as figure (4.32) shows, there is a remarkable increase in the intensity which becomes sharper above 200K. Apparently the non-radiative decay, which causes a decrease in the intensity of the emission in $A\ell_2O_3$ and YAG crystals is very weak so that the intensity is enhanced by the phonon assisted electronic interaction.

A plot of the variation of the centroid position of the emission peak with temperature figure (4.33) shows the usual shift towards lower wavelengths as the temperature decreases, although the shift is much smaller than that of the Ti^{3+}:sapphire. From the temperature dependent bandwidth of the luminescence spectra, in figure (4.34), the mean phonon energy broadening the transition was determined to be $\hbar\omega$ = 443 cm^{-1} and the zero temperature halfwidth was Γ_o = 1490 cm^{-1}. This bandwidth changed by only ~ 170cm^{-1}, or about 10.2%, between (10-300)K compared with the variation for $TiA\ell_2O_3$ of 19.3% in the same range of temperatures. Decay rate measurements for this crystal showed a lifetime of 16.1μ_s and 10μ_s for the temperatures 10K and room temperatures, respectively.

The decay rates for Ti^{3+}:doped glass are expected to be fast because it originates on a spin-allowed transition. Furthermore, since these transitions are from different sites in the glass matrix, a range of decay rate values is anticipated. Since different excitation lines will excite different sites, different lifetime values are also expected. With all the measured temporal decays

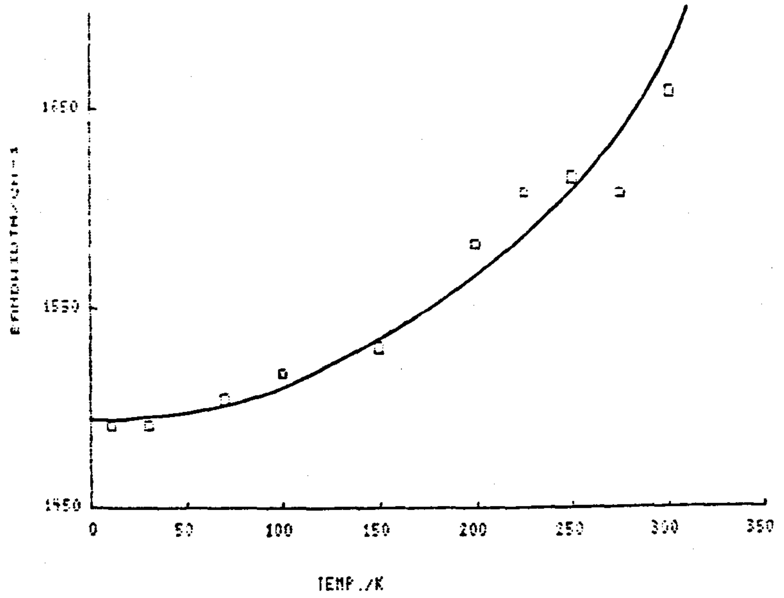

Fig 4.34 Temperature dependence bandwidth of Ti:YAP.

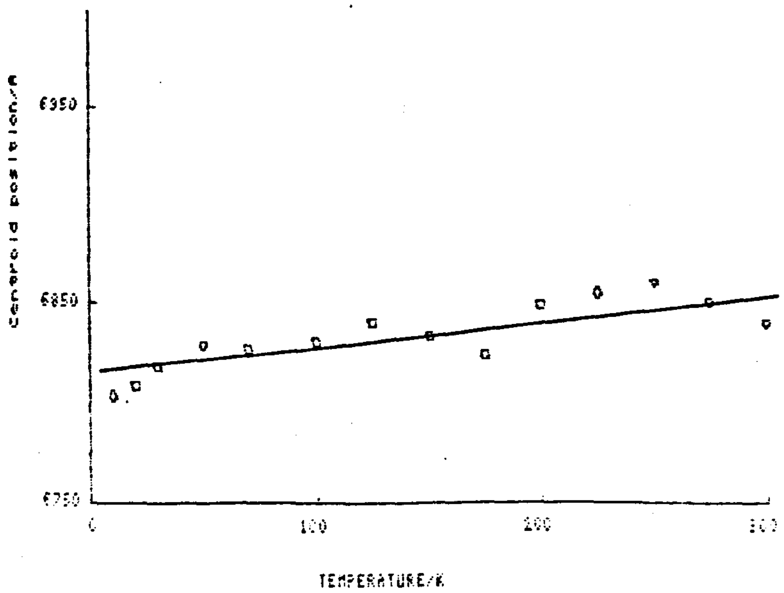

Fig 4.33 Variation of the centroid position with temperature for Ti:YAP.

of the fluorescence, the measured decay curves were non-exponential, as is expected from multisite glass samples. So the measured decay rates are quoted as upper and lower values. The decay rate of 1% Ti^{3+} concentration at room temperature and 10K are 7 ms^{-1} - 2.5 ms^{-1} and 4.4 ms^{-1} - 1.2 ms^{-1} respectively. For samples of higher concentration the luminescence decay is faster, the measured value for 2% concentration sample at 10K being 10.6 ms^{-1} - 7.6 ms^{-1}. Changing the excitation light gives the values 9.3 ms^{-1} - 3.9 ms^{-1} and 6.4 ms^{-1} - 2 ms^{-1} for the pumping lines 668nm and 488nm respectively. Pumping with longer wavelength lines means emission of lower field sites and hence faster decay.

Measuring the decay rate of Cr^{3+} impurities in Ti^{3+}:YAG and Ti^{3+}:YAP is one method of identifying these transitions. For Ti^{3+}:YAG a doublet at ~ 687 nm followed by a side band showed a slow decay value for which the lifetime was ~ 10 ms at 10K and ~ 1.9ms at room temperature, in good agreement with those of Cr^{3+}:YAG.[46] For Ti^{3+}:YAP the Cr^{3+} impurity transition is observed at ~ 723nm, with a lifetime of 53 ms at 10K. A similar value is measured for a 0.1 % wt Cr^{3+}:YAP crystal in which this value is reduced to 39 ms at room temperature.

It was noticed that the two Cr^{3+} impurity lines (R-lines) are situated at 7213Å and 7237.5 Å at 10K, while each of these values shifted towards longer wavelengths by about 24 Å at room temperature. The theory of thermal lineshift is discussed in detail in ref[32] and is explained as an algebraic sum of the shifts of the two levels involved in the transition due to ion-vibration interaction. The separation between the two R-lines of the Cr^{3+} impurity is measured from the temperature dependent intensity of the two lines, using the Boltzman thermal occupation equation, which resulted in a separation of 43.7 cm^{-1}. Similar measurements for the Cr^{3+} in Ti^{3+}:YAG system were carried out with the splitting of 22.5 cm^{-1} in agreement with the value measured by Wall et al.[78] which is another confirmation of the type of impurity.

4.7 Time-resolved Spectroscopy

A consideration of the selection rules for Ti^{3+} and Cr^{3+} emission in these materials suggests that the Ti^{3+} ion photoluminescence should be much faster than that of Cr^{3+} because a spin-allowed transition is involved in the former. This difference in transition rates makes it possible to differentiate the spectra by time-resolved spectroscopy. Indeed by utilizing a timing delay before the detection of the transition will allow discrimination between the different transitions. This characteristic is very useful, especially in the case of glasses, where different transitions with different frequencies may be distinguished. Luminescence spectra of Ti^{3+}:YAG at different delays (figure (4.35)) show that, after 1ms delay, where the Ti^{3+} transition is completely decayed, it is possible to identify the Cr^{3+} ion in this crystal as compared with the spectra shown in ref[46].

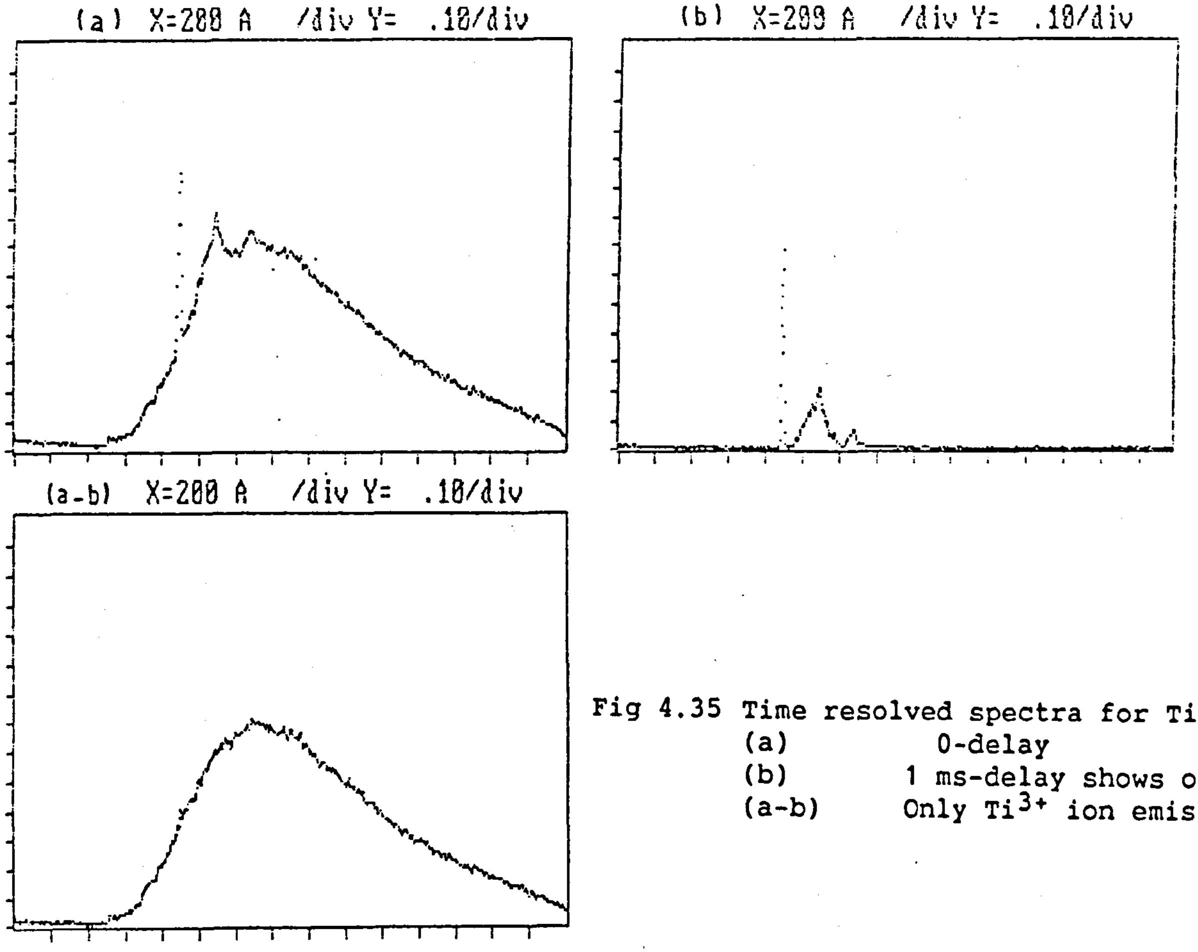

Fig 4.35 Time resolved spectra for Ti:YAG crystal
(a) 0-delay
(b) 1 ms-delay shows only the Cr^{3+} luminescence
(a-b) Only Ti^{3+} ion emission left.

The third spectrum (a-b) is the subtraction of the Cr^{3+} ion spectrum from the 0-delay spectrum, which shows only the Ti^{3+} emission spectrum. A similar separation of the emission by Cr^{3+} and Ti^{3+} ions in YAP was also accomplished. The two spectra are separated in figure (4.36) using the 0-delay and 90 μ_S-delay.

The case for Ti^{3+}:glass samples is quite different, since we are dealing with spectra of ions in many slightly different crystal field sites each with slightly different decay rates. Hence, and because of these small decay rate differences, it is not expected to get accurate results by using the mechanical chopping system. However, it was noticed that for three spectra shown in figure (4.37), for 0,200 and 400 μ_S-delays, the peak of the spectrum is shifted towards the high energy side of the spectrum as the delay increases. This result could be explained as, the application of a certain delay allows the slow decayed transitions to survive, while the fast components which belong to lower field sites have vanished. Hence only the high field sites with the longer liftime, can still emit.

4.8 Polarized Absorption/Emission

Measurements of the polarization effects on the emission spectra for Ti^{3+} ion in $A\ell_2O_3$ and YAP crystals were carried out using the set-up explained in section (3.4.2). Figure (4.38) shows the σ and π polarized emission of $Ti^{3+}:A\ell_2O_3$ at 10K. The π ($\parallel$c-axis)

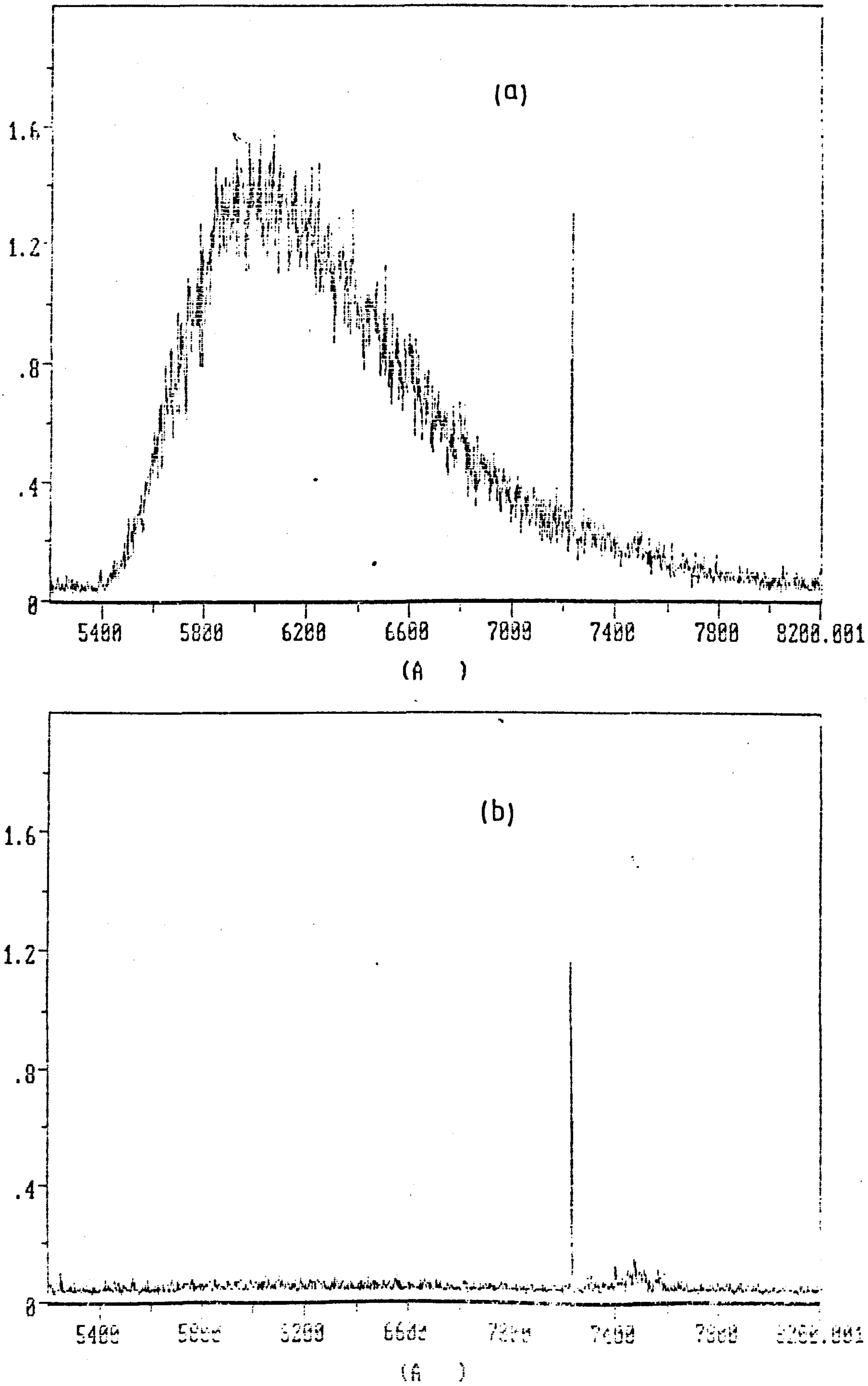

Fig 4.36 Time resolved emission spectra for Ti YAP
(a) 0-delay
(b) 90 μ_s-delay.

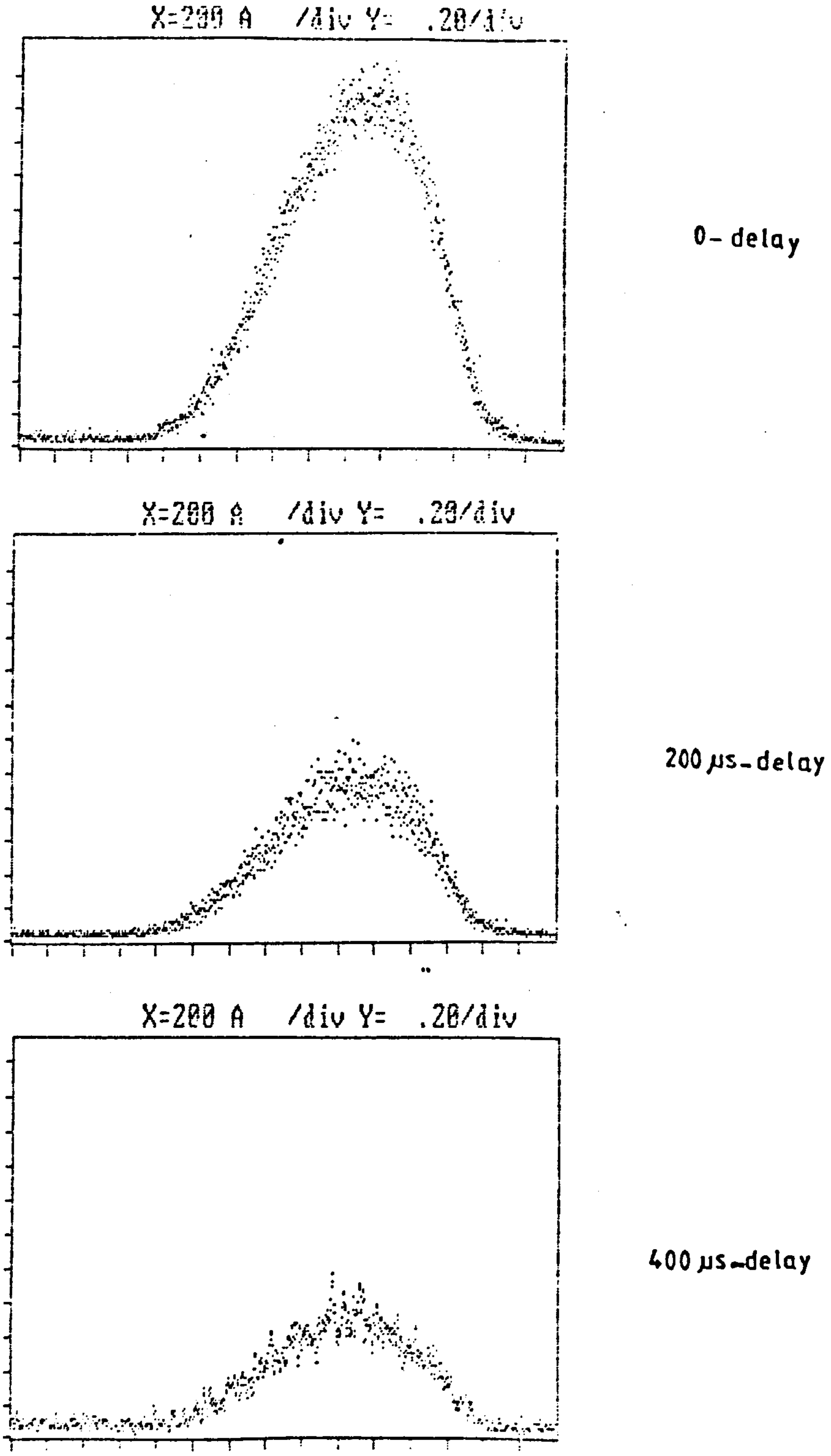

Fig 4.37 Time resolved Ti:glass emission spectra.

Fig 4.38 Ti-Al_2O_3

Polarized emission

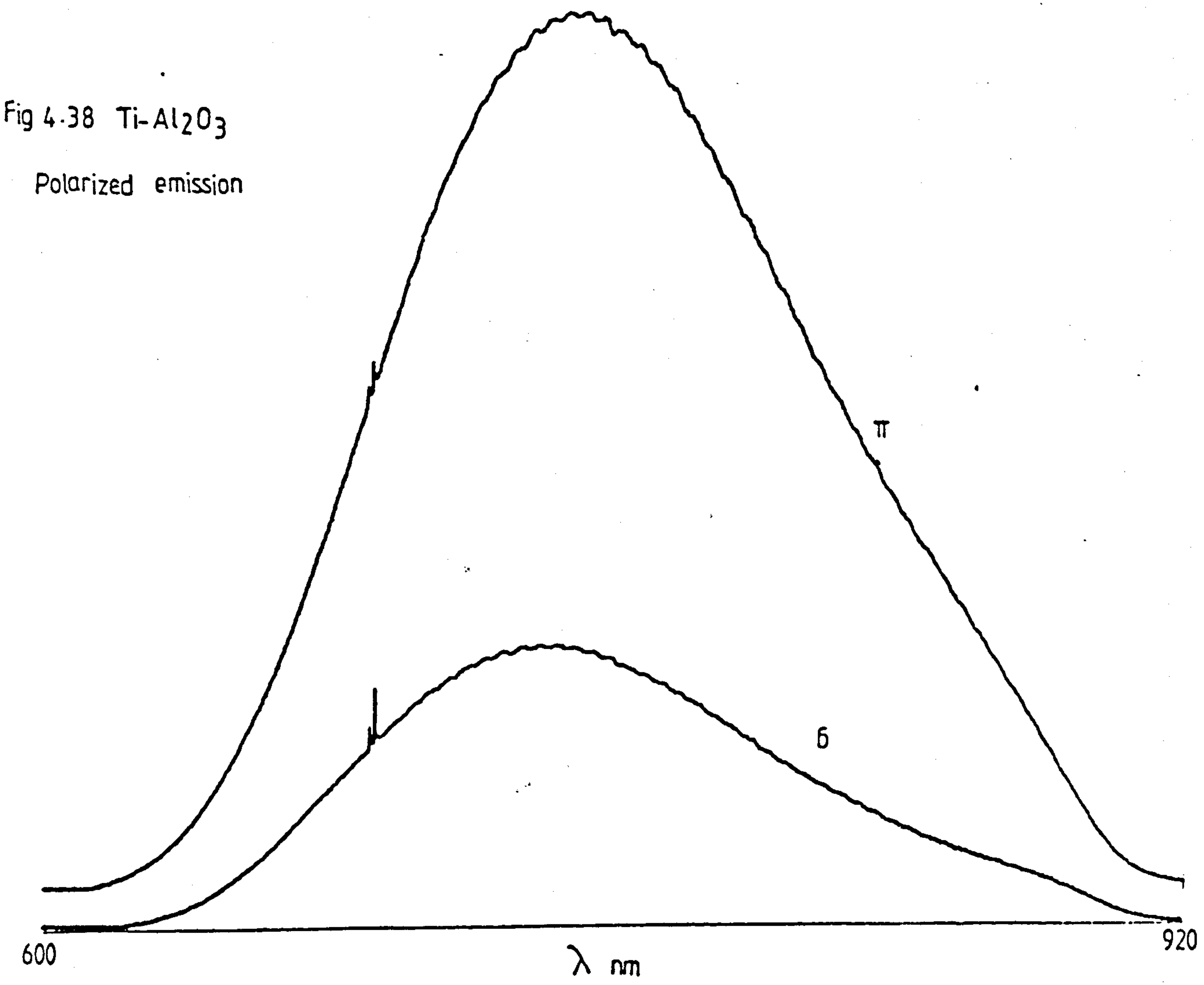

polarized spectrum is about 3 times more intense than the σ ($\perp$c-axis) polarized spectrum. The Cr^{3+} impurity lines show the opposite sense of polarization. Similar characteristics were noticed by Rapoport et al.[79] The reason for such a difference could be traced back to the selection rules for the ($^2E \rightarrow {}^2T_2$) Ti^{3+} transition which is induced by electric dipole processes, whereas the $^2E \rightarrow {}^4A_2$ transition in the Cr^{3+} is between two states of different spin. The unpolarized, π and σ polarized emission spectra for Ti^{3+}:YAP are shown in figure (4.39) from which we see that the π-polarized spectrum is still larger than the σ-polarized spectrum but to a lesser extent than that of $Ti^{3+}:Al_2O_3$. The intensity of the π-polarized emission is bigger than the σ-polarized spectrum by ~ 15% only. The other interesting feature is the variation of the two Cr^{3+} impurity lines at different emission polarizations.

The difference in the emission intensity between the π and σ polarized absorption/emission of the Cr^{3+} spectra can be explained as follows: the transition $^2E \leftrightarrow {}^4A_2$ is forbidden, but it could be allowed by the introduction of a combined effect of a static odd parity crystal field operator (between $^4A_2$ and $^4T_2$) and spin-orbit coupling (between $^4T_2$ and ^2E). The σ-polarized transition is induced by the dominant odd-parity operator $T_{1u}a_o$. While in the case of π-polarized transition there is no non-zero matrix elements between $^4A_2 \leftrightarrow {}^4T_2$, but it is induced by a weaker operator $T_{2u}x_o$, hence a weaker transition than in the σ-polarized case.

Fig 4.39 Ti-YAP
polarized emission

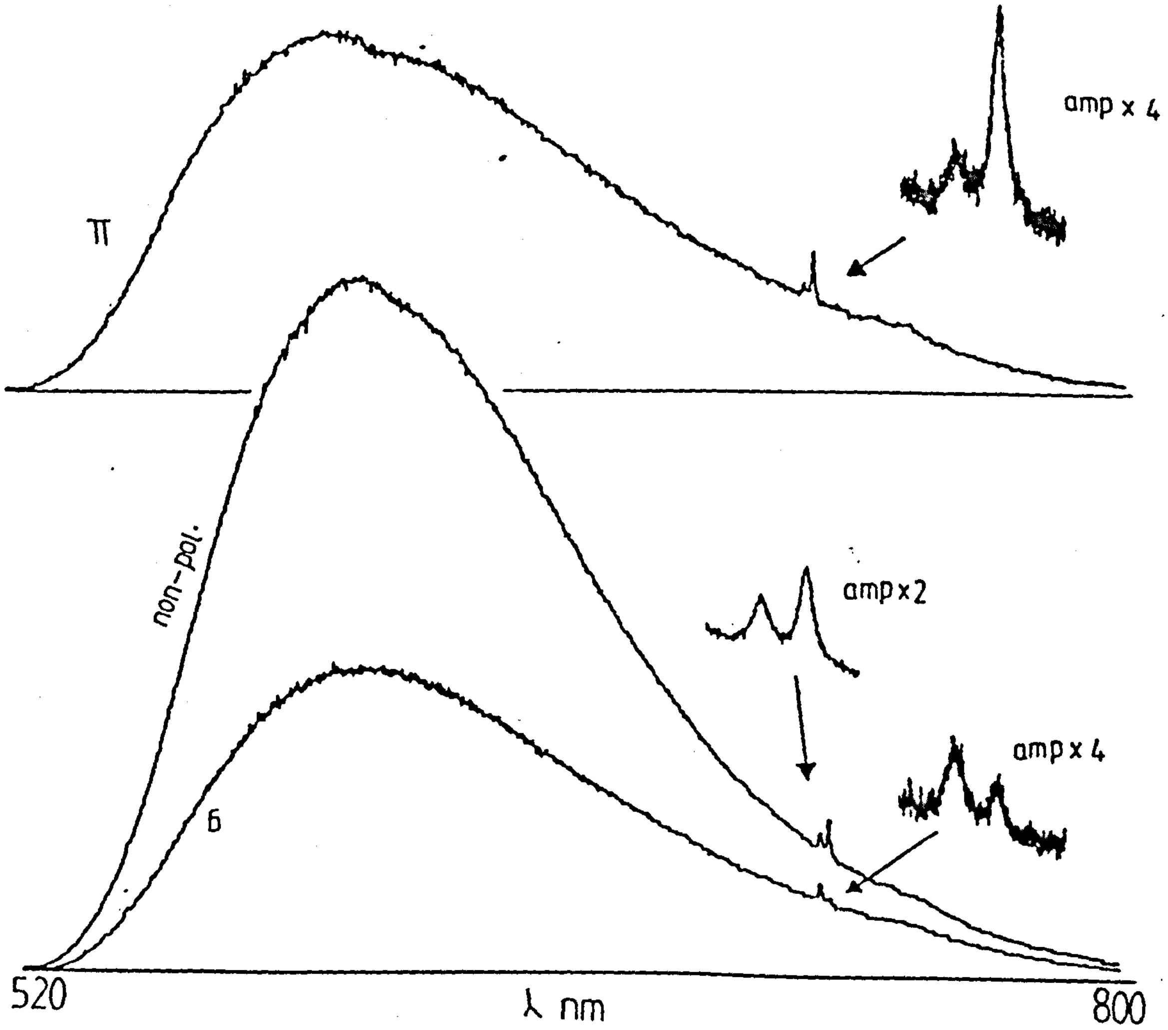

Consequently the feeding to the ^2E state is smaller in the π-polarization than in the case of σ-polarization which is the cause of stronger ^2E (R-lines) transition in the σ-polarized emission spectra.

4.9 Discussion

The interesting broad emission of Ti:doped solids is a result of the different interactions of the t_2 and e orbitals with the ionic environment, so that the equilibrium value of the configurational coordinate is different in the $^2T_2$ and the ^2E levels which causes the broadband transition between these two levels. Using spectral values from table (4.2) as well as values from the absorption spectra, the configurational coordinate diagram of $Ti^{3+}:Al_2O_3$ can be shown for the energy against the configurational coordinate Q as shown in figure (4.40). In order to find some important values which characterize the vibronic interaction (like Huang-Rhys factor (S)), we consider the broad transitions (emission and absorption) to be between the $^2T_{2g}$ and ^2E_g levels. In the configurational coordinate consideration, these two levels are represented as two potential curves with constants k and k' respectively. The difference in the energy value of the absorption peak and the bottom of the excited state parabola (the zero vibrational level) is the relaxation energy for this parabola and is equal to 4302cm^{-1}, while the value for the ground state is 3155cm^{-1}. And since the average of the two $\hbar\omega$ values is 240cm^{-1} for the ground state phonons and

168.5 for the excited state phonons (see table 4.2), the number of phonons in emission is 13.1, while for absorption it is 25.5. These numbers show how strong is the electron-phonon coupling in such a crystal which is the origin of broad emission and absorption bands.

The large Stokes' shift exhibited by these crystals (see table (4.4)) means no reabsorption of the luminescence by the ground state ions. In addition, the possibility of an excited state absorption (ESA) is eliminated since there is no higher d-electron levels, also (ESA) due to charge transfer of high p-state is a very small possibility, since those levels are very high in energy.

The polarized emission measurements of $Ti^{3+}:Al_2O_3$ and Ti^{3+}:YAP show that the ratio of the integrated intensity of the π-polarized to the σ-polarized is ~ 3.1 for the former sample and only ~ 1.2 for the later. These results can be attributed to the selection rules governing the $^2E \rightarrow {}^2T_2$ transition in the trigonally distorted octahedral field in $Ti^{3+}:Al_2O_3$ and the orthorhombic symmetry of the Ti^{3+}:YAP. The complete theoretical evaluation of these selection rules is under calculation.[119]

The short lifetime of Ti^{3+}:crystals in general, is a result of the spin-allowed transition compared to Cr^{3+} ion crystals in high to intermediate field sites where there is a metastable or intermediate level which elongates the lifetime of the upper state.

Consequently the emission cross-section is reduced in the latter case to a greater extent. The measured value of the emission cross-section for $Ti^{3+}:Al_2O_3$ is ~ 3-4 x 10^{-19} cm^2, while for Cr^{3+}:GSGG and Alexandrite it is only 0.8 x 10^{-20} cm^2 and 0.7-2 x 10^{-20} cm^2, respectively.[17]

Another interesting feature of Ti^{3+}:crystals is that their broad absorption bands overlap the output lines of many laser outputs (Ar^+ ion, frequency doubled Nd:YAG) and other sources including the white light for flashlamp pumping. Some problems working against Ti^{3+} doped materials are the thermal quenching (although Ti^{3+}:YAP looks an exception) and the absorption in the near infra-red. In addition $Ti^{3+}:Al_2O_3$ with its fast decayed transition lacks significant energy storage for effective Q-switching in flashlamp pumped operations. The other two Ti^{3+}:samples (YAG and YAP) showed longer lifetimes.

The competition between the two concurrent processes determines the suitability of the material as a laser medium. These processes are the radiative transition which could be quenched through the concurrence process of the non-radiative transitions. By observing the decay rate dependence on the temperature, the Ti^{3+} doped YAG crystal could be eliminated as a laser candidate for room temperature CW operation, because of its low quantum efficiency at high temperatures, unlike $Ti^{3+}Al_2O_3$ crystal. The reduction in quantum efficiency is due to a multiphonon non-radiative decay at

Table 4.4 Comparison of the Stokes' shift and bandwidth values for Ti^{3+} samples (all values are in cm^{-1}).

Sample	Absorption peak	Emission peak	Stokes' Shift	$\Gamma_{(300K)}$
$TiAl_2O_3$	20492	13035	7457	3085
TiYAG	19840	12975	6865	3470
TiYAP	22730	16502	6228	1660
Ti:glass	17668	11472	6196	2774

Table 4.5 Crossover energy values for Ti^{3+} crystals

Sample	ΔE_x (cm^{-1})
$TiAl_2O_3$	11393
TiYAG	12262
TiYAP	21862

high temperatures. In order to estimate the overlapping between the ground and excited transitions we show two potential curves for the ground and excited states (figure 4.41). We call the absorption energy $E_{ab} = h\nu_a^o$ and the emission energy $E_e = h\nu_e^o$ and assuming the potential constants for the two parabolae are of the same value k = k'. For estimating the crossover energy ΔE_x we will use the same formulae of ref[75] where

$$\Delta E_x = \frac{(h\nu_e^o)^2}{2h(\nu_a^o - \nu_e^o)} \qquad (4.9)$$

Substituting for the values of E_{ab} and E_{em} mentioned in sections (4.4, 4.5), the crossover energies for the three Ti^{3+} crystals are listed in table (4.5). We can draw the following conclusions from the values shown in table (4.5):

1. The high values of the crossover energies for the three samples suggested that the probability of non-radiative transitions is low even at room temperature and the radiative probability is still the bigger contribution.

2. Comparing between Ti^{3+}:YAG and Ti^{3+}:Al_2O_3 we can see, relatively, not much difference in values for the two crystals. So this result, strengthens our belief that the low quantum efficiency noticed in the YAG crystal at room temperature is not due to high probability of non-radiative decay but rather to the

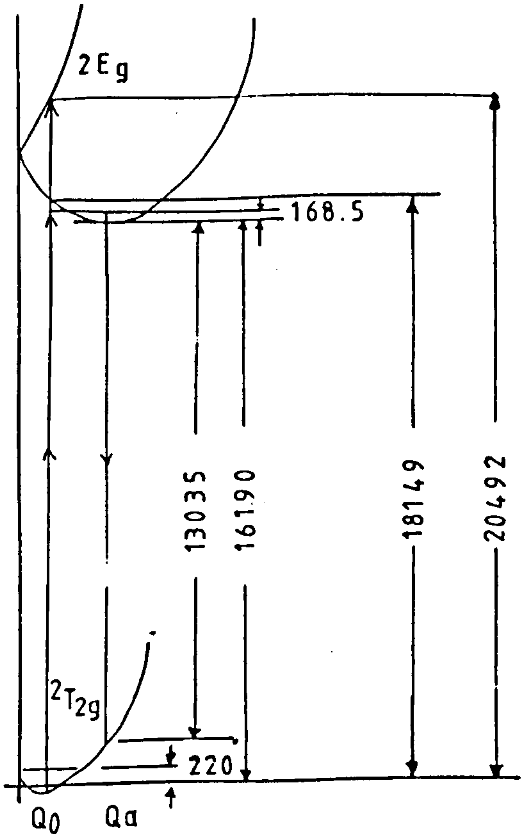

Fig 4.40 Schematic diagram of the configurational coordinates of $Ti:Al_2O_3$ crystal showing zero-phonon, side band and absorption transition energies between ground and excited states.

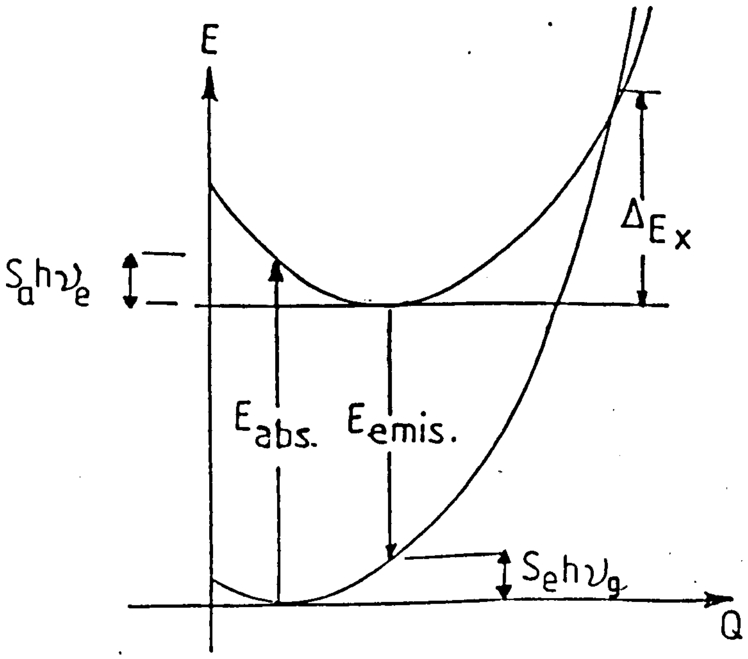

Fig 4.41 Schematic diagram of the two potential curves of the excited and ground states of $TiAl_2O_3$ showing the crossover energy ΔE_x, the absorption and emission transitions.

increase of the vibrational component of the radiativate decay at high temperatures. Also the two near values of ΔE_x results in about similar non-radiative decay rates, confirm the equal values of non-radiative decay rates measured by Albers.[69]

3. The very high values of the crossover energy of the YAP crystal, suggests very much smaller non-radiative decay rates for this crystal. This result is in good agreement with the observed spectra of this sample at low and high temperatures. For this sample we suggest that the total decay is shared by purely radiative decay rate plus a phonon-induced radiative rate, which could cause the reduction in the lifetime and the increase in the transition intensity at high temperatures.

Another characteristic which favours the laser crystal host is the good thermal conductivity where this property is an order of magnitude lower for glasses than for crystals. For comparison between crystals it was found[77] that the thermal conductivity for $A\ell_2O_3$ is 420 mw/cm.k while it is only 70 mw/cm.k for the YAG and 129 mw/cm.k for GSGG.[80] High thermal conductivity values allow more rapid dissipation of the resulting heat from the non-radiative processes and also due to Stokes'shift, so that thermal effects on the crystal will be minimized.

A disadvantage of the YAP host in laser applications was that the crystal shows[63] a brownish colour after growth, which even when it was reduced by annealing, it coloured again after a laser pumping. It might be worth mentioning that during the laser excitation of our Ti^{3+}:YAP sample, we noticed that the intensity of the emission was dropped down slightly at low temperature. On changing the excitation spot on the sample the intensity went up and then down again after a short while. Also there might be a relation between the two (self-absorption) lines mentioned before at 685 and 689nm with the conclusion noted in ref.[63]

CHAPTER FIVE

5. OPTICAL SPECTROSCOPY OF Cr^{3+} IONS IN SOME INORGANIC GLASSES

5.1 Introduction

The structure of amorphous materials has long been controversial. This could be because of the unique character of the vitreous state, which permits many of the mechanical properties of crystalline solids and yet structurally resembles a liquid in its lack of long range periodicity. At the time of Zachariasen's Random Network theory[82], it was thought that only oxide glasses and organic polymers could be prepared in the non-crystalline form. Recent developments in the fabrication techniques has shown that all materials can be prepared in a non-crystalline form when cooled sufficiently quickly. According to McKenzie's[83] definition the glassy material is an isotropic material which lacks three-dimensional atomic periodicity and has a viscosity in excess of 10^{14} poise.

The present work focuses on inorganic glasses which have a large forbidden gap, which in "pure" form are transparent in the visible region. However when they are doped with optically active ions, they show distinctive optical features depending on the type of the active ion as well as the structure of the glass host.

5.2 Theories of Glass Structure

The long struggle to understand the constitution of glasses has largely involved the applications to glasses of the techniques and concepts found useful in studying crystalline solids. A general view of the structure of glass is obtained using a bonding model in which groups of atoms in the glass are held together by different types of bonds, from strong, largely covalent bonds to the weaker vanderwaals forces. In general, amorphous materials have many properties resembling those of crystals containing the same atoms in approximately the same proportions. For example each silicon atom in tetravalent Si is bonded covalently to four oxygen atoms in a periodic tetrahedral arrangement of crystalline SiO_2. In this case, an optimum bond length which minimizes the bond energy and optimises the angle between the four bonds, whereas in amorphous SiO_2 (see figure (5.1)) a silicon atom is expected to occupy a site as ideal as possible. In actuality the non-periodic distribution of SiO_2 tetrahedra causes a spread in bond lengths and bond angles about the optimum values, although each silicon atom retains its bonding to four oxygens in octahedral configurations. Hence the differences in the physical and optical properties between crystalline and glassy materials are basically attributed to their structural differences.

A correlation of the ability of an oxide A_xO_y to form a glass with the ionic radius ratio $\rho = R_A/R_O$, was suggested by Goldschmidt.[84]

Values of between 0.2 - 0.4 are reported for ρ in glassy oxides like P_2O_5, SiO_2 and GeO_2. Zachariasen[82] noted that the radius ratio of BeO is very nearly the same as SiO_2 and yet glassy BeO has never been prepared. Zachariasen concluded in the continuous Random Network (CRN) theory that the atoms in the glass are linked by essentially the same forces as exist in crystals, the atoms oscillating about definite equilibrium positions, as is indicated by the strength of a glass being of the same order of magnitude as the strength of crystals. The equivalent of the lattice in the glassy state is known as the "network" or a matrix, and as in crystals, atoms in glasses must form an extended three-dimensional network. But the absence of sharp X-ray diffraction lines indicates the network is not periodic. However, the atomic positions are not entirely random, small regions up to ~ 500 Å may have an ordered structure[85] and interatomic distances cannot be less than certain minimum values. Zachariasen's glass formation condition stated that extended three-dimensional random networks can be formed by neighbouring molecular units and linked at the vertices by a bridging oxygen atom. Although this structure lacks periodicity it has an energy content of the same order as that of the crystal. This implies that the coordination number of the atom A in the glass should be approximately the same as that in the crystal as in the case of SiO_2 which both in crystalline and amorphous SiO_2 is surrounded by a tetrahedral arrangement of four oxygen atoms. Figure (5.2) shows an oxide A_2O_3 structure which may exist in either crystal or glass using the AO_3 triangles. The figure shows that

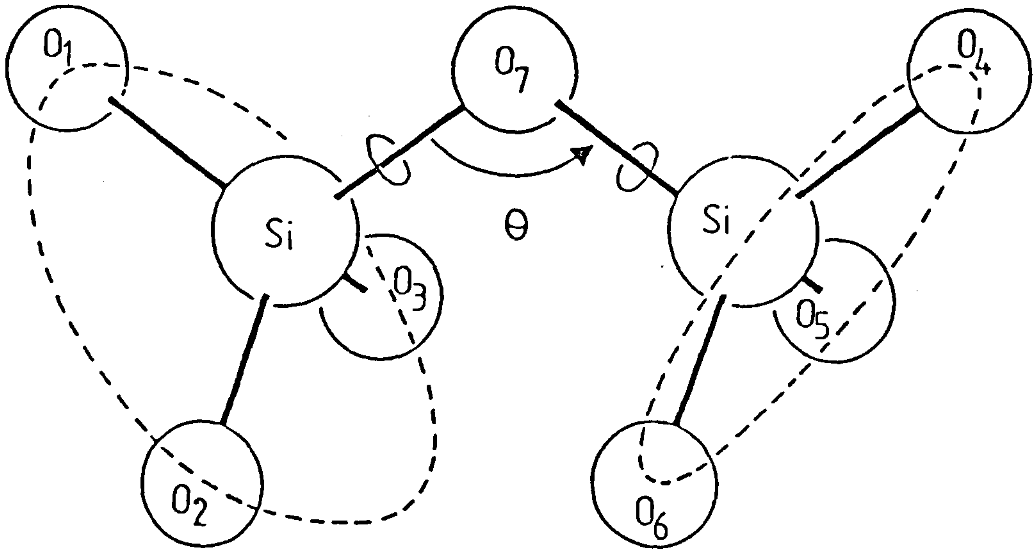

Fig 5.1 Two SiO_4 molecular units joined by a common, or bridging oxygen atom, the Si-O-Si angle θ varies from band to band.

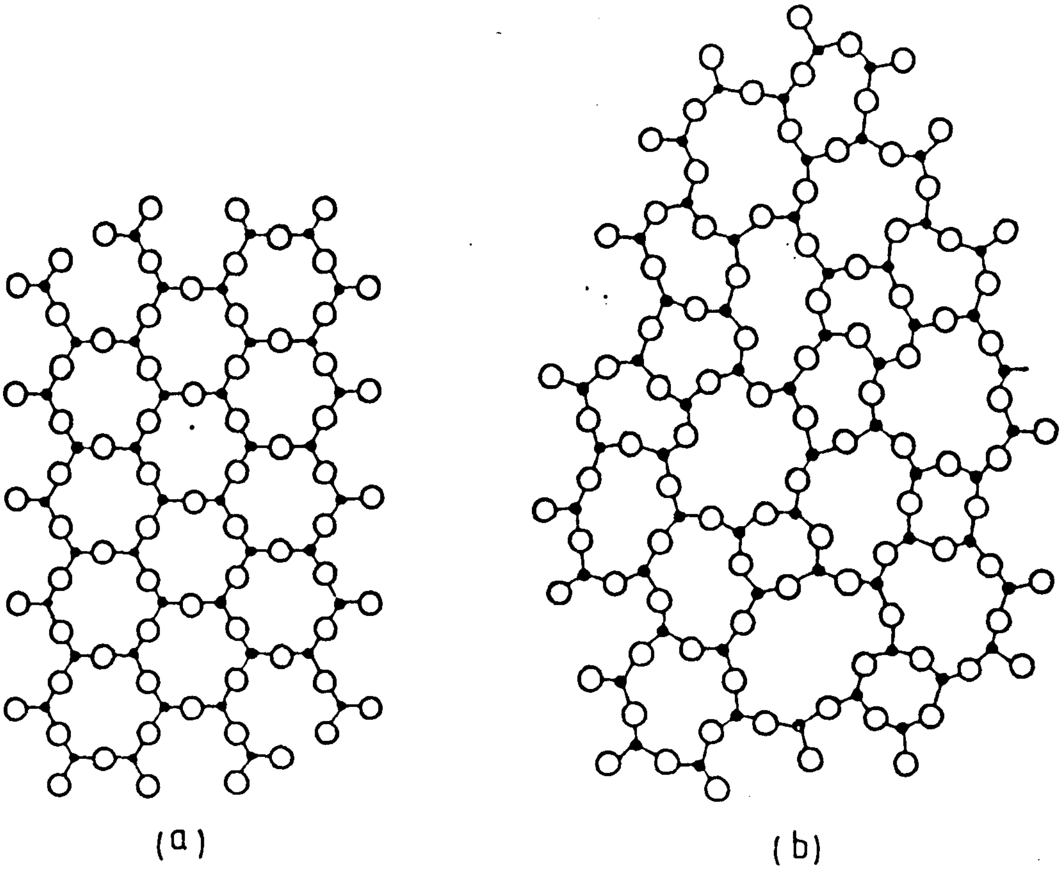

Fig 5.2 Schematic two-dimensional representation of the structure of (a) Crystalline compound A_2O_3
(b) The glassy form of this compound.

although the crystal has a symmetrical structure, the random distribution of bond angles in the glass has eliminated any long range periodicity. Zachariasen suggested four rules for oxide glass formation:

(i) oxygen atoms are linked to not more than two A atoms,
(ii) the number of oxygen atoms surrounding A must be small,
(iii) the oxygen polyhedra shares corners with each atom but not edges or faces,
(iv) at least three corners in each oxygen polyhedron must be shared.

Warren[86] studied a number of glasses including a range of simple sodium silicate glasses, using Fourier analysed X-ray diffraction techniques yielding results in agreement with Zachariasen postulates. Diffraction patterns of cristoballite and vitreous SiO_2 (see figure 5.3) showed the strongest line of the cristoballite to coincide with the peak of the broad line in the glass which had previously been attributed to inclusions of very small cristoballite microcrystals. The absence of small angle scattering from the glass confirmed that such microcrystals are not present in the glass.[86] From the experimental diffuse-angle X-ray diffraction patterns from the glass, the Radial Distribution Function (RDF) could be computed enabling an analysis of the distribution of the interatomic distances.

Assuming that the total diffracted intensity from the glass, $I_t(s)$ is the sum of interatomic interference scattering I(s), the coherent and incoherent atomic scattering intensities I_c; and I_i, i.e.

$$I_t(s) = I(s) + I_{c+i}(s) \tag{5.1}$$

where $s = \frac{4\pi \, \mathrm{Sin}\theta}{\lambda}$ is the scattering vector, and 2θ is the angle between the incident and the diffracted beams, the scattering intensity from vibrating point atoms may be expressed as an intensity function, i(s), given by

$$i(s) = I(s)/\Sigma f^2(s) = (I_t(s) - I_{c+i}(s))/\Sigma f^2(s) \tag{5.2}$$

where $\Sigma f^2(s)$ is the sum of the coherent atomic scattering factors for the unit of composition, e.g. SiO_2. Now if $\rho(r)$ is the number of atoms per unit volume at a distance r from an arbitrary atom and $\rho_{(o)}$ is the average density of the sample in atoms per unit volume, the radial distribution function is related to the fourier transform of si(s) by,

$$\mathrm{RDF} = 4\pi r^2 \rho_{(r)} = 4\pi r^2 \rho_{(o)} + \frac{2r}{\pi} \int_0^\infty \mathrm{Si(s)\ Sin(Sr)dr} \tag{5.3}$$

The intensity in the diffuse diffraction patterns of a SiO_2 glass is plotted in figure 5.4 which also plots the RDF against the interatomic distance (r). The oscillating curve about a parabola

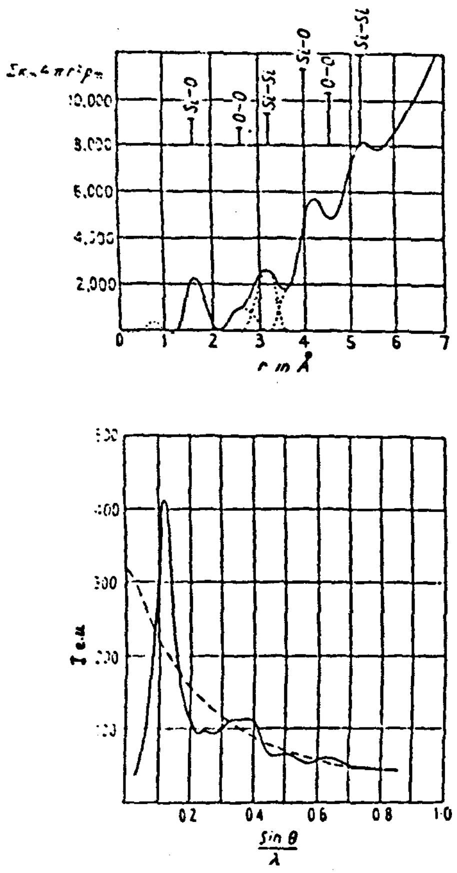

Fig 5.4 (a) Radial distribution curve for vitreous silica
(b) X-ray intensity curve[88].

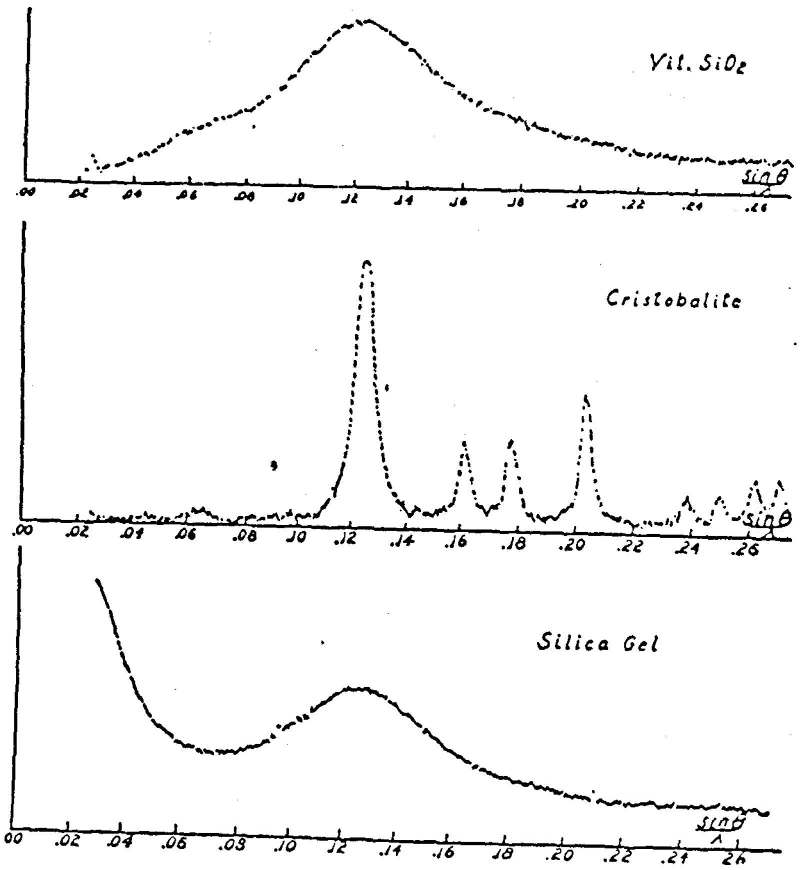

Fig 5.3 X-ray diffraction patterns of vitreous silica, cristoballite and dried silicaged. (After Stanworth[88]).

represents the average atomic density and describes the number of atoms in spherical shell between r and r+dr. The positions of the peaks gives the distances of atoms from a silicon or an oxygen,[87] while from the area under the peaks it is possible to calculate the number of neighbours at that distance.[88] Beyond the fourth or fifth peak the RDF merges into the rising background showing the random nature of the structure. However the existence of these well-defined peaks show a definite short range order. A substantial agreement was also noticed[87] between the theoretically computed RDF from the CRN model and the experimentally measured RDF obtained from X-ray and neutron diffraction experiments as shown in figure (5.5). From the computational studies it was known that the bond angle lies between 120°-180°, Bell and Dean[87] used a bond angle of 153° in their computation. Their model gives good agreement with the experimental measurements and to interatomic distances of 8 Å, the maximum separation for which experimental details are available. They reported that bond length has only a small effect, smaller than the bond angle variation.

5.3 Glass Formation

The volume-temperature relationship for liquid-solid equilibrium is portrayed in figure (5.6), on cooling a liquid from any temperature (T > Tm) to the temperature of the crystal (Tm), the path (a) will be followed if crystallization is to take place. However if the liquid is supercooled over some temperature range below (Tm) then

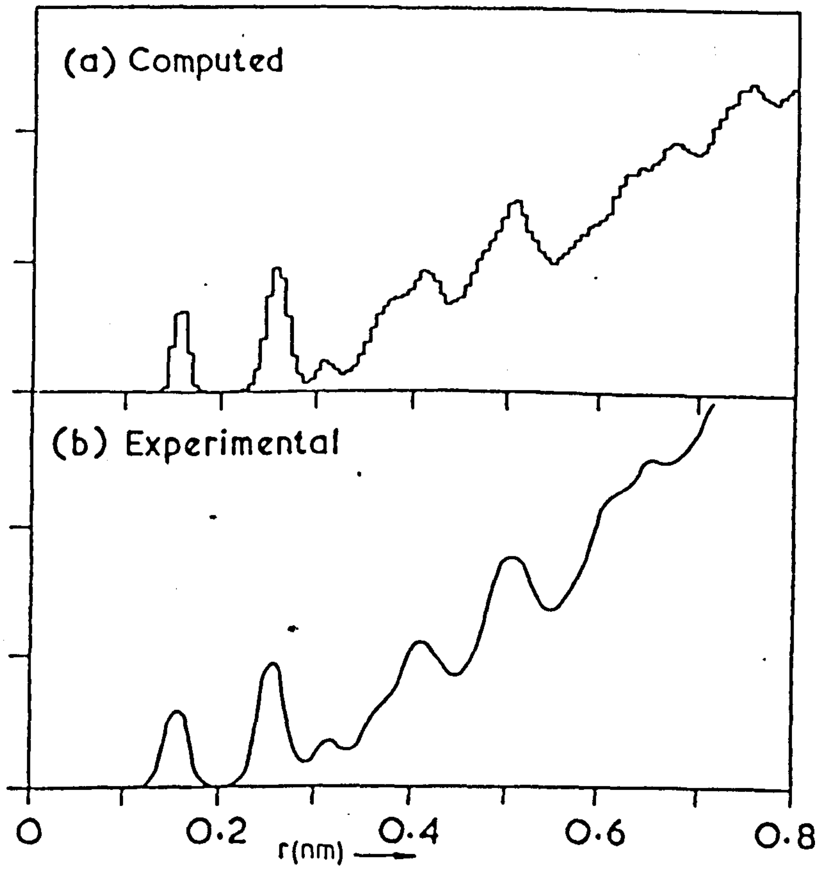

Fig 5.5 Radial distribution function for X-ray scattering from vitreous silica (after Bell and Dean[87]).

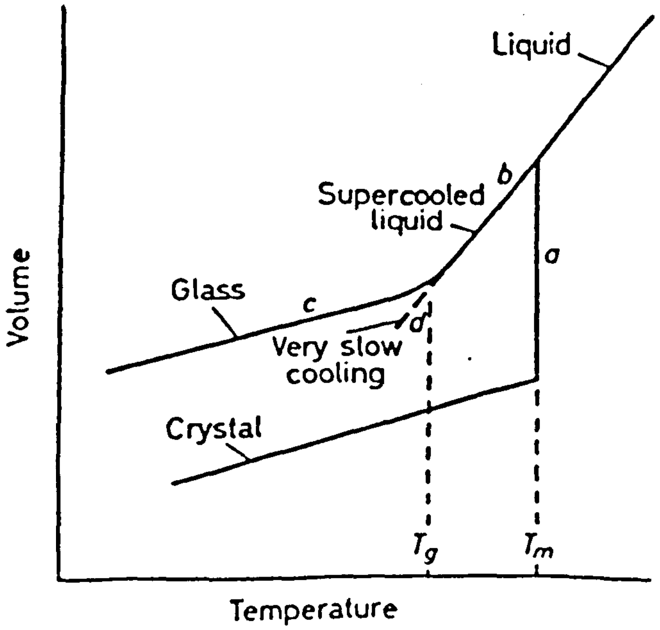

Fig 5.6 Volume-temperature relationship for glass forming systems.

path (b) is followed. Further cooling to temperatures below (Tg) at which the viscosity becomes $\sim 10^{14}$ poise, results in glass formation. (Tg) is known as the glass transition temperature. Notice in figure (5.6) that there is a gradual change in the slope of the curve between (b) and (c). This change occurs over a small interval of temperature near (Tg). The cooling rate must be very slow for crystal formation, whereas it must be very high for the glass formation. In consequence one may think of a glass as a supercooled liquid in which the cooling rate has been so rapid that its atoms have not had the chance to rearrange themselves into a symmetrical pattern before their motion was arrested. To this extent the glass is a liquid, the viscosity of which has increased upon cooling, so much so that the liquid becomes a solid. Nevertheless given sufficient time, the atoms tend to adopt the more symmetrical and stable crystalline structure even while in this highly viscous state. This process of gradual crystallization is called devitrification. The absence of symmetry in the glass structure allows the bond strengths to vary from one tetrahedron to the next. In consequence, there is not a single temperature at which all bonds are broken simultaneously, on heating glasses soften gradually rather than melt abruptly as in crystals. It is evident from figure (5.6) that the gradual change of the volume makes it difficult to define a precise temperature for the glass formation, although it is convenient to define it as the intersection of the extrapolation of the slopes of both the liquid and glass curves. An alternative definition of an amorphous solid undergoing a glass to liquid transition involves a sudden change in the derivative of thermodynamic properties from crystal to liquid-like values as the temperature changes. Although the volume, enthapy and entropy are continuous through Tg their derivatives

$$\frac{\partial \ell nV}{\partial \ell nT} = \alpha \text{ expansion coefficient}$$

$$\left[\frac{\partial H}{\partial T}\right] = C_p \text{ specific heat capacity}$$

are not.

A comparison of these thermal properties of glass, crystal and liquid is given in figure (5.7a), which shows the variation of the specific heat capacity with temperature for the three phases. Figure (5.7b) shows that crystallization is a first order transition with discontinuity in entropy at the melting point, in the glassy state it may be a second order phase transition, the change in the thermal properties occurs over a temperature interval rather than at single temperature.

The exact compositions of glasses can vary tremendously, although they must contain predominantly oxygen, silicon, boron, phosphor, etc.. In the above mentioned silicon-oxygen tetrahedra, silicon ions are called the glass forming ions while the oxygens are bridging atoms. Compounds such as Na_2O added to the glass structure break up the continuous silicon network by introducing non-bridging oxygen, figure (5.8), the sodium called network modifiers. Network formers allow the existence of rings, chains in three-dimensional network, while the modifier cation acts as a disturbing factor to these frameworks. It is useful sometimes to add a "network stabilizer" such as Aluminium or boron, to prevent crystallization after melting. "Refiners" such as Ce_2O_3 and As_2O_3 release oxygen during melting in order to eliminate gas bubbles and then to reabsorb the oxygen during the cooling.[85] It is worth mentioning that, while there is a strong largely covalent bonding between the silicon-oxygen tetrahedra, the modifying ions are held by rather weak ionic bonds with a number of oxygen ions. This explains the electrical conductivity in glasses consequent upon cation transport. The major role for the network modifiers is that they enable the paramagnetic ions to be incorporated in the glass matrix since it disturbs the tight bonding of the simple glass formers like SiO_2, P_2O_5 or B_2O_3 etc., especially for the accommodation of rare earths where the ions are quite large in size. For Cr^{3+} doped glass, these modifiers are particularly useful since the simple silicate glasses are usually in the form of tetrahedra, while Cr^{3+} ions prefer to occupy octahedrally coordinated sites.[89]

5.4 Chromium doped glasses

The early spectroscopic studies of Cr^{3+} doped glasses involved conventional absorption and luminescence measurements of different

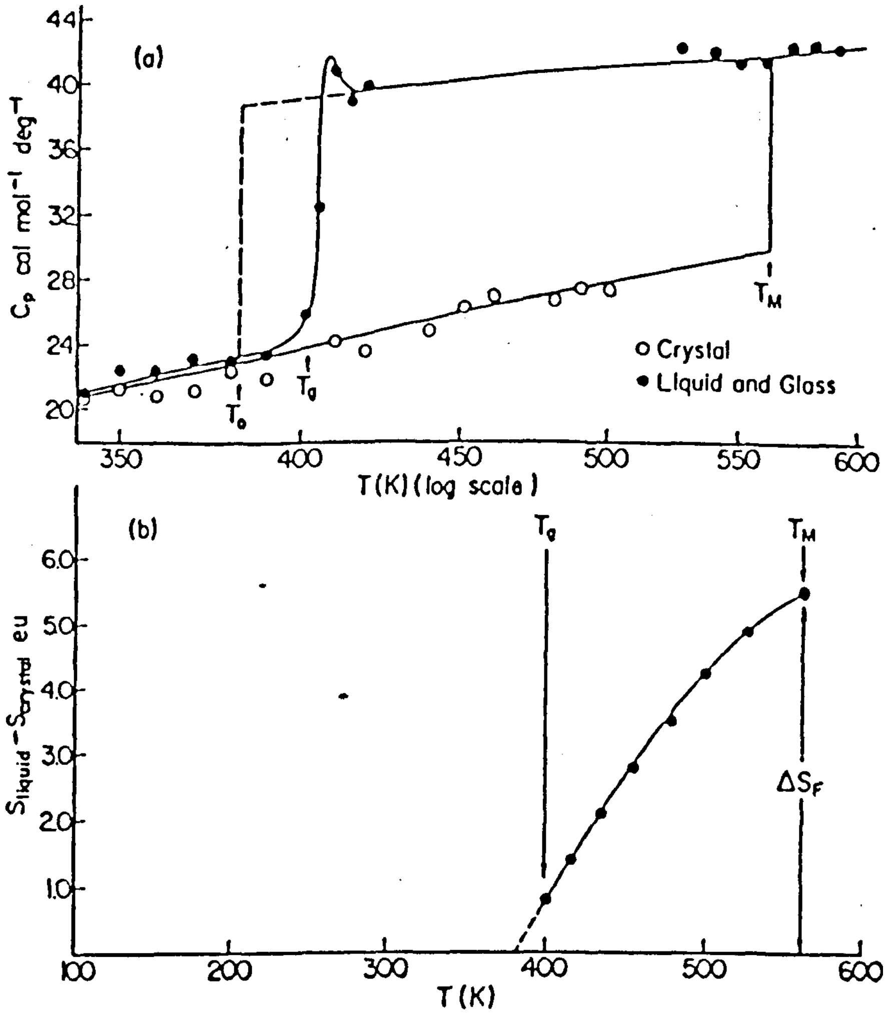

Fig 5.7 (a) Heat capacity of glassy, liquid and crystalline phases of lithium acetate plotted against the temperature.
(b) The difference in entropy between liquid and crystalline phases as a function of temperature.

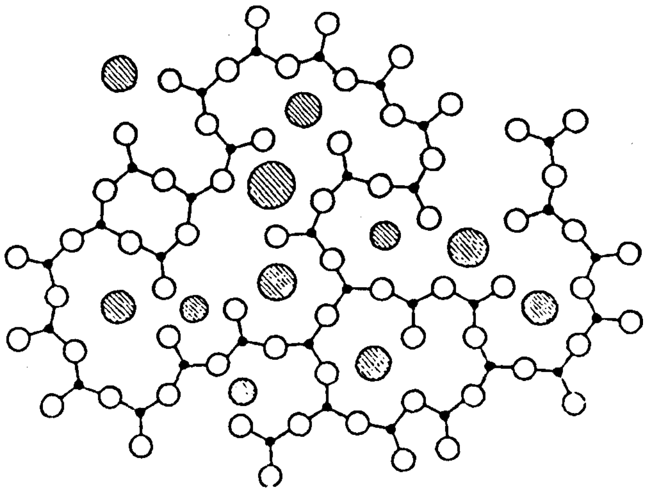

Fig 5.8 Schematic two-dimensional representation of the structure of a glass according to Biscol and Warren[86].

fixed temperatures. The interpretation of optical transitions within the Cr^{3+} doped glasses was suggested previously,[90] applying the well-known ligand field theory to the absorption spectra of the 3d ions doped glasses. This fundamental step towards understanding transitions of paramagnetic ions doped glasses came from correlations of the absorption spectra of these solids with the aqueous solutions as well as with the crystals themselves. By a comparison between crystalline and glass spectra Bates[90] was able to deduce the average coordination number of active ions. Also it was found that E/B values in glasses are ~ 5-10% lower than those of similar coordinates ions in crystals, which results in the shift of the absorption band peaks towards lower energies. Since the electronic transitions are determined primarily by the symmetry of the electrostatic field to which the T.M.I. is exposed, the spectral patterns found for the same ion in different hosts proved to be remarkably similar in shape, provided the arrangement of nearest neighbours is the same in each case. Thus the theoretical background of T.M.I. in crystals (as stated in chapter 1) and in solutions, all provide the basic material relevant for understanding glass spectra. Since the arrangement and chemical nature of the nearest neighbours determine the electric field acting on the d-orbitals of the Cr^{3+} ion, the energy splittings and the number of spectral lines can be predicted. However for T.M.I. the reverse sometimes is also possible, i.e. the nature and geometry of the nearest neighbour ions may be determined from the observed energies and intensities of the spectral bands it produces. The ability of a cation to coordinate with a negatively charged ligand increases greatly as the positive charge increases so unless their radii are very small, such ions are more likely to occur in octahedral coordination.[27] This situation is true for Cr^{3+} doped glasses[90] where the dopant ions occur in slightly distorted octahedral sites because the characteristic electronic structure of the $3d^3$ configuration gives the maximum stabilization energy in octahedral symmetry. Hence the Tanabe-Sugano diagram in figure (1.7) is appropriate for the Cr^{3+} doped glasses also. Fig (1.2) shows the Cr^{3+} doped glasses have sites with variable Dq/B values that cluster around the crossover point. Tischer[91] from studies of the effects of pressure and compositional changes on absorption spectra of different Cr^{3+} doped glasses, showed using aligand field description that the Cr^{3+} ions are located in octahedra of six oxygen ions, so confirming Bates earlier contention. A random distribution of Cr-0 distances was suggested consistent with only a small distortion from cubic symmetry. Electron paramagnetic resonance (EPR) has also been used to study Cr^{3+} doped inorganic glasses.[92,93] In these studies, spectra with effective g-values of ~ 2 and ~ 5-6 are always accompanied by strong optical absorptions spectra. The high magnetic field signal (g ~ 2) was assigned[93] to Cr^{6+} ions existing as ion pairs corresponding to the optical absorption peak at ~ 370nm. This signal did not appear in the presence of a reducing agent. The EPR signal at the low magnetic field (g ~ 5-6) was assigned to isolated Cr^{3+} ions.[92]

The dynamical behaviours (vibrations of the atoms about their equilibrium positions) for crystals and glasses could be discussed in terms of the vibrational density of state (VDS). In the Debye approximation for crystals, the density of vibrational states has the form $\rho(\omega) = 9(N/\omega_D^3)\omega^2$, where ω_D is the Debye cut-off frequency associated with a characteristic temperature of the crystal (θ_D). For glasses, the disorder of the atomic arrangement limits the vibrational wavelength to the same order as the interatomic spacing and it is not possible to represent glass vibrations by plane waves. For example, the specific heat variation with temperature in Debye's theory $C_V \propto T^3$. At low temperatures it is expected that as the phonon mean free path, and hence the vibrational wavelength increases, the disorder in the glass will be of no further importance. The thermal properties of glasses should be the same as those of crystals. Unfortunately this is not the case.[94] Figure (5.9a,b) shows that the temperature dependence of the specific heat and thermal conductivity of vitreous silica is different to that of crystalline SiO_2 (Quartz). Hence the specific heat temperature dependence for the glass is expressed:[95]

$$C_V = aT + bT^3$$

Also it can be seen from the figure that the thermal conductivity decreases monotonically with decreasing temperature, in contrast to the peaked behaviour characteristics of crystalline quartz. A considerable theoretical effort has been expended in understanding these behaviours.[96] The most successful account of such anomalies is expressed in the tunnelling model or two level system (TLS) in which atoms or groups of atoms vibrate in a double well potential with two configurational minima close to each other in energy as shown in figure (5.10), so that the atoms can tunnel between the two potential wells. These low energy excitations (10^{-5} ev $< E <$ 10^{-4} ev)[95] can give rise to the abnormal specific heat as well as acting as scattering centres for acoustic phonons, hence deciding the value of the mean free path, and then the thermal conductivity. This double well is characterised by Δ, the assymetry energy, the barrier height being denoted by V_0. Although the model successfully accounts for the abovementioned anomalies, its microscopic origin is not well understood. However the flipping between metastable states of low coordination oxygen atoms in Si-O-Si structure, or rigid rotations of SiO_4 tetrahedra from one position to another are possible mechanisms.[95]

The vibrational sideband which accompanies a zero-phonon transition should mimic the density of phonon states of the material. This feature was used in a comparison with the polarized Raman spectra of ED-2 glass doped with Cr^{3+}[50] to assess the effect of the strong vibronic interaction in such systems.

Taking into consideration static and dynamic effects of ligand fields in glasses, the luminescence of Cr^{3+} doped glasses mainly

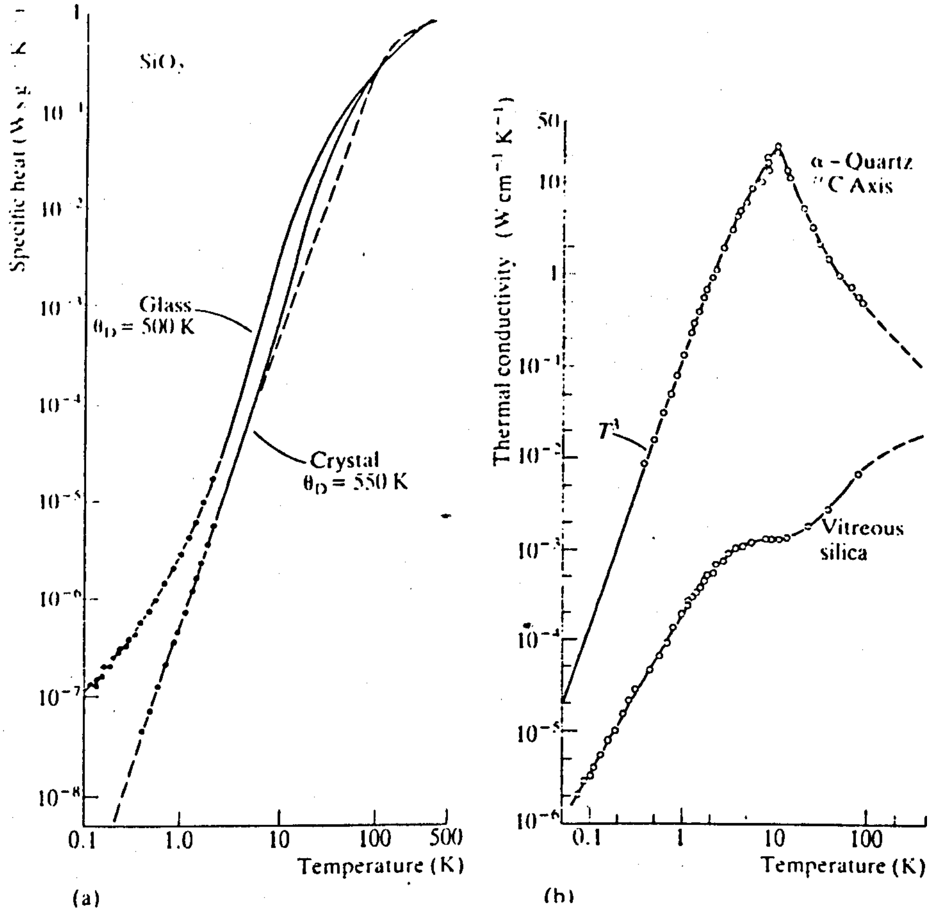

Fig 5.9 Comparison of (a) the specific heat and (b) the thermal conductivity of amorphous and crystalline SiO_2[50].

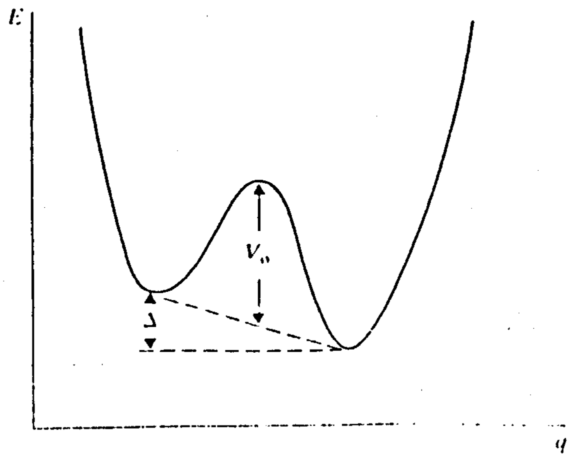

Fig 5.10 Schematic illustration of the double well potential characterizing a two level system plotted as a function of configuration coordinate (q), Δ is the asymmetry energy and V_o is the barrier height.

consist of the broadband $^4T_2 \rightarrow {}^4A_2$ emission from Cr^{3+} in weak field sites and a weaker and sharper $^2E \rightarrow {}^4A_2$ band from Cr^{3+} ion occupying strong field sites. The optical properties of impurity ions in glasses are similar to those of crystals. Yet transitions in glasses are modified by the glass disorder. For comparison, we take the example of Cr^{3+} ions in $Gd_3Sc_2Ga_3O_{12}$ and a silicate glass (figure 5.11). The emission spectrum in both materials is due to both ^2E and $^4T_2$ transitions. The sharp features shown for GSGG crystal resulted from the crystal field splitting. Such features in the glass are masked by the inhomogeneous broadening of the ^2E and $^4T_2$ - $^4A_2$ transitions caused by the effects of the glass structure. Essentially, Cr^{3+} ions occupy a large variety of different sites, hence while each ion will have a sharp transition frequency, this frequency varies from site to site, and the broad band is a composite of emissions at the different frequencies.

The broad band absorptions and emissions offer a choice of pumping schemes for such glasses, and suggest potential for use as vibronic lasers. However luminescence in such glasses is characterised by a low quantum efficiency compared to crystals. This led to the development of glass ceramics as alternatives to Cr^{3+} glasses. These materials have glassy matrices in which small crystallites embedded. This technique is found to improve the quantum efficiency by ~ 50%.

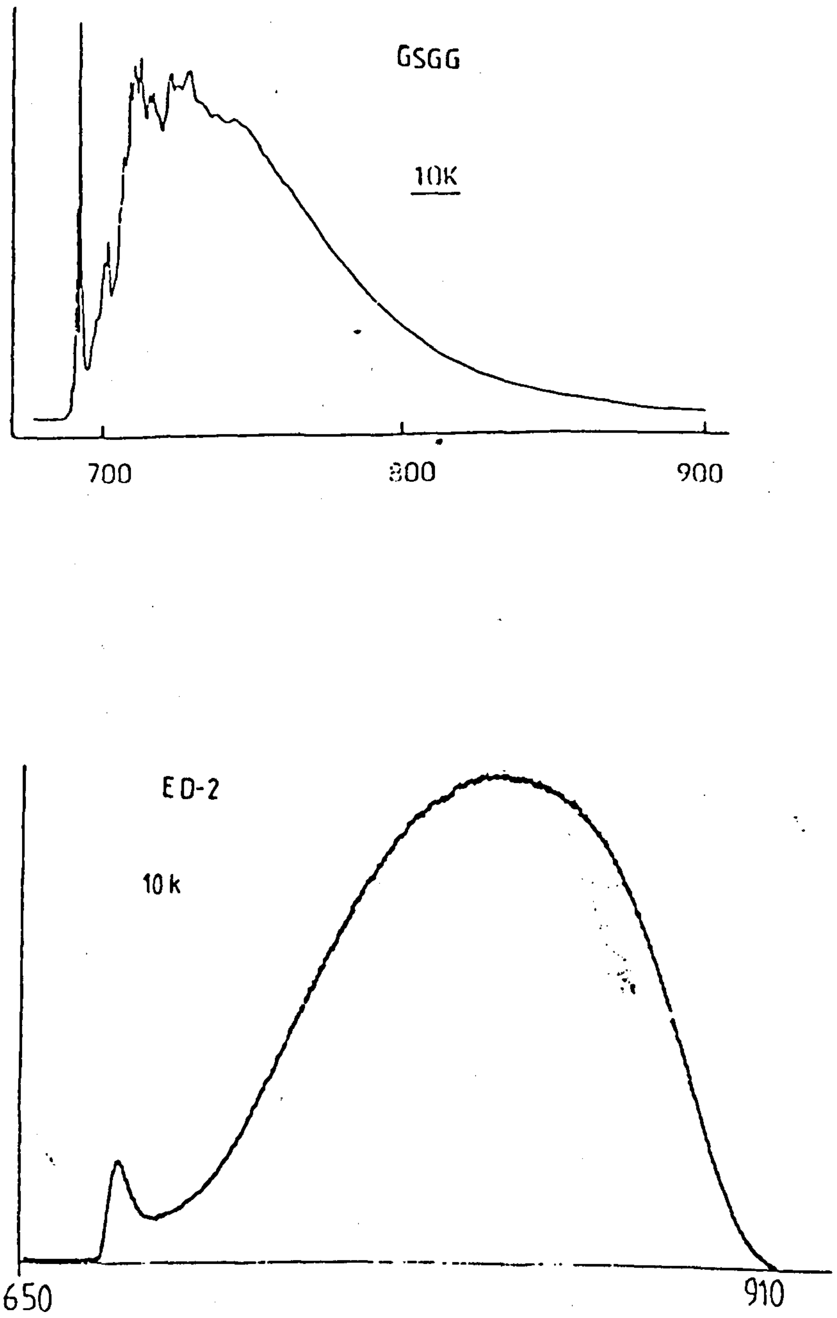

Fig 5.11 Comparison between the luminescence spectra of Cr^{3+}:GSGG crystal and Cr^{3+}:ED_2 glass showing the inhomogeneously broadened ^2E and $^4T_2$ transitions in the latter.

5.5 Experimental Samples

Different types of glass hosts (silicate, borate, phosphate, fluoride and tellurite) containing Cr^{3+} were used with the compositions shown in table (5.1). The first six samples in the table were provided by Dr S T Stokowski of Lawrence Livermore Laboratories, U S A. Another three silicate glasses with different modifiers (SLS7b/7 and SLS7b/4) were supplied by Sheffield University via RSRE (Malvern, UK), the ED-2 is a commercial sample. High resolution spectroscopy was also carried out on a fluorozirconate glass, provided by Dr D Hollis of Sheffield University. The fluorescence samples were typically 1 x 2 x 5 mm^3 in dimension, absorption samples were 5 x 1 x 7 mm^3. The samples were cut and polished by Mr R W B Dawson. Borate glasses contained B_2O_3 which is hygroscopic, preventing the use of water based polishing media. Samples were fixed to the sample holder in the cryostat in the closed cycle refrigerator using a silver loaded epoxy resin, or a Ge-varnish for good thermal contact to the sample. Also because of the low thermal conductivity of glasses as low pumping power as commensurate with required emission was used to reduce thermal gradient between the exciting point and other parts of the sample.

Table 5.1 Compositions of Cr^{3+} doped glasses

	Type of glass	Sample number	Compositions (wt %) (unless stated)	Cr^{3+} concentration (Cr_2O_3) %
Lawrence Livermore Lab. Samples	Lithium-borate	G8382	727B_2O_3, 24.2 Li_2O, 3.0 MgO	0.1
	K-borate	G8150	59.2 B_2O_3, 40.3 K_2O	0.5
	Tellurite	G8298	79.95 TeO_2, 20 Na_2O	0.05
	Fluoride	G8197	23 SrF_2, 12 BaF_2, 19 ALF_3, 13 LiF, 7 MgF_2, 17CaF_2 6.95 $Al(po_3)_3$, 2Al_2O_3	0.05
	Phosphate	G8222	74.1, P_2O_5, 8.3 ZnO, 7.6 Li_2O, 4.6 CaO, 3.7 Al_2O_3	0.09
	Silicate	G8035	68.4, SiO_2, 15.7 Li_2O, 10.7 CaO, 4.9 Al_2O_3	0.4
RSRE Samples	Silicate	SLS7b/7	(77.5 SiO_2, 24.1 K_2CO_3, 4.3 KNO_3, 2.84 H_3BO_4, 49.8 Red lead) mol %	0.106
	Silicate	SLS7b/4	(77.4 SiO_2, 32.2 Na_2CO_3, 12.6 $NaNo_3$, 17.4 $CaCo_3$) mol %	0.11
	Silicate	ED-2	(60 SiO_2, 27.5 Li_2O, 10 CaO, 2.5 Al_2O_3, 0.16 CeO_2) mol %	0.05
Sheffield Univ.	Fluoro-Zirconate		(5.0 ZrF_4, 20 BaF_2, 20 NaF, 5.5 LaF_3, 4.5 ALF_3) mol %	Not exactly known

5.6 Absorption Measurements

The optical absorption spectra of Cr^{3+} doped silicate, phosphate, fluoride and tellurite glasses are shown in figure (5.12). Another two silicate glass spectra (ED-2 and SLS7b/7) were measured by Dr P N Gibson in Ispra, Italy (see figure (5.13)). The predominant features of these spectra are two broad vibronic bands, $^4T_1(F)$ and $^4T_2$ at high and low energy sides of the spectrum, respectively. Two sharper peaks which overlap the $^4T_2$ broad band are due to transitions from the $^2T_1$ and ^2E states. Little difference is observed in the absorption spectra at 77K. These measurements accord with earlier measurements.[91,97] These bands are attributed entirely to Cr^{3+} ions, no evidence of Cr^{6+} ions was detected in those glasses, except for the ED-2 glass where a strong charge transfer band is observed at ~ 360nm in figure (5.13a). Since Cr^{6+} absorbs in the u.v. below 400nm, excitation of the Cr^{3+} ions alone requires that visible sources are used to pump the photoluminescence, Andrews et al.[97] have reported an additional broad band at 300nm attributed to the higher lying $^4T_1(p)$ band. We did not examine this band because the response of our detection system is restricted in this range, accounting also for the asymmetric shape at the high energy side of the spectra in fig (5.12). Nevertheless with such spectra, it is possible to identify the Cr^{3+} ion as situated in an octahedral arrangement of oxygen ions. No line splittings were identified which would have been due to lower symmetry distortion. Such low symmetry features are

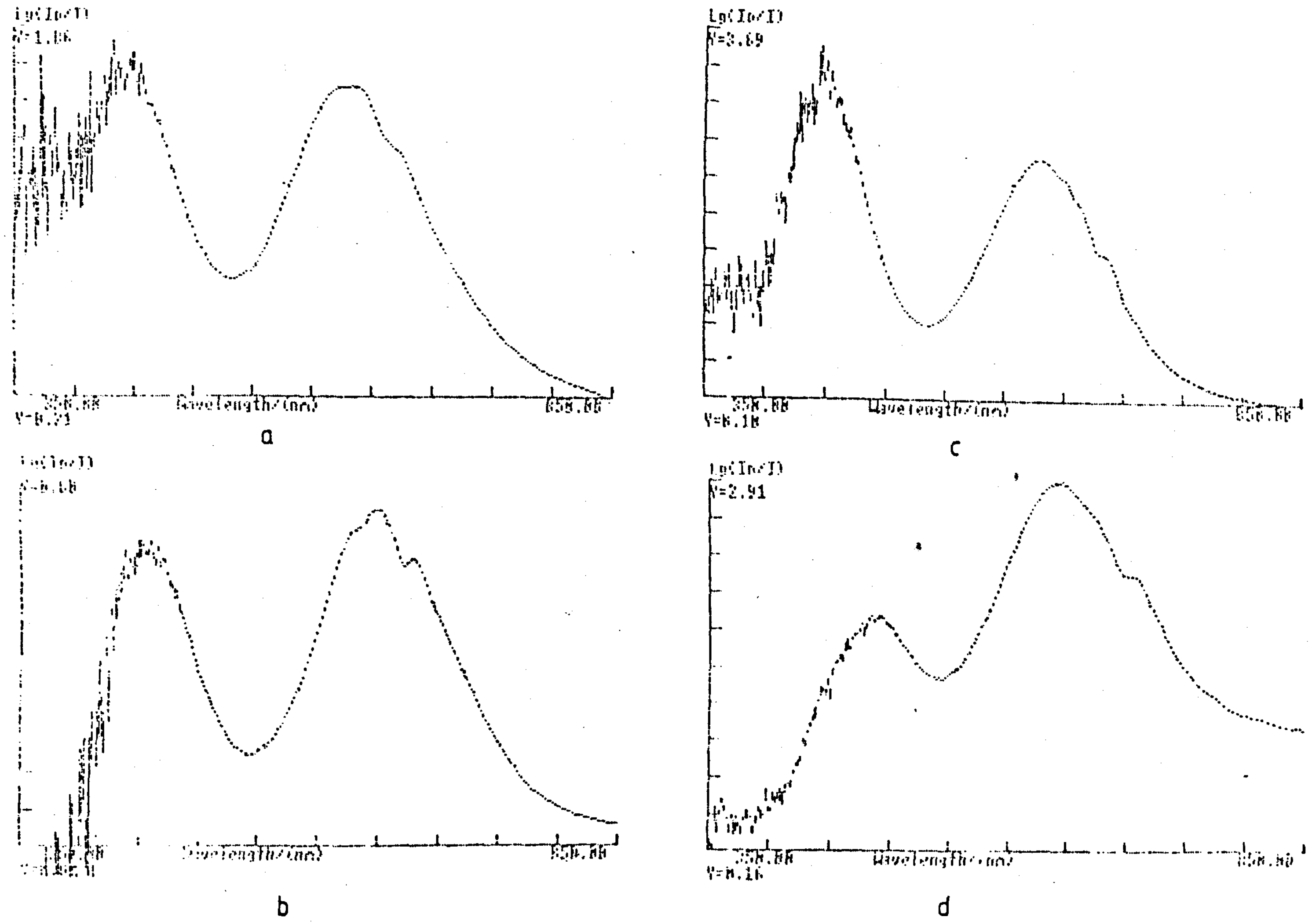

Fig 5.12 Absorption spectra at room temperature for (a) G8197, (b) G8222, (c) G8035, (d) G8298, the diffused part at the high energy side of the spectrum is due to the poor response of the detector.

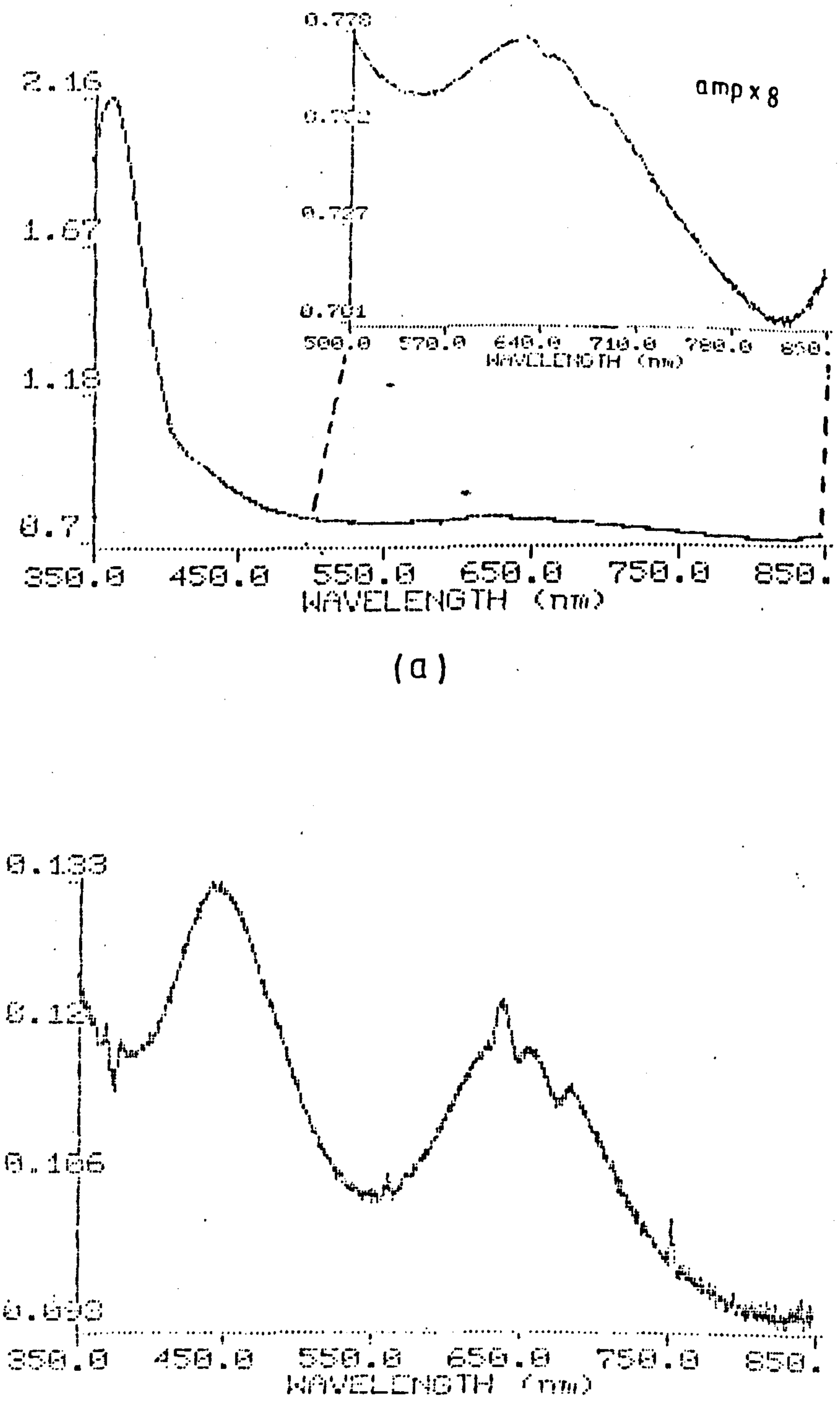

Fig 5.13 Absorption spectrum for
(a) Cr^{3+}:ED-2 silicate glass
(b) SLS 7b/4 silicate glass.

not possible to observe in Cr^{3+} doped glasses because of the extensive inhomogeneous broadening. Energies of the absorption bands for the various glasses are shown in table (5.2). The two Racah parameters B and C were calculated from the spectra in the following way, the theoretical calculations of Tanabe and Sugano[28] evaluate the matrix elements of the charge interaction using the strong field approach. For Cr^{3+} (refer to figure (1.7)), the free ion ^4F state splits in an octahedral field into $^4A_2$ state with the energy -15B and a $^4T_2$ state with the energy -15B + 10Dq: these energy values resulting from the diagonal matrix elements. The energy difference between these two states, the octahedral crystal field splitting of 10Dq. Locating the ground state $^4A_2$ at the zero in energy, the absorption peak of the $^4A_2 \rightarrow {}^4T_2$ band is at 10 Dq, and the value of Dq were measured directly from the position of the $^4T_2$ level. The value of B is determined by diagonalizing a 2 x 2 matrix which depends on both Dq and B. This procedure results in the formula:[36]

$$B/Dq = \frac{(\Delta E/Dq)^2 - 10(\Delta E/Dq)}{15(\Delta E/Dq-8)} \qquad (5.4)$$

where ΔE is the energy difference between the $^4T_1$ and $^4T_2$ levels which can be measured directly from the absorption spectra. Alternatively,

$$B = \frac{1}{3}(20Dq-v_2)(v_2-10Dq)/(90Dq-5v_2) \qquad (5.5)$$

Table 5.2 Absorption spectra values for Cr^{3+}:glasses

(Band position values are in cm^{-1})

Glass	^2E	$^2T_1$	$^4T_2$	$^4T_1$	B	Dq/B	C
SLS7b/7	14616	15697	15552	22727	758.5	2.05	2608.9
ED-2	14598	15389	15904	22989	739.7	2.15	3075.5
SLS7b/4	14616	15683	15106	22222	763.1	1.98	2585
Fluoride (G8197)	14859	15528	15385	23041	849.7	1.81	2947.7
Silicate (G8035)	14641	15898	15723	22779	741.5	2.12	3085.4
Phosphate (G8222)	14663	15873	15267	22371	755.8	2.02	3072.9
Tellurite (G8298)	14124	14925	15456	21739	633.6	2.44	3143

where v_2 is the energy value of the $^4T_1$ state which is the only value needed to evaluate B (since Dq is known from the previous stage).[12] The value of the C parameter is calculated by considering either of the two sharp doublets ^2E or $^2T_1$ of which ^2E is easier to identify with high precision. The energy value of the ^2E level is obtained theoretically by diagonalizing the 4 x 4 matrix and taking the lowest energy eigenvalues. In this case the energy value of the ^2E state is dependent on Dq, B and C. Hence the following equation can be used to evaluate C:[36]

$$E(^2E)/B = 3.05(C/B) + 7.9 - 1.8\,(B/Dq) \tag{5.6}$$

where Dq/B and C/B should be in the ranges (1.5 - 3.5) and (3 - 5) respectively. It should be mentioned that in measuring these Dq, B and C values, lower symmetries other than the octahedral symmetry were not taken into account. Hence these energy level values are only approximate. Nevertheless the Dq/B and C/B values may be used as an indication of the crystal field strength. From the positions of the Dq/B in the E/B vs Dq/B diagram, crystals of high field symmetry such as Cr:YAG have the value of Dq/B = 2.6, so that at low temperature emission is predominantly from the ^2E state situated below the $^4T_2$ level. In Cr^{3+}:GSGG and Cr^{3+}:GSAG crystals the Dq/B values are 2.38 and 2.46 respectively which categorize them as an intermediate between high and low field where both ^2E and the $^4T_2$ transitions are detected at low temperature. For the Cr^{3+}:Glasses, the Dq/B are mostly in the range of ~ 2 or less, so it is expected that the majority of Cr^{3+} ions are located at low field sites. This is confirmed by the predominant emission of the $^4T_2 \rightarrow {}^4A_2$ transition being much more intense than the $^2E \rightarrow {}^4A_2$ emission we now discuss.

5.7 Photoluminescence Studies of Cr^{3+} Glasses

5.7.1 Steady state luminescence

The emission spectra of three different (borate, silicate and phosphate) glasses are shown in figure (5.14). The sharp decrease in the intensity at the high wavelength side of the spectrum is due to the cut-off in the spectral response of the PMT. This illustrates the need for detection of the emission spectra of the Cr^{3+} glass samples using the Ge-detector. Such spectra measured at 10K and 300K and corrected for the spectral response of the system are shown in figure 5.15, 5.16 and 5.17. For K-borate, ED-2 silicate and fluorozirconate glasses, respectively. These spectra clearly show that $^4T_2 \rightarrow {}^4A_2$ transition to be dominant in these spectra. The narrower feature on the high energy side of some spectra is identified as the $^2E \rightarrow {}^4A_2$ transition. The coincidence of this transition with the sharp feature at ~ 685nm in absorption confirms the assignment of this emission to the $^2E \rightarrow {}^4A_2$ transition. However the variable relative intensities of the $^4T_2$ and the ^2E features reveal the existence of a wide range of different crystal field sites. No significant ^2E emission is seen

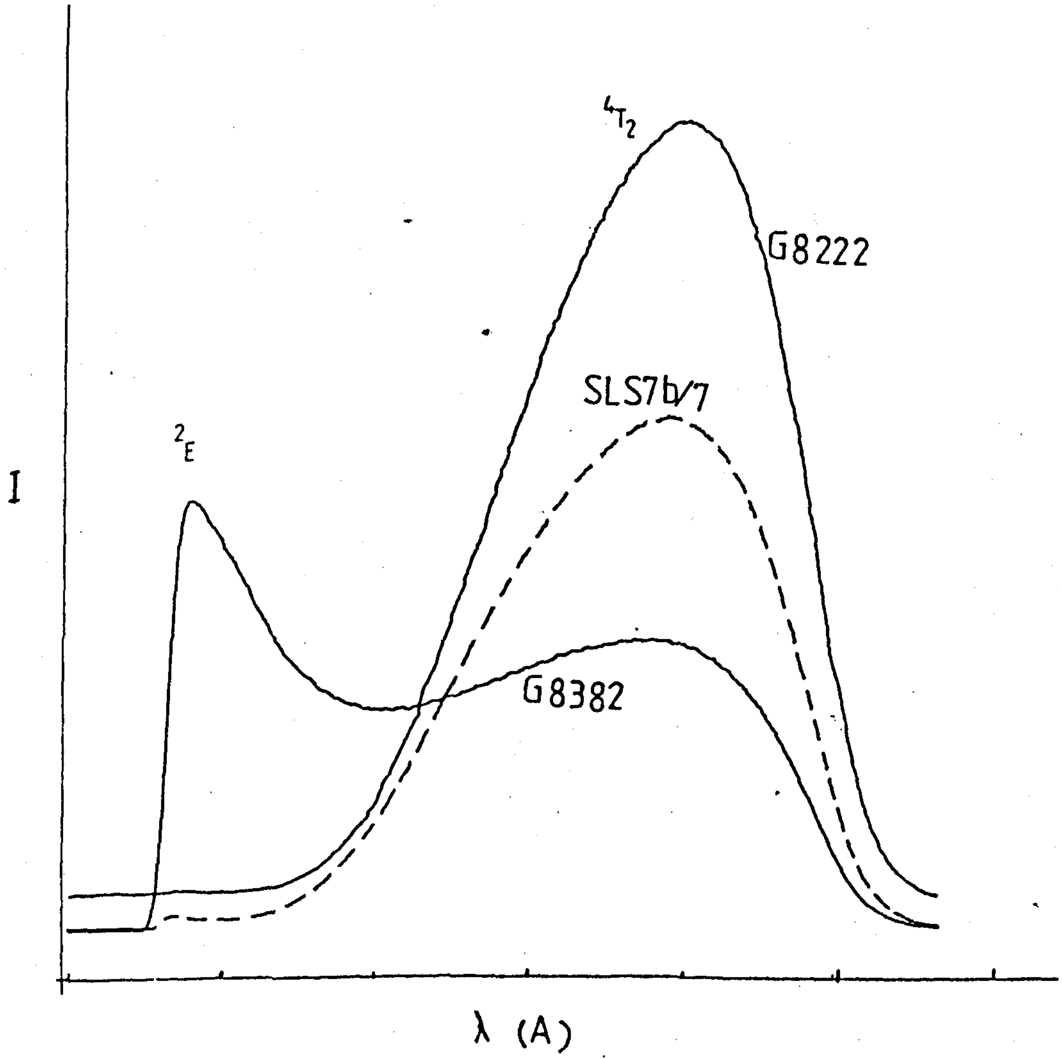

Fig 5.14 Emission spectra of different Cr^{3+} doped glasses at 10K. The ^2E and $^4T_2$ emission components can be seen in different proportions (the sharp decrease in the intensity at the long wavelength side is due to the P.M.T. response).

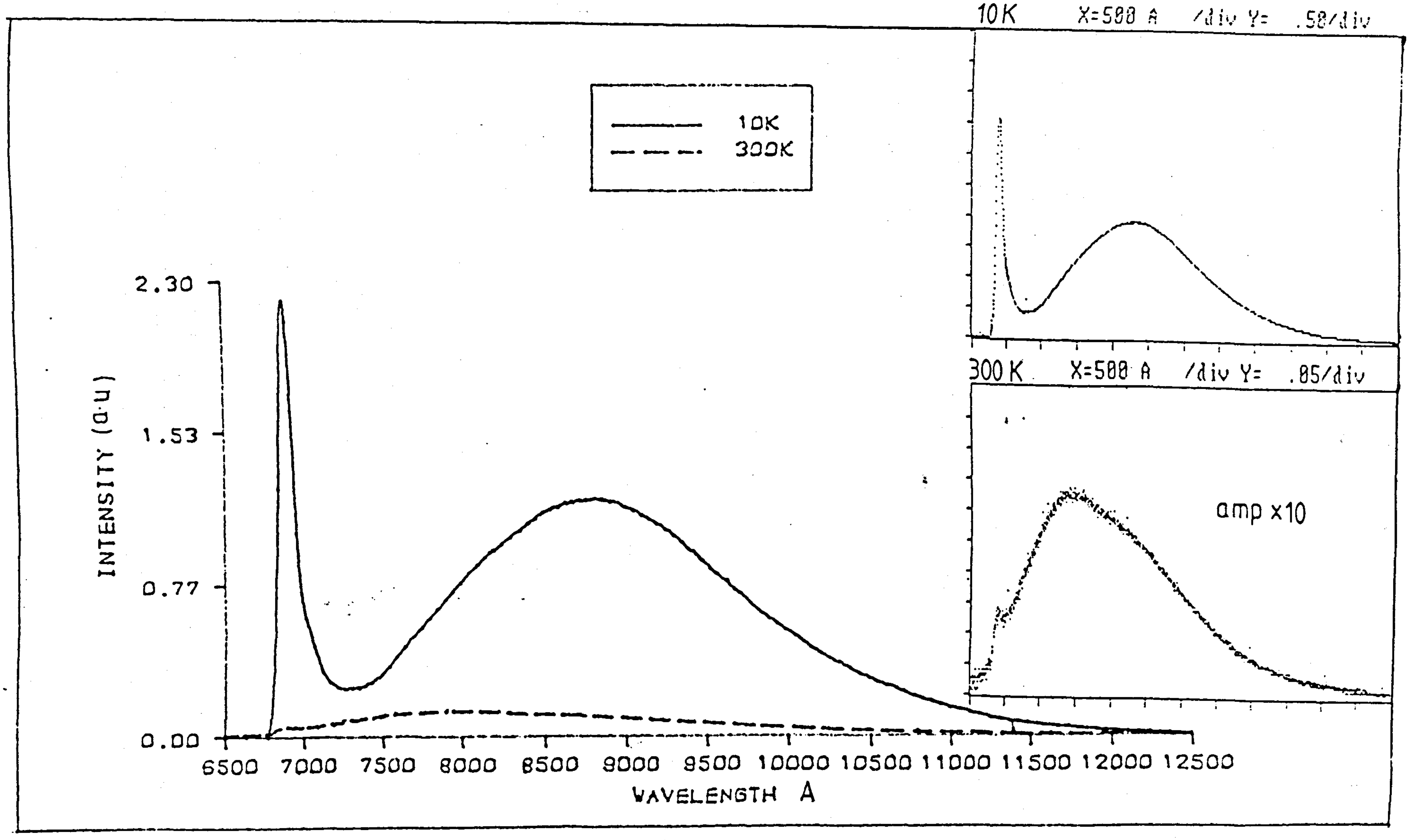

Fig 5.15 Luminescence of K-borate glass at 10K and 300K.

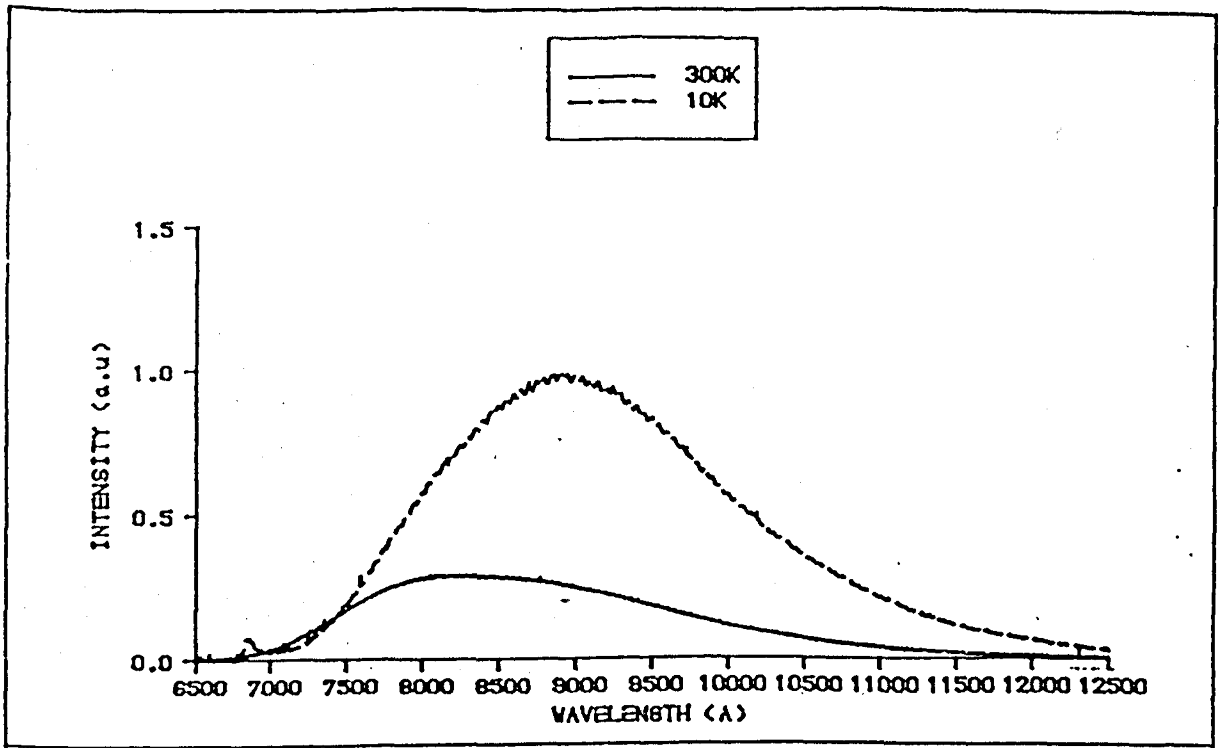

Fig(5.16) ED2 GLASS EMISSION AT 10K AND 300K

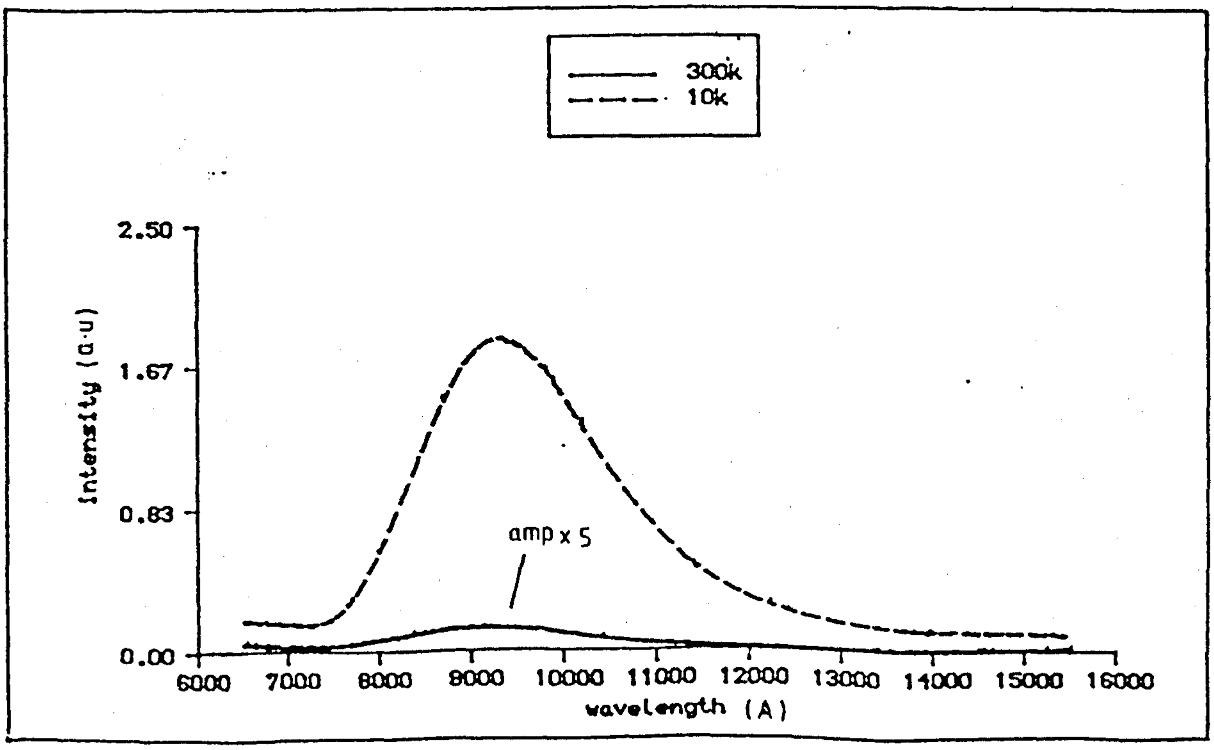

Fig 5.17 Fluorozirconate glass emission at 10 and 300K.

in fluorozirconate (Figure 5.17) or fluoride glasses, only a trace of ^2E emission is found in the phosphate glass. The dominance of the $^4T_2$ emission shows that the majority of Cr^{3+} ions occupy low field sites, where the $^4T_2$ level is below the ^2E level. The value of Dq/B gives an indication of the type of sites located in the glass matrix. Referring to table (5.2), it is clear that the crystal field strength varies as the tellurite has the highest Dq/B value which yields the higher crystal field splitting, the silicates have lower values, followed by the phosphates and fluorides. The latter have the lowest value of Dq/B. Although we have not determined Dq/B for the borate glasses, their values ($Dq/B \simeq 2.25$) have been measured elsewhere[97] and determined to be higher than those of the silicates. However, results from the absorptin spectra were verified by these luminescence measurements, where due to the predominantly high field sites, the ^2E emission is strong in the borate glass than in ED-2 silicate glass. The position of the ^2E emission is detected <u>ca</u> 683-688nm in most glasses, the $^2E \rightarrow {}^4A_2$ level being not much affected by the perturbing ligands. The ^2E emission for the tellurite glass (figure (5.18)) peaks at ~ 708 nm, coinciding with the peak wavelength in the absorption spectrum, similar value reported by Andrews et al.[97] A variety of values are observed for the $^4T_2$ peak position depending on the temperature of the sample and the excitation wavelength of the pumping laser. In these measurements on glasses the $^4T_2$ peak ranges between λ = 850-980nm.

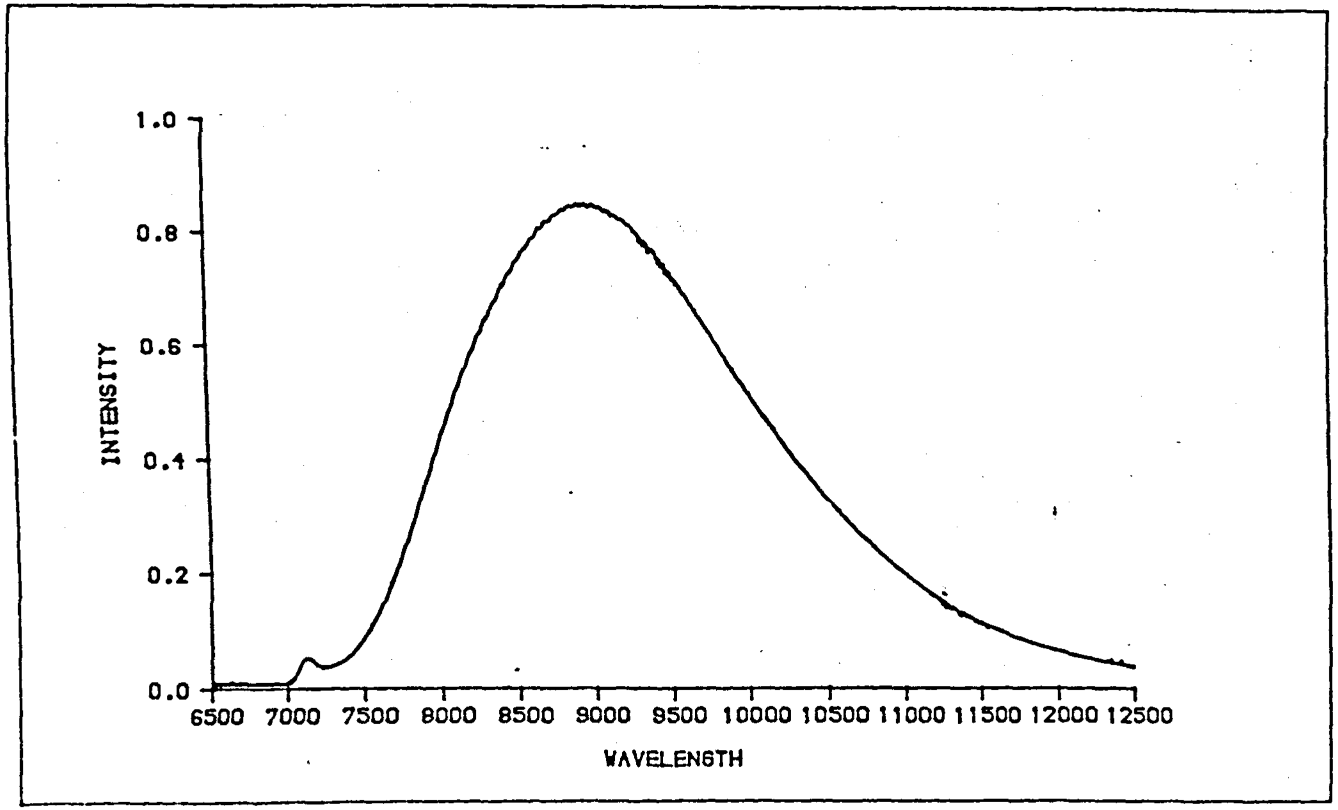

Fig 5.18 Luminescence spectrum of (G8298) Tellurite glass at 10K.

The temperature dependence of the luminescence intensity for the Li-borate glass (G8382 sample) is shown in figure (5.19). A separate measurement at high temperature (~ 340 K) showed even broader and weaker emission (figure 5.20). Values for the centroid (M_1), also the integrated intensity (M_0) and the bandwidth (M_2) are plotted against temperature in figures (5.21 and 5.22). The strong dependence on temperature of the luminescence intensity of the activated glass is likely to be an impediment against potential laser action of these materials. The band shape of the Li-borate glass emission at temperatures between 10 and 299K (figure 5.23) shows that the ^2E emission component broader than in any of the other glasses examined (silicate, K-borate and tellurite). Also another broad peak begins to develop at ~75K and becomes even more intense than the original $^4T_2$ peak. In view of the different component lifetimes of the various features, we decided to separate the ^2E band from the broad bands, using time resolved spectroscopy, such experiments are described in section 5.8. The sharp line at ~ 975nm accompanied by a lower energy side band is due to an optically active impurity occurred most probably due to neodymium impurity.

5.7.2 Site selective excitation and decay rates

In some glasses the emission spectrum shapes change with excitation wavelength; the examples in figure (5.24) are for the ED-2 silicate glass. These different lineshapes are also due to the site

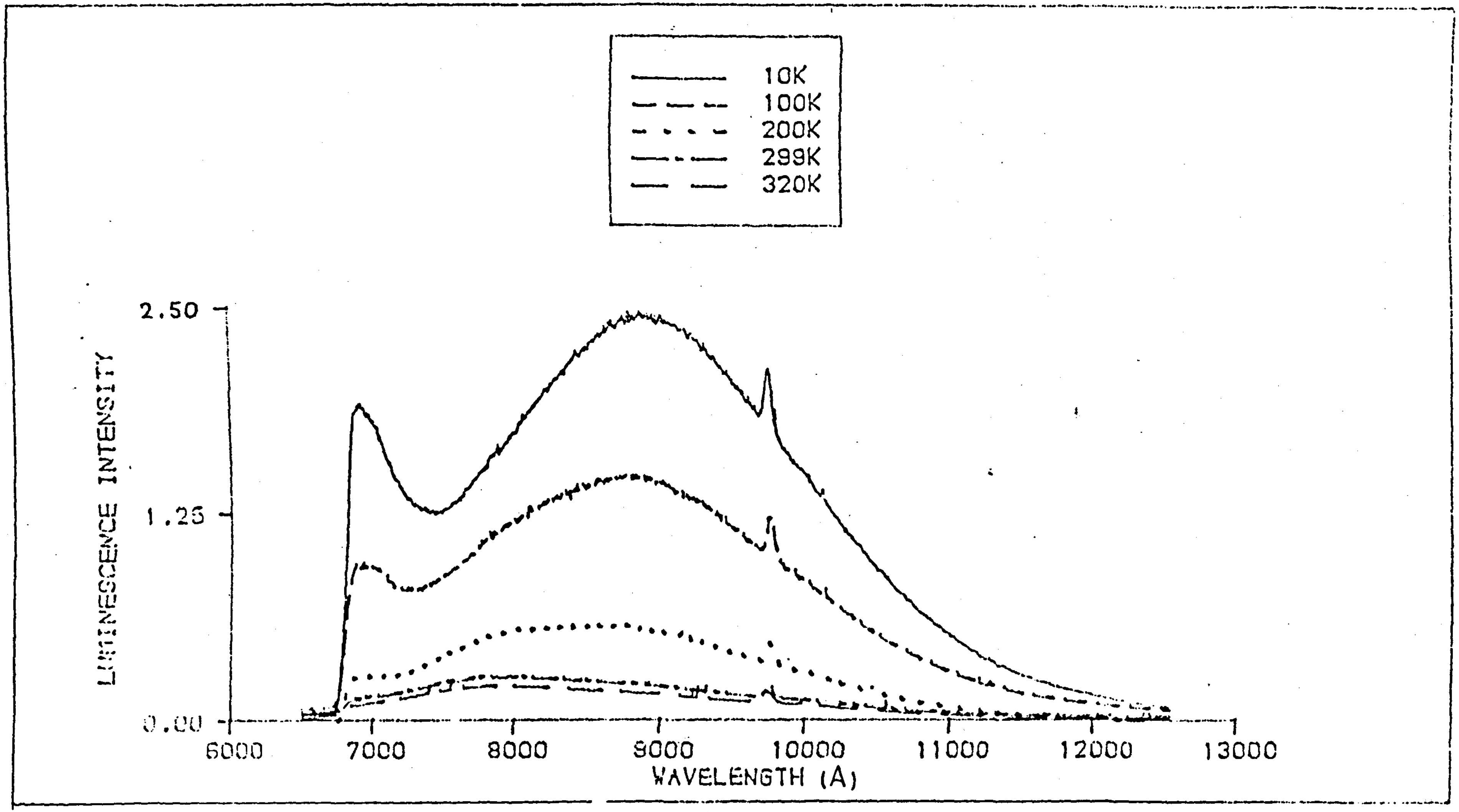

Fig 5.19 Emission spectra of (G8382) Li-borate glass at different temperatures.

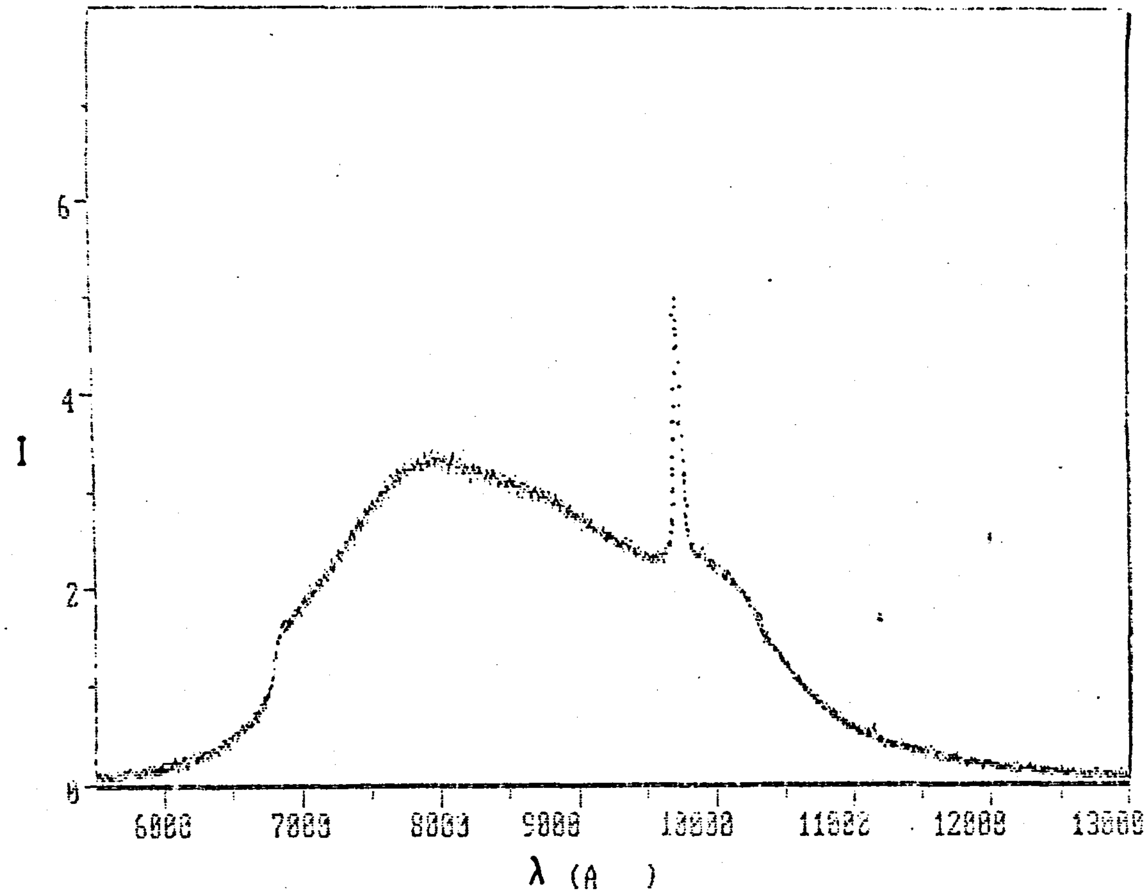

Fig 5.20 High temperature emission spectrum of G8382 showing very broad $^4T_2$ and ^2E bands, the impurity feature at ~ 975nm can be seen clearly because of the low $^4T_2$ intensity.

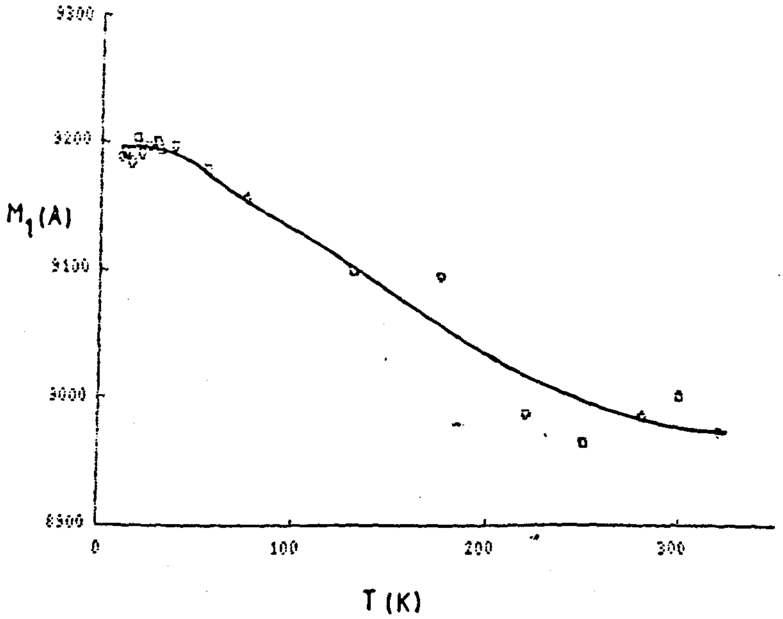

Fig 5.21 The variation of the centroid position with the sample temperature of the G8382 glass.

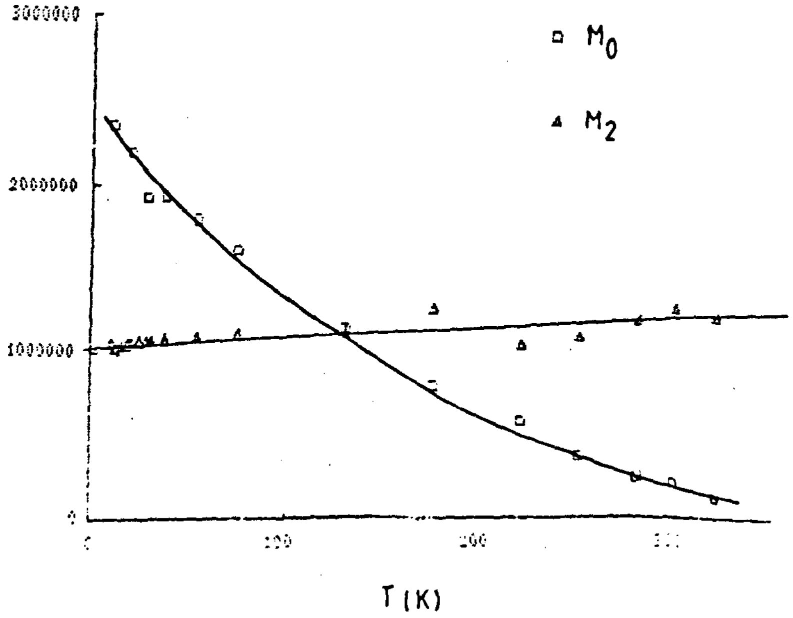

Fig 5.22 Temperature dependence integrated intensity and bandwidth for the G8382 glass.

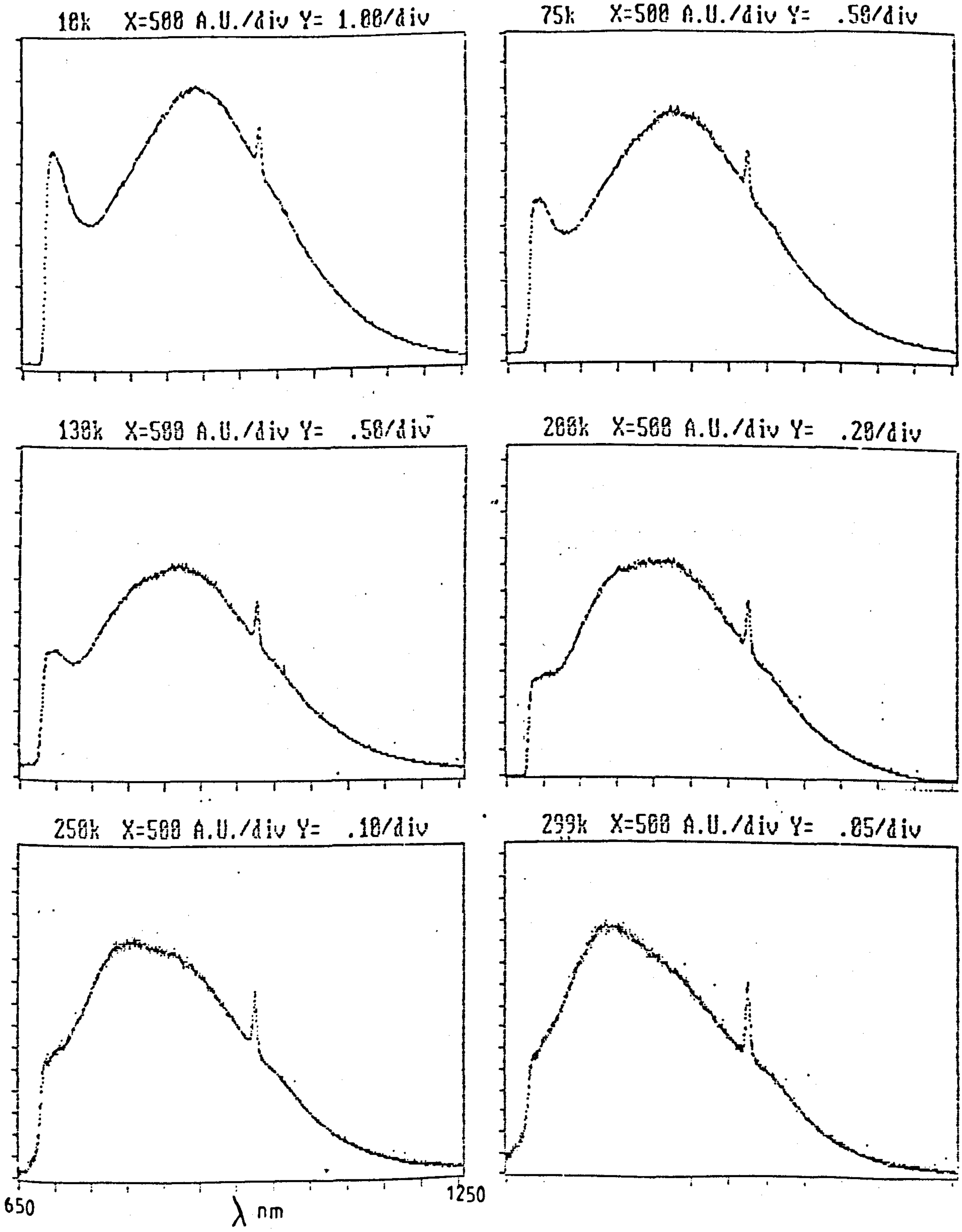

Fig 5.23 Luminescence of Li-borate glass at different temperatures.

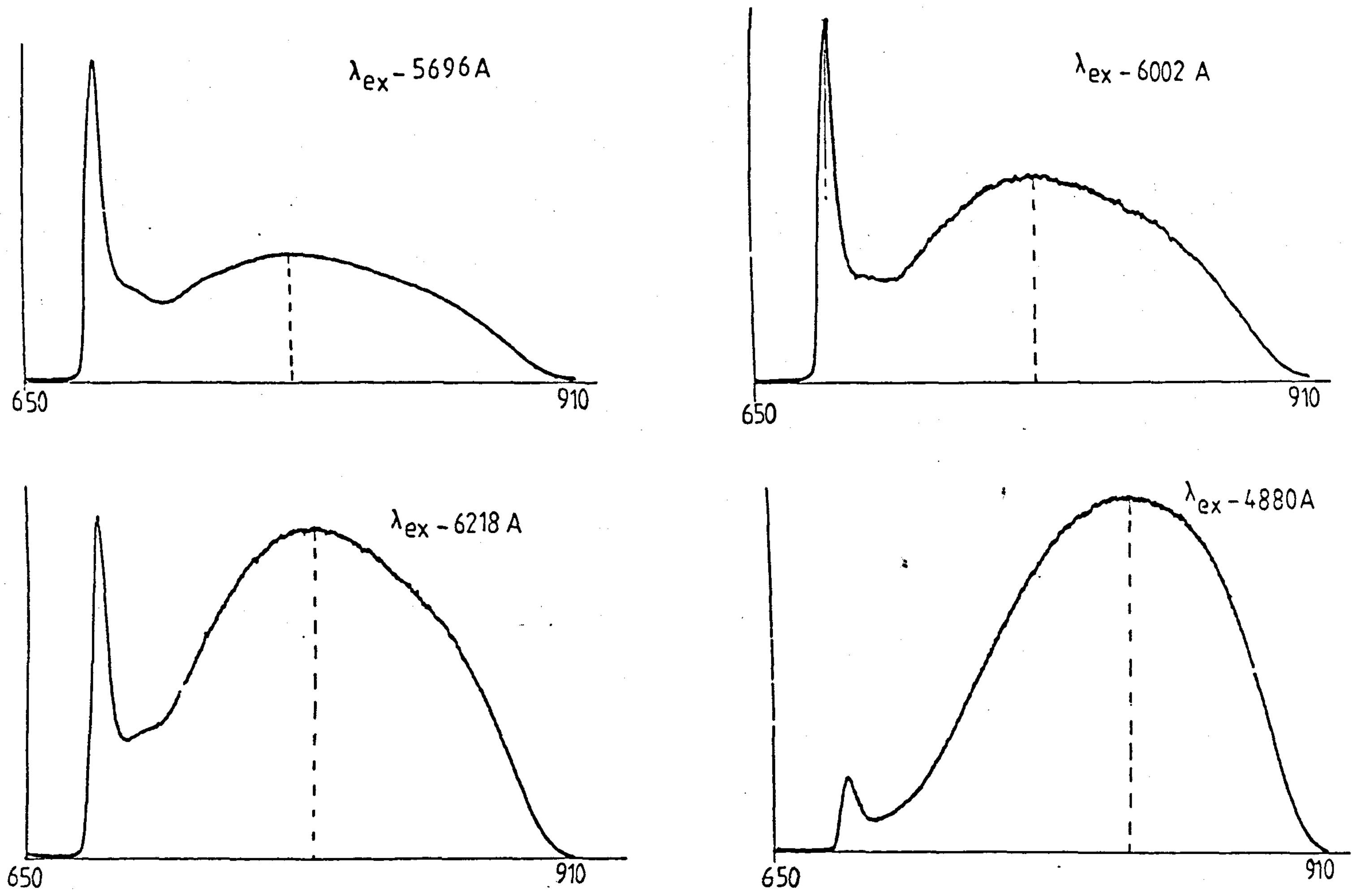

Fig 5.24 Emission spectra of ED-2 glass at 77K using different excitation wavelengths.

multiplicity in such glasses. Considering the $^4T_2$ broad band, we observe that the peak shifts towards longer wavelengths as the excitation wavelength gets longer. The exception is for the 488nm excitation, where the peak shift is towards even longer wavelengths. This is due to the 488 line excites the tail of the $^4T_1$ band rather than the $^4T_2$ as in the other cases, and hence its emission is Stokes' shifted towards a longer wavelength. Otherwise the shift in peak positions with excitation wavelength in $^4T_2$ band excites different amounts of ions in the different sites. Pumping with the shortest wavelength line means higher probability of exciting both low and high field sites. Exciting with longer wavelength radiation results in exciting mainly the low field sites with an enhanced intensity of emission at longer wavelengths. Similar behaviours were measured in other glasses. The variation in $^4T_2$ peak position and the ratio of the integrated intensity of the ^2E and the $^4T_2$ components for the K-borate (G8150) are plotted against excitation wavelengths in figure (5.25). Finally the shift of the Cr^{3+} emission for the fluorozirconate glass at 10K excited with the infra-red radiation from a diode laser at 783nm compared with the spectrum excited by a red laser line at 628nm is seen in figure (5.26). The very clear shift in the emission spectrum is typical of the very broad $^4T_2 \rightarrow {}^4A_2$ band (FWHM ~ 4600 cm^{-1}).

Because of the multicomponent decay processes in these inhomogeneously broadened spectra, measurements of emission lifetimes using phase-sensitive detection techniques are unreliable. Indeed

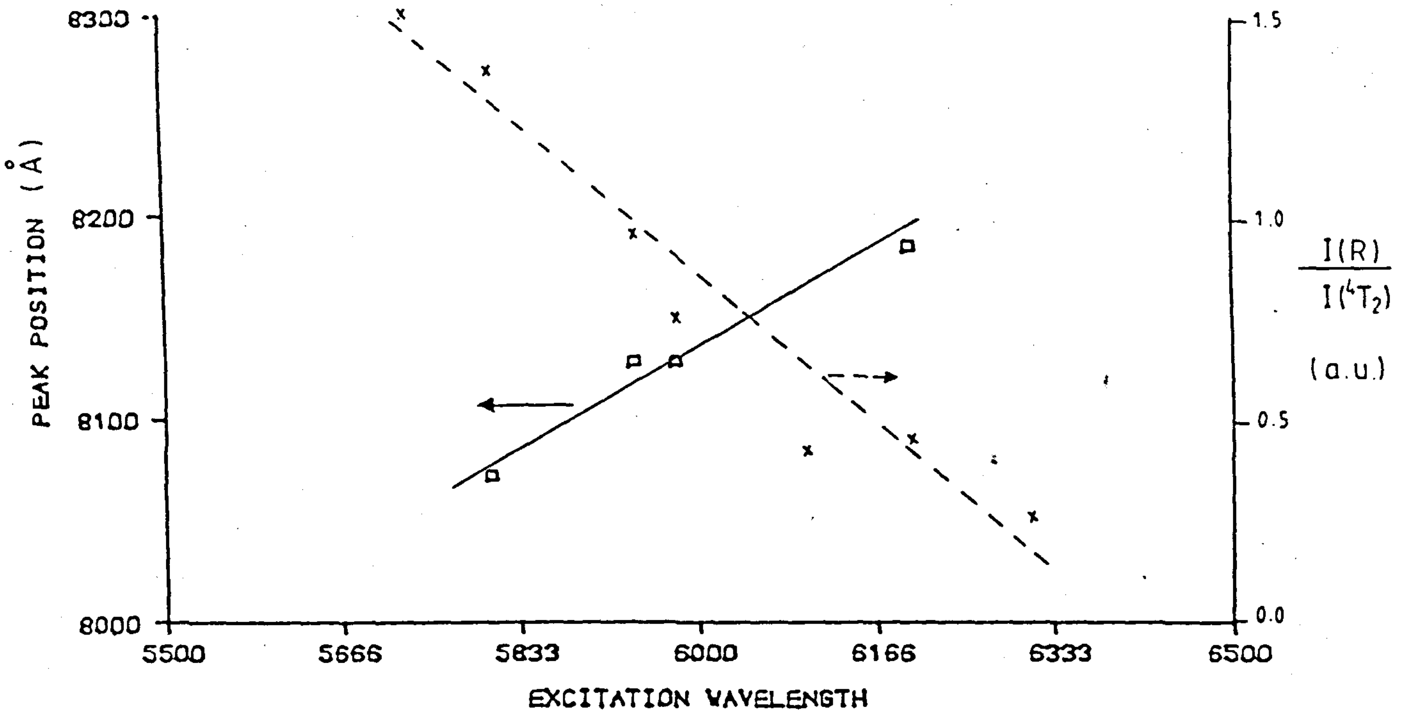

Fig 5.25 Effects of the excitation wavelength on the peak position and the ratio of the ^2E emission to the $^4T_2$ emission in K-borate glass.

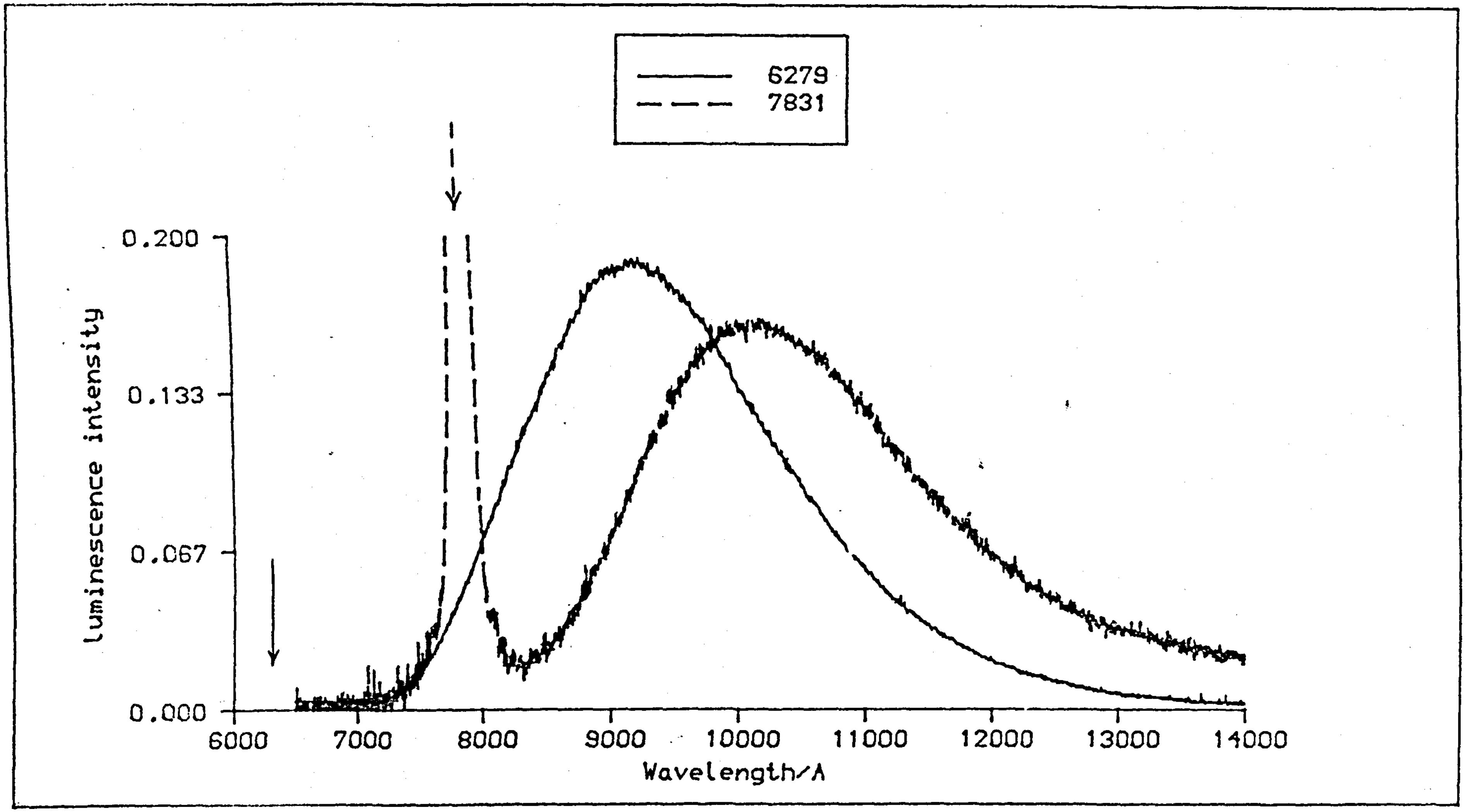

Fig 5.26 Comparison between the luminescence spectra of the fluorozirconate glass excited with red and IR excitation sources.

the decay curves of these glasses after pulsed excitation are for the most part non-exponential, varying with wavelength across the broadband. Such behaviour is observed even in very dilute Cr^{3+} doped glasses (e.g. G8197 and G8298), i.e. no contribution occurs from Cr-Cr pairs. Three decay spectra were recorded for the Li-borate glass using the boxcar detector as explained in section (3.5.2); the decy curves are shown in figure (5.27). These curves were measured at three different points in the emission spectrum to represent the ^2E emission , the $^4T_2$ and a point in between these two values. The ^2E emission decay (curve a) has the slowest rate, while the $^4T_2$ decay (curve c) is the fastest. Curve (b) appears to have two components, the $^4T_2$ decay and other is the ^2E decay curves. In figure (5.27) curves of d-f are log plots of curves a-c respectively. None of these curves is linear showing that the decay curves are non-exponential. Curve (d) shows that the decay rate of the ^2E emission most nearly exponential. This non-exponential characteristic of the decay patterns confirms the multi-site occupancy by Cr^{3+} ions in glasses, and the difficulty of resolving the homogeneously broadened components even in time resolved spectroscopy. Measurements of the decay rates across the ^2E emission in the G8150 sample show no change from that shown in figure 5.27 (a) and (d). The decay rates of the Li-borate glass at 10K ranged from $2.7 \times 10^{-1} - 7.7 \times 10^{-1}$ ms^{-1} for the ^2E emission, whereas that of the $^4T_2$ emission measured at 815nm is between $5.4 \times 10^{-3} - 9.9 \times 10^{-3}$ ms^{-1}. Similarly determined decay rates for the silicate glass (ED-2) ranged from 1.1×10^{-1} to 2.6 x

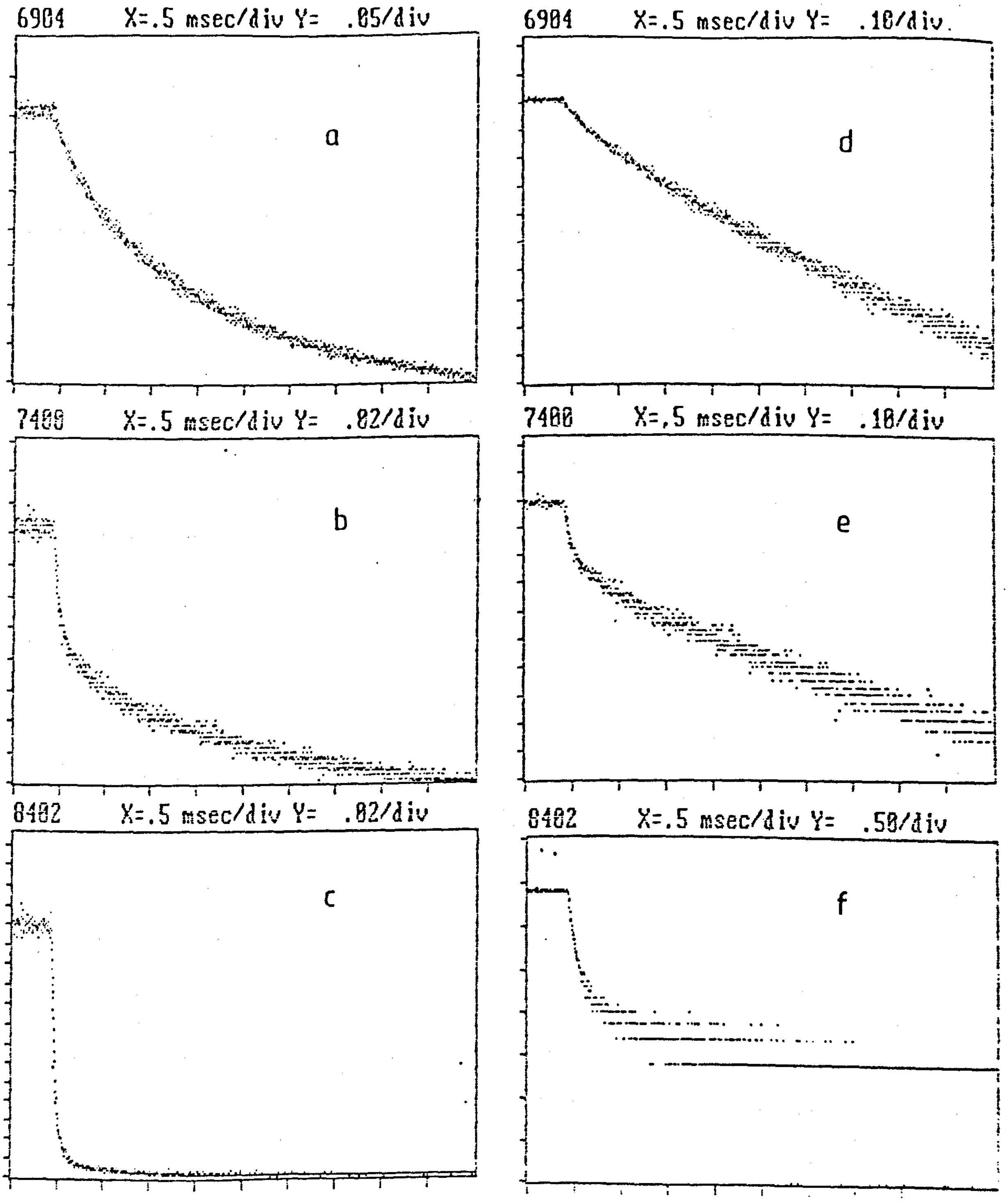

Fig 5.27 Decay rates for G8382 glass measured at different wavelengths of the emission spectrum. (a,b,c) normal decay rates at 6904, 7400, 8402. (d,e,f) log decay curves.

10^{-1} ms^{-1} for the ^2E emission and 2.3 to 11.1 ms^{-1} for $^4T_2$ measured at 820 nm and 10K. Similar results were found for the $^4T_2$ emission in other glasses (G8197, G8222). We have also measured the decay rates at different wavelengths across the unusual broad ^2E emission from sample G8382, the measured decay rate range at 705nm was $2.2 \times 10^{-1} - 7 \times 10^{-1}$ ms^{-1} slower than that measured at 690.4nm. The origin of this difference is explained in the next section. It is the difference between the decay rates of the ^2E and the $^4T_2$ components which makes it possible to resolve the various emission features which are normally masked by the overlapping transitions.

5.8 Time Resolved Spectroscopy of the Emission Spectra

Although time resolved spectroscopy makes it possible to resolve the $^2E \rightarrow {}^4A_2$ from the $^4T_2 \rightarrow {}^4A_2$ emission, there was no need to use such techniques on glasses having low Dq/B values because only the $^4T_2 \rightarrow {}^4A_2$ transition is observed. Phase sensitive detection with a lock-in amplifier in the detection system was firstly used. Later a chopped signal integrator was used to detect the signal after applying a certain delay. Finally a boxcar detector operates on the same basic principle was used especially in measurements with the G8382 glass to identify the complicating features in the cw emission spectra.

5.8.1 Time resolved spectroscopy with phase sensitive detection

The resolved spectra of a silicate (ED-2), tellurite and borate (G8150) glasses are shown in figures 5.28, 5.29, 5.30. For the Cr^{3+} doped ED-2 sample the low energy side band of the ^2E emission has a double-peaked structure. The tellurite glass shows a weaker vibronic sideband for the R-line. However, the weakest side band accompanied the $^2E \rightarrow {}^4A_2$ (R-line) transition in the (G8150) glass. The situation is different in the G8382 borate glass, the resolved ^2E emission being much broader than those of the previous three samples. Recalling the decay rates difference noted in the previous section, we tried to resolve the ^2E emission spectrum by nulling the ^2E emission peak at 683nm. In addition to the expected $^4T_2$ broad band, we recognized another structure peaked around 705nm (see figure (5.31)). (The downward structure is due to the phase difference.) In order to check this unprecedented feature, we nulled the spectrum at 705nm, which resulted in a spectrum with the broad $^4T_2$ band and a sharper ^2E emission band.

5.8.2 Time resolved spectroscopy using signal integrator and boxcar detector

The chopped signal integrator processes the low level signal detected when a chopped laser light illuminates the sample. This integrator was connected after the photomultiplier detector. In this arrangement, the synchronizing signal from the chopper is

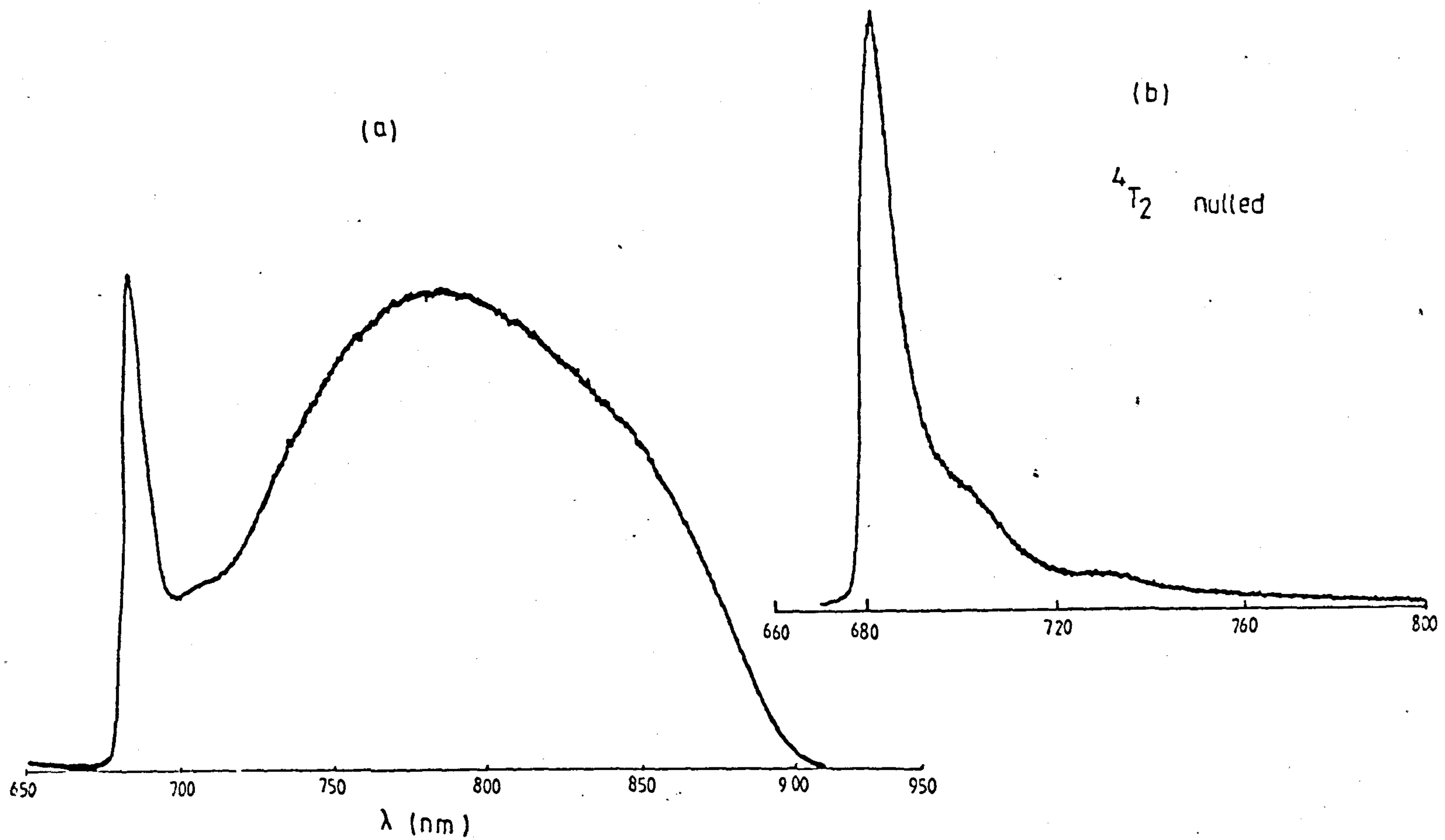

Fig 5.28 ED-2 emission at 77K excited with 6401 Å where the lock-in amplifier used to look at the whole spectrum (a), while only the ^2E emission can still be seen in (b) where the $^4T_2$ component has been nulled out.

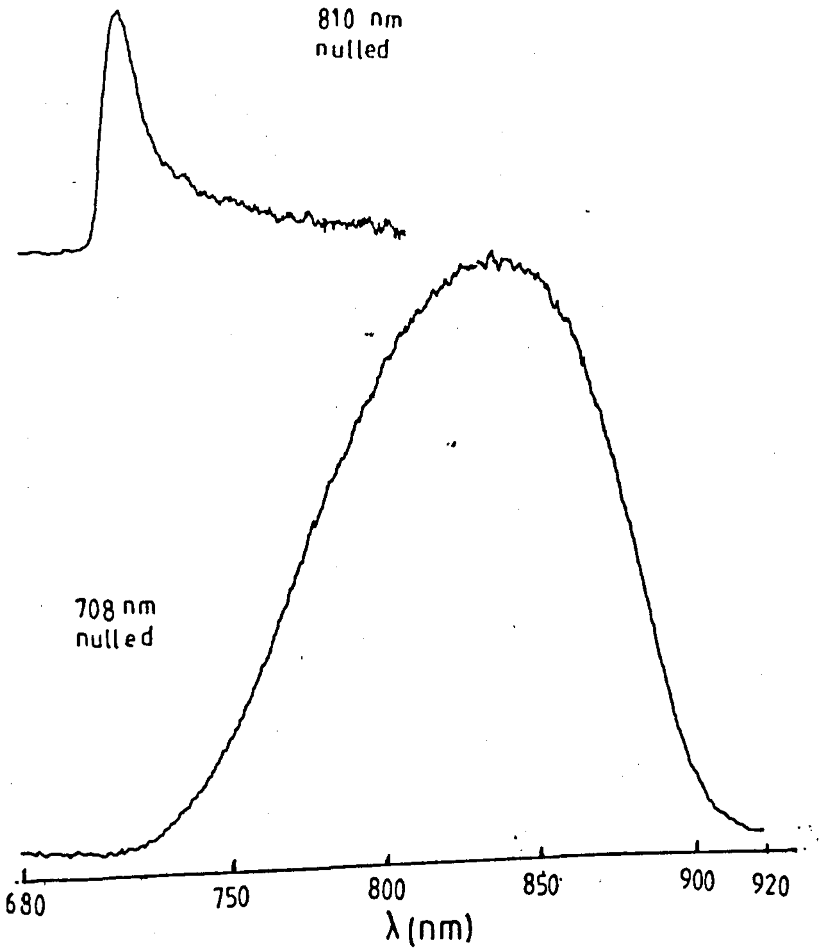

Fig 5.29 Emission of the (G8298) Tellurite glass resolved using the phase-sensitive detection technique.

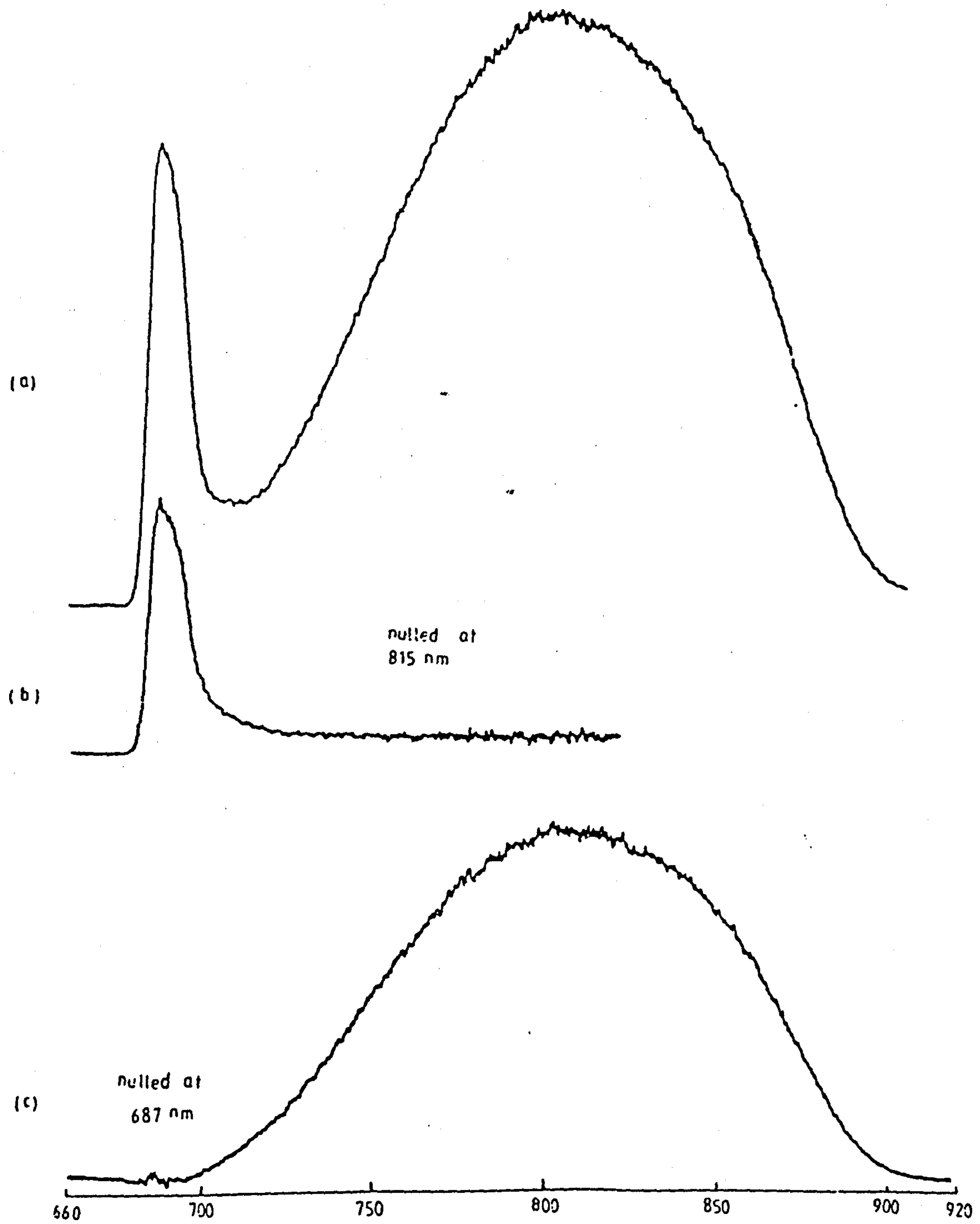

Fig 5.30 Phase sensitive detection of G8150 at 10K excited with 650nm line, (a) total emission, (b) $^4T_2$ component nulled, (c) ^2E component nulled.

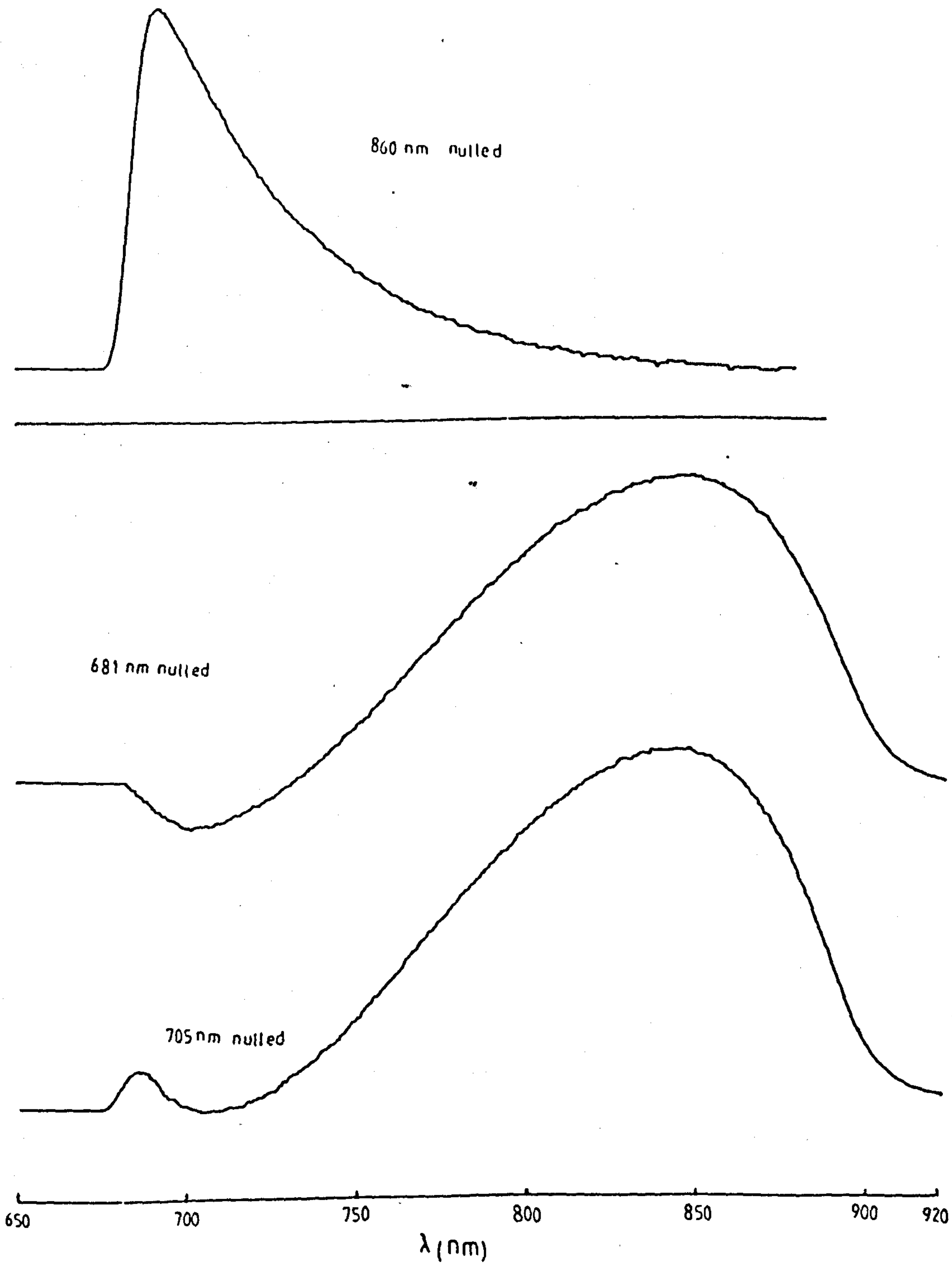

Fig 5.31 Resolved emission spectra of the G8382 glass at 10K where the broad ^2E emission is resolved into two components using the phase-sensitive detection technique.

delayed and stretched to define the two time windows shown in figure 5.32(a), one for the signal and the other for the reference zero. The signal voltages during these two time windows are separately integrated and then subtracted to give a steady state output signal. In principle, it is then possible to separate the ^2E from the $^4T_2$ emission by setting the signal window to the start of the decay while the zero window is set at the end part of the decay as shown in figure 5.32(b). In this situation only the longer lived component in figure (5.32c) is seen. Typical results for the G8382 glass at 77K and room temperature are given in figures 5.33 and 5.34. Clearly the $^4T_2$ emission remains at both temperatures. However the room temperature spectrum in figure 5.34b show two additional features, viz the double peaked nature of the ^2E emission and the broad side band of the impurity line at 976nm which is evident because of the reduced intensity of the $^4T_2 \rightarrow {^4A_2}$ band.

The temporal evolution of these changes was measured using the boxcar integrator. A series of spectra recorded after different delays is shown in figure 5.35. Evidently after a time of 2ms the fast $^4T_2$ emission has completely decayed and the peak of the ^2E emission broadens after longer delays. After 8ms the broadening of the ^2E emission confirms the existence of two components at 683nm and 705nm shown in figure 5.33 and 5.34. The decay curves of these two components together with their logarithmic versions are compared in figure 5.36(a,b,c,d). The decays are almost exponential but with different characteristic times. Figure 5.36(e)

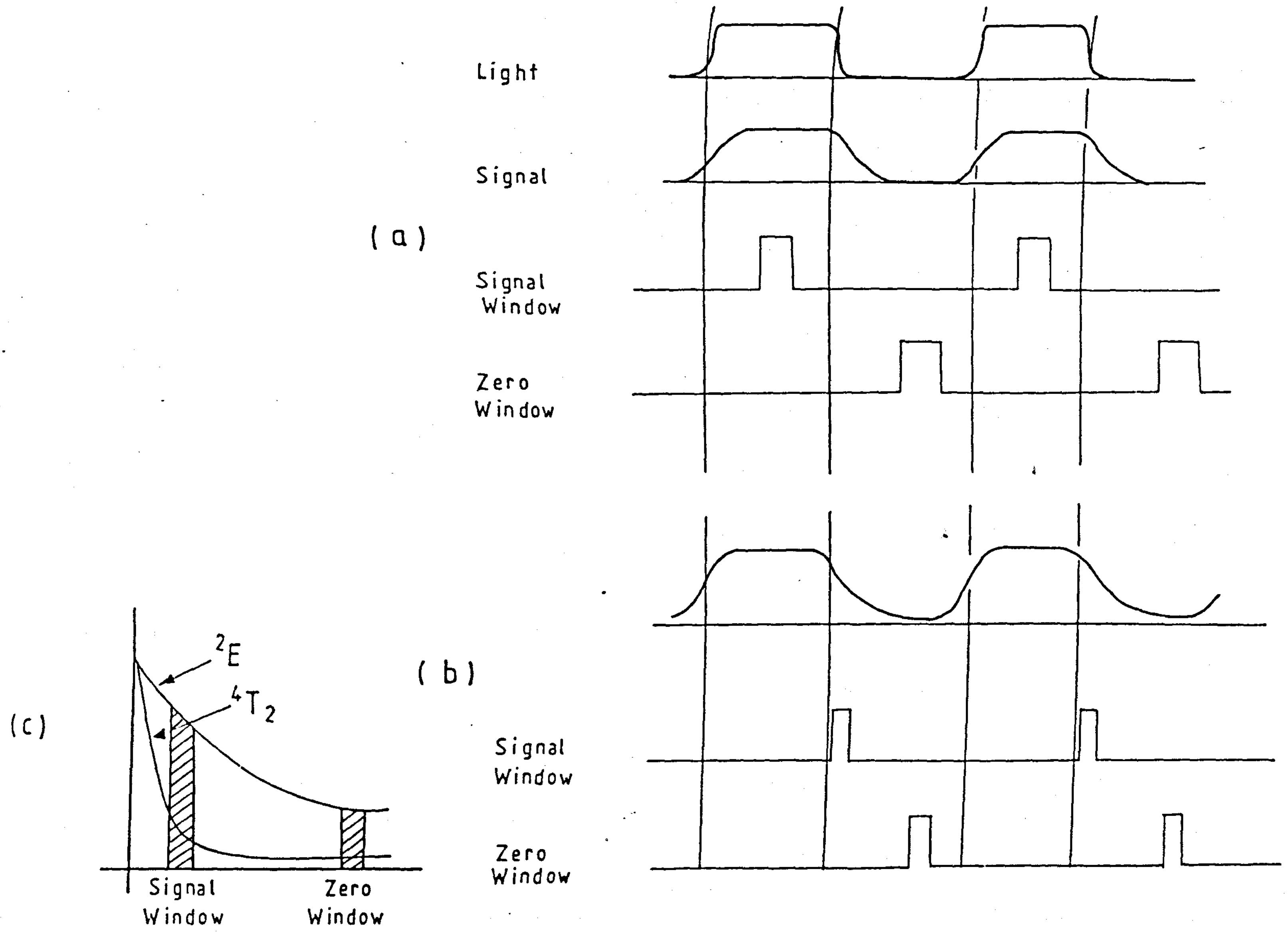

Fig 5.32 Chopped signal integrator setting for steady state and time resolved spectroscopy experiments.

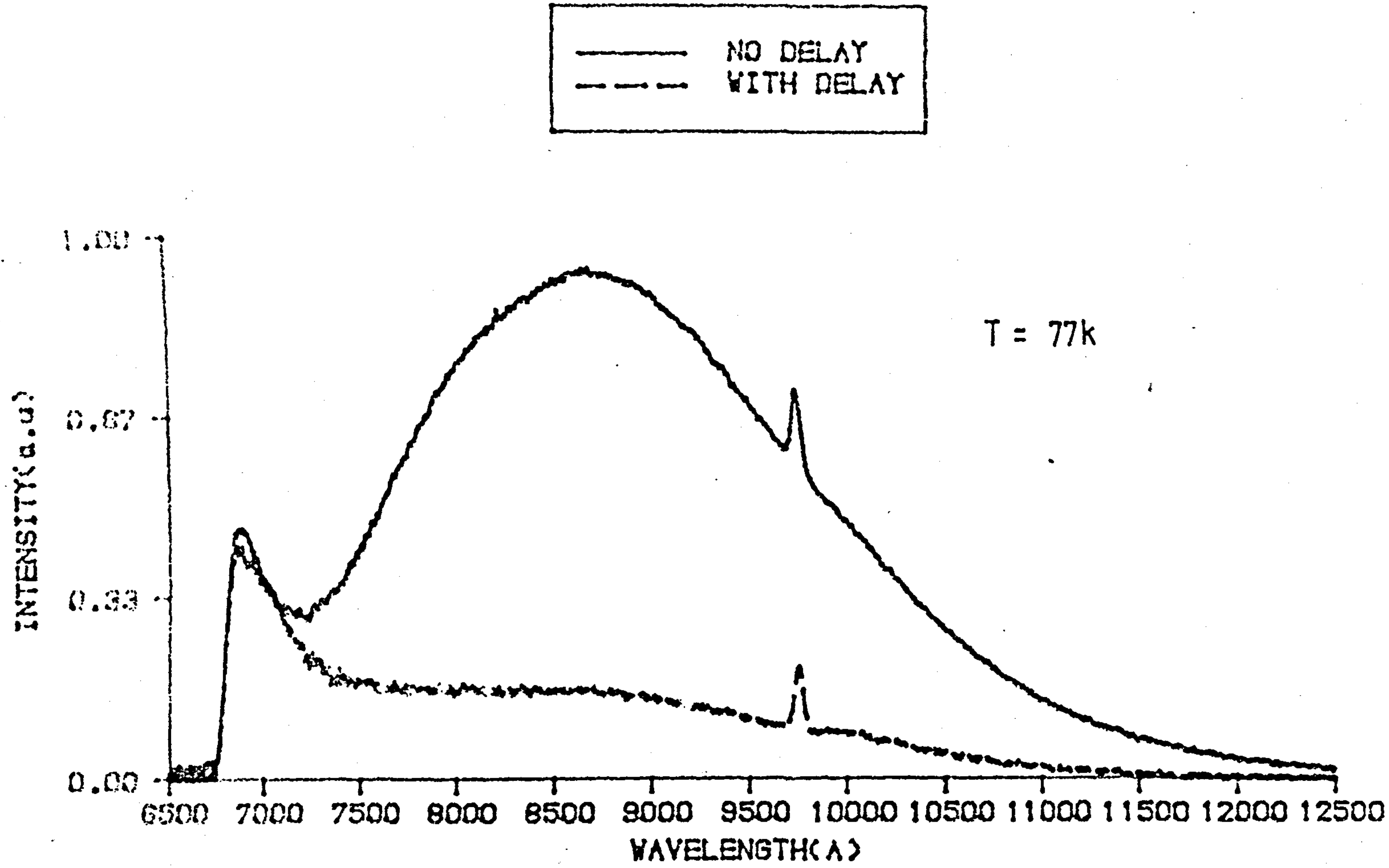

Fig(5·33) TIME RESOLVED EMISSION FOR LI-BORATE GLASS USING SIGNALINTEGRATOR

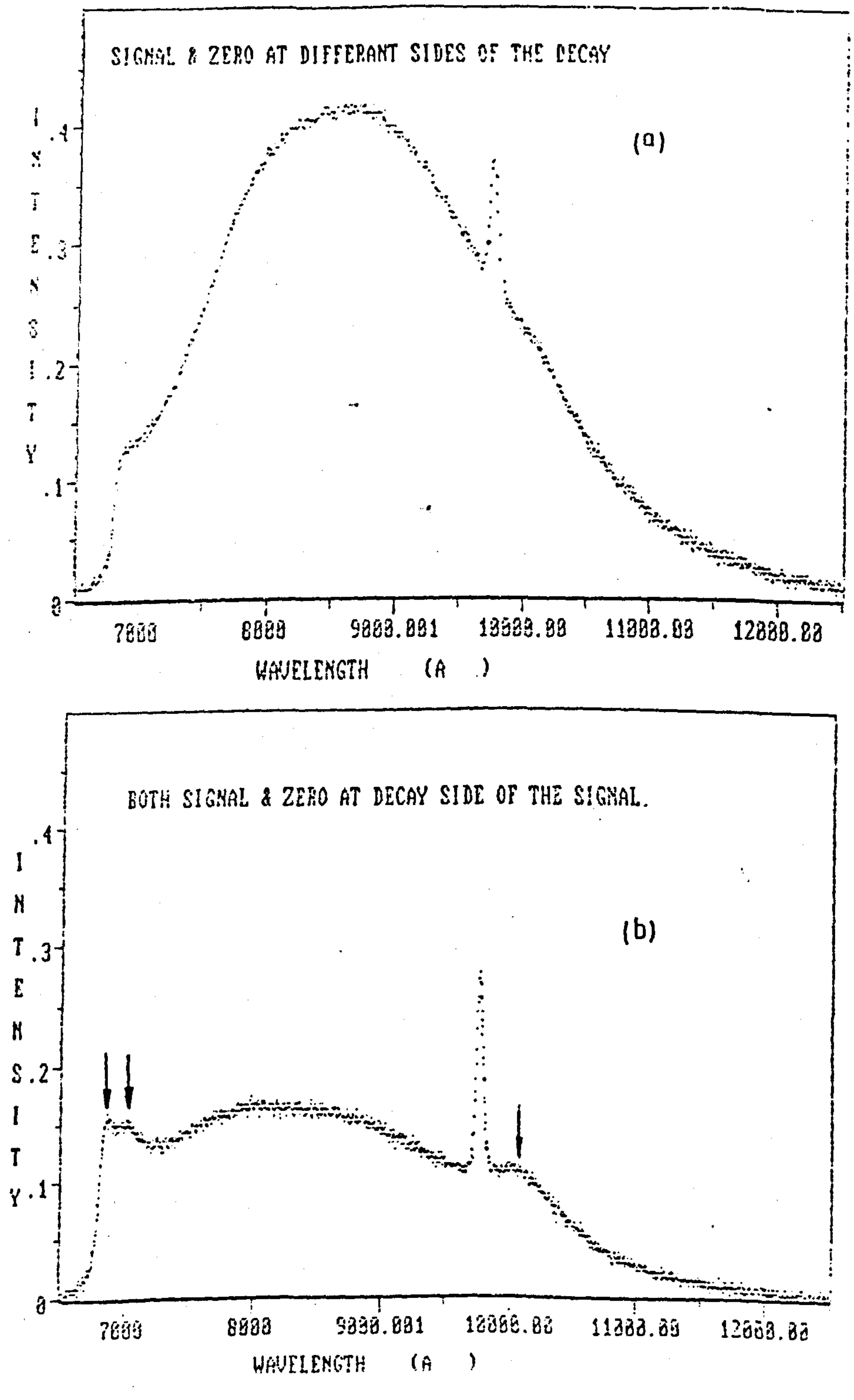

Fig 5.34 Emission spectra of G8382 glass at 300K using the signal integrator, (a) steady state emission, (b) resolved spectrum.

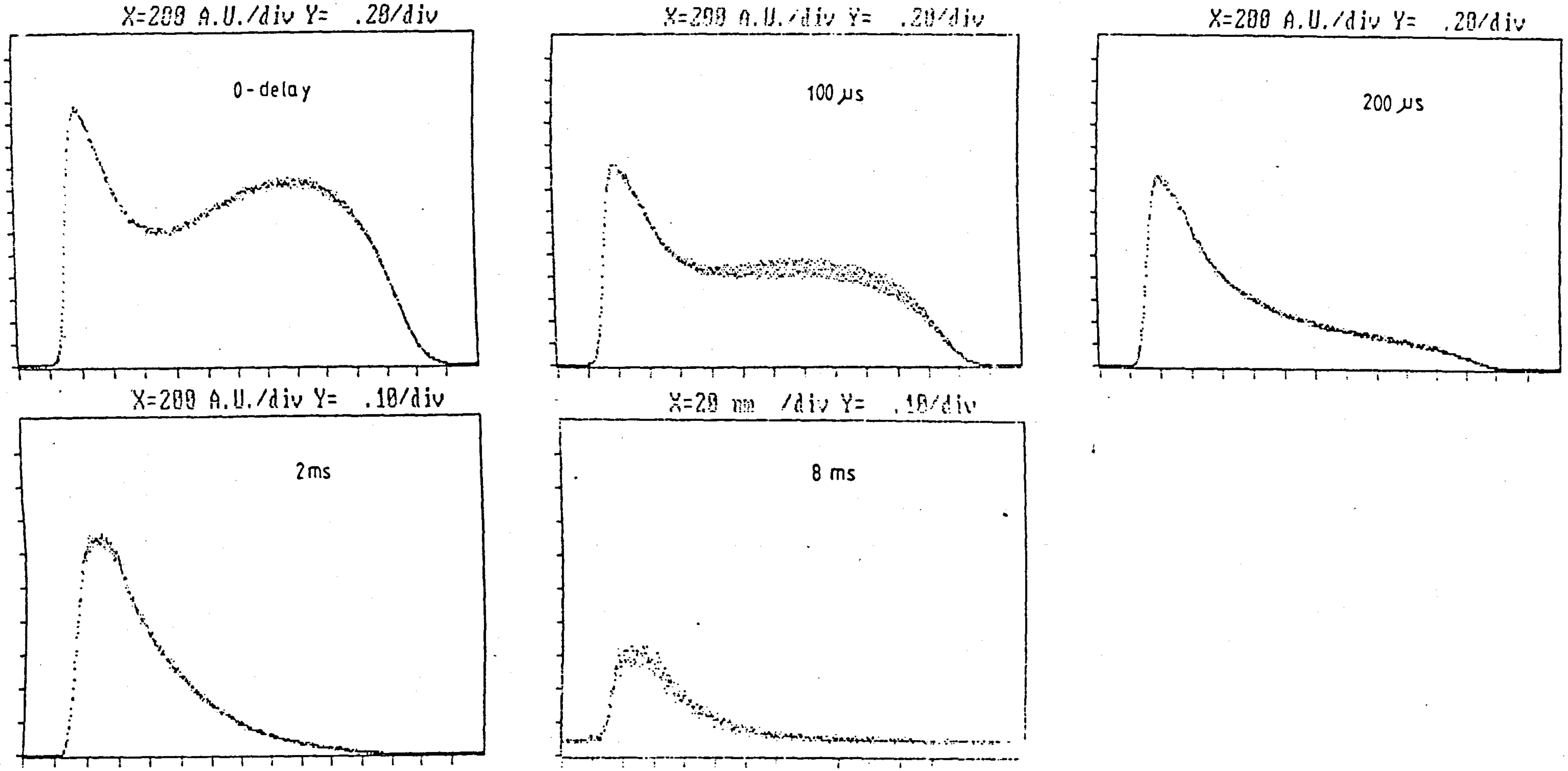

Fig 5.35 Time resolved spectra for the G8382 glass at 10K using the boxcar integrator.

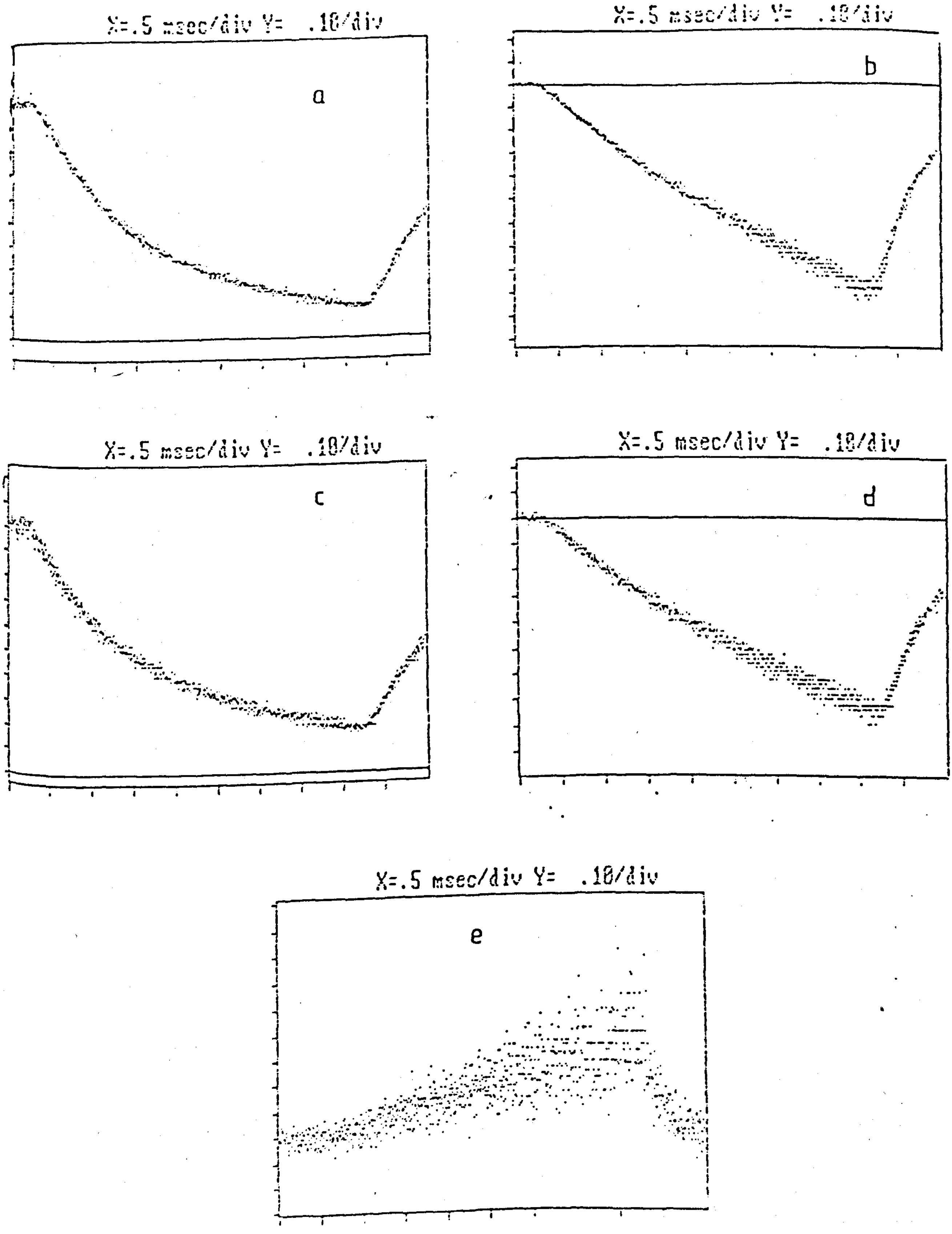

Fig 5.36 Decay rates of G8382 at (a) 685nm, (c) 702nm, (b,d) the logarithmic versions of the decay rates, (e) dividing (a) by (C).

is obtained by dividing curve (a) by curve (c). If both were the same, this would be a horizontal line. Instead the two separate, at an almost constant rate, indicating two components should be resolved at a sufficiently long delay using a very slow chopping frequency, long delay time and very high amplifier setting, two distinct component peaks at ~ 684nm and ~ 706nm were obtained. The two graphs shown in figure 5.37 are for delays of 10ms and 13ms. The origin of these overlapping components in the ^2E emission is not known, although it may be due to different Cr^{3+} centres. For example, a cluster of the form $Li^+ - O^{2-} - Cr^{3+}$ in addition to the slightly distorted octahedral sites is found in these glasses. The possibility of the Li-Cr clustering in the form Li-O-Cr is increased by the small ionic radius of the Li^+ ion. Exchange-coupled Cr-Cr pairs is unlikely because the Cr^{3+} concentration in this sample was low and in the other borate glass (G8150) there is no such emission even though the Cr^{3+} concentration is about five times larger than in G8382.

5.9 Discussion

In this chapter we have reviewed elements of the structure of glassy materials their formation and colouration using the Cr^{3+} optical activator. We then described a miscellany of measurements of the optical absorption and luminescence spectra of Cr^{3+} doped silicate, borate, tellurite, phosphate and fluoride glasses. To a greater or lesser extent each of these materials show emission from both $^2E \rightarrow$

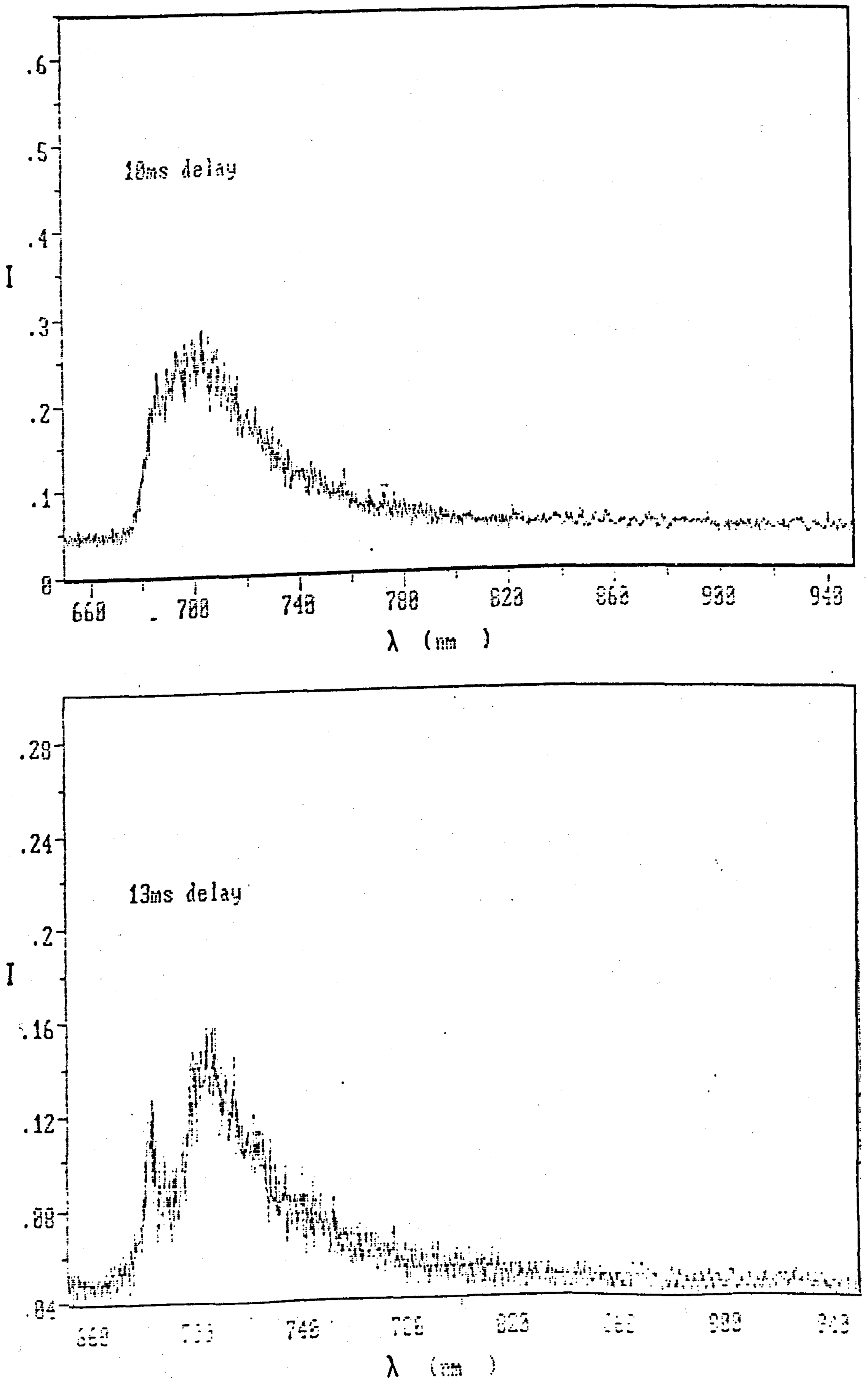

Fig 5.37 Time resolved ^2E emission complex, where two distinctive emission can be seen after a relatively long delay.

$^4A_2$ transition (R-line) and $^4T_2 \rightarrow {}^4A_2$ transition (broad band) depending upon the strength of the octahedral crystal field, Dq/B, experienced by each Cr^{3+} ions. In comparison with crystalline solids both R-line and broad band are considerably broadened, the broadening having its origin in multiple crystal field sites for the Cr^{3+} ions rather than lifetime broadening. Such inhomogeneous broadening is revealed in measurements of the spectral profile during laser excitation, whence the peak position and shape of the emission spectra are observed to vary with laser excitation wavelength. A further consequence of the multisite occupancy by Cr^{3+} ions is the lifetime dependence on wavelength in the luminescence bandshape, with the consequent multicomponent decay patterns following pulsed excitation. This latter feature makes it possible to time-resolve the Cr^{3+} emission into its component parts. Although we have used the excitation, site selectivity and time resolution techniques on all the glass samples available to us we have discussed only certain of the results to give examples of the power of the particular experimental technique. We now discuss a few additional aspects of the overall experimental results. In figure (5.38) we compare the intensity ratio

$$R = \frac{I(^2E)}{I(^4T_2)}$$

and the band centroid (M_1) for all of the glasses examined in this study. The plot demonstrates that there is a distribution of low and high field sites in all the glasses. However only in the G8150 and G8382 borate glasses are there comparable numbers of high field

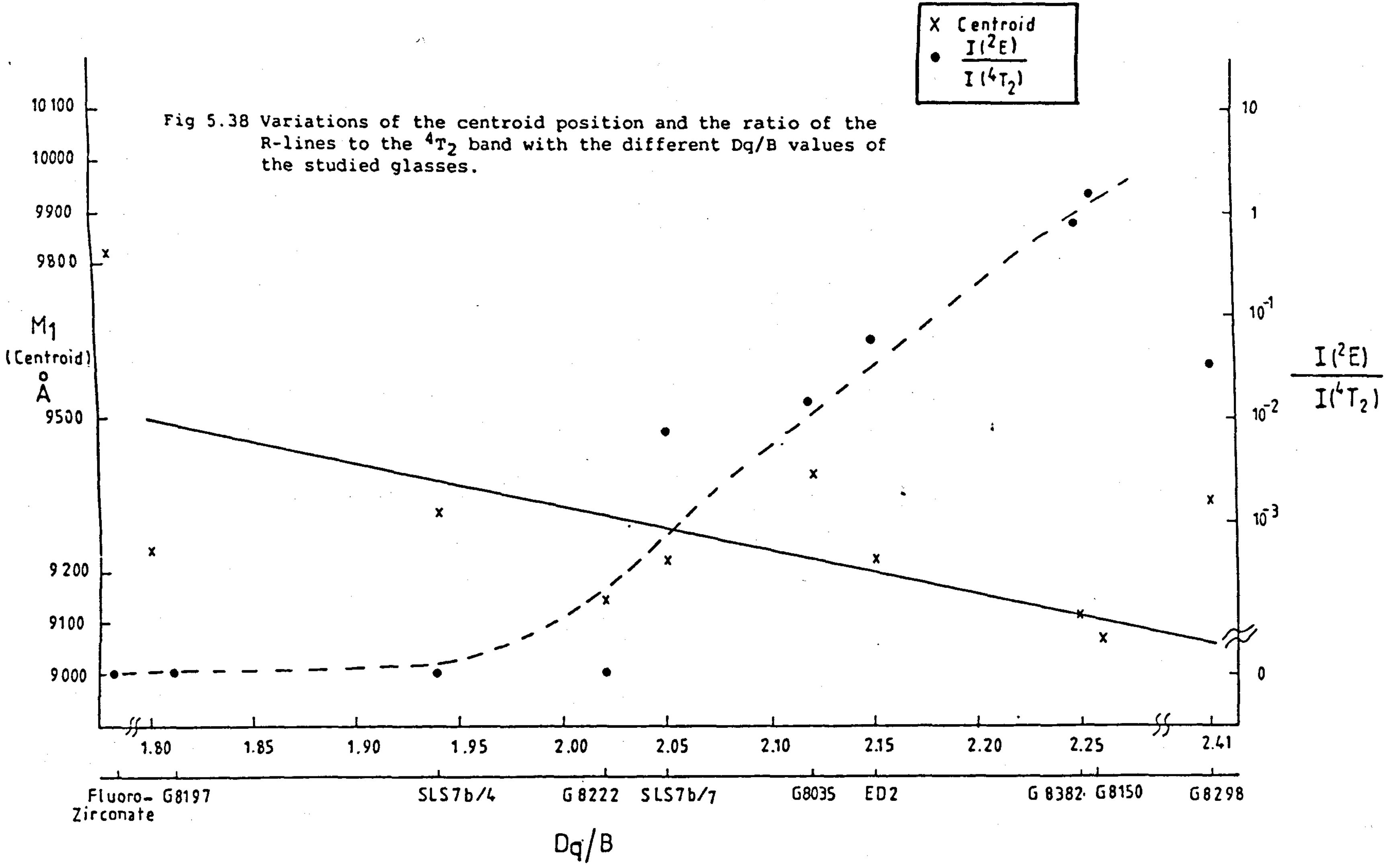

Fig 5.38 Variations of the centroid position and the ratio of the R-lines to the $^4T_2$ band with the different Dq/B values of the studied glasses.

and low field sites. For the most part these glasses are predominantly low field materials, the $^4T_2 \rightarrow {}^4A_2$ transition being dominant even at very low temperatures. The reason for this excess of low field sites over the high field ones may be because the glasses studied are either fluoride or oxides both of which are situated at the low field edge of the spectrochemical series[29] which is basically related the ionic radius to the ligand field strength.. Furthermore, since the oxygen ions are bonded to the (normally) highly charged network formers (B^{3+},Si^{4+},P^{5+}) there is a reduction in the number of electrons coordinated to the Cr^{3+} with a concomitant reduction in the higher field. In addition the lack of long range periodicity in glasses results in an open structure with long distances between Cr^{3+} ions and the ligands. The resulting crystal field is weaker than in crystals. The size of the modifier plays an important role in deciding the ratio of high field relative to low field sites. Indeed the existence of large modifiers will occupy a large space in the glass structure with high coordination, leaving the dopant sitting in small vacancies (low field sites), whereas small modifiers leave the dopants to occupy higher coordinates (i.e. high field sites). The SLS7b/4 and SLS7b/7 silicate glasses have Na and K modifiers respectively and yet the amount of ^2E emission is larger in the second, contrary to expectations. The explanation lies in the addition of H_3BO_4 in the SLS7b/7 sample which enhances the number of high field sites. In a previous work[85] it was noticed that the all-former glasses has the highest intensity in Cr^{3+} doped glasses where it was thought that an addition of a codopant or a modifier will disturb the glass and lowers its intensity.

Temperature dependence intensity measurements showed that the integrated fluorescence intensity of the fluoride glass is quenched at room temperature to ~ 1/7.3 of its value at 10K, while the value for the (G8035) silicate glass is only 1/3.5 (table 5.3). More drastic variations are noticed for the fluorozirconate glass.

Table 5.3 Intensity variation with temperature for some of the Cr^{3+} glasses.

(Intensity values are arbitrary units)

Temp ⁰K	fluoride G8197	silicate G8035	Li-borate G8382	fluoro-zirconate
300	0.27	2.36	0.15	0.02
10	1.97	8.3	1.32	1.41
I(10)/I(300)	7.3	3.5	8.8	70.5

These variations may be explained as follows: at high temperature the luminescence is quenched because of the overlap of $^4T_2$ and $^4A_2$ configurational coordinate curves. The activation energy for this process depends on the $^4T_2$ level energy being less for sites with lower $^4T_2$ position. Similar results were reported by Hollis et al.[85] who suggested that Jahn-Teller distortions of the octahedron by Cr^{3+} when in its excited $^4T_2$ state, was due to the very low ligand field in fluorides. Also different types of crystal field in the different glasses could be the cause of such differences in intensity with temperature. In view of the strong ion-lattice coupling in T.M.I., the configurational coordinates parabolae for fluoride glasses may be flattened by the lower ligand field which could cause an easier thermally assisted intersystem crossing from the excited $^4T_2$ to $^4A_2$ ground state. On the other hand, the non-exponential decay for both ^2E and $^4T_2$ transitions and the observed lifetime variations of different centres may be accounted for by the variations in the ion-lattice coupling. The origin of such non-exponentiality is probably related to a random distribution of site distortions[99] or ion-ion coupling between Cr^{3+} ions and dipoles randomly distributed in glasses.[85]

Concentration quenching of Cr^{3+}:glass was observed in several studies,[93,97] where the Cr-Cr ion pairs act as energy traps. The increase in concentration is accompanied by fast decay, the origin of which is thought to belong to either energy transfer to Cr-Cr traps or the increased non-radiative decay within the pair itself.

Such pairs have not been identified optically as in ruby. In any case the inhomogeneous broadening in glasses would inhibit optical detection of pair interaction. Instead EPR technique was used to monitor such characteristics at high concentrations.[93] The very low quantum efficiency of Cr^{3+} doped glasses is attributed to non-radiative decay processes. In the early developments of the molecular relaxation theory, it was pointed out that the electronic matrix element implied a selection rule, based on the presence or absence of vibrational modes of proper symmetry to mix electronic surfaces.[100] Subsequently, it was noted that many molecules may be classified as vibrationally deficient, relaxation between certain electronic states then being forbidden in first order by the absence of a required promoting mode of the appropriate symmetry. T.M.I. doped solids are associated with a high degree of symmetry. Hence it is expected that the energy levels of such ions couple only with local modes associated with nearest neighbours. For the octahedral symmetry the relaxation from $^4T_2$ to $^4A_2$ will not take place because of the absence of a t_{1g} mode. Also the difference in lifetime for $^4T_2$ emission between crystals and glasses is justified by the absence of the long range symmetry in the later. So for crystals of octahedral symmetry the absence of a promoting mode mitigates the non-radiative relaxation. While in glasses this dynamic restriction is absent and the mixing will take place by static assymetries of the crystal field where such lower symmetries were confirmed in glasses by the inhomogeneous width of transition and also by the broad EPR spectra.[92,93]

Inhomogeneous broadening in amorphous materials as seen in Ti^{3+} and Cr^{3+} doped glasses, plays an important role in the broadening of transitions originated from both high and low field sites. The spread of sites which was noticed by different techniques was the major cause for inhomogeneous broadening of these glasses, especially for the $^4T_2$ transition in Cr^{3+}:glasses which characterizes these glassy materials as potential prospects for broad vibronic lasers, although the low quantum efficiency from these materials still need to be enhanced first.

CHAPTER SIX

6 FLUORESCENCE LINE NARROWING OF Cr^{3+} DOPED GLASSES

6.1 Introduction

Homogeneous or lifetime broadening of optical spectra is unavoidable; it arises out of the relaxation processes involved in transitions between the different energy levels. If dopant ions in crystalline lattices occupy identical sites then at low temperatures the bulk sample might show sharp transitions identical to those of the isolated ions. In general, the spectra of ions or defects in crystals reveal another broadening type. Due to the existence of growth imperfections and strains each optical centre occupied a slightly different crystal field site having different energy levels giving rise to optical transitions at slightly different energies. These crystal field variations are a source of inhomogeneous broadening. The amount of such broadening depends mainly on the growth process of the crystal. The situation is more prominant in glasses, due to the ions occupying more strongly perturbed crystal field sites. The optical signal from these materials is usually many times broadened relative to similar centres in single crystal materials. For example, the inhomogeneous broadening of the $^2E \rightarrow {}^4A_2$ emission, the so-called R-line, has an emission bandwidth of around 200 cm^{-1} for silicate glasses compared to 1 cm^{-1} in ionic crystals. Under these circumstances many sharp features may be hidden by such broadening preventing the abstracting of energy level information using conventional spectroscopic means. One effective method to overcome this inhomogeneous broadening is Fluorescence Line Narrowing (FLN)[101] an effective means of suppressing the inhomogeneous broadening to reveal the intrinsic lineshape of certain optical centres. In principle in FLN spectroscopy the sample is probed with a narrow band laser beam ($< 10^{-2}$ cm^{-1}) which excites only a small subset of ions (depending on the laser linewidth relative to the homogeneous width of the transition). Only this subset of ions will decay radiatively over the sharp band of wavelengths comprising the packet of lines excited by the laser. The first FLN experiment was that of Denisov and Kitzel[102] where narrow luminescence resulted from the Eu-doped borate glass on ordinary mercury discharge lamp as excitation source. Narrow band tunable lasers become available somewhat later. The first laser induced FLN in solids was reported by Szabo[103] for ruby and Risberg[104] used it in glasses. The degree of narrowing observed depends on the pumping and de-excitation paths, hence FLN may be categorized into resonant fluorescence line narrowing (RFLN) and non-resonant fluorescence line narrowing (NRFLN). In the former, the excited ions decay directly to the ground state and the emission energy coincides with the excitation energy, figure 6.1a. This is the extreme case of narrowing and the emission linewidth is a convolution of the instrumental width and the homogeneous width. In NRFLN non-radiative de-excitation is to an intermediate state other than the ground state, then by radiative transition down to the ground state figure (6.1b). The spectra are narrowed significantly but are still broader than the resonant case.

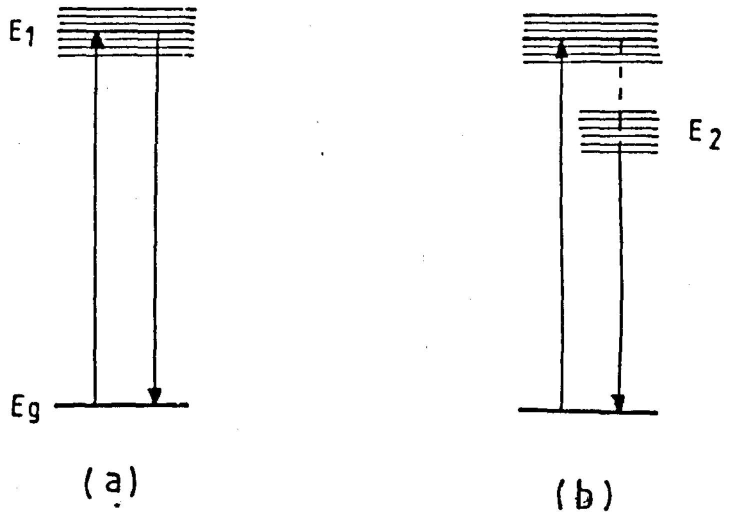

Fig 6.1 Illustration of resonant fluorescence line narrowing (RFLN) (a) and non-resonant fluorescence line narrowing (NRFLN) (b).

Experimentally, NRFLN is much easier to carry out, since the excitation laser is tuned into absorption states higher in energy than the emitting level. This technique is suitable for rare earth doped glasses which are characterized by sharp energy levels because of the weak interaction of the rare earth ions with the electrostatic crystal field. This is the main reason why most FLN studies have been on rare earth doped glasses.[103,48,105] The high sensitivity of T.M.I. to their environment causes strong coupling between the ions and their ligands, resulting in strong homogeneous broadening of absorption and emission bands. In consequence the application of NRFLN to Cr^{3+} doped glasses may not result in a considerable narrowing. This was discussed in chapter 5 where excitation into broad absorption bands using a narrow band ring dye laser showed little appreciable narrowing of the fluorescence. This is because the excitation of the Cr^{3+} ion in the homogeneously broadened $^4T_1$ and $^4T_2$ bands results in emission from many ions resulting in a broad emission spectra. In consequence the use of RFLN appear inevitable for the Cr^{3+} doped glass. This is experimentally more difficult, since the detection of the signal at the same frequency as the pumping light results in a large scattered laser signal that might saturate the detector. For this reason the arrangement discussed in section (3.6.1) was used successfully to extract the fluorescence signal. Because FLN can only be applied to purely electronic transitions, it has been used only for the $^2E \rightarrow {}^4A_2$ transition, at ions occupying high field sites. The time resolved spectra (see chapter 5) showed this transition to be a broad zero-phonon line, accompanied by a weak vibronic sideband at lower energies. The structure and the symmetry surrounding the Cr^{3+} ion occupying high field sites, and whether they are affected by lower symmetry distortion may be determined by monitoring the splitting of the ^2E energy level. Such characteristics are not identified with conventional spectroscopy measurements.

6.2 FLN Results

The FLN spectrum of the SLS7b/7 glass at 4.2K is shown in figure (6.2) as well as the R-line from which it was resolved. The narrowing of bandwidth from ~ 190 cm^{-1} down to less than 1 cm^{-1} is a remarkable illustration of the inhomogeneous broadening of the optical shape function in glasses. Also apparent from this low temperature FLN spectrum is the R_1-component of the line associated

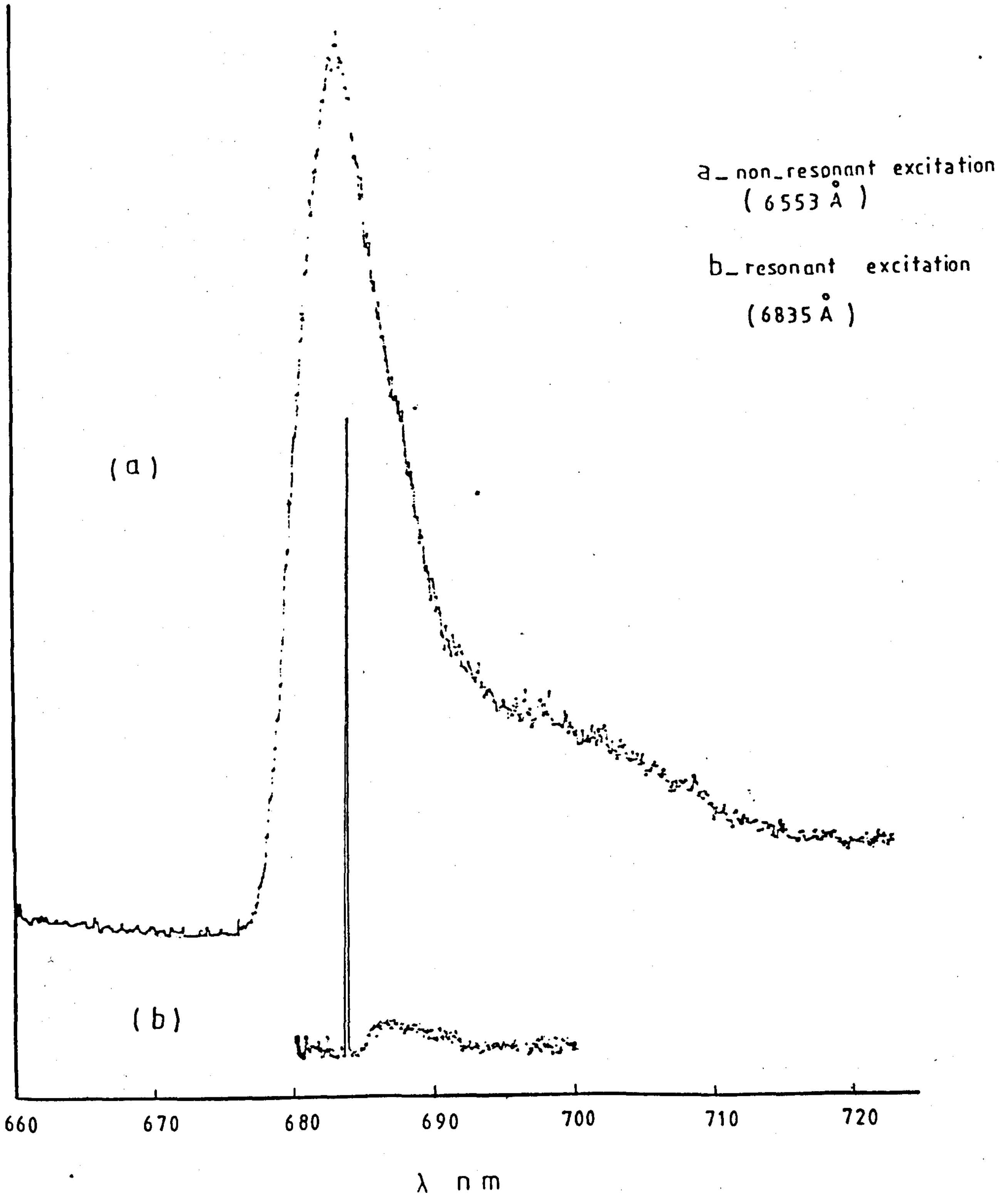

Fig 6.2 FLN for SLS7b/7 at He temperature, where only R_1 can be seen at this low temperature.

with the Ev-level at distorted octahedral sites. At higher temperatures the R_2-component from Eu-level is observed on the higher energy side of the resonant FLN signal. Such spectra were reported earlier[50] and the R_1 and R_2 components accompanying the resonant FLN signal, attributed to the ^2E-level splitting on Cr^{3+} ions occupying distorted octahedral sites where R_2 is from sites of energy levels above the FLN line, while energy levels above the FLN line, while energy levels below the FLN line belong to R_1. We attempt to identify the distortion symmetry later in this chapter. Tuning the exciting laser across the ^2E emission band of the SLS7b/7 sample shows the R_1-component which is separated from the FLN line by ~ 50-56 cm^{-1} for each of the different excitation wavelengths (see figure (6.3)). The FLN spectra for ED-2 glass measured at 77K for different excitation wavelengths with the R-line are shown in figure (6.4). As the excitation wavelength is tuned from the short wavelength edge of the R-line towards longer wavelengths the R_2-component of the ^2E emission increases in intensity while the R_1-component becomes smaller. This is because at shorter excitation wavelengths the laser excites mainly the R_2-components resonant at the laser wavelength. Thermal depopulation of the Ev level populates the Eu level giving rise to R_2-emission also. As this laser is scanned to longer wavelengths, the R_1 component at same sites is excited directly, the R_2 component at shorter wavelengths is then observed via thermal excitation of the higher lying E-level but only at high temperature (77K). The value for the splitting of the ^2E levels of ~ 50 - 54 cm^{-1} is similar to that

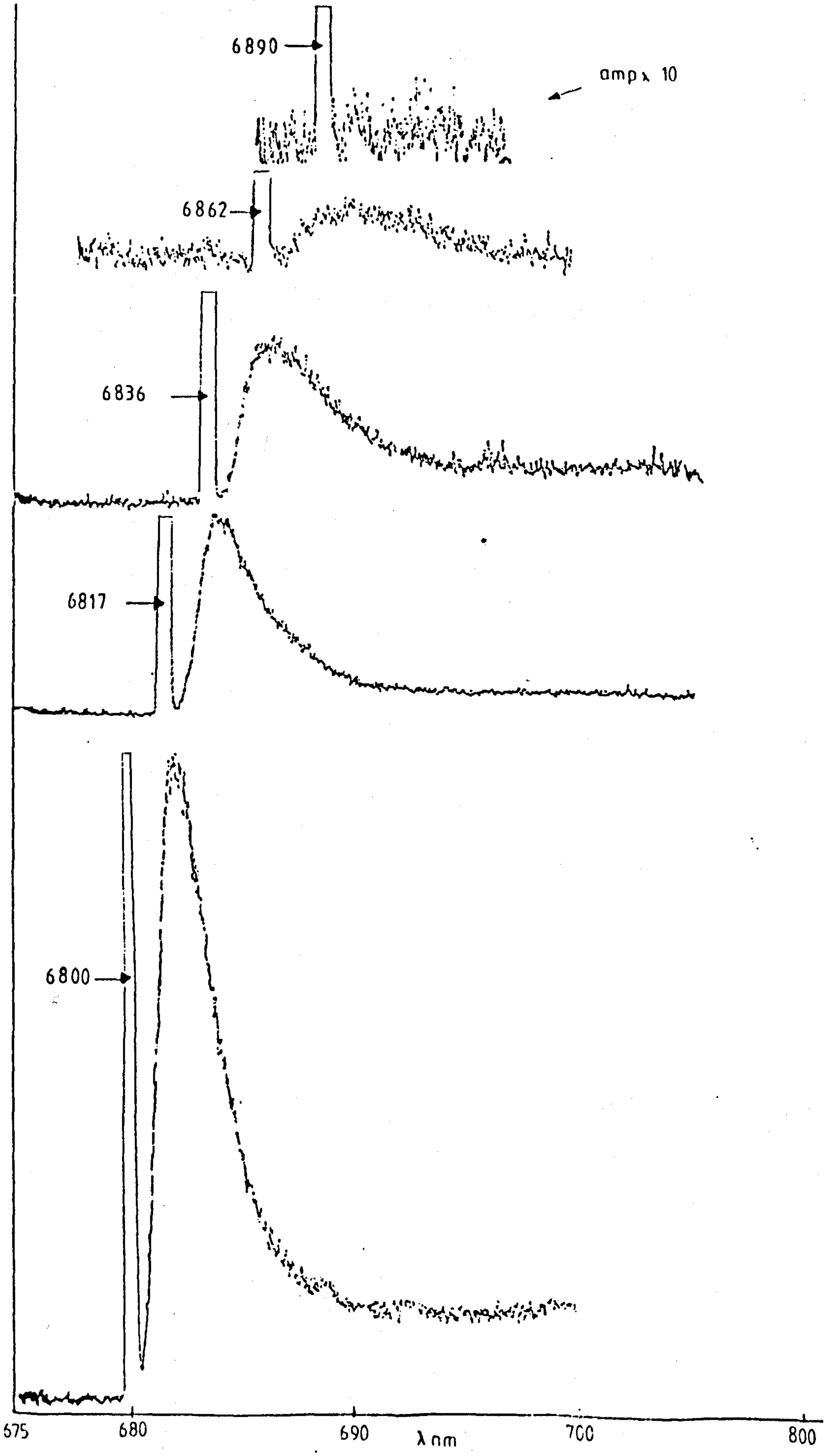

Fig 6.3 RFLN spectra for SLS7b/7 at He temperature with the laser tuned across the ^2E band.

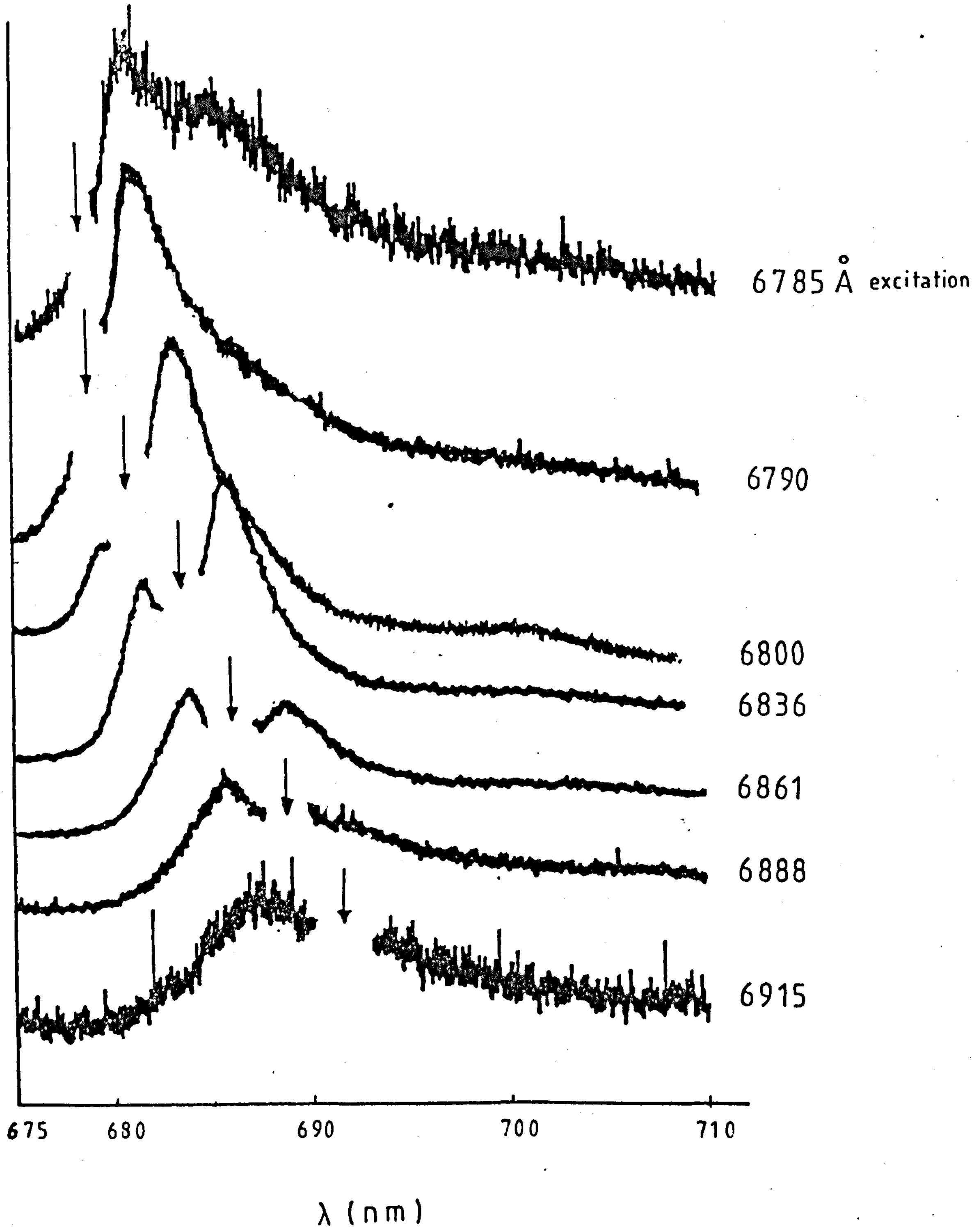

Fig 6.4 FLN for ED-2 glass at 77K and the laser exciting different regions of the ^2E band.

found in the silicate SLS7b/7 glass. At lower sample temperatures, the R_2-component becomes smaller until it disappears. This is illustrated for the ED-2 glass in figure (6.5) measured at liquid helium temperature. In this figure a weak but clearly resolved sideband of the R-line can still be detected when scanning the laser towards the lower energy wing of the R-line. The R_1-component gradually becomes weaker and almost disappears to leave only the sideband for excitation wavelengths of 6917 Å and 6953 Å. At 7046 only the FLN line can be seen. In figure (6.6) the laser is scanned towards the higher energy side of the R-line in the ED-2 glass. As the wavelength decreases the FLN line becomes weaker and a broad band other than the R_1-component begins to develop. The origin of this feature is the simultaneous excitation of some sites resonantly and others non-resonantly. Again in ED-2 glass the ^2E level splitting is of the order of 50-55cm^{-1}. The FLN and emission spectra for Li-borate (G8382) glass and K-borate (G8150) glass are shown in figure (6.7a,b). Scanning the laser through the R-line of the G8382 sample towards longer wavelengths gives the calculated splitting of the ^2E level as ~100-105cm^{-1} (see figure 6.8). We cannot rely on this value, since the emission from the clustered centre in this sample, which mentioned before, could still overlap the ^2E emission. The ^2E splitting has the value of ~ 58 cm^{-1} in G8150.

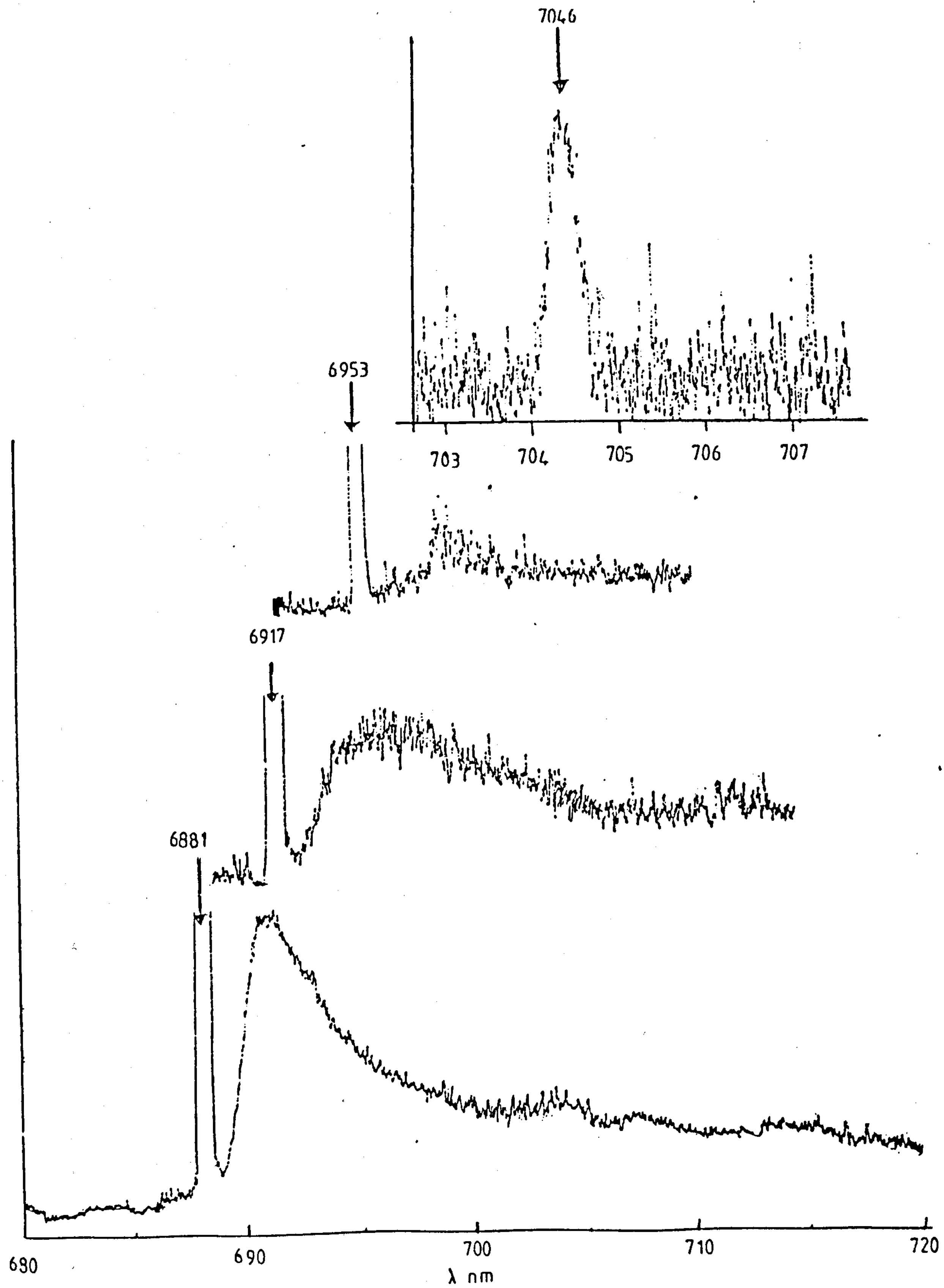

Fig 6.5 FLN for ED-2 glass at He temperature with the laser scans the low energy side of the ^2E emission band.

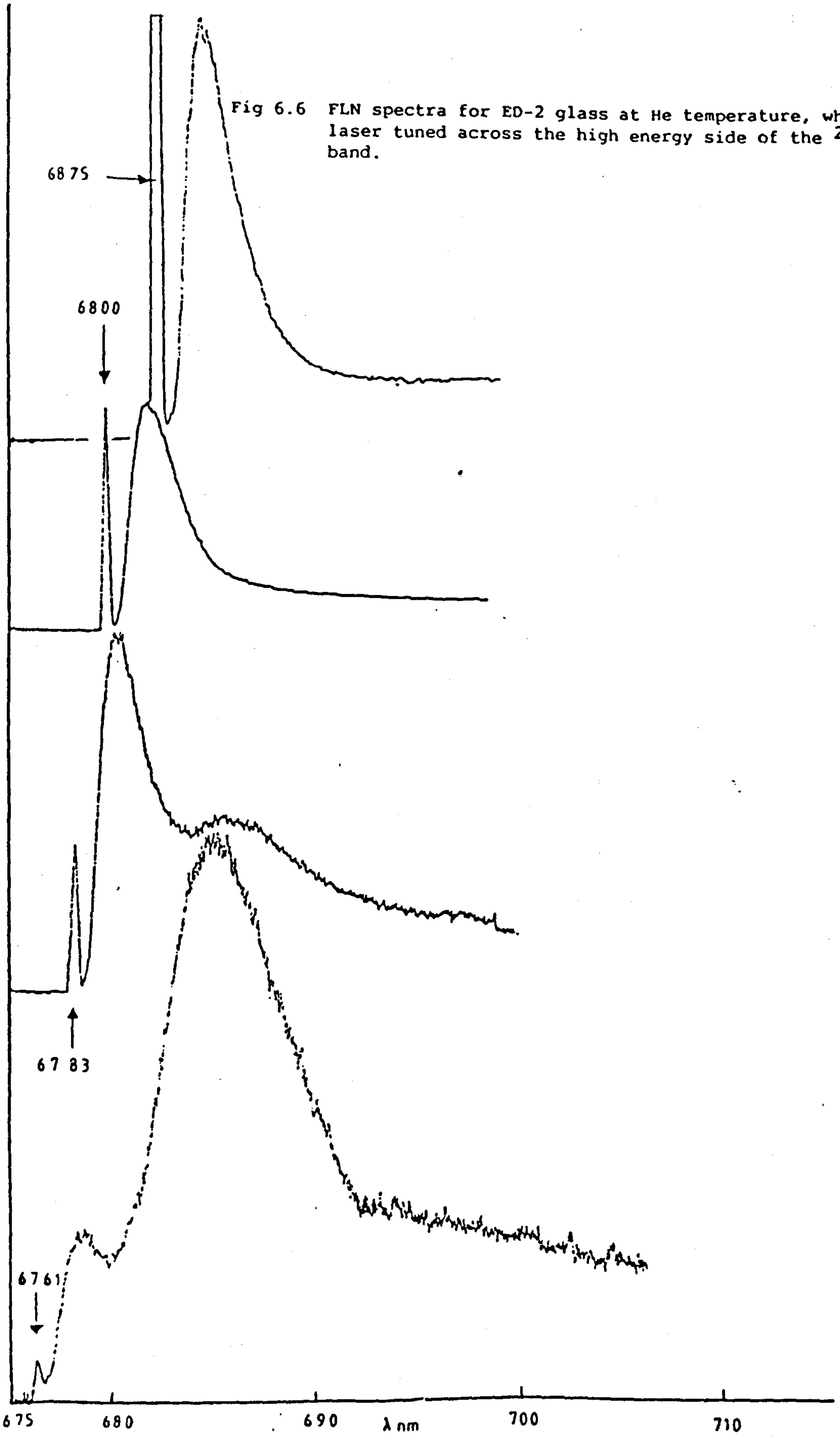

Fig 6.6 FLN spectra for ED-2 glass at He temperature, where the laser tuned across the high energy side of the ^{2}E emissio band.

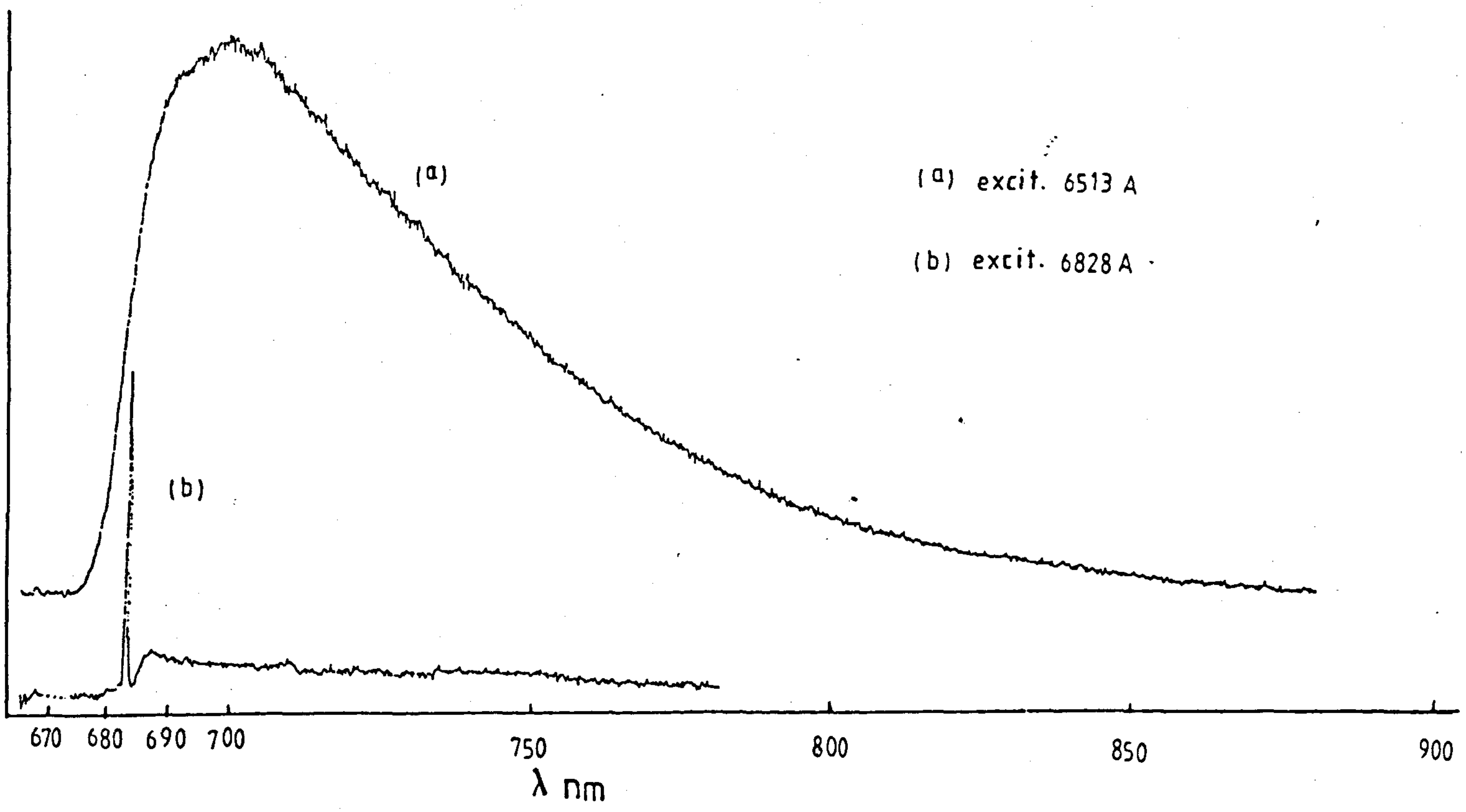

Fig 6.7a FLN spectrum for the G8382 Li-borate glass at 10K.

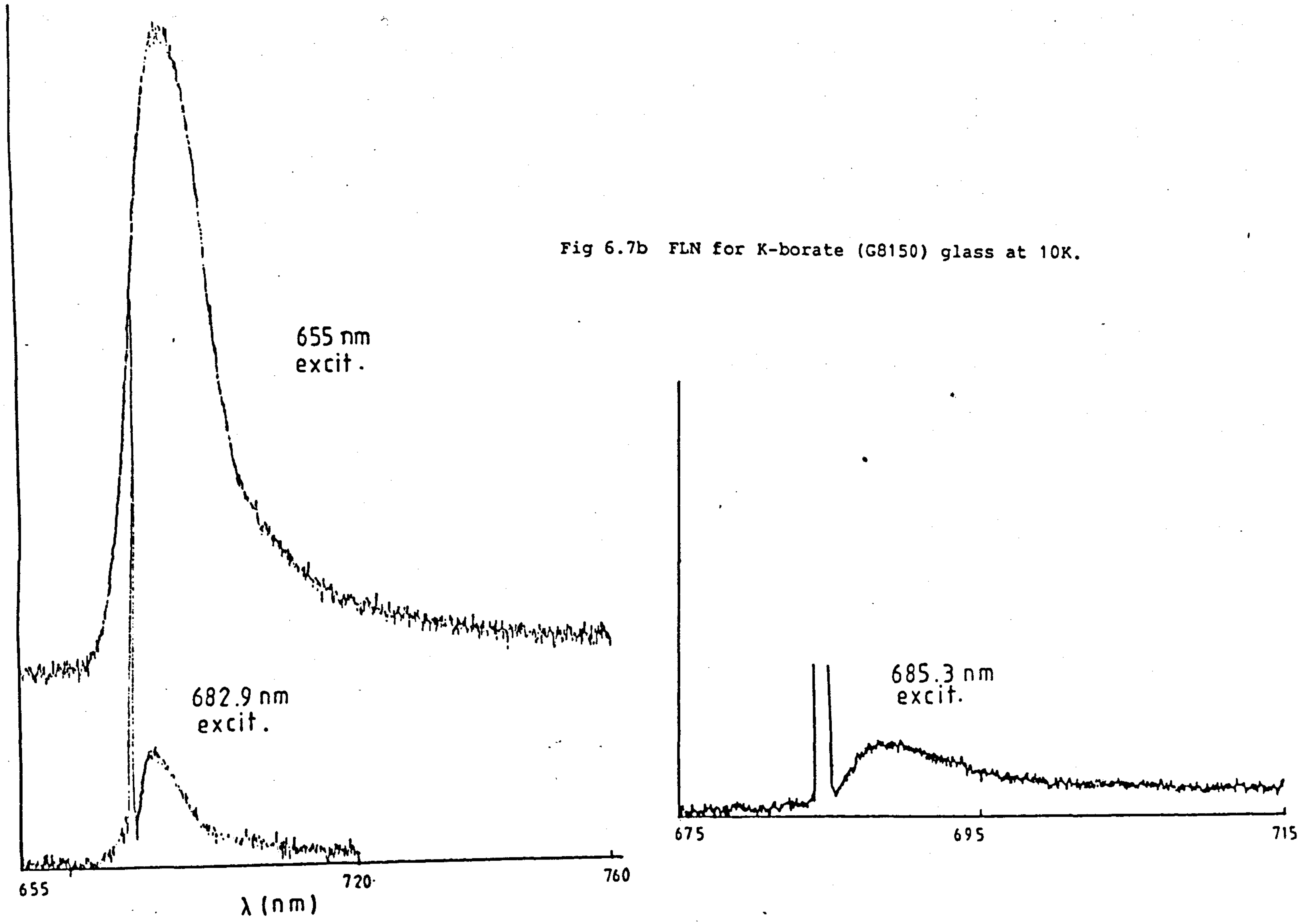

Fig 6.7b FLN for K-borate (G8150) glass at 10K.

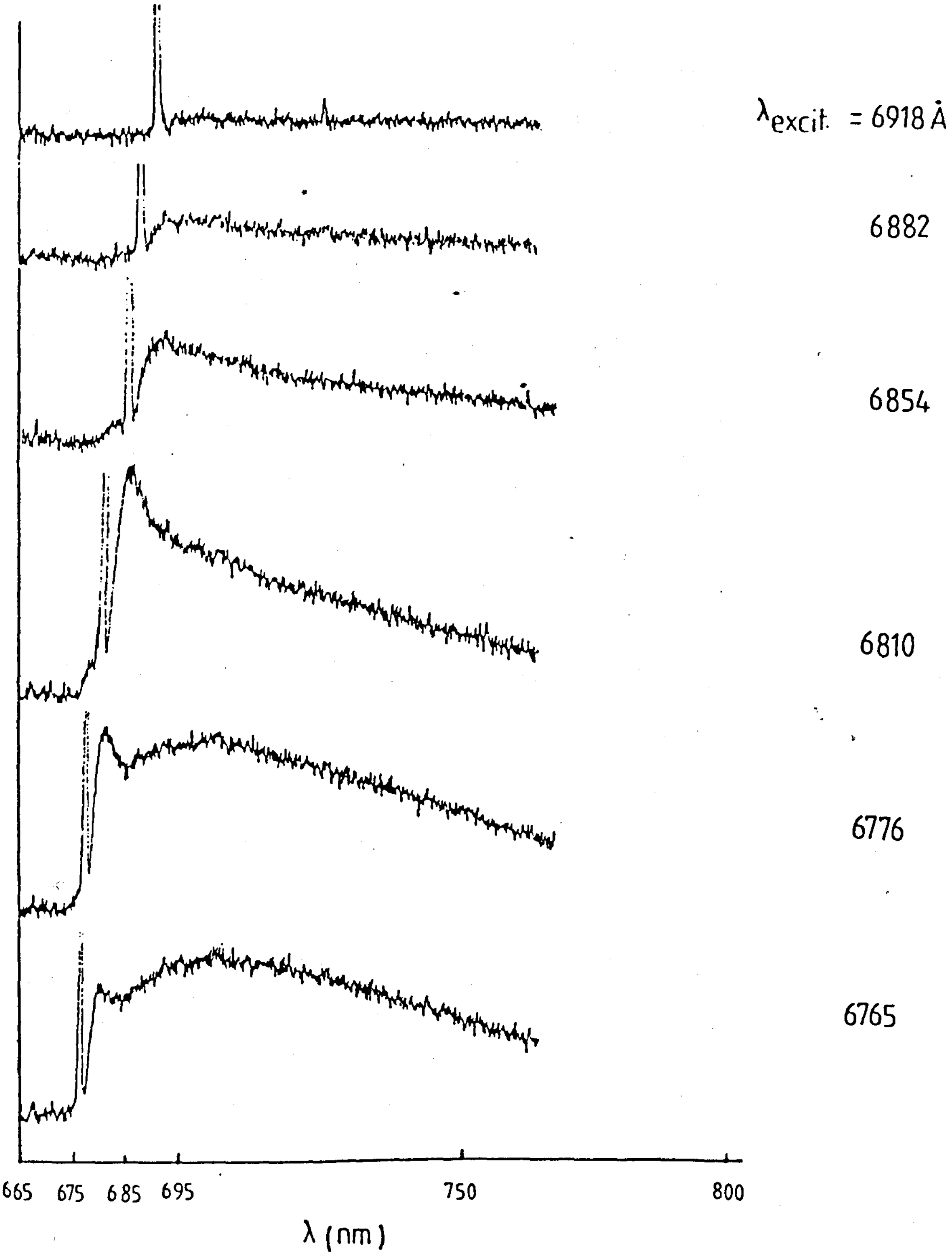

Fig 6.8 Laser scanning across the ^2E complex of the G8382 glass at 10K.

6.3 Temperature Dependent Broadening of the FLN Spectrum

Using FLN to extract the true homogeneous linewidth and its accompanying sideband from an inhomogeneously broadened line facilitate the measurement of temperature dependent homogeneous broadening of the emission spectrum in glasses. The measurements were carried out for two silicates and two borate glasses at temperatures between 10K and (in principle) 300K. The high temperature measurement was determined by the strength of the signal in each sample at higher temperatures. In the case of the G8035 silicate glass the signal almost disappeared at 60K, whereas a strong signal remains up to 150K in G8382 glass. As the detected FLN spectrum at each temperature is a composite of the system linewidth and the homogeneous broadening (the ground state splitting is neglected because it is very small[108]), the laser bandwidth $\Delta\nu_L$ and the homogeneous linewidth $2\Delta\nu_H$ were measured separately. The factor of 2 appears according to Kushida and Takushi[106] because of the resonant nature of the pumping process. A comparison between the observed FLN signal and the laser linewidth is given in figure (6.9). The detected spectrum width is written as

$$\Delta\nu_d = \Delta\nu_L + 2\Delta\nu_H \qquad (6.1)$$

The system linewidth is important at low temperatures where it is assumed to be Gaussian, while at high temperatures the detected spectrum becomes Lorentzian in shape due to the dominance of the homogeneous broadening. The deconvolution of the detected linewidth

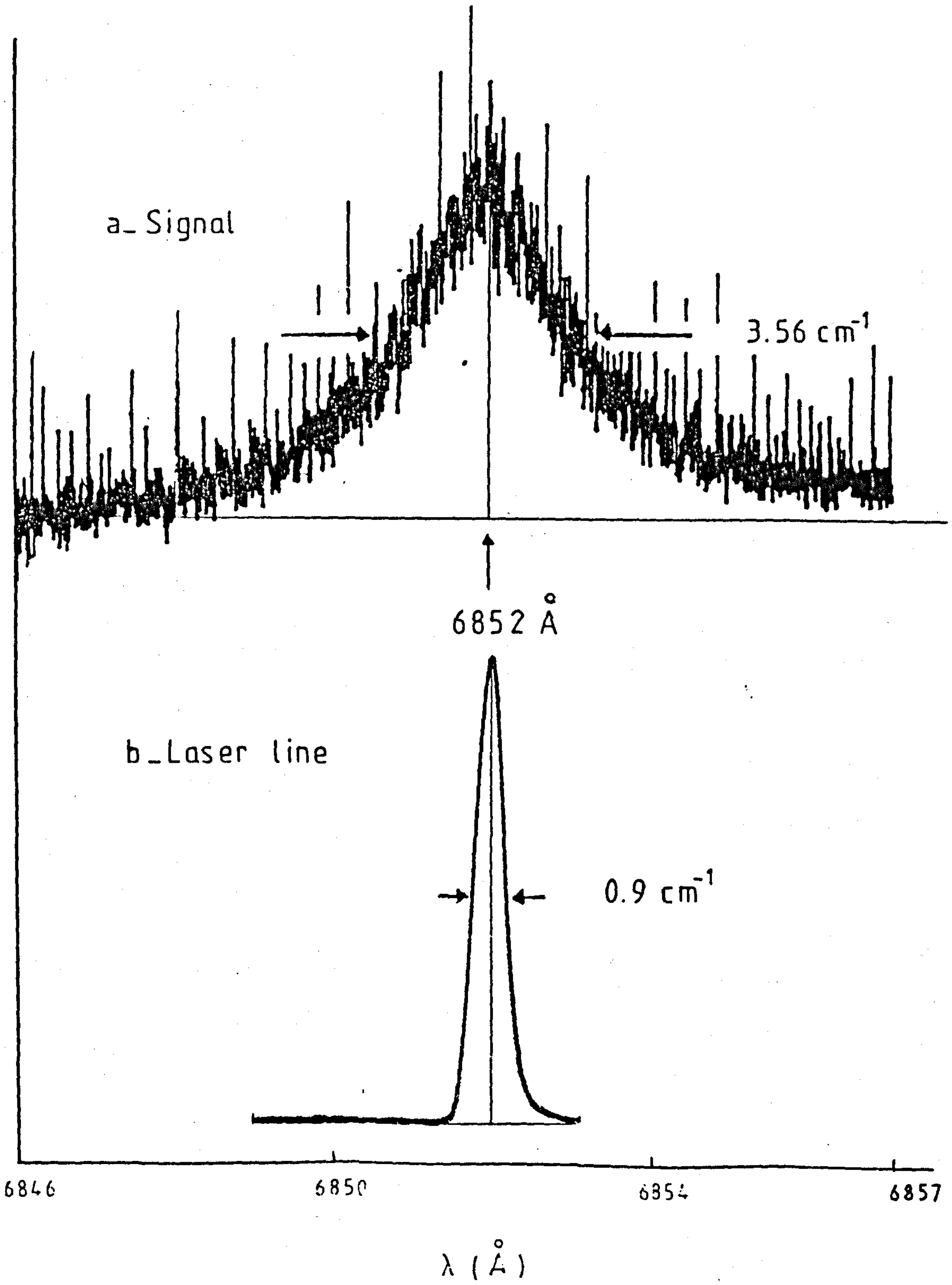

Fig 6.9 Comparison between observed laser and signal linewidths for the ED-2 glass at 77K.

into homogeneous and laser linewidths is necessary to determine the variation with temperature of the homogeneous process. To do this we may subtract the laser linewidth from the detected width point by point using a deconvolution computer program. Unfortunately the results of this process were not accurate enough since the number of the detected points in each FLN spectrum was insufficient to give a reasonably smooth spectra for such sensitive measurements. The alternative was to use standard curves for deconvoluting the composite line shape,[107] where the homogeneous linewidth can be evaluated knowing the detected width and the laser linewidth. The relations between the homogeneous linewidth determined by such a process and the sample temperature are shown for the four glass samples in figures (6.10, 6.11). The results for ED-2 glass are similar to those reported by Bergin et al.[50] although the low temperature linear region extends only to ~ 50K in our measurements, the rest of the curve increases more sharply. For Li-borate glass the linear portion extends up to 70K. The graphs show this similar behaviour of the linewidth verses temperature dependence for the four glasses. However the comparison of the temperature variations shown in figure (6.12) demonstrates that at a certain temperature the homogeneous width of the $^2E \rightarrow {}^4A_2$ transition in the two borates is larger than for the silicate glass.

To analyse the temperature dependent broadening of the homogeneously broadened FLN spectra of Cr^{3+} doped glasses, we choose the k-borate glass (G8150) for the analysis, where the observed sideband which

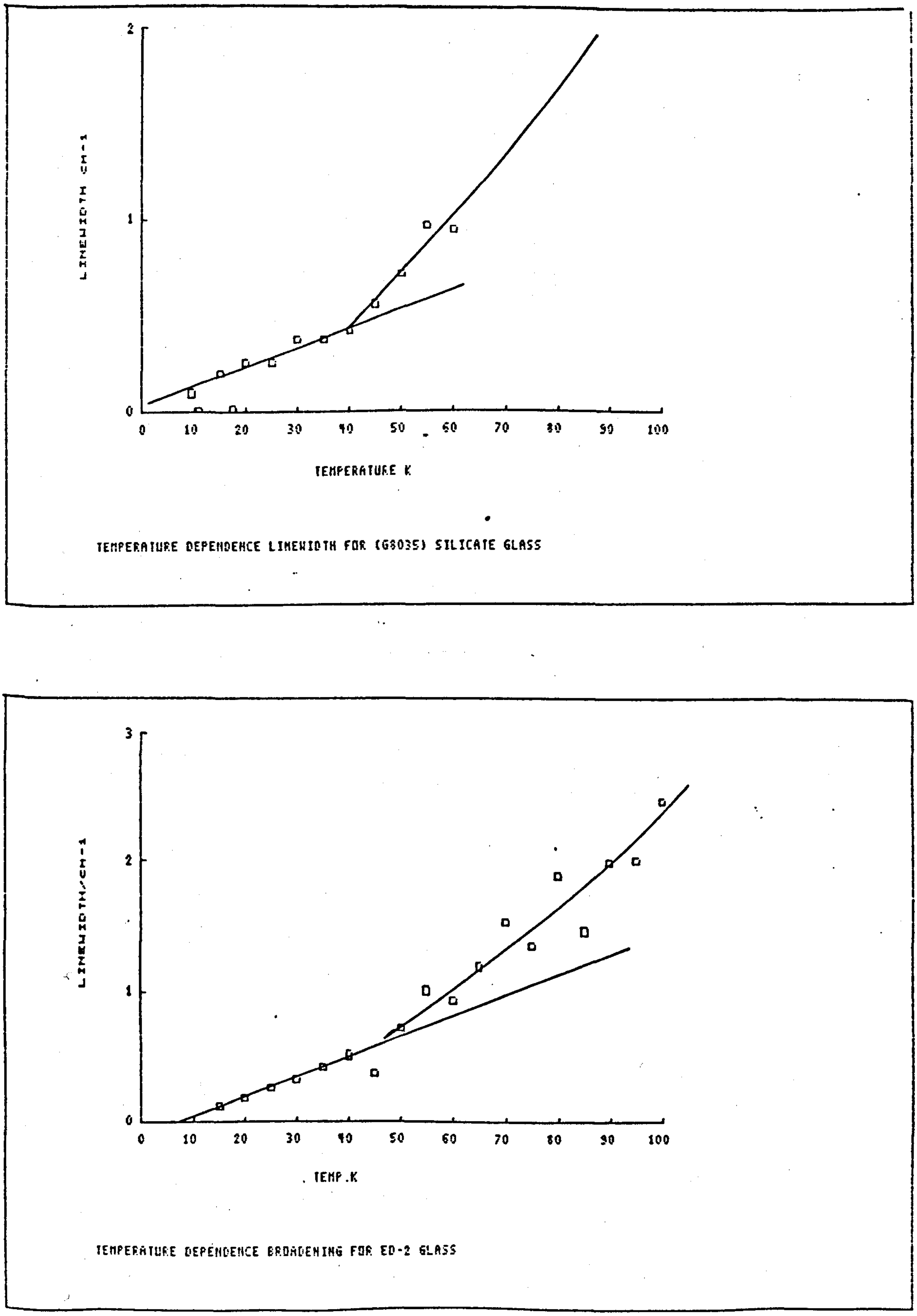

TEMPERATURE DEPENDENCE LINEWIDTH FOR (G8035) SILICATE GLASS

TEMPERATURE DEPENDENCE BROADENING FOR ED-2 GLASS

Fig 6.10 Homogeneous linewidth variation with temperature for
a - G8035 silicate glass
b - ED-2 glass

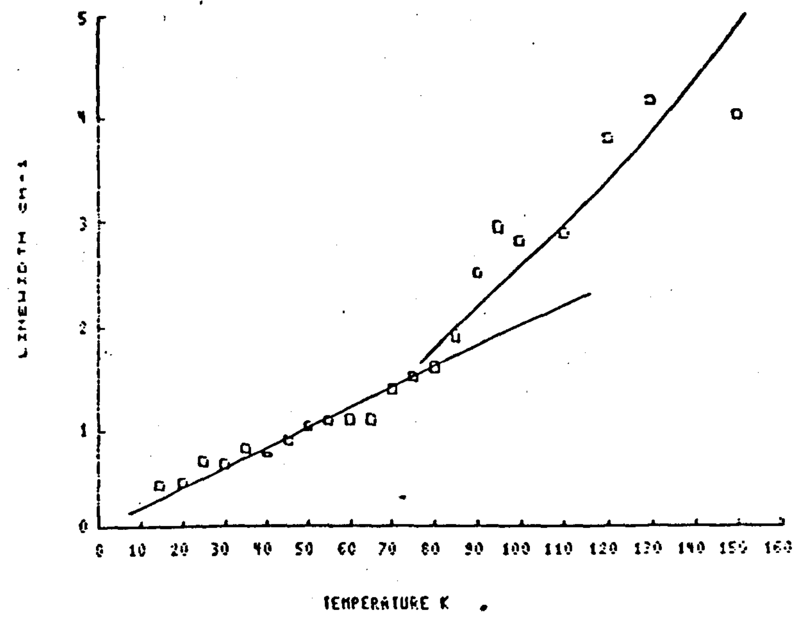

TEMPERATURE DEPENDENCE LINEWIDTH FOR Li-BORATE GLASS(G8382)

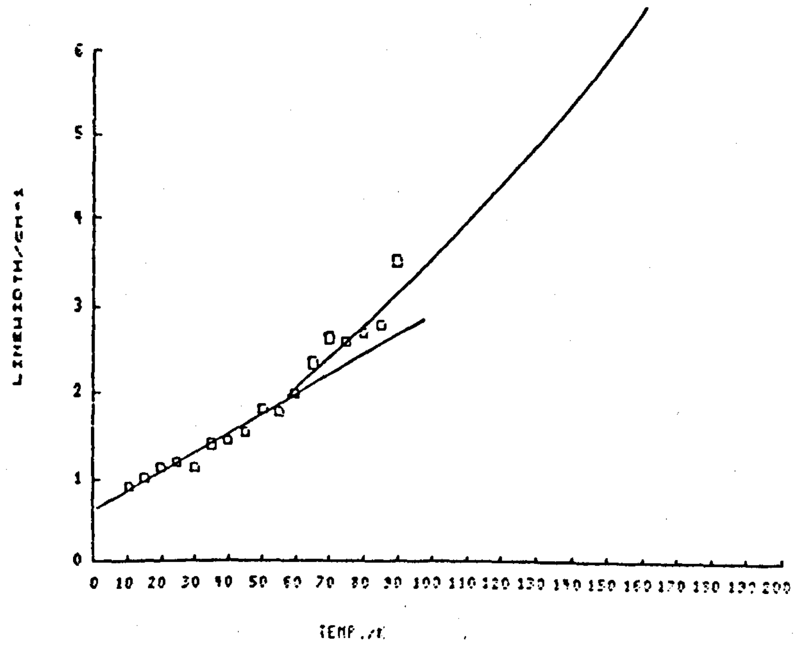

TEMPERATURE DEPENDENCE LINEWIDTH FOR (G8150)K-BORATE GLASS

Fig 6.11 Temperature dependent homogeneous linewidth results for
a - G8382 Li-borate glass
b - G8150 K-borate glass.

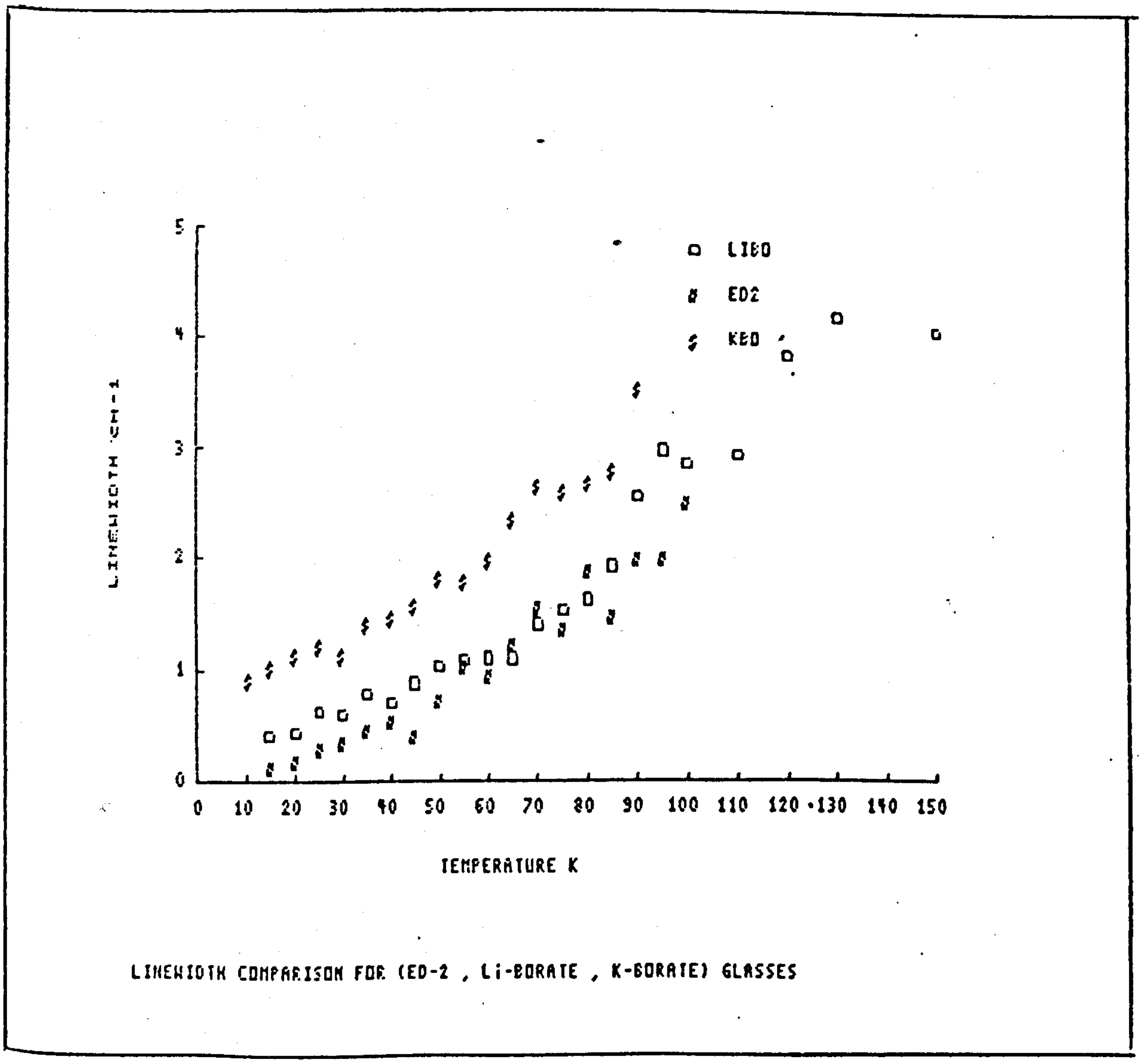

Fig 6.12 Comparison between the linewidths of silicate and borate glasses

accompanies the FLN line will be used to infer the density of the vibrational modes for the glass matrix in a method used by Bergin et al.[50] Two models of orbit lattice coupling are invoked, the strain model[121] which is used for crystalline hosts, while for glassy materials the amplitude model is more suitable.[50] This is because the effective coupling parameter is thought to be the localized amplitude of vibrations and not the strain of vibrations[120] due to the lack of long range forces and the disorder in the glass matrix.

The intensity of the sideband can be expressed as:

$$I^{s}(\omega) = \frac{C}{V^{2}} |\langle V\rangle|^{2} \omega\rho(\omega) \tag{6.2a}$$

according to the strain model, while for the amplitude model it is:

$$I^{a}(\omega) = C|\langle V'\rangle|^{2} \omega^{-1} \rho(\omega) \tag{6.2b}$$

where V is the average velocity of sound, C is the same constant for both relations, V and V' are the electronic sensitivity factors for the strain and amplitude models, respectively and $\rho(\omega)$ is the density of vibrational states at angular frequency ω. Bergin notes that using the strain model to derive the density of states yields a distribution which is heavily weighted at low frequencies,[50] hence the amplitude model is thought to be more appropriate to describe the ion-lattice coupling in the glass.

Because of the weakness of the sideband which accompanies the FLN line of the k-borate glass, fig (6.7b), the shape of the sideband is a result of the averaging of many runs of the spectra and the values of the intensity $I(\omega)$ against ω are shown in fig (6.13). According to the amplitude model, the density of vibrational modes should vary as $\omega I(\omega)$ (see eq. 6.2b). The density of modes for k-borate glass based on the amplitude model is also shown in fig (6.13). We will use the following approximate numerical expressions for the density of vibrational modes based on the amplitude model of the orbit-lattice coupling and utilizing the observed sideband

$$\rho^g(\omega) = \xi\omega^2 \qquad 0 < \omega < 50 \text{ cm}^{-1}$$

$$\rho^g(\omega) = 2\xi\omega_1^2 \qquad 50 = \omega_1 < \omega < 350 \text{ cm}^{-1}$$

For the case of crystals, the Debye formula was found to be suitable for the expression of the vibrational density of states.[121] Hence:

$$\rho^c(\omega) = \gamma\,\omega^2 \qquad 0 < \omega < 350 \text{ cm}^{-1}$$

For equal numbers of vibrational modes per unit volume of the glass and the crystal, it is possible to evaluate the ratio ξ/γ as follows:

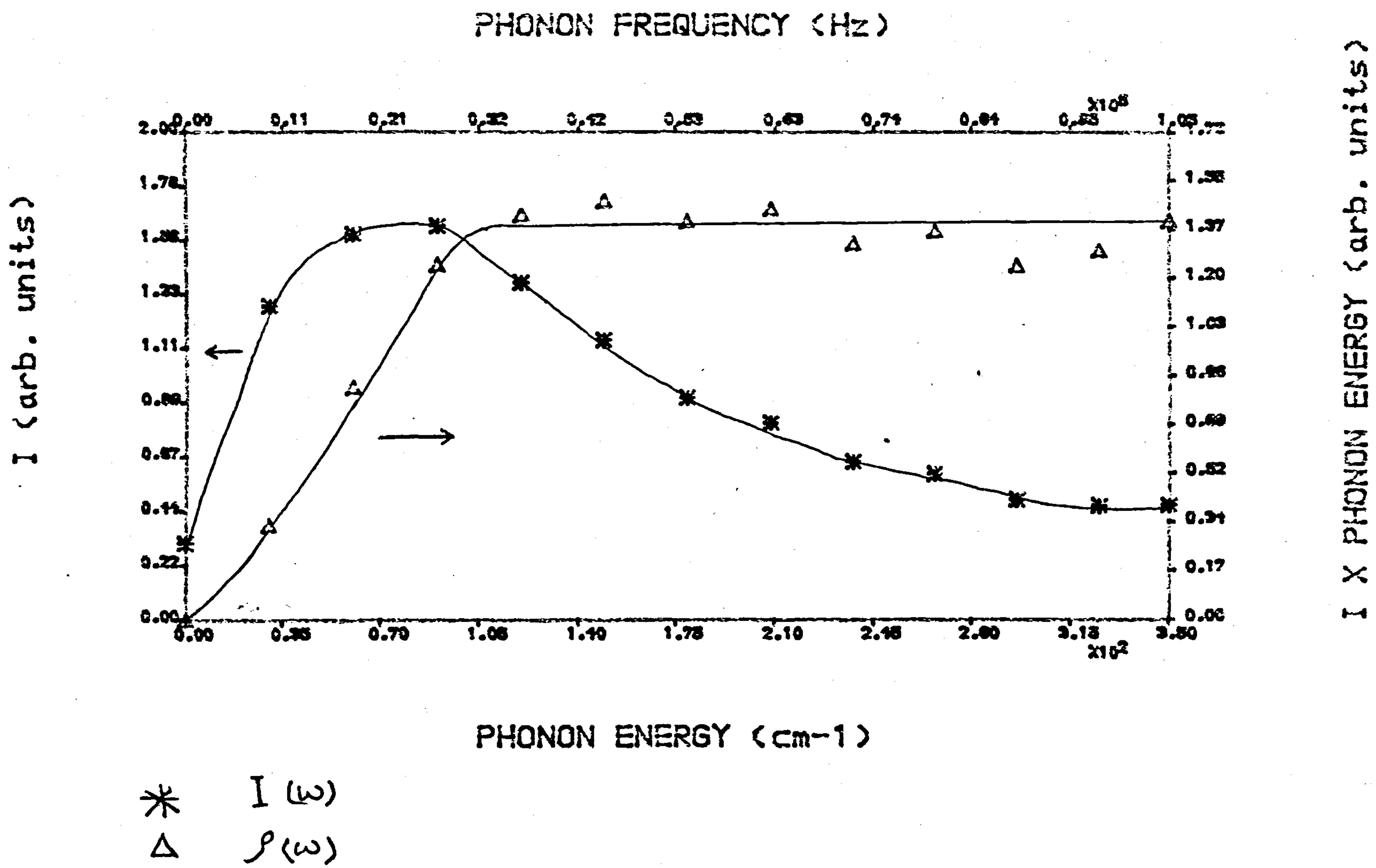

Fig. 6.13 Calculations of the vibrational density of states

$$\int_{0}^{\infty} \rho^{c}(\omega)\, d\omega = \int_{0}^{\infty} \rho^{g}(\omega)\, d\omega$$

$$\therefore \frac{\xi}{\gamma} = 53.6$$

The observed ratio of the zero-phonon line to the sideband of the G8150 glass, was approximated from many spectra and found to be around 6 (which is weaker than that of the ED-2 silicate glass). The ratio compared to a typical crystal, for which the value of ~ 1 is found, so :

$$\frac{\int_{0}^{\infty} I^{c}(\omega)d\omega}{\int_{0}^{\infty} I^{g}(\omega)d\omega} \simeq 6$$

Again substituting the Debye formula for the density of states of crystals and the amplitude model for the glass gives:

$$\frac{\frac{C}{v^2}|\langle v\rangle|^2 \int_{0}^{350} \gamma\ \omega^3\, d\omega}{C|\langle v'\rangle|^2 \int_{0}^{50} \xi_p \omega d\omega + \int_{50}^{350} 5000\ \omega^{-1}\ \xi\, d\omega} \simeq 6$$

Therefore $$\frac{|\langle v\rangle|^2\ \omega_1^2}{|\langle v'\rangle|^2 v^2} \simeq 0.6 \qquad (6.3)$$

which is the ratio of the "sensitivity factors" for the glassy and crystalline systems.

Now we examine the possibility that the higher power part of the temperature dependent homogeneous broadening curve of a Cr^{3+} doped glass is due to a Raman relaxation process (see section 2.7). The linewidth according to Raman relaxation mechanism can be written in the form:[120]

$$\Gamma(T) = A \int_0^\infty |\langle H^a_{oL}\rangle|^4 \rho^2(\omega) \frac{e^{\hbar\omega/kT}}{(e^{\hbar\omega/kT} - 1)^2}\, d\omega \qquad (6.4)$$

where A is a constant, and $H^{(a)}_{oL} = \alpha v' \sum_\omega \omega^{-\frac{1}{2}}(a^*_\omega + a_\omega)$, α is a constant.

In order to compare the value for the linewidth of the glass to that of the crystal at a certain temperature, the values of the sensitivity factors in the expressions for the sideband intensity (equation (6.3)) and the broadening (equation (6.5)) are assumed to have the same numerical values, and by using the amplitude model to substitute for the glass density of state, while the Debye density of states is used for crystals, equation (6.4) can be written as:

$$\Gamma^c(T) = \frac{A\alpha^4 |\langle v\rangle|^4 \gamma^2}{v^4} \int_0^\infty \frac{\omega^6 e^{\hbar\omega/kT}}{(e^{\hbar\omega/kT} - 1)^2}\, d\omega \qquad (6.5a)$$

$$\Gamma^{9}(T) = A\alpha^{4}|\langle v'\rangle|^{4} \int_{0}^{\infty} \frac{\omega^{-2}\rho^{2}(\omega)\, e^{\hbar\omega/kT}}{(e^{\hbar\omega/kT}-1)^{2}} \qquad (6.5b)$$

The value of the ratio of the homogeneous broadening of the crystal relative to that of the glass is evaluated from the last two expressions at the temperature $T = 80K$ and found to be

$$\frac{\Gamma^{c}(80)}{\Gamma^{g}(80)} = 0.021$$

This value is to be compared to the ratio of the experimentally measured values of the ruby crystal (0.17 cm^{-1} at 80 k[121]) and the k-borate glass (~ 2.8 cm^{-1}) which is equal to 0.065. The order of the observed and calculated ratio of the linewidth can be accepted recalling the simplified assumptions of the models used in the calculations of the vibrational density of states. However such results strengthen the idea that the Raman relaxation mechanism could be the cause for the broadening at high temperatures in glasses in a similar manner to the case of crystals.

6.4 Zeeman Splitting of the FLN Spectra

The splitting of the optical lines in the presence of a static magnetic field is related to the removal of the electron spin degeneracy of the energy levels involved in the transition. Normally hyperfine splittings in solids are masked by the effects of inhomogeneous broadening. In principle, Zeeman spectroscopy reveals the energy level structure of optical centres in solids. We noted in previous sections that the FLN is essentially an ultra-high resolution technique which reveals features in the emission spectrum that are obscured by the inhomogeneous broadening process. FLN is particularly useful in understanding the behaviours of the different Cr^{3+} doped glasses. However, although the observation of the R_1 and R_2 components implies site symmetry lower than the octahedral resulting in the split of the ^2E level,[108] the actual symmetry distortion has not been identified. One means of identifying the site symmetry is to measure the Zeeman splitting of the ^2E level in these glasses through the effect of a magnetic field on the resonant FLN component of the $^2E \rightarrow {}^4A_2$ transition. We recall from Section (3.6.2) that the energy separation equation

$$E = m_s g \mu_B B \qquad (6.6)$$

and the energy level separation is linearly related to the applied magnetic field. That the R-lines are observed in glass samples confirms the presence of Cr^{3+} ions in high field sites and the splitting of the R-line in the FLN spectra demonstrates that the octahedral symmetry is lowered by trigonal or tetragonal distortions. The number and strength of transitions in a magnetic field may be calculated for the two types of distortion using the techniques of Tanabe and Kamimura[109] for comparison with the experimentally observed Zeeman splitting of the $^2E \rightarrow {}^4A_2$ transition.

The pattern of Zeeman lines will identify the site symmetry of the Cr^{3+} ion. The Zeeman-split FLN spectra of the G8035 silicate glass measured at 1.6K for a range of magnetic fields parallel to the detection direction are shown in figure (6.14). At low fields, below B = 2T, the FLN line broadens; recognizable splittings are resolved at higher fields (e.g. B = 2.9 and 3.87T in figure (6.14)). Better resolution could not be achieved in this glass because of the weak FLN signal. However in the ED-2 glass, the amount of Li_2O is greater than that in G8035 yielding a larger number of high field sites and a larger $^2E/^4T_2$ intensity ratio. Moreover in the G8035 glass the lower R-line emission intensity may be due to concentration quenching in the presence of large Cr^{3+} concentrations. In consequence, rather better resolved Zeeman spectra can be seen in figure (6.15) for the ED-2 glass. Four strong lines are clearly resolved as the magnetic field increases to 3.87T. In both figures (6.14) and (6.15), one line is resonant with the laser line at all field values; this line always has the largest intensity. The other two strong lines originate on the lower Zeeman-split energy levels, where as the higher lying line is weaker by virtue of the Boltzmann factor.

Consider the case of a trigonally-distorted octahedral symmetry site in conjunction with spin-orbit interaction between the $^4T_2$ and the ^2E levels. This is just the case of Cr^{3+} in Al_2O_3, where the combined effects of trigonal field and the spin-orbit coupling split the ^2E level into $2\bar{A}(^2E)$ and $\bar{E}(^2E)$ sublevels, which are doubly

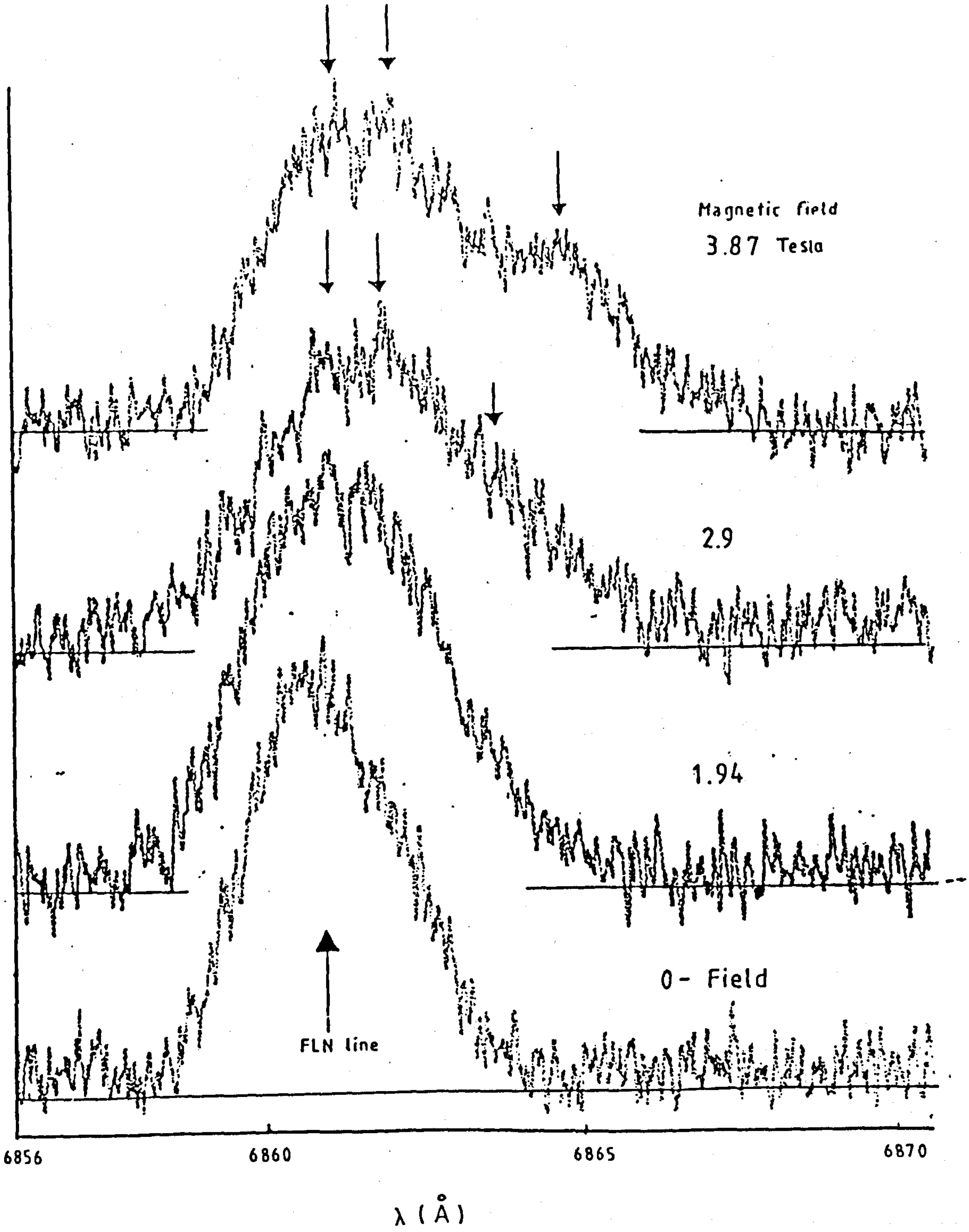

Fig 6.14 Zeeman splitting of the FLN spectrum of the G8035 silicate glass at 1.6K and 6861 Å excitation.

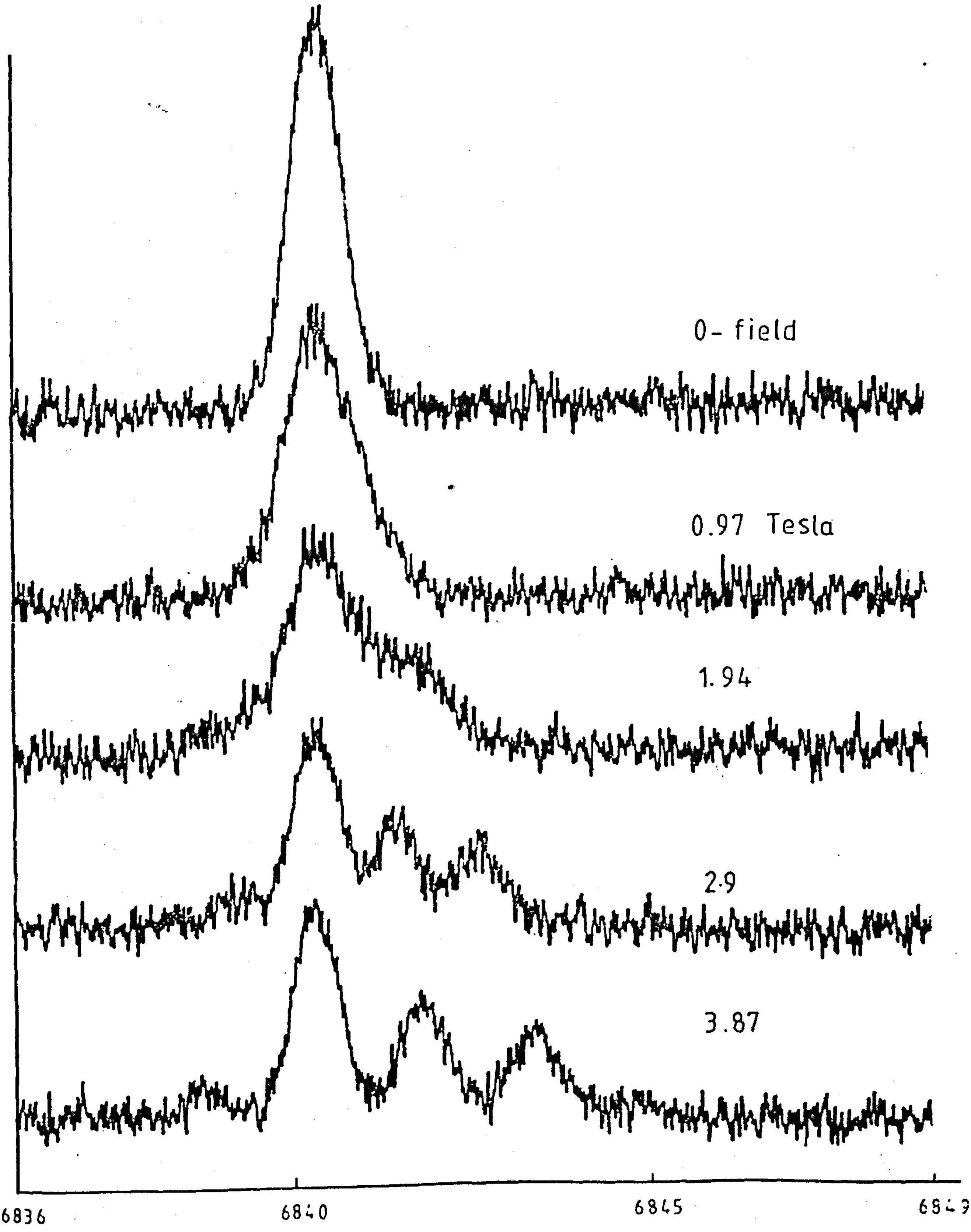

Fig 6.15 Zeeman splitting of the FLN spectrum of the ED-2 glass at 1.6K, excitation laser wavelength 6840 Å.

degenerate in spin, with the values of ± 1/2. The applied static magnetic field results in a coupling between the electron and field determined by the sign of the spin. This is just the Zeeman splitting energy in equation (6.6), for the values of $m_s = \pm 1/2$. The combined effects of trigonal distortion and spin-orbit coupling also split the ground $^4A_2$ state. However since the splitting is very small, ~ 0.5 cm^{-1},[108] compared to the ^2E splitting (~ 55 cm^{-1}) it may be neglected. Nevertheless the four-fold Zeeman splitting of the ground state due to spin degeneracy will be reflected in the transitions between the ^2E and the $^4A_2$ as is illustrated in figure (3.12). The intensities of the different Zeeman components may be calculated as follows. The spin forbidden radiative transitions between the ^2E and $^4A_2$ states become weakly allowed when spin-orbit coupling is introduced, while the electric dipole operator $\mu_e.E$ connects the $^4T_2$ and the $^4A_2$ states. Hence the intensity is derived from the $^4A_2 \rightarrow {}^4T_2$ transition intensity. The matrix element for the $^2E \rightarrow {}^4A_2$ transition is written as:

$$\frac{\langle {}^4A_2 m_s | \tilde{\mu}_e . E | {}^4T_2 \phi m_s \rangle \langle {}^4T_2 \phi m_s | H_{so} | {}^2E \phi' m'_s \rangle}{(E({}^2E) - E({}^4T_2))} \qquad (6.7)$$

where ϕ is the particular orbital participating in the transition, $\tilde{\mu}_e.E$ is the product of the odd parity electric dipole operator and an odd parity crystal field operator. The separation between the ^2E and the $^4T_2$ levels is ~ 700 cm^{-1} for silicate glasses (see chapter 5) while the $^4T_1$ level is too far from the ^2E level to make a significant contribution to the transition strength. In trigonal symmetry such as in Al_2O_3, the Cr^{3+} ion is placed between two oxygen triangles parallel to each other as discussed for Ti^{3+} in Al_2O_3 in chapter 4. There are numerous ways of breaking the inversion symmetry at the Cr^{3+} ion site (see reference [36]). A dominant odd parity crystal field term of type $T_{1u}a_o$ would be caused by displacement of the Cr^{3+} ion along the trigonal axis from a position midway between the two oxygen planes. When the electric vector of the radiation is parallel to the trigonal axis (π-polarization), the operator $\tilde{\mu}_e.E$ has the form $T_{1u}a_o \times T_{1u}a_o$. From the table of Clebsch-Gordon coefficients (Appendix A), we find that this contains even parity components $(-1/\sqrt{3})A_{1g}$ and $(-\sqrt{2}/\sqrt{3})T_{2g}X_o$. Since $A_2 \times A_1 = A_2$ and $A_2 \times T_{2g}X_o = T_{1g}a_o$, it is clear that there are no matrix elements of the π-polarized dipole operator between $^4A_2$ and $^4T_2$ states. Hence a distortion of different parity is needed. If this is an odd parity term $T_{2u}X_o$, the effective dipole operator is $T_{1u}a_o \times T_{2u}X_o$ giving $(-1/\sqrt{3})$ A_{2g} and $(\sqrt{2}/\sqrt{3})$ $T_{1g}a_o$ components. Hence the transition between $^4A_2$ and $^4T_2X_o$ is allowed in the presence of $T_{2u}X_o$ distortion. The other part of the matrix element (6.7), is the spin-orbit coupling between ^2E and $^4T_2$ levels. Since the experiments were carried out at low temperature and since the trigonal splitting is ~ 55 cm^{-1}, we can disregard any emission from the upper $2\bar{A}(^2E)$ state, expecting that the thermalization of the state is much faster than the radiative lifetime, so operating $^4T_2X_o$ on $\bar{E}(^2E)$ of the ^2E state via the spin-orbit coupling and using the tables in Appendix B to find the non-zero matrix elements suggests the involvement of $^4T_2X_o$

orbitals with H_{so} and $\bar{E}(^2E)$ states.

For the case of the emission polarized linearly in the X-direction perpendicular to the trigonal axis (σ-polarization), the operator of the odd parity electric dipole is of the type $T_{1u}(-a_+ + a_-)/\sqrt{2}$. Combining this operator with the odd parity trigonal crystal field operator yields $T_{1u}(-a_+ + a_-)/\sqrt{2} \times T_{1u}a_o$. Again the Clebsch-Gordon coefficients can be found from Appendix A. The two components $T_{1g}a_+$ and $T_{1g}a_-$ give non-zero matrix elements of the $\mu_e.E$ between $^4A_2$ and $^4T_2X_+$, and $^4A_2$ and $^4T_2X_-$. The spin-orbit coupling part of the matrix element is evaluated using Appendix B to find the value of the matrix elements

$$\langle {}^4T_2X_+ + 1/2 | H_{so} | {}^2E \begin{matrix} u_+ - 1/2 \\ \\ u_- + 1/2 \end{matrix} \rangle, \quad \langle {}^4T_2X_- - 1/2 | H_{so} | {}^2E \begin{matrix} u_+ - 1/2 \\ \\ u_- + 1/2 \end{matrix} \rangle$$

The square of these matrix elements gives the intensity of the emission components. Recalling the measurements in figure (6.15), the three strong lines may be attributed to transition from the lower component of $\bar{E}(^2E)$ level only, while the weak line at the high energy side of the spectrum could be due to a transition from the upper sublevels of the $\bar{E}(^2E)$ level. This assignment could be justified by the expected thermalization due to the very low temperature of the sample (1.6K). Figure (6.16) illustrates the expected emission for the $\bar{E}(^2E) \rightarrow {}^4A_2$ transition. Such results

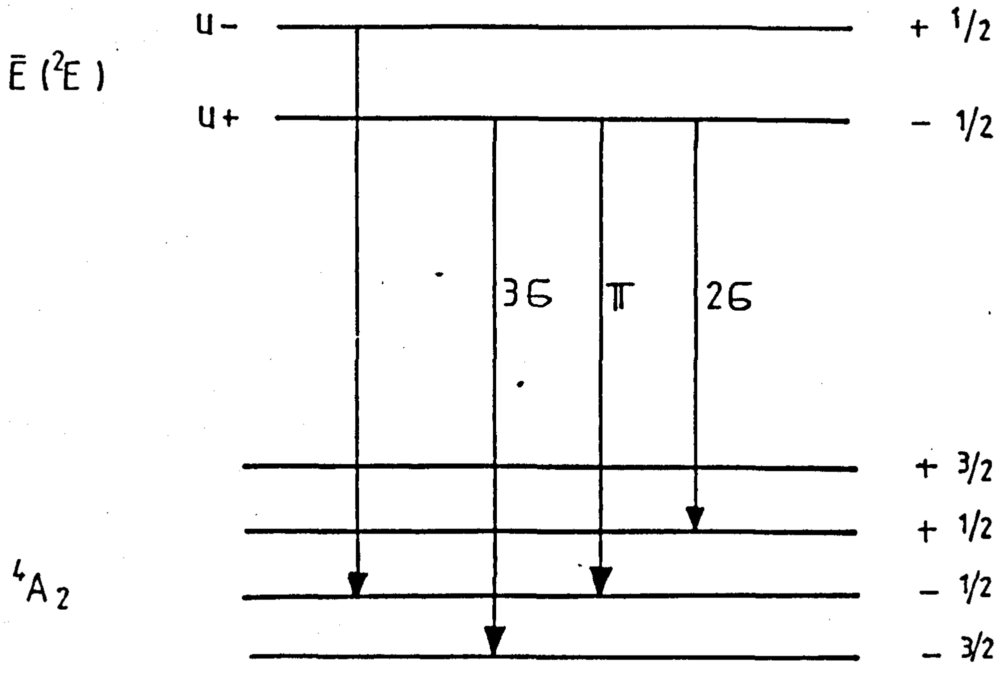

Fig 6.16 Emission pattern for the $\bar{E}(^2E) \rightarrow {}^4A_2$ transition of the Cr^{3+} doped glass treated as trigonally distorted octahedral sites (the σ-polarization intensity is normalised to the π-polarization value).

cannot be explained using a tetragonal distortion of the oxygen octahedra.

6.5 Discussion

FLN measurements for different Cr^{3+} doped glasses revealed features which are not identified using conventional spectroscopy because of the strong inhomogeneous broadening. the splitting value of the ^2Ed level measured as ~ $52cm^{-1}$, $57cm^{-1}$, $58cm^{-1}$ and $105cm^{-1}$ for the ED-2, SLS7b/7, G8150 K-borate, and G8382 Li-borate glass, respectively, being almost constant when measured over the total width of the ^2E emission of these samples. Together with the nearly constant measurements of the decay rates across the ^2E emission discussed in the previous chapter, it may be possible to invoke some general order governing the behaviour of high field sites in these materials, similar to the case of crystalline solids. FLN spectra for the G8382 glass showed that the resonant-excitation of the ^2E complex identifies the existence of the ^2E level which peaked at ~ 681nm as an electronic level which is resolved from the other centre discussed in the previous chapter.

Most of the homogeneous linewidth measurements in inorganic glasses have been carried out using rare earth doped systems[110,111,48] showing that the homogeneous linewidth at low temperatures were some two orders of magnitude broader than that in crystals, and that linewidth increased quadratically with temperature. Similar results were obtained for Eu^{3+} doped glass over the temperature range 300-650K.[112] The quadratic variation of the homogeneous linewidth with the temperature is consistent with a two-phonon Raman relaxation process similar to that observed in crystals.[113] That phonon-like acoustic and compressional excitations of the amorphous solid are involved, is suggested by comparing the homogeneous linewidth variation with temperature and the velocity of sound[114] for crystalline and glassy solids. In fact for Nd^{3+}-doped glass the homogeneous width of the $\Delta\nu_H'$ is proportional to $v^{-2.5}$, v being the velocity of sound. However at very low temperatures, a linear relation was measured for the $^3H_4 \leftrightarrow {}^1D_2$ homogeneous linewidth of Pr^{3+} in silicate glasses using spectral hole burning.[111] In other measurements on Nd^{3+} doped silica optical fibre using a photon-echo method showed a $T^{1.3}$ variation over the range 0.1-1K.[114] Similar results obtained for Yb^{3+} doped phosphate glass over the temperature range 7-90K.[105] The deviation from the crystal-like linewidth at low temperatures suggests an additional broadening mechanism broadens the line in glasses. By general agreement, this originates with the interaction of the doped ion and the tunnelling modes of a two level vibrational system or simply (TLS). Such vibrational excitations of glasses were discussed in chapter 5 to explain the anomalous thermal properties in glases. Huber et al.[115] have suggested that the optical dephasing results from the electric dipole-dipole interactions between the rare earth ions and the TLS, this mechanism gives a satisfactory account of the observed temperature dependence of the linewidth in the low temperature region. Theoretical calculations for the broadening assuming the interaction between the ion and the spectrum of the TLS also accounts for a $T^{1.3}$ law.[116] Organic glasses showed a similar $T^{1.3}$ variation.[117]

Unlike the rare earth ions, the linewidth studies for T.M.I. in glasses were very little. The study of the linewidth-temperature variation of Cr^{3+} doped ED-2 glass, Bergin et al.,[50] shows two contributions, a linear variation at low temperatures (5-70K) and an approximately quadratic part at higher temperature interpreted as Raman Scattering of thermally excited vibrational excitations which have a non-Debye density of states. The temperature dependence linewidth measurements of the FLN lines for the four samples, including the ED-2 glass, show similar variation results to those found previously in Cr^{3+}:ED-2 glass,[50] which confirms that at high temperature the transition is broadened by a Raman relaxation mechanism which varies approximately quadratically with temperature similar to that observed in some rare earths. The variation is almost linear at low values of temperature (see figures 6.10, 6.11). The homogeneous linewidth of the K-borate glass is also calculated using the same procedures followed in reference [50], where the shape of the effective density of state of the vibrational modes was inferred from the emission sideband shape. To derive the density of vibrational modes, two models for the coupling between the ion and the host were invoked, the strain and the amplitude models. The results are consistent with the conclusion that a higher density of low frequency modes compared to the crystalline materials causes an increased homogeneous broadening of the R-line in glasses.

An effort to detect the circular polarization of the FLN spectra of both the G8035 and ED-2 silicate glasses, using the magnetic circular polarization (MCP) technique explained in section (3.6.2), showed no significant signal in either of the senses of the circular polarization, even for the quite strong, well resolved signal as for the ED-2 glass. This suggests that the orbital angular momentum operators are strongly quenched in these glassy materials so destroying the circular polarization.

The direct Zeeman splitting of the ^2E excited and $^4A_2$ ground state energy levels was observed, the separation between the four lines is ~1.9 Å at 3.87T. The relation between the applied magnetic field and the energy of these lines for the ED-2 glass is shown in figure (6.17), where the resonant FLN line can be seen fixed at certain energy with different field values. The reason could be that when there is a shift of the energy levels among the subset of sites, the laser line keeps pumping certain sites at the same energy value. A nearly similar assignment of the Zeeman splitting lines for the measurements of Cr^{3+} in an organic material (tri (acelylacetanto)),[118] although the excited state in this material was assigned to a $^2T_1$ rather than the ^2E state, also the weak fourth line was placed as the lowest energy level.

Fig 6.17 Energy level splitting variation with the applied magnetic field for the ED-2 glass at 1.6K.

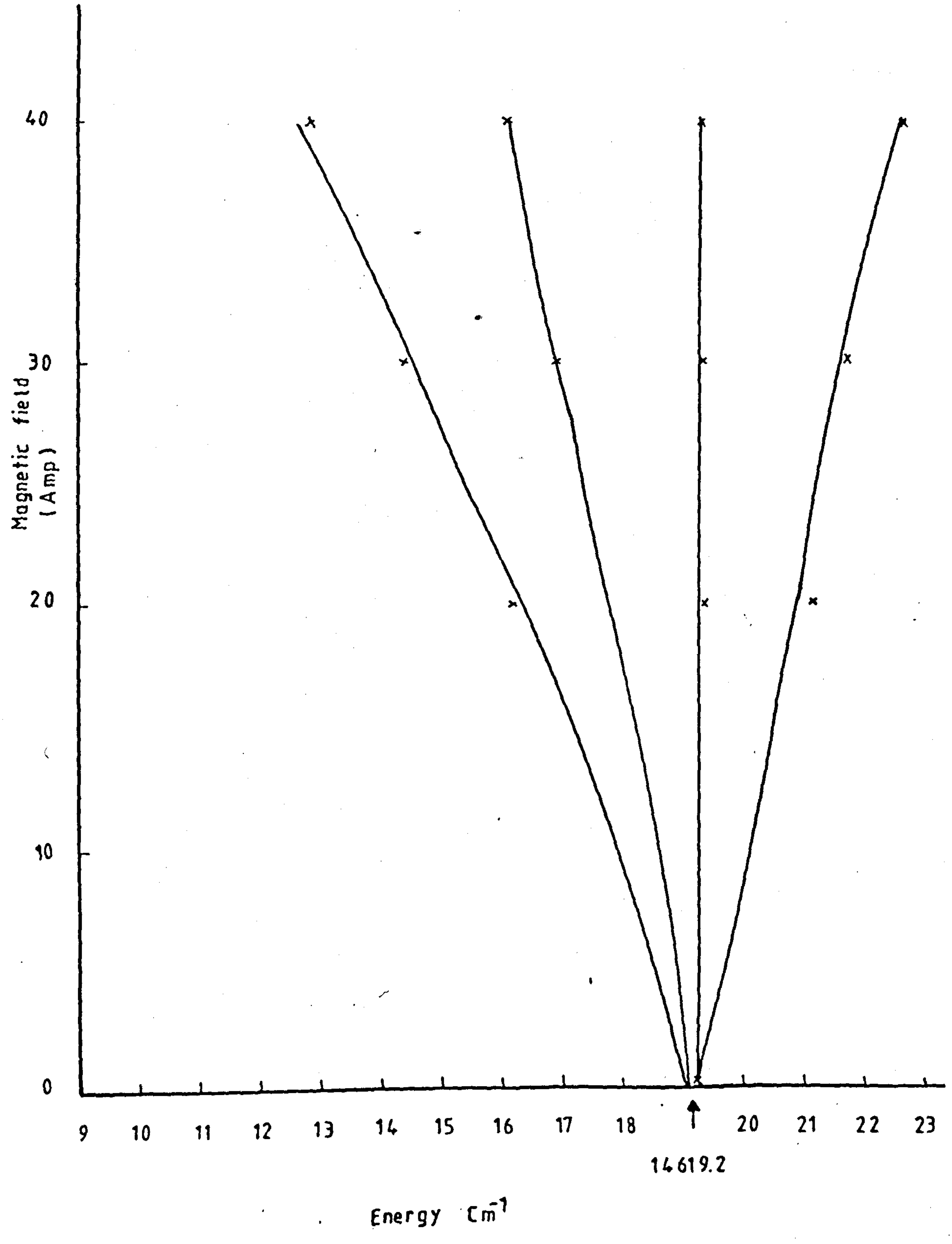

The assumption of the similarity of the high field Cr^{3+} site in glasses and that in ruby, also that the electric dipole transition is activated by the odd parity crystal field component of $T_{1u}a_o$, gives a resonable agreement between the results of the detected spectrum and the theoretical calculations of the transition intensities.

In order to calculate a value for the excited state g-value for the ED-2 glass utilizing the Zeeman splitting values measured from fig (6.15), the Zeeman splitted line positions are shown in the energy level diagram (fig. 6.18) where these transitions are governed by the selection rule $\Delta m_s = 0, \pm 1$ for the transitions $|-\frac{1}{2}\rangle \rightarrow |+\frac{1}{2}\rangle, |-3/2\rangle, |-\frac{1}{2}\rangle$ and the weak transition $|+\frac{1}{2}\rangle \rightarrow |-\frac{1}{2}\rangle$. Since the ground state splitting is very small,[108] the energy values of the last two transitions can be written as:

$$E_1 = E_o - \tfrac{1}{2}\, g_e\, \mu_B\, B + 3/2\, g_g\, \mu_B\, B \qquad (6.8)$$

$$E_2 = E_o + \tfrac{1}{2}\, g_e\, \mu_B\, B + \tfrac{1}{2}\, g_g\, \mu_B\, B \qquad (6.9)$$

where g_e and g_g are the excited and ground state g-values respectively. Although two values for the ground state g-value were noted before[92] (see section 5.4), our EPR measurements of the ground state g-value for the ED-2 and the SLS7b/4 glasses (mentioned in section 3.6.2) showed only one value at ~ 1.95. Recalling the Low Cr^{3+} ion concentration in both glases (0.05 wt % for ED-2 and 0.11 wt % for SLS7b/4 glasses) we believe that this g ~ value measured for such glasses, which is consistent with values measured for Cr^{3+} doped oxides (e.g. Cr^{3+}:MgO), is due to Cr^{3+} ion sites and not to Cr-Cr pairs as noted before, so from equation (6.8, 6.9) and referring to fig (6.15), the energy splitting E_1-E_2 is ~3.4 cm^{-1}, and substituting for g_g, the excited state g-value is found to be equal to 3.8. Having g_e-value higher than g_g justifies the existence of the weak transition at the high energy side of fig. (6.15).

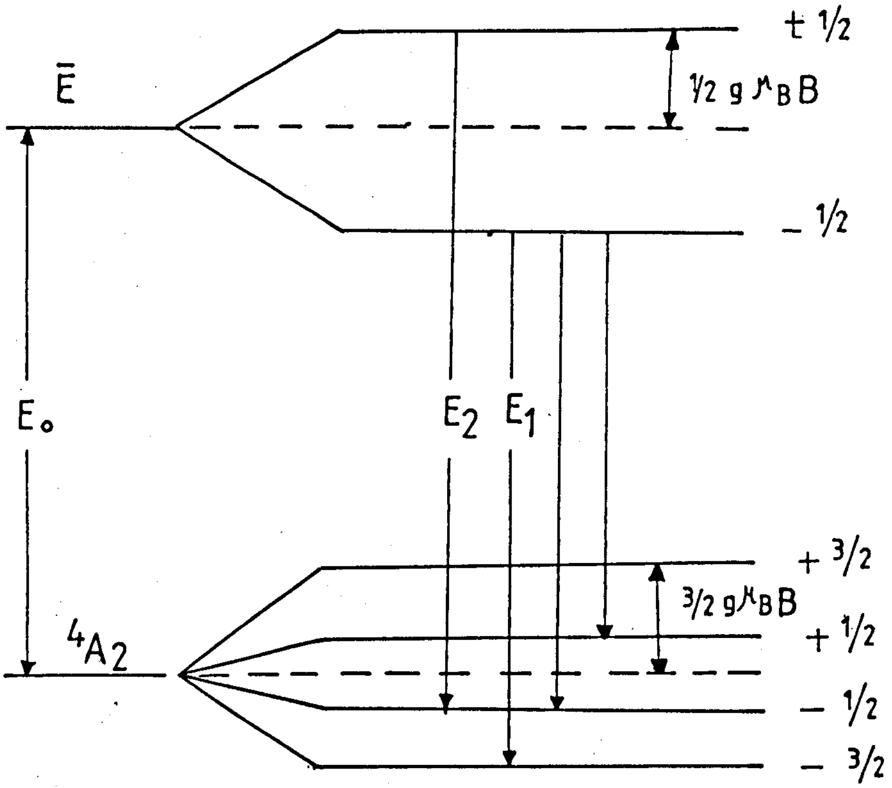

Fig 6.18 Calculations Of the energy level positions for the Cr^{3+} doped glass (See section 6.5)

CONCLUSIONS

In this study we carried out spectroscopic measurements of Ti^{3+} and Cr^{3+} ions doped in some crystalline and glassy materials. The coupling of Ti^{3+} to different crystal hosts showed wide emission bands (~3000cm^{-1} except for Ti:YAP which was about half this value) as well as the emission at different regions of the visible - near infra-red parts of the spectrum (Ti:YAP peaked ~600nm while the Ti:Al_2O_3 peak was at ~760nm). Considering the temperature dependence emission intensity, the bandwidth measurements and the crystal structure showed that the quantum efficiency was reduced down to 9% for the Ti:YAG and to 80% for Ti:Al_2O_3. While the observed intensity for the Ti:YAP crystal was increased with increasing temperature, without an indication of the non-radiative decay. Absorption measurements of these crystals showed an absorption band at ~750nm due to another site. the overlapping of such absorption band with the emission band, could be a deletrious effect for the lasing action. Time resolved spectra for Ti^{3+}:glass revealed a wide range of sites in such systems. The temperature quenching was high, as well as the concentration quenching which was found to be a very effective factor on the emission. However Ti^{3+} doped crystals have good characteristics which favour them as laser candidates like the broad emission and absorption bands, the absence of the excited state absorption (ESA), the large Stokes' shift (~6500cm^{-1}) which reduces the reabsorption of the emission, the high thermal conductivity and more other properties. With better growth conditions, most of the disadvantages like the infra-red absorption which was mentioned in section (4.4) and the Cr^{3+} inclusions will have a lower effect.

Since the main difference between Ti^{3+} and Cr^{3+} in high to medium field crystals is the existence of a metastable level in the latter. This elongates the lifetime of the upper state and resulting in a reduction of the emission cross·section as discussed in chapter 4. On the other hand one of the disadvantages of Ti^{3+} doped crystals is their short lifetime.

The absorption measurements of the Cr^{3+} doped in a variety of glass matrices showed that the normalized field strength Dq/B is between (2.4-1.8) which suggests a range of crystal fields near the crossover point between the ^2E and the $^4T_2$ states in such materials, categorizing the crystal field strength in the order of Borate > silicate > phosphate > fluoride. In the site selection measurements for Cr^{3+}:glasses a wide range of sites was observed with band maxima of the $^4T_2 \rightarrow {}^4A_2$ broad transition from (820-1000)nm, with a non-exponential relaxation time. A shift of the emission peak towards longer wavelengths as the excitation wavelengths goes to higher values is noticed, also the peak is shifted towards higher wavelengths as the temperature lowered down, in contrast to the case of crystals. The data showed that the luminescence is quenched due to the overlapping of the $^4T_2$ and the

$^4A_2$ potential energy curves, where high values of non-radiative decay is expected to be dominant in such materials. Consequently the quantum efficiency is very low (~ 1% at room temperature).

Time resolved spectra showed vibronic sideband features accompanying the ^2E zero phonon line in different high field sites in glasses. Also the identification of a new site in the (G8382) Li-borate glass was possible which suggested a O^{-2}-Cr^{3+}-Li^{2+} cluster. The wide coverage of the emission spectrum of those glasses (e.g. 700-1400nm for the fluorozirconate) in addition to the cheap cost of fabricating such samples is still the interesting factor of more studies in Cr^{3+} doped glasses.

The wide ^2E emission (~200cm^{-1}) for Cr^{3+} doped glasses reflects the spread of crystal fields affecting the Cr^{3+} ion in the high field sites. The RFLN technique was applied to the $^2E \rightarrow {}^4A_2$ in different glasses where an almost constant splitting around 50-55cm^{-1} was found for the silicates and as high as 100cm^{-1} in the Li-borate glass. These nearly constant values could suggest a certain arrangement of the Cr^{3+} ion at those high field sites, similar to the case of crystals. This postulation is strengthened by the similar decay rates measured across the ^2E emission. The temperature dependence linewidth of the FLN signal of four glasses confirmed a previous result by Bergin et al.[50] which was the only Cr^{3+} glass measurement, that the linewidth variation at high temperature is almost quadratic in a similar mechanism to that found in crystals, while the relation was nearly linear at low temperatures, which is similar to values found in rare earth doped glasses.

Finally, Zeeman experimnents for the FLN signals showed for the first time the splitting of the zero phonon lines in Cr^{3+} doped glasses, from which the type of symmetry was concluded.

APPENDIX A

Relevant Clebsch-Gordon coefficients with trigonal bases for the products $T_1 \times T_1$ and $T_1 \times T_2$.

$T_1 \times T_1$

	Γ	A_1	E		T_1			T_2		
M_1	M_2 M	e_1	u_+	u_-	a_+	a_-	a_0	x_+	x_-	x_0
	a_+	0	0	$-1/\sqrt{3}$	0	0	0	0	$-\sqrt{2}/\sqrt{3}$	0
a_+	a_-	$1/\sqrt{3}$	0	0	0	0	$i/\sqrt{2}$	0	0	$-1/\sqrt{6}$
	a_0	0	$-1/\sqrt{3}$	0	$i/\sqrt{2}$	0	0	$1/\sqrt{6}$	0	0
	a_+	$1/\sqrt{3}$	0	0	0	0	$-i/\sqrt{2}$	0	0	$-1/\sqrt{6}$
a_-	a_-	0	$1/\sqrt{3}$	0	0	0	0	$\sqrt{2}/\sqrt{3}$	0	0
	a_0	0	0	$-1/\sqrt{3}$	0	$-i/\sqrt{2}$	0	0	$1/\sqrt{6}$	0
	a_+	0	$-1/\sqrt{3}$	0	$-i/\sqrt{2}$	0	0	$1/\sqrt{6}$	0	0
a_0	a_-	0	0	$-1/\sqrt{3}$	0	$i/\sqrt{2}$	0	0	$1/\sqrt{6}$	0
	a_0	$-1/\sqrt{3}$	0	0	0	0	0	0	0	$-\sqrt{2}/\sqrt{3}$

$T_1 \times T_2$

	Γ	A_2	E		T_1			T_2		
M_1	M_2 M	e_2	u_+	u_-	a_+	a_-	a_0	x_+	x_-	x_0
	x_+	0	0	$-i/\sqrt{3}$	0	$\sqrt{2}/\sqrt{3}$	0	0	0	0
a_+	x_-	$1/\sqrt{3}$	0	0	0	0	$1/\sqrt{6}$	0	0	$i/\sqrt{2}$
	x_0	0	$i/\sqrt{3}$	0	$-1/\sqrt{6}$	0	0	$i/\sqrt{2}$	0	0
	x_+	$1/\sqrt{3}$	0	0	0	0	$1/\sqrt{6}$	0	0	$-i/\sqrt{2}$
a_-	x_-	0	$-i/\sqrt{3}$	0	$-\sqrt{2}/\sqrt{3}$	0	0	0	0	0
	x_0	0	0	$-i/\sqrt{3}$	0	$-1/\sqrt{6}$	0	0	$-i/\sqrt{2}$	0
	x_+	0	$i/\sqrt{3}$	0	$-1/\sqrt{6}$	0	0	$-i/\sqrt{2}$	0	0
a_0	x_-	0	0	$-i/\sqrt{3}$	0	$-1/\sqrt{6}$	0	0	$i/\sqrt{2}$	0
	x_0	$-1/\sqrt{3}$	0	0	0	0	$\sqrt{2}/\sqrt{3}$	0	0	0

Appendix B

Spin-orbit matrix elements $\langle {}^4T_2 \phi m_s | H_{so} | {}^2E \phi' m_s' \rangle$ using trigonal basis functions. (All values are to be multiplied by $-2\sqrt{2} i \xi$.)

		ϕ'	U_+		U_-	
ϕ	m_s	m_s'	1/2	-1/2	1/2	-1/2
X_+	3/2		0	0	$-i/2\sqrt{3}$	0
	1/2		$i/3\sqrt{2}$	0	0	-1/6
	-1/2		0	$1/3\sqrt{2}$	0	0
	-3/2		0	0	0	0
X_-	3/2		0	0	0	0
	1/2		0	0	$-i/3\sqrt{2}$	0
	-1/2		$-i/6$	0	0	0
	-3/2		0	$-i/2\sqrt{3}$	0	0
X_0	3/2		$i/2\sqrt{3}$	0	0	0
	1/2		0	$i/6$	0	0
	-1/2		0	0	$-i/6$	0
	-3/2		0	0	0	$-i/2\sqrt{3}$

REFERENCES

[1] A Einstein, Phys. Zeit., 18, 121 (1917).

[2] C H Townes and A L Schawlow, Phys. Rev., 112, 1940, (1958).

[3] Maiman, Nature, 187, 493, (1960).

[4] L F Johnson, R E Dietz and H J Guggenheim, Phys. Rev. Lett., 11, 318, (1963).

[5] D E McCumber, Phys. Rev. 134, A299 (1964).

[6] L F Johnson, R E Dietz and H J Guggenheim, Appl. Phys. Lett., 5, 2 (1964).

[7] L F Johnson, H J Guggenheim and R A Thomas, Phys. Rev. 149, 179, (1966).

[8] J C Walling, H P Jenssen, R C Morris, E W O'Dell and O G Petersen, OSA Annual Meeting, San Francisco, Calif., Oct 30 - Nov 3 (1978).

[9] D J Ehrlich, P F Moulton and R M Osgood, Opt. Lett., 5, 339 (1980).

[10] P P Sorokin and M J Stevenson, IBM J Res. Dev., 5, 56 (1961).

[11] Y S Vagin, V M Marchenko and A M Prokhorov, Sov. Phys. JETP, 28, 902 (1969).

[12] L F Johnson and H J Guggenheim, IEEE J.Q.E., 10, 442 (1974).

[13] A A Kaminiskii, (Laser Crystals, their physics and properties), Springer-Verlag, ( ). Also A Yariv and J P Gordon, Proc. IEEE, pp 4-29 (1963).

[14] B D Guenther and R G Buser, IEEE, J.QE-18, 1179 (1982).

[15] P Moulton, Optics News, p 9 Nov-Dec (1982).

[16] S J Still, Topical Meeting on Tunable Solid State Lasers, Arlington, VA, 16 and 17 May (1985).

[17] J C Walling, (Tunable lasers), Ed. L F Mollinauer and J C White, Springer-Verlag (1987).

[18] B Henderson and G F Imbusch, Contemp. Phys. 29, 235 (1988).

[19] P T Kenyon, L J Andrews, B McCallum and A Lampicki, IEEE, J.QE-18, 1189 (1982).

[20] A Budgor, Proc. SPIE, 46, 64 (1984).

[21] C K Jorgensen, (Absorption Spectra and Chemical bonding in complexes), Pergamon, New York (1962).

[22] H L Schlafer, H Gausmann and H Zander, Inorganic Chem 6, 1528 (1967).

[23] D L Dexter and J H Schulmann, J. Chem. Phys. 22, 1063 (1954).

[24] G F Imbusch, Phys. Rev. 153, 326 (1967).

[25] R Orbach, (Optical Properties of Ions in Solids) Ed. B. Di Bartolo, Plenum Press (1975).

[26] G F Imbusch (Luminescence of Inorganic Solids) Ed. B Di Bartolo, Plenum Press (1978).

[27] J Wong and C A Angell (Glass Structure by Spectroscopy) Mercel Dekker (1976).

[28] Y Tanabe and S Sugano, J. Phys. Soc. Japan 9, 753 (1954).

[29] C J Ballhausen (Introduction to Ligand Field Theory), McGraw-Hill (1962).

[30] J M Ziman (Electrons and Phonons), the Clarendon Press, Oxford, (1960).

[31] J A Reisland (The Physics of Phonon), John Wiley, (1973).

[32] B Di Bartolo (Optical Interactions in Solids) John Wiley (1968).

[33] G E Devlin, J A Ditzenberger and M D Sturge, Bull. Am. Phys. Soc. 7, 258 (1962).

[34] S E Stokowski, S A Johnson and P L Scott, Phys. Rev. A 147, 544, (1966).

[35] D F Nelson and M D Sturge, Phys. Rev. A 137, 1117, (1965).

[36] B Henderson and G F Imbusch (Optical Properties of Inorganic Solids), Oxford University Press (1988) (in press).

[37] A E Hughes (Defects and Their Structure in Non-Metallic Solids) Ed. B Henderson and A E Hughes, Plenum Press (1976).

[38] S Sugano, Y Tanabe and H Kamimura (Multiplets of Transition Metal Ions in Crystals), Academic Press (1970).

[39] W B Fowler (Physics of Colour Centres) Academic Press (1968).

[40] M J Weber (Physics of Q.E.) Ed. P L Kelly, B Lax and P E Tannenauld, McGraw-Hill (1966).

[41] W D Partlow and H W Moos, Phys. Rev. 157, 252 (1967). Also J R Chamberlain, D H Paxman and J L Page, Proc. Phys. Soc. (London), 89, 143, (1966).

[42] M D Sturge, Phys. Rev. B 8, 6 (1973).

[43] F Auzel (Luminescence of Inorganic Solids), Ed. B Di Bartolo, Plenum Press, (1978).

[44] L A Riseberg and H W Moos, Phys. Rev. 174, 429 (1968).

[45] C W Struck and W H Fonger, J. Lum. 10, 1, (1975).

[46] W H Fonger and C W Struck, Phys. Rev. 11, 3251 (1975).

[47] H Engstrom and L F Mollenauer, Phys. Rev. B7, 1616 (1973).

[48] J Hegarty, W Yen and M J Weber, Phys. Rev. B18, 5816 (1978).

[49] C Brecher, L a Riseberg, Phys. Rev. B21, 2607, (1980).

[50] F J Bergin, J F Donegan, T J Glynn and G F Imbusch, J. Lum., 34, 307 (1986).

[51] P Moulton, Laser Focus, p83, (May 1983).

[52] F Schmidt and C P Khattak, Laser Focus, p147 (September 1983). Also M Kokta, Topical Meeting on Tunable Solid State Lasers, Arlington, VA, Calif, (May 1985).

[53] D S McClure, J. Chem. Phys. 36, 2757 (1962).

[54] E D Nelson, J Y Wong and A L Schawlow, Phys. Rev. 156, 298 (1967).

[55] R M McFarlane, J Y Wong and M D Sturge, Phys. Rev. 166, 250, (1968).

[56] R R Joyce and P L Richards, Phys. Rev. 179, 375, (1969).

[57] L S Kornienko and A M Prokhorov, Sov. Phys. JETP, 11, 1189, (1960).

[58] B Struve and G Huber, J. Appl. Phys. 57, 45, (1985).

[59] F S Ham, Phys. Rev. A138, 1727, (1965). Also F S Ham, Phys. Rev. 166, 307, (1968).

[60] M A Gilleo and s Geller, J. Appl. Phys. 29, 380, (1958).

[61] S C Abrahams and S Geller, Acta. Cryst., 11, 437, (1958).

[62] S Geller and E A Wood, Acta. Cryst. 9, 563, (1956).

[63] R Diehl and G Brandt, Mat. Res. Bull., 10, 85, (1975).

[64] R S Rawal and R K MacCrone, J. Non-Cryst. Solids, 28, 337, (1978).

[65] A Paul, J. Mat. Science, 10, 692, (1975).

[66] S Arafa and A Bishay, Phys. Chem. Glasses, 11, 75, (1970). Also S Arafa, J. Am. Cer. Soc., 55, 137, (1972).

[67] Y M Kim and P J Bray, J. Chem. Phys. 53, 716 (1970).

[68] K Huang and A Rhys, Proc. R. Soc. London A204, 406, (1950).

[69] P Albers, E Stark and G Huber, J. Opt. Am. Soc. B3, 134, (1986). Also P Albers, PhD Thesis, Hamburg Univ., Hamburg, FRG, (1985).

[70] M D Sturge, Solid State Physics, 20, 91, (1967).

[71] F Bantien, P Albers and G Huber, J. Lum. 36, 363, (1987).

[72] H K Eigenmann, PhD Thesis, Nr 4552, (Swiss Federal Institute of Technology) Zurich, Switzerland, (1970).

[73] P Lacovara, L Esterwitz and M Kokta, IEEE J.QE 21, 1614, (1985).

[74] P Moulton, J. Opt. Soc. Am. 3, 125, (1986).

[75] C E Byvik and A M Buoncristiani, J.QE 21, 1619, (1985).

[76] B F Gachter and J A Konnigstein, J. Chem. Phys. 60, 2003, (1974).

[77] Djeva, Industrie de Pierres Scientifiques, Hrand Djevahirdjian, S A., CH. 1870 Monthey Schweiz.

[78] W A Wall, J T Karpick and B Di Bartolo, J. Phys. C. Solid State Physics, 4, 3255 (1971).

[79] W R Rapoport and C P Khattak (Solid State Laser II), Ed. A L Shawlow, Springer-Verlag (1986).

[80] E V Zharikov, V F Kitaera, V V Osiko, I R Rustonov, N N Sobolev,.Sov. Phys., Solid State, Preprint 200, Lebedev Inst., Moscow, (1983).

[81] H A Jahn, E Teller, Proc. R. Soc. London, A161, 220, (1937).

[82] W H Zachariasen, J. Am. Chem. Soc., 54, 3841, (1932).

[83] J D McKenzie (Modern Aspects of the Vitreous State) Ed. J D McKenzie, Butterworth, London, (1960).

[84] V M Goldschmidt Geochemische Verteilungsgesatze der Element VIII, Vid. Akad. Skr., Oslo, No. 8, 137 (1926).

[85] D B Hollis, S Parke and M J Payne (Solid State Laser II) Springer-Verlag (1986).

[86] B E Warren and A D Loring, J. Am. Cer. Soc. 18, 269 (1935), B E Warren, J. Am. Cer. Soc., 17, 249 (1934), also J Biscoe and B E Warren, J. Am. Cer. Soc., 21, 287 (1938).

[87] R J Bell and P Dean, Phil. Mag. 25, 1381, (1972).

[88] J E Stanworth, (Physical Properties of Glass), Oxford (1950).

[89] F A Catton and G Wilkinson (Advanced Inorganic Chemistry), Interscience, New York, (1972).

[90] T Bates and R W Douglas, J. Soc. Glass. Tech., 43, 289, (1959), also T Bates (Modern Aspects of the Vitreous State) Vol. 2, Ed. J D McKenzie (1960).

[91] R E Tischer, J. Chem. Phys., 48, 4291, (1968).

[92] R J Landry, J T Fournier and G G Young, J. Chem. Phys., 46, 1285, (1967), also J T Fournier, R J Landry and R H Bartram, J. Chem. Phys., 55, 2522, (1971).

[93] R H Clarke, L J Andrews and H A Frank, Chem. Phys. Lett., 85, 161, (1982).

[94] R C Zeller and R O Pohl, Phys. Rev. B4, 2029, (1971).

[95] R Elliot (Physics of Amorphous Materials), Longman, London, (1983).

[96] P W Anderson, B I Halperin and C M Varma, Phil. Mag., 25, 1, (1972), also W A Phillips, J. Low Temp. Phys., 7, 351, (1972).

[97] L J Andrews, A Lempicki and B C McCallum, J. Phys. Chem., 74, 5526, (1981).

[98] S A Brawer and W B White, J. Chem. Phys., 67, 2043, (1977).

[99] D L Huber in (Coherence and Energy Transfer in Glasses), Ed. P Fleury and B Golding, Plenum Press (1984). (Theoretical Studies of Optical Energy Transfer in Glasses and other Disordered Systems).

[100] S H Lin, J. Chem. Phys., 44, 3739, (1966).

[101] P M Selzer (Laser Spectroscopy of Solids), Ed. W M Yen and P M Selzer, Springer-Verlag, Vol. 49, (1986).

[102] Y V Denisov and V A Kitzel, Opt. Spec., 23, 251 (1967).

[103] A Szabo, Phys. Rev. Lett., 25, 924, (1970).

[104] L A Riseberg, Phys. Rev. Lett., 28, 789 (1972).

[105] R T Brundage and W M Yen, Phys. Rev. B33, 4436, (1986).

[106] T Kushida and E Takushi, Phys. Rev. B12, 824 (1975).

[107] G K Wertheim, M A Butler, K W West and D N F Buchanan, Rev. Sci. Instr., 45, 1369, (1974).

[108] G F Imbusch, Physica Scripta, T19, 354, (1987).

[109] Y Tanabe and H Kamimura, J. Phys. Soc. Japan, 13, 394, (1958).

[110] P M Selzer, D L Huber, D S Hamilton, W M Yen and M J Weber, Phys. Rev. Lett., 36, 813, (1976).

[111] R M McFarlane and R M Shelby, J. Lumin. 36, 179, (1987).

[112] D Hsu and J L Skinner, J. Chem. Phys. 81, 1604, (1984).

[113] J Hegarty, M M Broer, B Golding, J R Simpson and J B McChesney, Phys. Rev. Lett., 51, 2033 (1983), also M M Broer, B Golding, W H Haemmerle, J R Simpson and D L Huber, Phys. Rev. B33, 4160, (1986).

[114] J M Pellegrino, W M Yen and M J Weber, J. Appl. Phys., 51, 6332, (1981), also J M Pellegrino and W M Yen, Phys. Rev. B24, 6719, (1981).

[115] D L Huber, M M Broer and B Golding, Phys. Rev. Lett., 52, 2281, (1984).

[116] R Silby and K Kassner, J. Lum. 36, 283, (1987).

[117] H P H Thijssen, A I M Dicker and S Volker, Chem. Phys. Lett., 92, 7, (1982), also H P H Thijssen, R E Van Den Berg and S Volker, Chem. Phys. Lett., 103, 23, (1983).

[118] R A Fields, E Haindl, C J Winscom, Z H Khan, M Plato and K Mobins, J. Chem. Phys., 80, 3082, (1984).

[119] B Henderson and M Yamaga (Private Communication).

[120] D L Huber, J. Non. Cryst. Solids, 51, 241, (1982).

[121] D E McCumber and M D Sturge, J. Appl. Physics 34, 1682, (1963).